Universidad de Guanajuato

División de Ciencias e Ingenierías

ν_μ-Induced CC Coherent π^+ Production Off Carbon, Hydrocarbon, Iron, and Lead Using the MINERνA Detector

Manuel Alejandro Ramírez Delgado

Thesis submitted in partial fulfilment for the degree of Doctor of Philosophy

Advisor **Dr. Julián Félix Valdez**

Co-Advisor **Dr. Jorge G. Morfín**

León, Guanajuato - 2020

The inelastic coherent pion production induced by neutrinos is a rare process where the neutrino interacts with the nucleus as a whole. The final state particles of the interaction are a lepton and a π meson created in small angles with regards to the incoming neutrino direction. During the interaction, a small four-momentum is transferred to the nucleus, leaving it in its initial state (no nuclear breakup), with a recoil energy below the detection threshold. The process has been observed in both charged and neutral current interactions, in a variety of materials, from a few to hundreds of GeV.

Experiments struggled to find evidence of the charged current channel at low neutrino energies ($\sim$ 1 GeV), until 2014 when the MINERvA collaboration, using both muon neutrinos and muon anti-neutrinos in a CH target, was able to observe it by looking at model-independent features of the interaction.

This thesis also makes use of the MINERvA detector in the NuMI neutrino beam at Fermilab, to analyze the CC coherent production of pions, but with a more energetic and intense ν_μ beam ($2 < E_\nu < 20GeV$, peaked at $\sim 6GeV$), and including measurements from hydrocarbon, carbon graphite, iron (steel) and lead targets, allowing a wide range of nuclear sizes.

This work represents the first simultaneous measurement of the CC coherent production of pions in different materials. The first observation of the process using a pure carbon target, and the first observation in iron and lead ever. Hints of the dependence of the interaction's cross section on the number of nucleons (A) in the nucleus are also shown (A-dependence of the interaction scaling). Current models predict a cross section scaling of $A^{1/3}$, $A^{2/3}$ or even an energy-dependent one.

ACKNOWLEDGEMENTS

This goes to all the people involved. The results presented here are just another branch in which the amazing effort of many scientists, engineers, technicians and students, transformed. I am grateful to the MINERvA collaboration in general for allowing me to lead such important analysis, and for being confident in myself and in the large number of students members of the collaboration.

Special thanks go to Doctors Aaron Mislivec and Aaron Higuera who started this analysis and who published such amazing results. Of course they were guided by great advisors and scientists, with whom I also had the fortune and pleasure to work. Doctors Jorge Morfín, Kevin McFarland, Deborah Harris, Laura Fields, and Julián Félix, always delivered top notch feedback, and first class advice.

Doctors Trung Le and Daniel Ruterbories helped me with their expertise on a daily basis, also with unsurpassable quality and patience. A special mention to Doctor Leo Bellantoni, the first one to dedicate a lot of time an effort in myself as a grad student.

My parents Irma and José who always showed me the example to follow and the inspiration to move forward. I cannot express how much I thank you for teaching me to pursue what I want.

My siblings Pepe, Juan and Mariana, perhaps not aware of your contribution, thank you for always being there.

My wife Maricruz and my Daughter AnaMá, my strongest reason, the pushing force, and the most precious beings I could ever met. I owe you so much, you have given me everything. This is for you.

Content

List of Figures

List of Tables

Chapter 1

INTRODUCTION

Throughout history, apparently disconnected natural phenomena ended up being different representations of the same underlying mechanism. A falling object on the surface of the earth can be explained by the same formalism describing the movement of astronomical objects in the solar system: the law of "universal" gravitation, by Issac Newton. A thunderbolt hitting the ground follows the same laws, as those followed by salt melting ice: the laws of electromagnetism, brilliantly summarized in James Maxwell's equations. In the process of such unification, well established theories are often superseded by more complete and far reaching theories that expand the limits of the old ones. That is the case of general relativity developed mostly by Albert Einstein; and quantum mechanics built by a myriad of scientists. Both pushed Newtonian mechanics in two different directions, the former into the fast and astronomically big, the latter into the fast and atomically (and sub atomically) small, both containing Newtonian mechanics as a special case.
These are the best two theories physics currently has to explain the universe. But despite their success, they are not compatible with each other, avoiding a long searched "theory of everything", which intend to explain all known physical phenomena under the same theoretical ground.
Although incompatible with general relativity, quantum mechanics is successfully compatible with the theory of special relativity. The union of both, called "quantum field theory", is the basis for a modern understanding of particle physics.

Greek philosophers of the fourth century BC thought of matter as irreducible and indivisible particles they called "atoms" (individual in Greek), and that different properties of macroscopic matter were different arrangements of such atoms. It was not until the nineteenth century AD that John Dalton concluded experimentally that the different elements involved in chemical reactions, interact in discrete units of matter, what is now

known as atoms. By the end of that century, J.J. Thomson showed the existence of "electrons", particles almost two thousand times lighter than the lightest atom (hydrogen), with the same charge-to-mass ratio regardless of the material. He conceived the atom as a uniform positively charged substance with the negatively charged electrons embedded in it, keeping the atom electrically neutral. In 1911 Ernest Rutherford found that most of the alpha particles (helium nuclei) fired onto foils with the thickness of a few atoms, passed through them with a slight deflection. Surprisingly some were deflected in huge angles, meaning that the positive charge was concentrated in a small but very dense "nucleus". Rutherford himself would found that nuclei consist of positively charged particles, the "protons". The fact that the charge of different nuclei does not increase linearly with their mass, was explained by the presence of neutral particles in the nucleus, slightly heavier than the proton: the "neutron", discovered by James Chadwick in 1932 completing the classic model: a solar-system-like atom, with "planetary" electrons turning around the "solar" nucleus by the pull of the electromagnetic force.

Protons and neutrons existing bound in the nucleus, required the existence of a force able to hold them together, overcoming the repulsive electric force protons exert on one another. It was named the "strong force". Its range had to be about the nuclear radius (otherwise all atomic nuclei would stick together). In the late 1940s many different particles were discovered in cosmic rays, increasing the number of apparent elementary particles, without any obvious order. In 1961 Murray Gell-Mann did a successful classification of the chaotic scenario, predicting with it new hadrons (particles like the proton and neutron), which were later discovered with the exact properties foretold. He himself predicted that all hadrons must be made of arrangements of three particles called "quarks". Quarks are never observed freely, but experiments similar to Rutherford's indicate that nucleons have internal structure, in great accordance with the quark model. Quarks are bound inside the nucleons by the strong force.

The so called "beta decay", discovered by Henri Becquerel in 1896, is the process in which the atoms of some elements emit beta radiation (electrons), turning the original nucleus into a nucleus of a different element. The detailed mechanism consists of the spontaneous "mutation" of a nuclear neutron into a proton (captured by the nucleus), which is ultimately explained by the change of a "down" to an "up" quark, and an electron escaping the nucleus at high speed. This mechanism constitutes yet another elementary force, "the weak force", capable of changing the identity of fundamental particles. The force range is about the diameter of a nucleon, basically a "point" interaction between the initial particle and its decay products. The weak decay of a single particle is an stochastic event, with a very low probability.

When measuring the energy of the outgoing electrons in beta decays, it was completely baffling that a continuous energy distribution appeared, instead of the expected well defined single energy due to the difference between the initial and final nuclear masses. This meant that either energy conservation was an statistical process only, or that the electron was being accompanied by an unobserved chargeless particle of negligible mass that carried away the missing energy. The ghostly particle was later named "neutrino" (little neutral one in Italian), to differentiate it from the neutron. The neutrino was not discovered until 1956 by Frederick Reines and Clyde Cowan near a nuclear reactor, in a similar process called inverse beta decay. Two more kinds of neutrinos would later be found, one associated to a muon and one to the tau lepton (two heavier versions of the electron).

The fundamental particles and forces involving the electromagnetic, strong, and weak interactions are explained in a very precise theoretical framework called "the standard model" (SM), developed mostly during the second half of the twentieth century, that summarizes most of the knowledge of theoretical and experimental particle physics at the time. It includes two fundamental types of particles, Fermions and Bosons. The former are particles that make up ordinary matter and obey Pauli's exclusion principle, they include quarks and leptons. Bosons, on the other hand don't follow Pauli's exclusion principle. As currently understood, they are the mediators of the forces, they include the photons, Z and Ws for the electroweak interaction, and gluons for the strong force.
Richard Feynman, Shin'ichir$\bar{o}$ Tomonaga and Julian Schwinger elaborated a "relativistic quantum field theory of electrodynamics" (QED), based on previous work by Paul Dirac and Hans Bethe. This was the first successful component of the SM.
In the 1970s, attempts to create a gauge theory for the weak force similar to QED, demanded the inclusion of the electromagnetic force in the same framework. Abdus Salam, Steven Weinberg and Sheldon Glashow successfully developed the "electroweak theory" in which the electromagnetic and weak forces are treated as a single kind of interaction. This unification required the existence of a field responsible for giving mass to the neutral Z and the two charged W bosons (the carriers of the weak force), the "Higgs field".
The strong force was included in the SM also as a gauge field theory, called quantum "chromodynamics" (QCD), using QED as its base. It was built by Harald Fritzsch, Heinrich Leutwyler, and Murray Gell-Mann. As opposed to the other two forces, the strength of the strong interactions increases with the separation between quarks (this phenomenon is called confinement, the fact that quarks can only exist inside hadrons), and it gets reduced as the probing energy increases (asymptotic freedom). The carriers of the force, the "gluons", carry the strong charge themselves.

Despite its descriptive power and accuracy, the SM has failed in correctly describing

important aspects of nature.

- It cannot include the most utterly common of the macroscopic forces, "gravity". For it to fit, a theory of quantum gravity is needed. In highly dense quantum states, like in black holes or the early stages of the universe, gravity should be the dominant force, warping space-time, but no quantum theory has managed to successfully achieve the quantization of space-time itself. Different attempts such as "string theory" or "quantum loop gravity" have been proposed, but the lack of experimental evidence to their abstract concepts avoid their acceptance.

- It offers no answer to the baryon asymmetry (matter-antimatter asymmetry) of the universe, which is naturally expected due to charge conservation. It requires that mechanisms such as CP and C-symmetry violation, and baryon number violation out of thermal equilibrium had occurred in the early universe.

- The anomalous rotation of the outer regions of some galaxies is believed to be caused by "dark matter", that is supposed to interact with "normal" (baryonic) matter only through gravity. A possible candidate for dark matter are the so called "WIMP" (Weakly Interacting Massive Particles), which are not contemplated by the SM.

- The accelerated expansion of the universe implies the existence of a force able to overcome the gravitational attraction of all the matter in the universe, the so called "dark energy". It is not predicted by quantum mechanics, neither by general relativity.

- Strong and electroweak interactions (let alone gravity) have not been put under the same unified theory "grand unified theory".

- Massive neutrinos are not predicted. The SM considers them massless and therefore moving at the speed of light, which has been proven wrong by the phenomenon of neutrino oscillations, where neutrinos change flavor as they travel.

Besides this, many free parameters in the equations involved, come apparently out of nowhere, and are ultimately established by experiment. As any successful theory, it is waiting for a new and better one that can account for the lack of knowledge in the unsolved questions above, and ultimately replace it. For this to happen, going beyond the SM is needed.

Of the particles in the SM, neutrinos (and perhaps the Higgs boson) are the less understood, and remain as a source of profound mystery, and as a source of active research.

Perhaps one of the most intriguing results not accounted for in the SM, is the oscillation of neutrinos. Their oscillation depends among other variables, on the distance the neutrino travels, so if neutrinos can tell distance, they can also tell time, which means they do not travel at the speed of light, and therefore, they do have mass.
Neutrino oscillations could shed light to the baryon asymmetry in the universe, and could be a key to understanding matter and anti-matter imbalance by looking at oscillation parameters of neutrinos and anti-neutrinos and seeing if they oscillate somehow different.

Two of the "biggest" experiments (both in physical size and collaborative effort) ever designed, the DUNE and Hyper Kamiokande experiments, are meant to answer some of the fundamental questions about neutrinos. They could allow us to:

- Understand whether neutrinos and anti-neutrinos oscillate identically.
- Do neutrino astrophysics with way higher statistics than current and previous experiments, by studying neutrinos from supernovae around the Milky Way. Such neutrinos are among the most energetic in the universe.
- Do a very detailed measurement of some decays, with the search for proton decay being the most noticeable.

Neutrino oscillation experiments like DUNE will not be able to answer those important questions by themselves, they already use and will need data and results from previous neutrino experiments, specially from the ones measuring interactions of neutrinos with nuclei and nucleons. These interactions are the biggest source of systematic uncertainties in neutrino oscillation experiments, particularly in determining the energy of the neutrinos at the points they interact with the detectors (before and after oscillation). Given that neutrinos cannot be detected directly, the way their energy is measured is by measuring the energy of the detectable secondary particles produced in such interactions. The energy miss-reconstruction comes from the inability of the detectors to fully contain some produced particles, or detect neutral ones. Also, neutrinos in a given energy range can undergo different interactions that have the same or similar observables. For such reasons, neutrino interaction experiments must themselves rely on models and/or data from other particle and nuclear physics experiments. Those helper models are further constrained by performing better neutrino experiments, which in turn will be used to guide new measurements.

This thesis is aimed to unveil how the coherent production of charged pions due to the inelastic interaction of muon-neutrinos with nuclei (CC coherent pion production),

depends on the nuclear media (material) the interaction takes place on. More specifically, it compares the cross section also known as interaction probability, of coherent pion production in Hydro-carbon with the cross section of the same reaction in graphite (pure carbon), steel (mostly iron) and pure lead. It has been predicted that the cross section scales as the number of nucleons to different powers: $A^{1/3}$ or $A^{2/3}$. There is also a model that predicts an energy-dependent scaling. Knowing how the cross section scales with "A" is very useful to extrapolate neutrino interaction measurements from one material where the measurement has taken place to a material where it has not. The interaction also can mimic the signature of the "muon-neutrino disappearance" in neutrino oscillation experiments, where the pion can be mistaken as a proton. Thus by measuring the cross section in carbon, iron and lead will allow to reduce the systematic uncertainties of oscillation experiments using those materials.

Chapter 2

NEUTRINO PHYSICS

"We are ready now, turn on the sun" (Ray Davis during the first data taking at the Homestake mine). Neutrinos are nowadays one of the most active research topics in physics, in diverse areas like astrophysics, cosmology and of course particle physics. They are the second most abundant particles in the universe after photons ($\sim$ 10 billion per second pass through every cm^2 on earth), and yet the most elusive ones, as they basically just couple to the weak field (their coupling to the gravitational field is negligible). They have a mean free path of around one light-year in lead, which gives an idea of its elusiveness. This peculiarity makes them very useful, as they are the only source of study for some otherwise inaccessible regions of the cosmos, like the core of stars, from where they travel basically straight to the point of detection. They play a very important role in the energy production mechanism in medium size stars like the Sun, and carry $\sim$ 99% of the energy produced in supernovae. Despite their great importance, neutrinos are probably the particle within the standard model with most unknowns. Seminal discoveries on the field during the second half of the twenty century, have completely changed some aspects of neutrino physics with respect to the SM view, and have opened a wide spectrum of new physics beyond the SM.

2.1 The Standard Model of Particle Physics

The standard model is a gauge theory based on the $U(1) \times SU(2) \times SU(3)$ local gauge symmetry (the standard model symmetry group), from which the three "fundamental" strong ($SU(3)$), weak ($SU(2)$) and electromagnetic ($U(1)$) interactions can be derived, and furthermore, the electromagnetic and weak forces can be united in the same physical

and mathematical description, "the electroweak force". The SM is ultimately derived from Quantum Field Theory (QFT), which explains all forces and elementary particles in terms of quantized fields to which the particles are coupled. It is quite remarkable that despite being one of the biggest scientific achievements of all times, it still cannot explain gravity. Leaving gravity aside, the SM is capable to describe the majority of natural phenomena with great precision.

The overall picture of the model consists of the interaction of matter particles (fermions), by the emission and absorption of force carrier particles (bosons), plus the mechanism by which particles acquire mass. As simple as the idea may seem, some fermions are only affected by some of the forces and are completely immune to the others. These forces have some quite different, and very peculiar features that at the end make the whole picture a very complex one. Figure 2.1 shows all the particles composing the standard model.

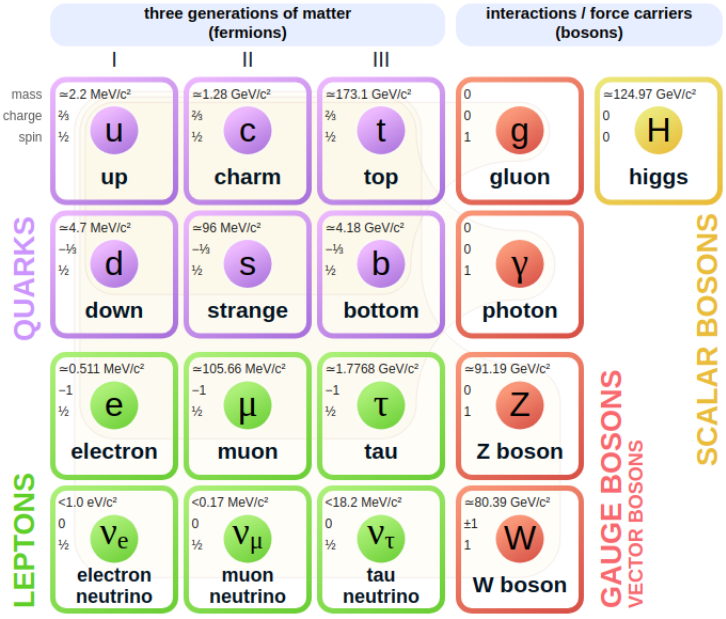

Figure 2.1: Fermions and bosons in the Standard Model. A dim line associated to each force carrier boson surrounds the fermions each boson acts upon. There exists an equal amount of fermions made of anti-mater (anti-fermions).

2.1.1 Fermion Generations

Fermions in the standard model exist as six quarks, six leptons and their corresponding anti-particles (table 2.1). All fermions are assigned "quantum numbers" that reflect their internal symmetries, which determine their coupling to the force fields and how they

interact with them. Fermions can be arranged in three generations of pairs of particles (doublets) where mass increases from the first to the third. All quarks and leptons have spin of 1/2 and therefore obey the Fermi-Dirac statistics, and Pauli's exclusion principle. Each generation carries a different lepton and quark flavor.

Generation	Leptons	Mass	Electric Charge	Quarks	Mass	Electric Charge
1st	Electron e	0.5 MeV	-1	Up u	2.3 MeV	+2/3
	Electron Neutrino ν_e	<2 eV	0	Down d	4.8 MeV	-1/3
2nd	Muon μ	105.6 MeV	-1	Charm c	1270 MeV	+2/3
	Muon Neutrino ν_μ	<0.17 MeV	0	Strange s	95 MeV	-1/3
3rd	Tau τ	1776.9 MeV	-1	Top t	173200 MeV	+2/3
	Tau Neutrino ν_τ	<15 MeV	0	Bottom b	4660 MeV	-1/3

Table 2.1: Generations of leptons and quarks in the standard model. Masses are obtained from the Particle Data Group (PDG) [20].

Charged particles from the third and second generation are unstable and decay into lighter particles. The charged lepton in the first generation, the electron, is stable. While the quarks in the first generation decay into each other ($u \leftrightarrow d$). Neutrinos in all generations are stable.

Lepton Generations

Each lepton generation consists of a charged and a neutral particle. Charged leptons: electrons, muons and taus, are coupled to the electromagnetic and weak fields; and neutral leptons: electron neutrinos, muon neutrinos and tau neutrinos couple only to the weak force. Leptons in different generations have a "flavor" or lepton number associated to that generation, and in any lepton interaction, lepton numbers of the three generations before and after the interaction are the same, which is known as lepton number conservation. There is no explanation in the SM for why charged particles have mass and the neutral particles are massless in each generation.

Quark Generations

Quark generations consist of two quarks, one with positive and one with negative electric charge of 2/3 and 1/3 of the electron charge, respectively. All six quarks couple with the strong, electromagnetic and weak fields, but unlike leptons, quarks of the same generation do not share flavor, each of the six quarks has its own flavor and a flavor number attached to it: up, down, charm, strange, top and bottom. These "flavor numbers" are conserved

in strong but not in electroweak interactions[1]. Because of their coupling to the strong force, quarks also carry "red", "blue" and "green" charge. These "color" charges, are the charge of the strong interaction. Quarks are always confined in the interior of baryons such as protons and neutrons in groups of three quarks, and in mesons such as pions and kaons in pairs of quark anti-quark. The color charge is needed to comply with Pauli's exclusion principle, as baryons can have more than one of the same quark flavor, but with different color. All baryon and meson combinations are "colorless", meaning that quark combinations are always such, that bare color charge is never observed (red, blue and green combinations in baryons and color anti-color combinations in mesons).

2.1.2 Force Carriers Bosons

Each of the three fundamental forces of the SM has a force carrier, these are called gauge bosons, they all have a spin of 1 and therefore are ruled by the Bose-Einstein statistics and do not follow Pauli's exclusion principle. Each force acts on different particles, or said other way, every kind of particle interacts through different forces. For instance, the weak force acts on all fermions, the electromagnetic force acts on quarks and charged leptons, and the strong force only on quarks (figrue 2.2).

Boson (GeV/c^2) ($1.6\times10^{-19}C$)	Mass Electric Charge Particles It Acts On		
$W^{\pm}$	80.4	±1	All fermions
Z	91.2	0	All fermions
γ	0	0	All quarks and charged leptons
g	0	0	All quarks

Table 2.2: Gauge bosons, carriers of the fundamental forces in the standard model. There are also quantum numbers for the charge equivalent for the strong and weak forces, but are omitted here for simplicity.

[1] in fact, by definition there is no flavor for the up and down, since the absence of all the other flavors would indicate the presence of quarks from the first generation, up or down

Electromagnetic Force

The electromagnetic force consists of the emission and absorption[2] of "virtual" photons by particles carrying electric charge[3]. Its range of influence is infinite and decreases as the inverse of the square of the distance $\left(1/r^2\right)$. QED is the quantum field theory of the electromagnetic field that describes the interactions among all electrically charged particles, and so, the interaction between electromagnetic waves and matter, at the fundamental level [34], [35], [36]. It was built upon Dirac's equation (which made the first relativistic version of a quantum theory, which naturally included the spin of the particles), but accounting for the infinites present at second and higher orders of perturbation theory, in a process called "renormalization" [37]. All electromagnetic processes like Compton scattering, pair annihilation, pair creation, etc., can be represented using Feynman diagrams in figure 2.2, these are a fair visualization of the process.

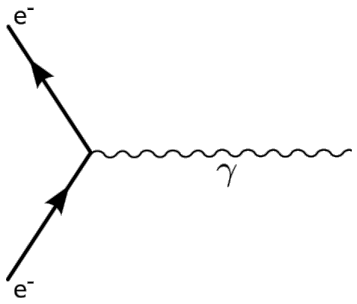

Figure 2.2: Visualization of the basic electromagnetic interactions in QED, using Feynman diagrams. Feynman depicted fermions and bosons as straight and wavy lines, respectively. The time flow goes from bottom to top, an electron comes in, exchanges a photon and leaves.

Strong Force

The strong force consists of the exchange of virtual gluons between particles carrying color (see figure 2.3). There are three color charges: blue, green and red. There exist eight different gluons, each carries a unit of color and a unit of anti-color [37]. Its range is restricted to about the size of the nuclei of the atoms $\left(10^{-15}m\right)$. Given that the gluon mass is zero, as that of the photon, its range should also be infinite. The force between

[2]this is better explained in terms of "exchange" of virtual particles, since in QFT it is not clear which of the particles emitted and which absorbed the virtual boson.

[3]virtual particles are temporary excitations of the gauge field, which time span is determined by the Heisenberg uncertainty principle.

quarks and gluons increases as their distance also increases, and the energy required to separate them, will create new hadrons. Therefore quarks and gluons cannot exist freely [4], a phenomenon called confinement [38]. Because of confinement, the range of the gluons is limited and so is the range of the strong force. The force between nucleons in the atomic nucleus is just the residual force between quarks and gluons confined inside hadrons.
In high energy interactions, as the distance between quarks and gluons decreases, the strong interaction decreases as well, at the point where the particles can be treated as "free" particles (kinematically speaking), this phenomenon is called "asymptotic freedom". Unlike the electromagnetic force, the strong force does not have a classic counterpart, it was developed in a quantum mechanical framework from the beginning, called quantum chromodynamics (QCD). It is the quantum field theory of the color field describing the interactions between quarks and gluons, mathematically based on quantum electrodynamics (QED). However, the Feynman calculus of QED can only be applied in the asymptotic freedom regime, it does not work in the long-range regime of quantum confinement. Lattice QCD is a promising candidate to work in this regime [39].

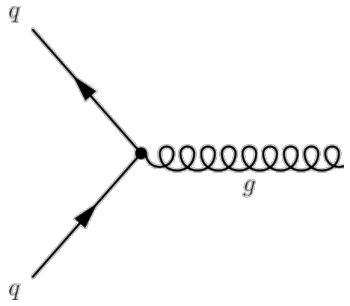

Figure 2.3: Visualization of the fundamental interaction in QCD using Feynman diagrams. Quarks and gluons are depicted as straight and curly lines, respectively. The time flow goes from bottom to the top of the image, where a quark comes in, exchanges a gluon and leaves.

The Weak Force

The weak interactions are governed by the exchange of virtual $W^{\pm}$ and neutral Z bosons, between particles carrying weak isospin, the "charge" in weak interactions. Since all fermions carry isospin ($+1/2$ for all neutrinos and up-like quarks and $-1/2$ for all massive leptons and down-like quarks), the weak force is the only elementary force that affects all fermions. Its range is even smaller than that of the strong force, about the diameter

[4] not below the so called "Hagedorn" temperature of $\sim 2 \times 10^{12} K$

of a proton $\left(\sim 1.6 \times 10^{-15} m\right)$, and was actually considered a point interaction in the first theory of beta decay [40]. Its short range is due to the fact that, unlike the other forces, the mass of the force carrier bosons, not only is not zero, but it is remarkably big (according to the Heisenberg's uncertainty principle the larger the mass of the particle, the shorter its lifetime, and the shorter its range). There is a theory of weak interactions called "quantum flavor dynamics" (QFD), but it is not commonly used to explain the weak interactions, as shown later in this section, the electroweak theory is preferred. By means of the "weak" decay, the weak force is the only force that changes the identity of the particles at the fundamental level, this implies that the quark flavor is not conserved in charged current interactions (interactions mediated by $W^{\pm}$ bosons) [41], [42] (lepton flavor is always conserved in weak interactions). In strong or electromagnetic decays, none of the fundamental particles decay into another particle.
The weak force only couples to left-handed fermions and right-handed anti-fermions, which means that it maximally violates parity. This was observed by Chien Wu in 1956 [43]. In 1964, James Cronin and Val Fitch showed that charge-parity (CP) symmetry was violated by weak kaon decays [44]. CP violation is not maximal, and its limited occurrence is associated to the dominance of matter over anti-matter (matter anti-matter asymmetry) in the universe.

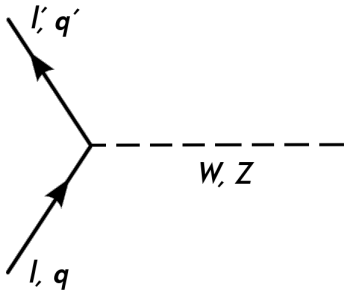

Figure 2.4: Visualization of the fundamental interaction of leptons and quarks by the exchange of intermediate vector bosons. A quark or lepton comes in, exchanges a $W^{\pm}$ or Z boson and leaves.

Because weak interactions maximally violate parity by only coupling to left-handed fermions and right-handed anti-fermions, the weak current cannot have a vector structure as in QED or QCD [37]. It needs a structure that can account for parity violation, while being relativistic invariant. The only operators compliant with both, are the vector and axial-vector (pseudovector) operators. This notation is useful in the process of unification of the electromagnetic and weak forces, where both electromagnetic and weak currents can be written in terms of "chiral spinors" [45]. The charged and neutral weak currents are

expressed in equations 2.1 and 2.2

$$j_{\mu}^{CC} = \overline{u}_f \frac{-ig_w}{2\sqrt{2}} \gamma^{\mu} \left(1 - \gamma^5\right) u_i \tag{2.1}$$

$$j_{\mu}^{NC} = \overline{u}_f \frac{-ig_z}{2} \gamma^{\mu} \left(C_V - C_A \gamma^5\right) u_i \tag{2.2}$$

where g_w and g_z are the charged and neutral coupling constants, $u_{i,f}$ are the Dirac spinors, γ^{μ} are the 4x4 $\gamma^{1,2,3,4}$ matrices, $\gamma^5 = i\gamma^1\gamma^2\gamma^3\gamma^4$, C_V and C_A are coeficients depending on the quark or lepton in the interaction.

Electroweak Unification and the Higgs Mechanism

It may seem weird and stubborn trying to unify the electromagnetic and weak forces knowing their big differences, to say, the electromagnetic force boson is massless, with infinite range and acts on particles with electric charge only, and it does not violate parity nor CP symmetries; while the weak force gauge bosons, on the other hand, are heavy and short-lived, whereby the force range is quite short, and acts on all fermions, furthermore it violates both parity and CP symmetries. However some of these properties were unknown at the moment, and when constructing the gauge theory for the weak force, including the electromagnetic force seemed to fit naturally. Hints of unification first appeared when Sheldon Glashow, Abdus Salam and Steve Weinberg were working on a renormalizable gauge theory for the weak force. Glashow first found the need for a neutral massive particle. Salam and Weinberg predicted three massive and one massless boson. The massive bosons accounted for the very short range of the weak force. The electroweak theory predicts that both forces are indistinguishable above energies $\sim$ 250 GeV and a temperature $\sim 10^{15} K$ where the four gauge bosons are massless. This temperature was attained in the early stages of the universe. As the universe cooled down, there was an spontaneous breaking of symmetry where three of the bosons acquired mass by coupling to the "Higgs field" below the temperature threshold, through the so called "Higgs mechanism" [46], [47]. The photon remains massless because it does not interact with the Higgs field at all. All other particles in the SM get their mass by interacting with this field. The different masses depend on the strength of the interaction with the field.

2.2 Neutrinos in the Standard Model

Neutrinos are described in the SM practically as originally proposed by Wolfgang Pauli: electrically neutral and very light particles (actually massless in the SM), that saved

the conservation of energy and momentum in the process known as nuclear β-decay (see chapter 1). They were first put in theoretical ground by Enrico Fermi, in a theory that tried to explain this decay [40], in which he treated it as a "point" interaction, where the range is considered zero (figure 2.5). The theory describes the weak interactions with good agreement at energies lower than $\sim 100GeV$, above which the predicted cross section increased considerably and so did the disagreement with experimental data.

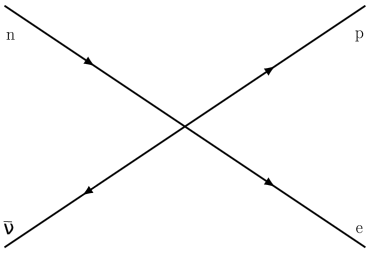

Figure 2.5: Fermi coupling for $\beta - decay$.

The neutrino (actually the anti-neutrino) was discovered in a similar process called inverse β-decay (see figure 2.6) in the Savannah River experiment performed by Frederick Reines and Clyde Cowan in 1955 [48]. They used a tank of water with cadmium chloride dissolved. In it, electron anti-neutrinos from a near nuclear reactor interacted with the quasi-free hydrogen protons in the water, resulting in a positron and a neutron. The positrons annihilated with electrons almost instantaneously creating a pair of gammas, the neutron would be captured by a nucleus of cadmium some microseconds after (figure 2.6). The signature was unmistakable and the measured cross section in close agreement with the theoretical prediction, $\sim 6.3 \times 10^{-44} cm^2$ and $\sim 6.0 \times 10^{-44} cm^2$, respectively

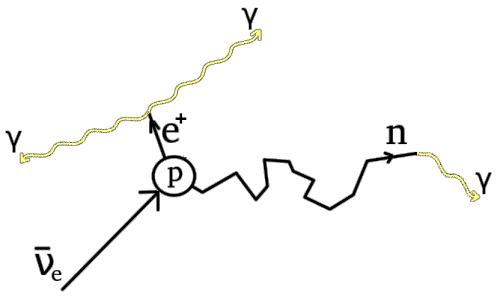

Figure 2.6: Detection signature for the electron anti-neutrino. An anti-neutrino from the nuclear reactor hits a proton in the tank, producing a positron and a neutron (broken line), in the process called inverse β-decay ($\overline{\nu}_e + p \rightarrow n + e^+$).

Particle accelerators became capable of producing neutrinos in a more controllable envi-

ronment thanks to the technique developed by Leon Lederman, Melvin Schwartz and Jack Steinberger at Brookhaven, where a proton beam impacted a fixed target, from which mesons (pions and kaons) are produced. The mesons later decay in flight into muons and muon neutrinos. The neutrino energy and direction are correlated to the initial mesons energy and direction. The muons accompanying the neutrinos were stopped by a dense steel shield. Using this technique, they discovered there was a second type of neutrino, by observing the reaction $\overline{\nu} + p \rightarrow \mu^+ + n$ and no events of the reaction $\overline{\nu} + p \rightarrow e^+ + n$ [49]. This demonstrated the existence of a neutrino associated to muon interactions, the muon neutrino ν_μ. In 2002, the DONUT collaboration at Fermilab would find the third neutrino, the one associated to tau interactions, the tau neutrino ν_τ [50], [51].

After parity violation was observed in weak processes by Chien Wu in 1956 [43], Maurice Goldhaber designed an experiment to measure the helicity of the neutrinos by measuring the circular polarization of gamma rays from the "orbital electron capture" by Europium, with the neutrino helicity being the same as that of the gamma rays [52]. He and his team found that all neutrinos had a negative helicity, confirming the maximum violation of parity in weak interactions and strongly supporting the zero mass of the neutrino, inasmuch as, had neutrinos been massive they would not have had definite helicity.

With the experimental evidence until then, the SM showed neutrinos as the only fermions with no mass and no charge. They came in three generations (flavors), and were left-handed (maximal parity violation), interacting only through the weak force.

2.2.1 Neutrino Interactions

As neutrinos only interact through the weak force, their scattering off nuclei occurs only through the exchange of $W^\pm$ in charged current (CC) interactions or through Z bosons in neutral current (NC) interactions, making these interactions very rare, due to their small cross sections. A neutrino can interact with the electrons surrounding the target nucleus, with the nucleus as a whole, with correlated or individual nucleons bound inside the nucleus, and with quarks inside nucleons. The probability that a given neutrino undergoes any of these interactions depends on its incoming energy, figure 2.7.

Going deeper into the atomic and nuclear structure, these are the important neutrino interactions for this analysis

- Neutrino-Electron Scattering - It is a rare interaction, usually a background in neutrino-nucleus or neutrino-nucleon scattering. It occurs via the CC or NC when

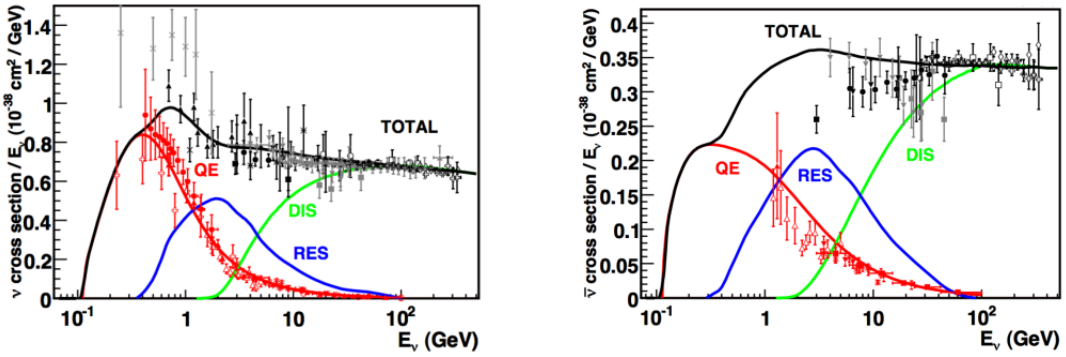

Figure 2.7: Neutrino and anti-neutrino total cross section as a function of the neutrino energy. Contributions from quasi-elastic scattering, resonance pion production and deep inelastic scattering are shown. [Figure by G.P. Zeller, Fermilab.]

the incident neutrino is an electron neutrino, and through the NC channel when the neutrino flavor is muon or tau. This is considered a point-like interaction as both the electron and neutrino are point-like fermions. The signature of such interactions is a forward going electromagnetic shower developed by the outgoing electron, figure 2.8.

- Neutrino-Nucleus Coherent Scattering - In this process the wavelength of the four-momentum transfer to the nucleus is larger than the radius of the nucleus, allowing the nucleus to act as a bound state of nucleons, where all react in phase (coherently). This is called neutrino coherent scattering, and can happen elastically (NC only) and inelastically (NC and CC). The signature in both cases is the nucleus recoiling with small energy and the creation of a forward-going lepton. The inelastic scattering produces a forward charged (neutral) pion in CC (NC) interactions, which scatters elastically off the entire nucleus, figure 2.9.

- Scattering off Correlated Nucleons - This process is mediated by the so called meson exchange current (MEC) [53], which is the exchange of mesons (pions) between nucleons. Here the scattering is from two or more nucleons, in any of the possible combinations of proton and neutron, or from the exchanged mason itself, figure 2.10.

- Neutrino-Nucleon Scattering - Momentum transfer is big enough to interact with individual nucleons within the nucleus. This includes the well known quasi-elastic scattering off neutrons and protons and resonant pion production, figure 2.11.

- Neutrino-Quark Scattering - Upon increasing momentum transferred, smaller distances can be probed. When the wavelength of the interaction is smaller than the

nucleons size, and the quark structure of the nucleus is observed. In these "deep inelastic scattering" (DIS) interactions, nucleons are broken apart, and high number of hadrons (high multiplicity) due to quark hadronization is observed, figure 2.12. It is important to remember that quarks are bound in the nucleon and interacting with each other by gluon exchange, so quarks cannot just generally be considered free particles inside the nucleus.

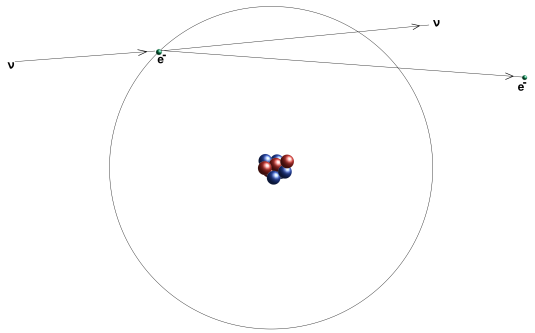

Figure 2.8: Neutrino-electron scattering. Either CC or NC.

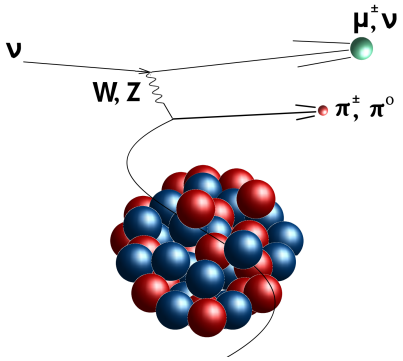

Figure 2.9: Neutrino-nucleus scattering. The example is the CC coherent pion production, where the wavelength of the momentum transferred to the nucleus is larger than the nuclear radius.

A classification of the interactions can be done more conveniently in terms of the invariant mass of the hadronic system W, defined as

$$W^2 = p_h^2 = (p_\nu + p_N - p_l)^2 \tag{2.3}$$

where p_h, p_ν, p_N and p_l are the hadronic, neutrino, target nucleon, and outgoing lepton, four-momenta, respectively. Equation 2.3 is valid just for interactions with free nucleons.

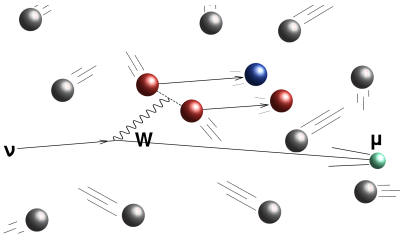

Figure 2.10: Scattering off correlated nucleons. The correlated nucleons are knocked out off the nucleus, leaving "holes", for what the interaction is called "npnh" (n-particles, n-holes). The figure shows the example of two particles being knocked out.

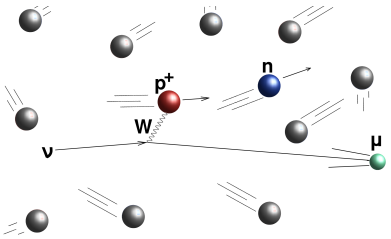

Figure 2.11: Scattering off single nucleons. The image shows a typical $\overline{\nu}$ charged current quasi-elastic (CCQE) interaction.

The invariant mass of the hadronic system is related to its multiplicity (the number of hadrons in the final state). The higher the invariant mass, the higher the multiplicity. As it will be shown shortly, understanding these interaction mechanisms for neutrinos is very important for neutrino oscillation experiments (see section 2.3.1).

Quasi-elastic Scattering

The invariant mass of this interaction is just the mass of the final state nucleon (proton or neutron mass $\sim 1.0 GeV$), it is the process with the second smallest invariant mass, after coherent pion production. In charged current quasi-elastic scattering, for instance, a neutrino (anti-neutrino) scatters off a neutron (proton) creating a muon (anti-muon) and a proton (neutron) (see figure 2.13). The scattering is always off a nucleon which is considered at rest and "free" inside the nucleus. Oscillation experiments reconstruct the neutrino energy for identified QE scattering using muon kinematics only

$$E_\nu^{QE} = \frac{m_n^2 - (m_p - E_b)^2 - m_\mu^2 + 2\,(m_p - E_b)\,E_\mu}{2\,(m_p - E_b - E_\mu + p_\mu \cos\theta_\mu)} \tag{2.4}$$

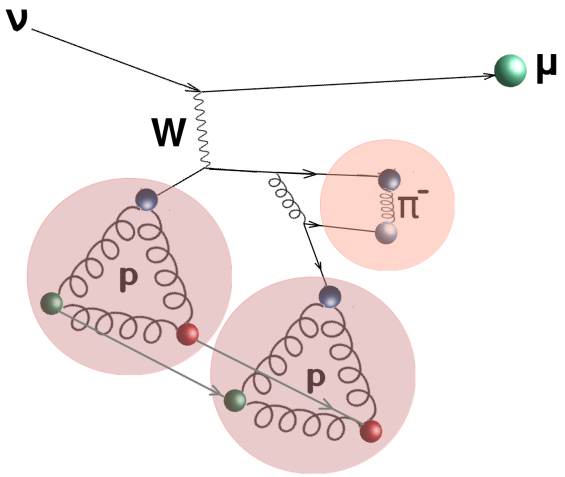

Figure 2.12: Neutrino-quark scattering (DIS). In the picture, a neutrino interacts with one of the u quarks inside a proton, turning it into a d quark. The d emits a gluon which fluctuates into a u-$\overline{u}$ pair. The "new" u couples with the spectator u and d (gray arrows), while the $\overline{u}$ couples with the "turned" d to create an anti-pion. The process is known as re-hadronization. See Feynman diagram for this interaction in figure 2.15.

where m_μ, m_n and m_p are the masses of the muon, neutron and proton, E_b is the binding energy, E_μ and p_μ are the muon energy and momentum, and θ_μ is the muon angle with regards to the neutrino beam. The Llewellyn-Smith model is used to get the predicted cross section [54]. The expression is valid for both ν and $\overline{\nu}$ interactions

$$\frac{d\sigma}{dQ^2} = \frac{m_N^2 G_F^2 \cos^2\theta_C}{8\pi E_\nu^2}\left(A\left(Q^2\right) \pm B\left(Q^2\right)\frac{s-u}{m_N^2} + C\left(Q^2\right)\frac{(s-u)^2}{m_N^4}\right) \tag{2.5}$$

where m_N is the mass of the target nucleon, G_F is the Fermi constant, θ_C is the Cabibbo angle [37], $Q^2 = -q^2 = -\left(p_\nu - p_l\right)^2$, $s = \left(p_\nu + p_N\right)^2$, $u = \left(p_l - p_N\right)^2$, $A\left(Q^2\right)$, $B\left(Q^2\right)$, and $C\left(Q^2\right)$ are functions of nucleon vector and axial form factors from electron scattering measurements [55]

Resonance Pion Production

In resonance pion production, neutrinos scatter off a nucleon, producing an excited nucleon resonance such as the Δ, which then decays into a pion and a nucleon (figure 2.14).

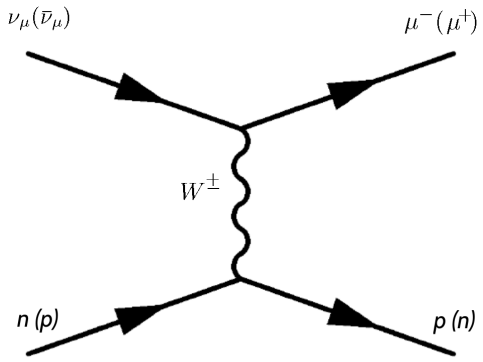

Figure 2.13: Feynman diagram for neutrino and anti-neutrino induced CCQE scattering. Particles between parentheses correspond to the particles produced by an anti-neutrino interaction.

Resonance production happens at hadronic invariant mass less than about $2GeV$. Resonance production yielding a single pion, is best modeled by the Rein-Sehgal model [56], where the cross section is calculated as

$$\frac{d^2\sigma}{dQ^2 dE_{Had}} = \frac{G_F^2}{4\pi^2}\frac{Q^2}{|\vec{p}|^2}\kappa\left(\frac{m_N^2 - M_{res}^2}{2m_N}\right)\left(u^2\sigma_L + v^2\sigma_R + 2uv\sigma_0\right)\delta\left(W - M_{res}\right) \qquad (2.6)$$

where Q^2 is the negative of the four-momentum square of the W boson, $\vec{q}$ and ν are the three momentum of and the energy transferred to the W boson , $u = \left(E_{\nu l} + E_l + |\vec{q}|\right)/2E_{\nu l}$, $v = \left(E_{\nu l} + E_l - |\vec{q}|\right)/2E_{\nu l}$, σ_L, σ_R and σ_S are the left-handed, right-handed and zero helicity partial cross section of the target nucleon, W is the invariant mass of the hadronic system, and M_{res} is the mass of the resonance.

Deep Inelastic Scattering

DIS interactions have a momentum transfer larger than $\sim$ 1 GeV and typically a hadronic invariant mass larger than $\sim$ 2 GeV. With increasing invariant mass, hadron (primary pions) multiplicity also increases. In DIS processes the nucleon structure is probed. Although the neutrino interaction happens at the quark level, quarks are always bound in the nucleon and cannot be considered free (figure 2.15). The model used in neutrino simulations is the one by Bodek and Yang [57], which uses the cross section from the fundamental theory of $\nu - q$ scattering.

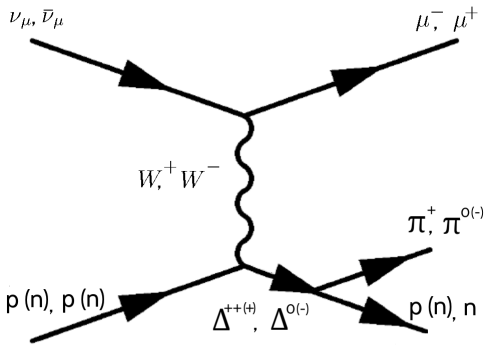

Figure 2.14: Feynman diagram for neutrino and anti-neutrino induced delta resonance pion production. Coma separated particles are neutrino and anti-neutrino induced particles. Particles within parentheses correspond to the particles produced when the nucleon target is a neutron.

$$\frac{d^2\sigma}{dxdy} = \frac{G_F^2}{2\pi} s \left(1 + \frac{Q^2}{M_W}\right)^{-2} \left[xy^2 F_1\left(x, Q^2\right) + (1-y) F_2\left(x, Q^2\right) \pm xy\left(1 - \frac{y}{2}\right) F_3\left(x, Q^2\right)\right] \quad (2.7)$$

where $x = Q^2/2p_N \cdot q$ is the fraction of the target nucleon four-momentum (p_N) taken by the quark that interacted with the W boson, and $y = pN \cdot q/pN \cdot p_{\nu l}$ is the fraction of the neutrino energy transferred to the target nucleon, $F_1\left(x, Q^2\right)$ and $F_2\left(x, Q^2\right)$ are nucleon structure functions dependent on Q^2 [57].

There exist other processes whose cross sections and models are not shown for being of little importance for the present analysis and because of their rareness. Examples of these, are the neutrino-electron cross sections for CC and NC channels, or the elastic NC coherent scattering. The theory of coherent pion production is treated in greater detail in chapter 3 as this interaction is the object of study in this thesis.

Nuclear Effects

The processes covered so far relate to the neutrino interaction itself, and the particles created from that interaction. Such particles are the signature and means by which interactions are defined. However, besides neutrino-electron scattering and neutrino interactions (like coherent pion production), all particles produced in the neutrino interaction with nucleons or with quarks within a nucleus are likely to be affected by the dense nuclear environment. This is of great importance for neutrino oscillation experiments, as these

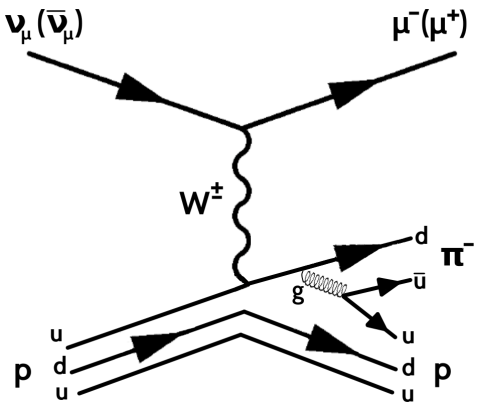

Figure 2.15: Feynman diagram for neutrino and anti-neutrino induced deep inelastic scattering. Particles within parentheses correspond to the particles produced by an anti-neutrino interaction. Here, a particular DIS interaction is shown, where a proton and a pion are created.

effects can completely change the original signature of events, or suppress the event rate for a given interaction, having as major effect the miss-reconstruction of the neutrino energy, which is crucial for calculating oscillation probabilities. These effects can be divided into "suppressing/enhancing" effects, mostly dependent on the Q^2 of the interaction; and in final state interactions (FSI) effects, due to the re-interaction of the neutrino-induced particles inside the nucleus. The cross section of these processes are not obtained from exact theoretical calculations, due to the fact that all nuclei are a many-body problem, for which there are no exact solutions.

Suppressing/Enhancing Effects These kind of nuclear effects do not modify an initial state interaction, they actually prevent them or make them happen, modifying the event rate itself.

- Pauli Blocking - In events with low Q^2, knocked out nucleons need to have enough energy to escape the nucleus, otherwise, due to the Pauli exclusion principle, its creation may be suppressed, as there will be no available states for those low-energy nucleons to occupy, so this effect reduces the event rate when the momentum transfer $\left(Q^2\right)$ is sufficiently small. This is modeled sufficiently well by the relativistic Fermi gas model (RFG) [58], [59].
- Short-Range Correlations - This happens when the wave functions of close nucleons overlap. Its range is short, less than $3fm$. This has an enhancing effect for QE

scattering at low Q^2. One or more nucleons can be knocked out. The effect is modeled using the Bodek-Ritchie tail to the RFG and spectral functions [60].

- Medium-Range Correlations - In this process neutrinos also scatter from more than one nucleon (proton-proton, neutron-neutron or proton-neutron, for instance) and is referred to as "Meson Exchange Current" (MEC) where two or more nucleons exchange mesons when they are close enough. At low Q^2 this process enhances the event rate, knocking out "n" nucleons and leaving "n" "holes" in the nucleus, leading to the "npnh" classification. Such effects are characterized by the Valencia model [61].

- Long-Range Correlations - The "random phase approximation" models the screening effect of all the nucleons have over the nucleon the neutrino is scattering off, by suppressing the coupling between the exchange $W^{\pm}$ or Z boson with the target nucleon at low Q^2. This screening is an analogy of the electromagnetic screening of molecules in a dielectric. It is usually characterized by the Nieves model [62].

Final State Interactions (FSI) The probability of re-interactions inside the nucleus is relatively high (the bigger the nucleus the larger the number of nucleons and the larger the probability). The original particles created in the neutrino interaction, can undergo different stochastic processes inside the nucleus:

- Elastic Scattering - Initial state particles can bounce off a nucleon, loosing some of its initial momentum, and changing its initial angle. By the time the particle is detected out of the nucleus its momentum and angle are changed.

- Hadron Absorption - This happens mainly for pions absorbed by proton-neutron pairs, although it also occurs in more than two nucleons. Absorption by one nucleon is kinematically forbidden by momentum and energy conservation.

- Pion Production - A pion or nucleon created in the first interaction can interact with a nucleon, producing multiple particles, such as pions.

- Charge Exchange - It consists on the hadron conversion of $p \rightarrow n$, $n \rightarrow p$; and $\pi^{\pm} \rightarrow \pi^0$, $\pi^0 \rightarrow \pi^{\pm}$ inside the nuclear medium.

All these effects are modeled using a mostly classical "hadronic cascade model" [63], it carries the initial state interaction particles through steps inside the nucleus. The probability of any of the processes for happening depends on its cross section, usually obtained

from previous data. When data is not available, extrapolations from different nuclei are performed, this has high uncertainties, given that the A-dependence of the scaling is not always well understood. More recently the GiBUU event generator has implemented a more theoretical-oriented nuclear transport approach based on the Boltzmann-Uehling-Uhlenback equation [64].

2.3 Neutrinos Beyond the Standard Model

In 1960, just a few years after the discovery of neutrinos, Raymond Davis Jr. and John Bahcall proposed the famous Homestake experiment that aimed to measure the flux of neutrinos created by the Sun. Ray Davis took on the experimental design and construction, while John Bahcall did the theoretical calculation based on the "standard solar model" (SSM) which he also helped to develop, and for which they were trying to get experimental evidence [65]. The experiment consisted in filling a tank of $\sim$ 380 m^3 at $\sim$1500 m underground with C_2Cl_4 (tetrachloroethylene) and count the number of neutrinos coming from the Sun, by looking at the reaction $\nu_e + {}^{37}Cl \rightarrow {}^{37}Ar + e^-$ and counting the number of chloride atoms that turned into argon inside the tank. Ray Davis counted only about a third of the neutrinos predicted by John Bahcall's calculation. Both the experimental method and calculation shed doubts over the scientific community, who suspected that at least one of them was wrong. Several attempts to find flaws in Bahcall's calculation were unfruitful, and later experiments like Kamiokande II [66] and Super-Kamiokande [67] using ultra pure water, and GALLEX [68] and SAGE [69] using liquid gallium confirmed the neutrino deficit, although not as low as in Davis' experiment (figure 2.16). The deficit seen by all experiments and the disagreement among them, came to be known as the "solar neutrino problem" [70].

A proposal for solving the problem was given by Bruno Pontecorvo [71] where oscillations, similar to those of kaons, would be possible if neutrinos had mass. Neutrino oscillations were latter observed by the Super-Kamiokande experiment, using muon neutrinos created in the atmosphere (atmospheric neutrinos), a difference between the muon neutrino fluxes coming from above and below ground was observed [72]; and by the SNO experiment that was able to observe the total flux of neutrinos by using heavy water [73], see figure 2.17. The SNO experiment showed that Bahcall's predictions for the total solar neutrino flux was correct, and that in accordance with neutrino oscillations, the ν_e rate seen by experiments was also correct. Both Bahcall and Davis were vindicated. Neutrino oscillations opened a new branch of physics beyond the standard model. Due to their newly discovered properties, such as mass, lots of experiments trying to measure them,

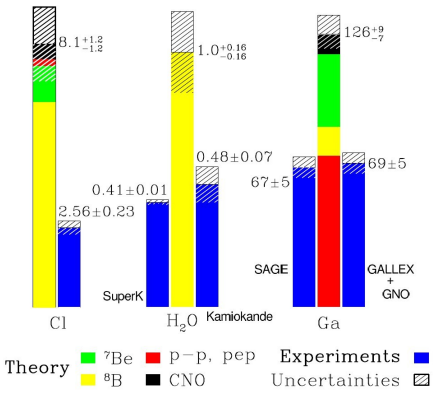

Figure 2.16: Comparison of the events predicted by the SSM and the events detected in chlorine, ultra-pure water and gallium. Blue bars are the measurements in each material, while the highest bar in each case, shows the contribution of different neutrino production mechanisms that account to the total neutrino flux. [Figure from [1].]

began to appear.

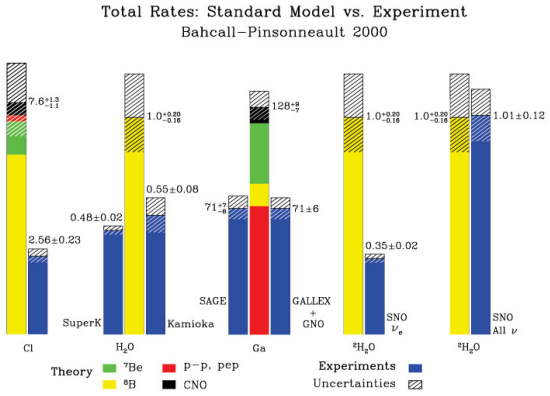

Figure 2.17: Extension to figure 2.16, in which the SNO results are included. It can be seen in the pair of columns at the far right that, the SNO measurement is in close agreement with the solar model, once all neutrino flavors have been considered. The second column from the right corresponds to the electron neutrino flux only, which is also in agreement with the Ray Davis' result. [Figure from [1].]

2.3.1 Neutrino Oscillations

As seen in section 2.1.2, CC weak interactions do not conserve quark flavor, this means there is a "mixing" of flavors in the quark sector, shown in the Kobayashi-Maskawa matrix [74]. Similarly there is a flavor mixing in the neutrino sector, where neutrinos are "allowed" to change flavor. The neutrino flavor state is defined in terms of the neutrino mass state and a mixing matrix as

$$|\nu_\alpha\rangle = U^*_{\alpha j} \, |\nu_j\rangle \tag{2.8}$$

where $\alpha = e, \mu, \tau$ are the neutrino flavors; $U_{\alpha,j}$ is the PMNS mixing matrix [75]; and $j = 1, 2, 3$ are the neutrino masses. Neutrinos travel as a superposition of all neutrino mass states, but their interaction with matter is through flavor states. The mixing matrix shows how a given flavor is related to all three masses, seemingly each neutrino mass state can be represented as a superposition of neutrino flavor states

$$\begin{aligned} U &= \begin{pmatrix} U_{e1} & U_{e2} & U_{e3} \\ U_{\mu 1} & U_{\mu 2} & U_{\mu 3} \\ U_{\tau 1} & U_{\tau 2} & U_{\tau 3} \end{pmatrix} \\ &= \begin{pmatrix} c_{13}c_{12} & c_{13}s_{12} & s_{13}e^{-i\delta} \\ -c_{23}s_{12} - s_{13}c_{12}s_{23}e^{+i\delta} & c_{23}c_{12} - s_{13}s_{12}s_{23}e^{+i\delta} & c_{13}s_{23} \\ s_{23}s_{12} - s_{13}c_{12}c_{23}e^{+i\delta} & -s_{23}c_{12} - s_{13}s_{12}c_{23}e^{+i\delta} & c_{13}c_{23} \end{pmatrix} \\ &\times \begin{pmatrix} 1 & & \\ & e^{i\alpha} & \\ & & e^{i\beta} \end{pmatrix} \end{aligned} \tag{2.9}$$

where $s_{ij} = \sin\theta_{ij}$ and $c_{ij} = \cos\theta_{ij}$, θ_{12}, θ_{23}, and θ_{13} are the mixing angles (rotations between flavor and mass phases); δ is the Dirac phase; and α and β are the Majorana phases [76]. The best estimates for these parameters are reported in the Particle Data Group [20].

As neutrinos travel, there is a probability they will be detected as flavor β given they started out as flavor α

$$P\left(\nu_\alpha \to \nu_\beta\right) = \Big| \left\langle \nu_\beta | \nu_\alpha \left(t\right) \right\rangle \Big|^2 = \Big| \sum_j U^*_{\alpha j} U_{\beta j} e^{-iE_j t} \Big|^2 \tag{2.10}$$

where the time-dependent version of equation 2.8 has been used

$$|\nu_\alpha(t)\rangle = U^*_{\alpha j} e^{-iE_j t} |\nu_j\rangle \tag{2.11}$$

For ultra-relativistic neutrinos ($E \gg m$), $t \sim L$, and the energy can be approximated as $E \simeq p + \frac{m^2}{2p} \approx E + \frac{m^2}{2E}$, L being the distance traveled by the neutrino, letting equation 2.10 as

$$P(\nu_\alpha \to \nu_\beta) = \left| \sum_j U^*_{\alpha j} U_{\beta k} e^{-im_j^2 L/2E} \right|^2 \tag{2.12}$$

The mixing matrix 2.9 can be approximated for the probability of oscillation between just two neutrino flavors, like

$$U = \begin{pmatrix} c_{12} & s_{12} \\ -s_{12} & c_{12} \end{pmatrix} \tag{2.13}$$

The equivalent of equation 2.12 considering also just two neutrino flavors, after some algebra and trigonometric substitutions, is

$$P(\nu_\alpha \to \nu_\beta) = \sin^2 2\theta \sin^2 \frac{\Delta m^2 L}{4E} \tag{2.14}$$

Δm^2 is just the difference of the squared masses of neutrinos 1 and 2, it determines the frequency of the oscillation, while the mixing angle θ determines the amplitude of the oscillation. This results shows that oscillations imply that neutrinos are massive, but also that neutrino oscillation experiments are only sensitive to differences of the neutrino masses and not to the absolute values. Because of that, there are two possibilities for the "mass hierarchy" (which of the masses is the greatest) of neutrinos. Figure 2.18 shows these two possibilities.

There are still some important unknowns for neutrinos that current oscillation experiments are trying to unveil: 1) is $\sin\delta \neq 0$?, which is to say, is there CP violation in the neutrino sector?; 2) is $m_3 > m_1$ or is $m_1 > m_3$, or what is the right mass hierarchy?; 3) what are neutrinos absolute masses?; 4) are there more than three neutrinos?; 5) are neutrinos their own anti-particles?

Last two questions are not going to be solved by neutrino oscillation experiments, because as it was mentioned, they are not sensitive to absolute masses, neither to the Majorana phases.

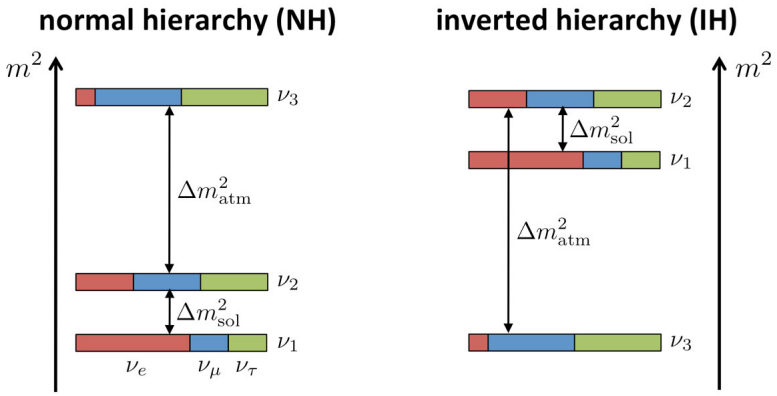

Figure 2.18: Normal and inverted mass hierarchy of neutrinos. The normal hierarchy in the left side considers the possibility when ν_3 is larger than ν_2. ν_2 has been determined to be larger than ν_1. Colors show the flavor content in each mass eigenstate. [Figure taken from [2].]

Neutrino Oscillation Experiments

Oscillation experiments seek for the collective precise measurement of all oscillation parameters present in the PMNS matrix, which will ultimately help answer questions about the nature of neutrinos. They use a "near" (usually a few hundreds of meters from the neutrino source) and a "far" detector (separated L km from the near one, as determined from equation 2.14). No experiment is capable of measuring all by itself, each one is sensitive to a given channel for which it was designed. Experiments are classified by its baseline as short-baseline (from few meters to around 100 km) and long-baseline (on the order of hundreds of km). The baseline in neutrino experiments is determined by the mass splitting Δm^2 and the energy of the neutrino beam. In any case L/E in equation 2.14 is adjusted to try to maximize the oscillation probability and event rate in the far detector. Given the difficulty in creating ν_τ beams, all experiments use neutrino or anti-neutrino beams of one of the other two flavors, and either look at the disappearance of ν_μ or ν_e (their survival probability) or at the appearance of ν_e (the $\nu_\mu \to \nu_e$ oscillation probability).

The liquid scintillator neutrino detector (LSND) was one of the first short-baseline experiments, it analyzed $\overline{\nu}_\mu \to \overline{\nu}_e$ oscillations. An excess of $\overline{\nu}_e$ was found that suggested the existence of an extra type of neutrino flavor [77]. Most of the following short-baseline experiments focused on the LSND excess or on the search for "sterile neutrinos" (neutrinos that only interact through gravity and are immune to all other forces), which were candidates to explain the extra neutrino suggested by LSND. The MiniBooNE experi-

ment at Fermilab, using different detector technology, showed agreement with the LSND excess [78], although without requiring the sterile neutrino as an explanation. Anomalies found in gallium and reactor experiments also suggest the existence of an extra neutrino, usually explained with sterile neutrinos.

The first generation of long-baseline oscillation experiments followed the result for Δm^2_{23} obtained by Super-Kamiokande from atmospheric neutrinos. K2K [79] and MINOS [80] measured more precise values of Δm^2_{23} and θ_{23} by looking at the disappearance of ν_μ. The KamLAND experiment [81] measured the Δm^2_{12} and the θ_{12} parameters, using $\overline{\nu}_e$ disappearance. θ_{13} was better measured and constrained by the Daya Bay collaboration [82]. Current experiments like T2K and NOvA are aiming to measure δ_{CP} and find the right mass hierarchy. New, more ambitious experiments, DUNE [83] and Hyper Kamiokande [84] are under construction. With baselines of 1300 and 295 km, using liquid argon and water, respectively, are the best candidates to make a meaningful measurement of δ_{CP}. Both are also suitable for improving the precision of some of the oscillation parameters (figure 2.19). ν_τ appearance is expected to be covered by DUNE, as it will be able to pass the τ lepton rest mass threshold and have way more statistics than the OPERA experiment, which recorded five of these events [85].

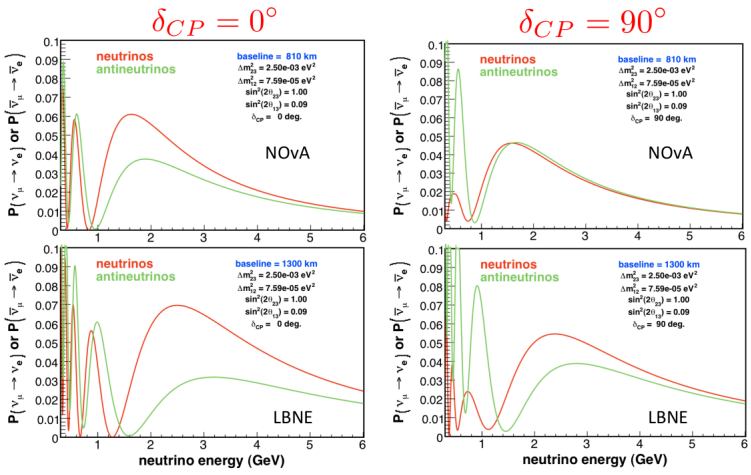

Figure 2.19: $\nu_\mu \to \nu_e$ or $\overline{\nu}_\mu \to \overline{\nu}_e$ oscillation probability as a function of the neutrino energy for NOvA and DUNE, with two different δ_{CP} phases. It is clear how in both cases, DUNE overcomes NOvA's capability to separate neutrino and anti-neutrino probabilities. [Figure taken from [3].]

The main source of systematic uncertainties in neutrino oscillation experiments is the neutrino energy, which is ultimately reconstructed from the final state particles produced in neutrino interactions (see section 2.2.1). Each of these particles have different

detector response. Neutral and escaping particles, for instance, do not deposit all of their energy. These particles often re-interact before exiting the nucleus with the possibility of undergoing different interactions that disguise both the true topology and energy of the original process. Theoretical calculations of these effects are not possible in most cases, for which models are tuned to available data in order to make predictions and comparisons. Performing more accurate, higher-statistics, and more model independent measurements can help further constraint current models and perhaps, guide theorists towards an exact calculation of the process.
Oscillation experiments mostly use charged current quasi-elastic (CCQE) interactions at low E_ν (where it dominates) to perform their measurements. In muon-neutrino beams, for instance, the signature of the process is a muon plus a proton (neutron) in neutrino (anti-neutrino) interactions. There exist background events (events with signature similar to the interaction searched for, that comes from a different process) with very different energy distributions, that if not constrained and subtracted correctly, make the true neutrino energy be over or underestimated.

The MSW Effect - Determining the Neutrino Mass Hierarchy

The Mikheyev-Smirnov-Wolfenstein (MSW) effect introduces modifications to neutrino oscillations when the beam propagates through matter [86]. When density changes, it creates resonances that further modify the mixing of neutrinos. The effect is caused by the electrons in the material, due to CC coherent scattering of the traveling neutrinos off electrons in the medium, the effect is different for anti-neutrinos given the lack of positrons. The effect is important for long-baseline experiments, since it modifies in a different way the ν_α and $\overline{\nu}_\alpha$ appearance probabilities depending on the mass hierarchy. For normal hierarchy the neutrino probability increases while the anti-neutrino one gets reduced. If the hierarchy was inverted, the opposite would be observed (figure 2.20). The MSW effect is also important for the theoretical explanation of the solar neutrino problem.

2.3.2 Other Beyond-the-Standard-Model Consequences

A large variety of beyond-the-standard-model consequences have derived from the non-zero neutrino masses, starting from the puzzling fact that their mass is several orders of magnitude smaller than all other fundamental fermions. The "seesaw" mechanism [87] explains the smallness of the neutrino masses without the need of the Higgs mechanism, if neutrinos are their own anti-particle ("Majorana neutrinos"). If that is the case, neutrinoless double beta decay would be allowed. Experiments for neutrinoless double beta

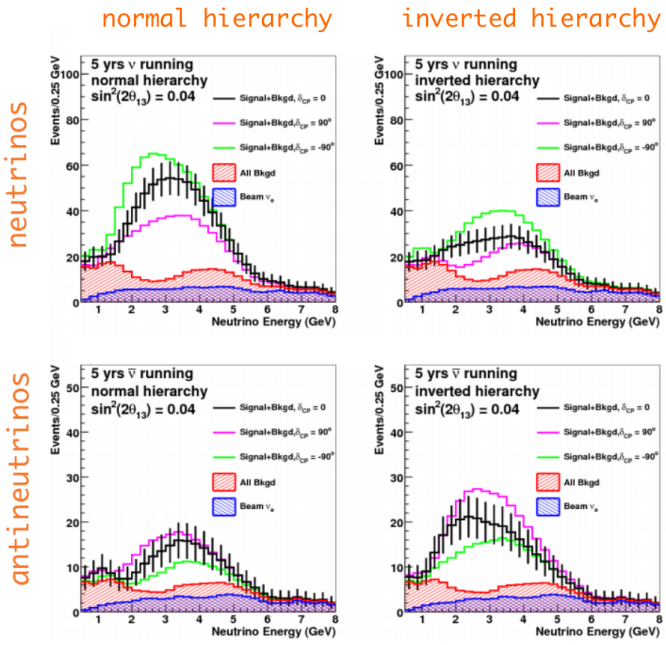

Figure 2.20: Event rate comparisons in the DUNE simulation for normal and inverted hierarchy in neutrinos and anti-neutrinos, with 0°, 90° and −90° for δ_{CP}. [Figure from [3].]

decay are already operating [88].

CP violation in the quark sector is not enough to understand why there is a matter anti-matter asymmetry in the universe ("leptogenesis"), new sources of CP violation are needed to account for the asymmetry. CP violation in the neutrino sector could offer an explanation or at least a guidance to this puzzle. In order to find $\delta_{CP} \neq 0$, precise measurements are needed, and the DUNE and Hyper-Kamiokande experiments are being designed for that.

It is interesting that all neutrino data so far can be successfully explained by the existence of only three neutrinos, besides the LSND anomaly that suggests the existence of a fourth one, the sterile neutrino. Neither the number nor the mass of sterile neutrinos have been theoretically determined.

Neutrino oscillations opened up the floor for exciting physics, whatever the answer to the neutrino puzzles are, our understanding of particle physics will change dramatically.

Chapter 3

NEUTRINO-INDUCED COHERENT PION PRODUCTION

Neutrino-induced coherent pion production is a neutrino-nucleus inelastic interaction[1] where a neutrino produces a forward-going lepton by exchanging a $W^{\pm}$ or Z boson in the proximity of a nucleus. In the PCAC approach [90], [91], the boson then fluctuates to heavy meson states, which add up and act like a pi-meson, which scatters elastically off the nucleus. The pi-meson transfers momentum to the nucleus by the exchange of a pomeron $\mathbb{P}$, which is interpreted in QCD as the exchange of two gluons [92][2]. The wavelength of the momentum transferred by the meson to the nucleus is larger than the nucleus radius, making the protons and neutrons in the nucleus react in phase (coherently) as a whole, and leaving the nucleus in its initial state, with just a small recoil energy.
The interaction is allowed to occur in both charged and neutral weak currents, and can be induced by a neutrino or anti-neutrino of any flavor

$$\nu + A \rightarrow l + \pi + A \tag{3.1}$$

where A is the nucleus, l and π are the outgoing lepton and pion. All the allowed channels for the interaction are depicted in the Feynman diagram for the coherent pion production.

[1]The elastic neutrino-induced coherent scattering can only happen through the exchange of a Z boson, its final state is an outgoing neutrino and a recoil nucleus with energy on the order of keV. It was recently observed by the "coherent" collaboration [89].

[2]The phenomenology of the interaction is not well understood, that is why PCAC is treated as a hypothesis.

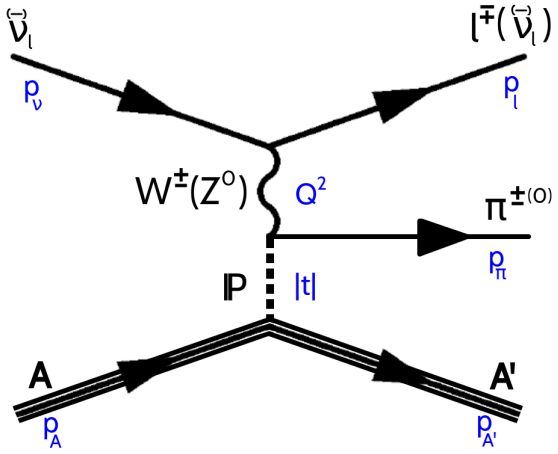

Figure 3.1: Feynman diagram of the neutrino-induced inelastic coherent pion production. Letters in black are particles, and the ones in blue are their four-momenta. Besides the anti-neutrino top bar, those particles within parenthesis are from NC interactions. A is the nucleus.

From the diagram in figure 3.1:

$$\begin{aligned} p_\nu - p_l &= p_{A'} - p_A + p_\pi \\ p_\nu - p_l &= k + p_\pi \\ k^2 &= (p_\nu - p_l - p_\pi)^2 \\ |t| &= |(p_\nu - p_l - p_\pi)^2| \end{aligned} \tag{3.2}$$

where $k \equiv p_{A'} - p_A$ is the four-momentum transferred to the nucleus, and by definition $t \equiv -k^2$.

The magnitude $|t|$ must be within a given range for the interaction to take place and remain coherent. The minimum momentum is [93]

$$|t|_{min} \simeq \left(\frac{Q^2 + m_\pi^2}{2E_\pi}\right)^2 \tag{3.3}$$

and the maximum momentum, after which the nucleus breaks up, is [10]

$$|t|_{max} = \hbar^2 / R_N^2 \tag{3.4}$$

where Q^2 is the square of the four-momentum carried by the $W^{\pm}$ or Z boson, m_π and E_π are the mass and energy of the pion, $\hbar$ is the reduced Planck's constant, and R_N is the nuclear radius.

3.1 Experimental Signature

For the CC interaction, the final state particles are the charged lepton and charged pion, plus the recoil nucleus. The observable characteristics are two charged forward particles, with negligible energy around the interaction vertex, besides the energy deposited by the charged lepton and pion, which are considered minimum ionizing particles. The nucleus is not observed, due to its small recoil energy (∼keV)

$$\nu_l + A \rightarrow l^{\mp} + \pi^{\pm} + A \tag{3.5}$$

The final state particles in the NC process, are the neutrino and the neutral pion in the forward direction, plus the recoil nucleus. Given the small recoil energy of the nucleus, the improbable detection of the neutrino, and the prompt decay of the π^0 ($\sim 8.4 \times 10^{-17}$ s), the only observables are the products of the neutral pion decay, two gammas being the dominant decay mode [20]

$$\begin{aligned} \nu_l + A &\rightarrow \nu_l + \pi^0 + A \\ \pi^0 &\rightarrow \gamma + \gamma \end{aligned} \tag{3.6}$$

When isolating events with the characteristics of a coherent pion interaction, $|t|$ is the most important signature. Unlike other parameters such as the energy around the interaction point or the momentum transferred to the recoil system Q^2, $|t|$ is a model-independent parameter.

In the CC channel, the two outgoing charged particles allow the measurement of their energy, momentum and angles (with regards to the beam or any other reference axis). That enables a direct measurement of $|t|$. Considering that the nucleus remains at rest and the energy transfer to it is then negligible, the neutrino energy can be approximated as

$$E_\nu \simeq E_l + E_\pi \tag{3.7}$$

Considering equation 3.7, $|t|$ in equation 3.2 can be approximated as follows

$$|t| \simeq \left(\sum_{i=l,\pi} p_T^i \right)^2 + \left(\sum_{i=l,\pi} \left(E^i - p_L^i \right) \right)^2 \tag{3.8}$$

where p_T and p_L are the transverse and longitudinal momenta of the pion or lepton, and E the pion or lepton energy.

In the NC channel, the outgoing neutrino is not observed, and $|t|$ cannot be determined. The condition for isolating coherent candidate events has to be obtained from the π^0 kinematics only [94]

$$E_\pi \left(1 - \cos\theta_\pi\right) \lesssim 1/R_0 \tag{3.9}$$

where E_π is the pion energy, θ_π is the angle of the pion with regards to the neutrino beam, and $R_0 = \sqrt[3]{A}\,(1.12 \pm 0.02)\,fm \sim R_N$ is the Woods-Saxon radius [94], [95]. This condition makes it a model-dependent analysis, given that imposing the above condition requires imposing conditions on the lepton kinematics and Q^2 when using equation 3.8. And given that Q^2 depends on the extrapolation from $Q^2 = 0$ to $Q^2 > 0$ in the Rein-Sehgal model, it becomes model dependent [18]. Furthermore, because the outgoing neutrino cannot be observed, it is not possible to determine the energy of the incoming neutrino, which has to be taken as the average of the beam energy [18].

3.2 Importance of Coherent Pion Production

3.2.1 Weak Currents Nature

Coherent pion production on its own, has the capability to test the nature of the weak current, by providing a test of the partially conserved axial-vector current (PCAC) hypothesis [90]. This hypothesis is important because it allows to relate the neutrino-nucleus coherent scattering to the elastic pion-nucleus interaction. Per equation 3.4, the maximum momentum transferred to the nucleus before breaking coherence, depends on the nuclear radius, and the cross section of the neutrino-nucleus interaction (equation 3.21) depends on the number of nucleons "A" present in the nucleus. As it will be shown in chapter 6, this thesis provides valuable data that can help test the PCAC hypothesis in different materials. It includes the first measurement of the coherent pion production from iron and lead.

3.2.2 Neutrino Oscillation Experiments

Neutrino oscillation experiments rely on the energy reconstruction of the neutrino to measure oscillation probabilities. The neutrino interaction used as signal in those experiments, is the dominant interaction in the neutrino energy regime designed for the detector (figure 2.7). In any case, there are always backgrounds that mimic the signal. In low-energy experiments ($\lesssim$ 2 GeV), the dominant neutrino interaction is the CCQE scattering, which has as signature a muon and a proton in ν_μ beams, and an anti-muon and a neutron in $\overline{\nu}_\mu$ beams. This process is used as the signal in ν_μ-disappearance measurements, for which the CC coherent pion production is a background. In neutrino beams the charged pion can be misidentified as the proton, while in anti-neutrino beams the pion can have very low energy and escape detection, also faking the signal.
The NC coherent pion production represents a background for ν_e-appearance measurements in cases where the gammas from the π^0 decay are mistaken as electrons from the signal.
Although the inelastic coherent pion production is considered a rare process in comparison to DIS, resonance production, or CCQE scattering, which dominate in different regions of the neutrino energy spectrum (see figure 2.7), it still represents a significant percent of the total event rate in neutrino and anti-neutrino interactions (in a previous measurement by MINERvA in a hydrocarbon target, at 3 GeV neutrino energy, around 1% (3%) of the total neutrino (anti-neutrino) event rate corresponded to CC coherent pion production [18]).

3.2.3 Cross Section Scaling

Although the neutrino-nucleus coherent scattering has already been observed in a variety of materials (section 3.4) at both low and high neutrino energies, in both NC and CC, it has never been measured in different materials simultaneously. This thesis presents the measurement of the CC channel in carbon, iron, lead and hydrocarbon in a muon-neutrino beam. This first simultaneous measurement of different materials has the benefit of spanning over quite different nuclei, which provides the chance to determine the scaling of the cross section as a function of the number of nucleons "A". Scalings of $A^{1/3}$ and $A^{2/3}$, as well as energy dependent are predicted [4], [93], [96]. This scaling gives the possibility of extrapolating parameters like the cross section of the interaction, to materials where measurements are not available.

3.3 Theoretical Formalism

The neutrino energy region this analysis is focused on ($2.0 < E_\nu < 20.0$ GeV), requires a model that can make predictions in that region. There exist two different approaches that models for coherent pion production by neutrinos are based on

- PCAC hypothesis [94], [97], [4], [98], [91], [93], [5], [6], [99], [100]. PCAC relates the weak charged and neutral currents to the pion through the divergence of the axial-vector current. These models make use of Adler's theorem (section 3.3.1), which allows them to get an expression for the neutrino-nucleus coherent pion production. These models are valid for neutrino energies from $\sim$ 1 GeV to hundreds of GeV.
- Microscopic models [101], [102], [103], [104], [105]. These models include different neutrino-nucleon processes added in phase to produce a constructive interference of all the nucleons in the nucleus, such that the net result is the nucleus interacting as a whole, while leaving all the nucleons in their initial state. Below $\sim$ 1 GeV, the dominant neutrino-nucleon process involved in constructing the coherent pion production process, is the production of a Δ resonance, which is modified along with the pion wave function to account for the nuclear medium. Above $\sim$ 1 GeV, other processes, involving higher invariant mass, are also relevant, but for which no similar modifications exist yet, making the models limited below that neutrino energy as of now. They are currently undergoing the necessary modifications to give predictions at higher neutrino energies.

Therefore this analysis and all others involving energies grater than $\sim$ 1 GeV, use at least one of the PCAC models. This analysis uses the PCAC model of Rein and Sehgal [5] to perform all the model-dependent calculations and comparisons.

3.3.1 The Rein-Sehgal Model

Adler's Theorem

All PCAC models are based on the Adler's PCAC theorem. This theorem proposes the case of a high-energy neutrino reaction $\nu + \alpha \rightarrow l + \beta$, where ν is the incoming neutrino, α the target nucleon or nucleus, l the outgoing lepton, and β is a system of strongly interacting particles. With the incoming neutrino and the outgoing lepton parallel to each other (the so called "parallel configuration", where $Q^2 = 0$), and the mass of the lepton is

neglected. In that configuration the squared matrix element of the interaction, averaged over lepton spin, only depends on the divergences of the vector and axial vector weak currents [106]. The matrix element of the interaction is

$$\mathcal{M} = \frac{G_F}{\sqrt{2}} \overline{u}_l \gamma_\mu \left(1 - \gamma^5\right) u_\nu \left\langle \beta \right| V^\mu + A^\mu \left| \alpha \right\rangle \tag{3.10}$$

where G_F is the Fermi constant, V and A are the vector and axial currents, and the spinors u and the Dirac matrices γ were already explained in chapter 2. Averaging over spin states, and requiring Adler's conditions (parallel configuration and zero lepton mass), the amplitude of the interaction is

$$\begin{aligned} \left\langle \left| \mathcal{M} \right|^2 \right\rangle &= \frac{2G_F^2}{\nu^2} E_\nu E_l q_\mu q_\nu \left\langle \beta \right| V^\mu + A^\mu \left| \alpha \right\rangle \left\langle \beta \right| V^\nu + A^\nu \left| \alpha \right\rangle^* \\ &= \frac{2G_F^2}{\nu^2} E_\nu E_l \left\langle \beta \right| \partial_\mu \left(V^\mu + A^\mu\right) \left| \alpha \right\rangle \left\langle \beta \right| \partial_\nu \left(V^\nu + A^\nu\right) \left| \alpha \right\rangle^* \\ &= \frac{2G_F^2}{\nu^2} E_\nu E_l \left\langle \beta \right| \partial_\mu \left(A^\mu\right) \left| \alpha \right\rangle \left\langle \beta \right| \partial_\nu \left(A^\nu\right) \left| \alpha \right\rangle^* \end{aligned} \tag{3.11}$$

where ν and $q_{\mu,\nu}$ are the energy and four-momentum transferred to the recoil system, and E_ν and E_l are the neutrino and lepton energies. The divergence of the vector current vanishes using the conservation of the vector current (CVC) hypothesis [107], [106]. This is only valid in the parallel configuration, when $Q^2 = 0$. Because of PCAC, the divergence of the axial-vector current is related to the pion decay

$$\left\langle 0 \right| \partial_\mu A^\mu \left| \pi \right\rangle = f_\pi m_\pi \phi \tag{3.12}$$

where f_π is the pion decay constant or pion form factor, m_π is the pion mass, and ϕ is the pion field, the $|0\rangle$ and $|\pi\rangle$ are the vacuum and pion states. The divergence of the vector current has again vanished because of CVC. Based on PCAC, Adler's theorem allows to relate the reaction $\alpha \to \beta$ (neutrino coherent pion production) to $\pi + \alpha \to \beta$ (pion-nucleus elastic scattering)

$$\left| \left\langle \beta \right| \partial_\mu A^\mu \left| \alpha \right\rangle \right|^2 = f_\pi^2 \left| \mathcal{M}\left(\pi + \alpha \to \beta\right) \right|^2 \tag{3.13}$$

Substituting equation 3.13 into equation 3.11, and putting the amplitudes in terms of cross sections

$$\left.\frac{d^3\sigma_{coh}^{CC}}{dQ^2 d\nu d|t|}\right|_{Q^2=0} = \frac{G_F^2 f_\pi^2}{2\pi^2}\frac{E_l}{\nu E_\nu}\frac{d\sigma^{\pi^\pm A}}{d|t|} \tag{3.14}$$

where the triple differential cross section, is the cross section of the CC coherent pion scattering with regards to the square of the four-momentum transferred to the W or Z boson, the energy transferred to the recoil system, and the square of the four-momentum transferred to the nucleus; and $d\sigma^{\pi^\pm A}/d|t|$ is the differential cross section of the pion-nucleus scattering, as a function of the four-momentum transferred to the nucleus squared.

This allows the models based on PCAC to get a cross section for the neutrino-nucleus interaction based on the cross section of the elastic pion-nucleus scattering.
D. Rein and L. Sehgal [4] used this expression to model the coherent pion production of neutral pions, adding a propagator term to the cross section obtained by Adler (equation 3.14) in order to include non-forward interactions $\left(Q^2 > 0\right)$.

Extrapolation to $Q^2 > 0$

The extrapolation is done by adding a propagator term $\left(\frac{m_A^2}{m_A^2+Q^2}\right)^2$, where $m_A \approx 1$ GeV, is the axial vector mass.

The differential cross section of the elastic pion-nucleus interaction can be expressed as

$$\frac{d\sigma^{\pi^\pm A}}{d|t|} = A^2\Big|F_N\left(|t|\right)\Big|^2\left.\frac{d\sigma^{\pi^\pm N}}{d|t|}\right|_{|t|=0} \tag{3.15}$$

where A is the number of nucleons inside the nucleus, $F_N\left(|t|\right)$ the nuclear form factor, and $d\sigma^{\pi^\pm N}/d|t|$ is the differential cross section of the pion with the "nucleons", in the forward direction ($|t| = 0$). The nuclear form factor is expressed as

$$\left|F_N\left(|t|\right)\right|^2 = e^{-b|t|}e^{-\frac{9A^{1/3}}{16\pi R_0^2}\sigma_{inel}^{\pi^\pm N}} \tag{3.16}$$

where $b = \frac{1}{3}R_N^2$ is the slope of the exponential in the $|t|$ distribution, $R_N = R_0 A^{1/3}$ is the nucleus radius, and $R_0 = \sqrt[3]{A}\left(1.12 \pm 0.02\right) fm \sim R_N$ (see equation 3.9). Using the optical

model [108], the differential cross section of the pion-nucleon cross section can be written as

$$\left.\frac{d\sigma^{\pi^{\pm}N}}{d|t|}\right|_{|t|=0} = \frac{1}{16\pi}\left[\sigma_{tot}^{\pi^{\pm}N}\right]^2\left(1+r^2\right) \tag{3.17}$$

where $r = Ref_{\pi N}(0)/Imf_{\pi N}(0)$ is the ratio of the real and imaginary parts of the $\pi^{\pm}N$ amplitude, $\sigma_{tot}^{\pi^{\pm}N}$ is the pion-nucleon total cross section, for which two parametrizations were used, obtaining similar results.

Inserting equations 3.17 and 3.16 into equation 3.15, and then inserting equation 3.15 into equation 3.14 and multiplying by the propagator term, the triple differential cross section can be written as

$$\begin{aligned}\frac{d^3\sigma_{coh}^{CC}}{dQ^2d\nu d|t|} &= \frac{G_F^2 f_\pi^2}{2\pi^2}\frac{E_l}{\nu E_\nu}A^2\left(\frac{m_A^2}{m_A^2+Q^2}\right)^2 \\ &\times \left(e^{-\frac{1}{3}R_0^2A^{2/3}|t|}e^{-\frac{9A^{1/3}}{16\pi R_0^2}\sigma_{inel}^{\pi^{\pm}N}}\right)\frac{1}{16\pi}\left[\sigma_{tot}^{\pi^{\pm}N}\right]^2\left(1+r^2\right)\end{aligned} \tag{3.18}$$

Equation 3.18 is the one used by most of the experiments measuring cross sections of CC coherent interactions before 2007, when new correction including the mass of the lepton (muon) were added [5]. Experiments measuring the NC channel used a similar expression, which is related to the CC cross section, valid in the parallel configuration, and for isoscalar nuclei

$$\left.\frac{d^3\sigma_{coh}^{NC}}{dQ^2d\nu d|t|}\right|_{Q^2=0} = \frac{1}{2}\left.\frac{d^3\sigma_{coh}^{CC}}{dQ^2d\nu d|t|}\right|_{Q^2=0} \tag{3.19}$$

Rein-Sehgal calculation predicts a scaling of the total NC and CC coherent cross sections with the number of nucleons, close to $A^{1/3}$ (figure 3.2)

Lepton Mass Inclusion

S. Adler proposed a correction to the cross section where the mass of the lepton is not neglected [109]. The original reaction $\nu + \alpha \rightarrow l + \beta$ receives a contribution from the

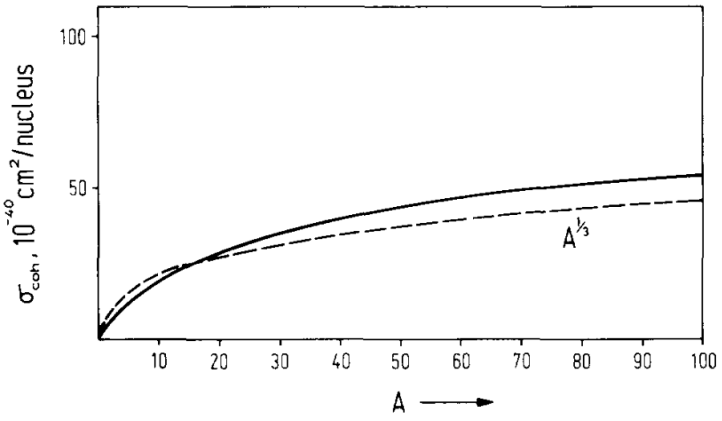

Figure 3.2: Total NC coherent cross section as a function of the nuclear number A, using neutrinos of 2 GeV. The same scaling is predicted for CC and anti-neutrino interactions. The dashed line is the scaling pattern if the cross section scaled exactly as $A^{1/3}$, while the solid line is the scaling obtained using the calculation by Rein and Sehgal. [Figure from [4].]

exchange of a charged pion between the lepton vertex $\nu \to l$ and the hadron vertex $\alpha \to \beta$. The amplitude of this contribution creates a destructive interference with the remaining amplitude. This has a suppression of the cross section at Q^2 values smaller than ~ 0.1 GeV, as shown in figure 3.3. The correction is

$$\begin{aligned} \mathcal{C} &= \left(1 - \frac{1}{2}\frac{Q^2_{min}}{Q^2 + m^2_\pi}\right)^2 + \frac{1}{4}\frac{\nu}{E_\nu}\frac{Q^2_{min}\left(Q^2 - Q^2_{min}\right)}{\left(Q^2 + m^2_{min}\right)^2} \\ &\times \theta\left(Q^2 - Q^2_{min}\right)\theta\left(y - y_{min}\right)\theta\left(y_{max} - y\right) \end{aligned} \tag{3.20}$$

where $Q^2_{min} = m^2_l \frac{\nu}{E_\nu - \nu}$, $y = \nu/E_\nu$, $y_{min} = m_\pi/E$ and $y_{max} = 1 - m_l/E$

The cross section for the CC coherent interaction (equation 3.18), with the correction due to the lepton mass, reads

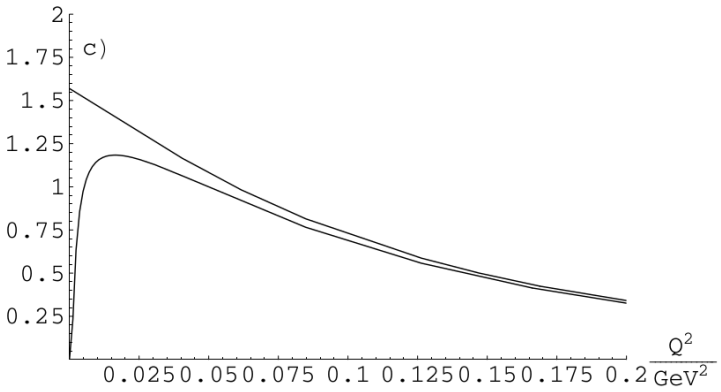

Figure 3.3: Suppression of the CC cross section on carbon for $Q^2 \lesssim 0.1 GeV/c^2$ and $E_\nu = 2.0$ GeV. The upper (lower) distribution corresponds to the cross section without (with) the lepton mass correction. [Figure from [5].]

$$\begin{aligned}
\frac{d^3\sigma_{coh}^{CC}}{dQ^2 d\nu d|t|} &= \frac{G_F^2 f_\pi^2}{2\pi^2}\frac{E_l}{\nu E_\nu} A^2 \left(\frac{m_A^2}{m_A^2+Q^2}\right)^2 \\
&\times \left(e^{-\frac{1}{3}R_0^2 A^{2/3}|t|} e^{-\frac{9A^{1/3}}{16\pi R_0^2}\sigma_{inel}^{\pi^\pm N}}\right) \frac{1}{16\pi}\left[\sigma_{tot}^{\pi^\pm N}\right]^2 \left(1+r^2\right) \\
&\times \left(1-\frac{1}{2}\frac{Q_{min}^2}{Q^2+m_\pi^2}\right)^2 + \frac{1}{4}\frac{\nu}{E_\nu}\frac{Q_{min}^2\left(Q^2-Q_{min}^2\right)}{\left(Q^2+m_{min}^2\right)^2} \\
&\times \theta\left(Q^2-Q_{min}^2\right)\theta\left(y-y_{min}\right)\theta\left(y_{max}-y\right) \qquad (3.21)
\end{aligned}$$

Berger-Sehgal Model

The original Rein-Sehgal model [4] and its later modification [5], modeled the pion-nucleus elastic interaction in terms of pion-nucleon differential cross sections. The modeling of nuclear effects for the pion (like absorption and nuclear scattering) results in high uncertainties for pion energies less than about 1 GeV. The availability of pion-carbon scattering data in that energy region, allowed the parametrization of the pion-nucleus cross section using a simple ansatz

$$\frac{d\sigma^{\pi^\pm C}}{d|t|} = A_1 e^{-b_1|t|} \qquad (3.22)$$

where the constants A_1 and b_1 are energy dependent (function of the pion energy) and fit to the pion-carbon scattering data. For pion energies larger than about 0.7 GeV the

Berger-Sehgal modification agrees with the original Rein-Sehgal model. But for energies around 0.3 GeV, the Rein-Sehgal model over predicts the pion-carbon cross section as shown in figures 3.4 and 3.5.

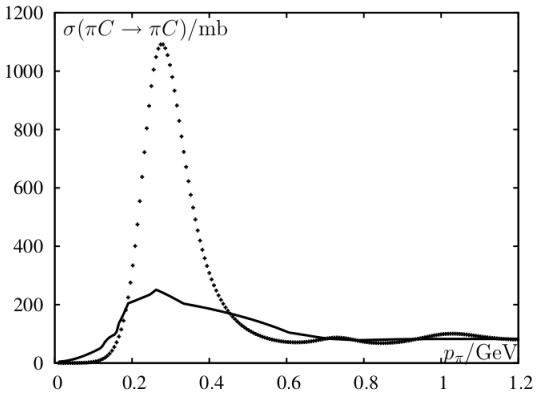

Figure 3.4: Comparison of the Rein-Sehgal (dashed line) and Berger-Sehgal (solid line) models for the elastic pion-carbon cross section, clearly overestimated by the former in the Δ resonance region. Both agree at pion energies larger than ~ 0.7 GeV. [Figure from [6].]

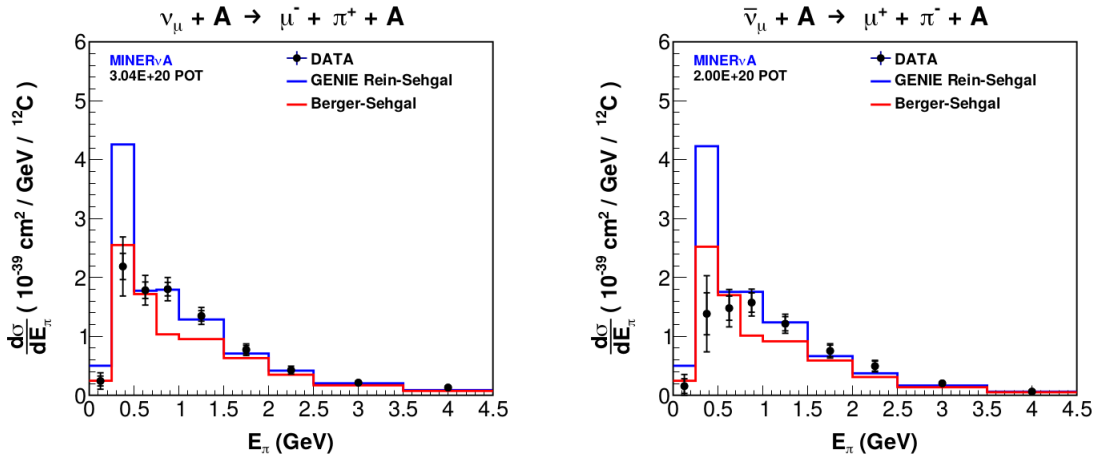

Figure 3.5: Measurements of the differential cross sections $d\sigma/dE_\pi$ on carbon, by a previous MINERvA measurement [7]. The data shows a better agreement with the Berger-Sehgal model at $0.2 \lesssim E_\pi \lesssim 1.5$ GeV.

The Berger-Sehgal model is not used in this analysis. Further comparisons to it, are expected. Even though this analysis uses data from carbon targets, iron and lead are also used, in which case there are no pion-nuclei data. So it is not obvious the need to use the Berger-Sehgal model.

3.4 Previous Measurements

This section summarizes the measurements of the neutrino-induced coherent production of pions in both "Neutral" and "Charged" currents up to date. Their importance regarding the study of weak currents, and neutrino oscillation experiments, are included.

3.4.1 NC Measurements

Coherent pion production by neutrinos was first observed in the Neutrino-Electron Reactions (NUE) spark chamber at CERN [110], [111]. It was reported by the Aachen-Padova collaboration in 1983 [8], using a sample of forward going particles consistent with single NC π^0s produced by both muon neutrinos and muon anti-neutrinos scattering off ^{27}Al, with an average neutrino energy close to 2 GeV (figure 3.6)

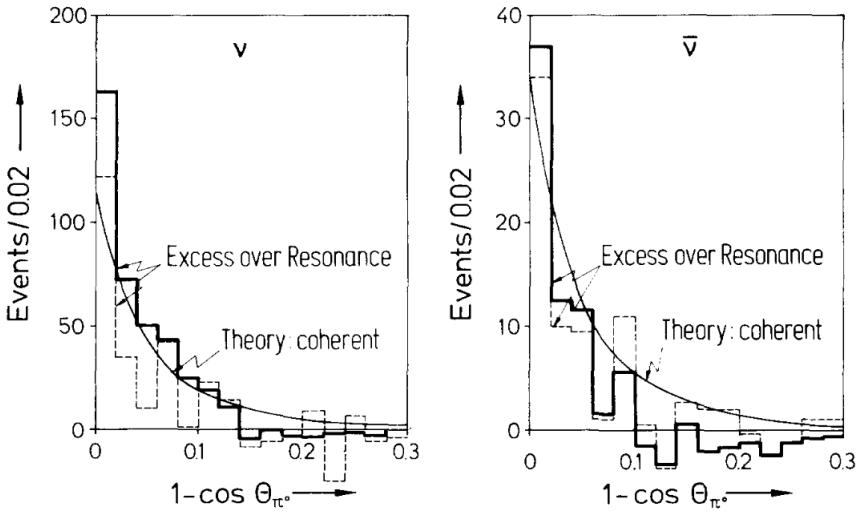

Figure 3.6: First observation of neutrino and anti-neutrino induced coherent pion production. Neutrino and anti-neutrino angular distributions, where an excess of forward particles due to π^0 is shown. The solid and dashed histograms are the MC prediction and the data sample, respectively, after the resonant pion production background has been subtracted. The solid curves are the theoretical predictions from the Rein-Sehgal model [4]. [Figure from [8].]

More experiments during that decade continued seeing coherent pions from NC, at different targets (aluminum, Freon, marble and neon), with average neutrino energies $2 \lesssim E_\nu \lesssim 31$ GeV (see table 3.1). Due to the impossibility of measuring $|t|$, these experiments had to rely on the condition in equation 3.9, looking for electromagnetic showers from two

gammas in the forward direction, with almost null activity around the vertex. Despite their limited statistics and therefore huge cross section uncertainties, they were still able to make meaningful comparisons of their results to PCAC models such as those of Lackner [94] and Rein-Sehgal [4]. These comparisons allowed testing the PCAC hypothesis about the nature of the recently discovered weak neutral current. Data were in good agreement with the Rein-Sehgal model, but with huge uncertainties, specially at high neutrino energies.

After the discovery of neutrino oscillations, the interaction became significant once more, due to the importance of the NC coherent pion production channel as a background for ν_e appearance experiments. New experiments had to be designed to work at the lower neutrino energy regime used by oscillation experiments, $1 \lesssim E_\nu \lesssim 10$ GeV. The first NC low-energy experiment measuring coherent pions from neutrinos, was done by MiniBooNE using the Booster beam (chapter 4) with energies < 2 GeV on a mineral oil target (CH_2). It increased the statistics by a factor ~ 100 compared to the early high energy measurements. MiniBooNE then showed that the NC process exists in low energies, although in a lower rate than predicted by the Rein-Sehgal model. This result reduced the uncertainty on the π^0 production in neutrino oscillation experiments from $\sim 25\%$ to $\sim 5\%$ [26].
Two more measurements by the NOMAD [27] and SciBooNE [12] collaborations also observed this interaction, and had fairly good agreement with the Rein-Sehgal model.
It can be seen in table 3.1 that the NC coherent pions were successfully observed in low and high energies in both neutrino and anti-neutrino beams.

EXPERIMENT	**YEAR**	**BEAM**	$< E_{\nu(\overline{\nu})} >$**, range** $[GeV]$	**MATERIAL**	$< A >$
Aachen-Padova	1983	$\nu/\overline{\nu}$	2	Al	27
Garmamelle	1984	$\nu/\overline{\nu}$	2	CF_3Br (Freon)	36
SKAT	1985	$\nu/\overline{\nu}$	7	CF_3Br (Freon)	36
CHARM	1985	$\nu/\overline{\nu}$	31 (24)	$CaCO_3$ (Marble)	20
15' BC	1986	ν	20	NeH_2	20
MiniBooNE	2008	ν	0.7	CH_2	12
NOMAD	2009	ν	24, 2.5-300	C	12.8
SciBooNE	2010	ν	0.8	C	12

Table 3.1: Summary of NC coherent pion production experiments. The neutrino beam energies go from less than 1 GeV to ~ 300 GeV. Materials used are: aluminum, Freon, marble, neon and carbon. Information is from [8], [21], [22], [23], [24], [25], [26], [27], [12]

3.4.2 CC Measurements

The first evidence of the CC interaction was obtained by the WA59 collaboration [9] using an anti-neutrino beam of 40 GeV of average neutrino energy and the Big European Bubble Chamber (BEBC) [112] at CERN, filled with NeH_2 as the target (see figure 3.7).

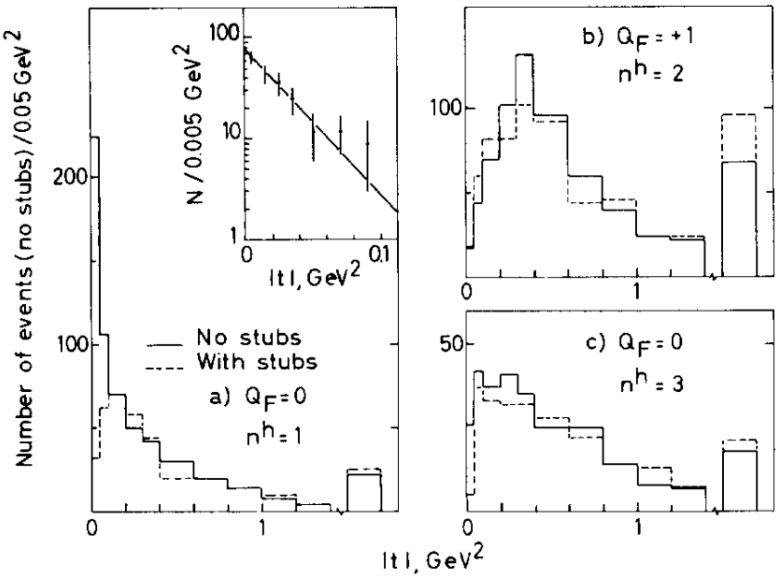

Figure 3.7: First observation of the CC neutrino induced coherent pion production. Anti-neutrino $|t|$ distributions for $Q_F = 0, n^h = 1$; $Q_F = 1, n^h = 2$, and $Q_F = 0, n^h = 3$. Where Q^F and n^2 are the electric charge and number of hadrons in the final state. The solid (dashed) lines show events without (with) vertex activity. It is clear the high $|t|$ peaks near zero. The insert plot is a logarithmic zoom from $0.0 < |t| < 0.1$. [Figure from [9].]

As the momentum transferred to the nucleus $|t|$ was available, more experiments were able to observe the CC coherent interaction. Experiments in the 80's and 90's obtained the cross section of the CC channel in a variety of materials (carbon, neon, glass and Freon), with an average neutrino energy range of $7 \lesssim E_\nu \lesssim 150$ GeV (see table 3.2). In figure 3.8 all high energy CC, neutrino and anti-neutrino measurements are compared with the Rein-Sehgal and the Bel'kov-Kopeliovich [96] models. The data is described fairly well by both models at those energies.

K2K [11] and SciBooNE [30], searched for the CC interaction in the energy relevant for neutrino oscillations, trying to constraint the uncertainties in ν_μ disappearance experiments due to charged coherent pions. Unlike MiniBooNE, NOMAD and SciBooNE in the NC channel, they found NO evidence of the CC coherent π^+ interactions. This interaction

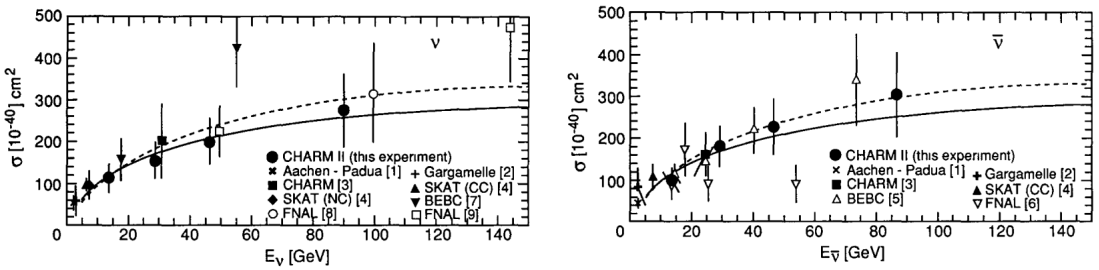

Figure 3.8: Neutrino and anti-neutrino cross sections of the CC and NC experiments in a wide neutrino energy range ($2 \lesssim E_\nu \lesssim 150$) GeV. All materials were scaled to the glass used in the CHARM II experiment (number of nucleon $\langle A \rangle = 20.7$) to make the comparison. The solid (dashed) line corresponds to the Rein-Sehgal (Bel'kov-Kopeliovich) model. [Figure from [10].]

was supposed to happen at this energy regimen according to the Rein-Sehgal model that also predicted its occurrence at the higher energy levels where it was already observed. Both K2K and SciBooNE could not fully contain the pions and therefore could not reconstruct their energy. Because of that and per equation 3.8, they could not reconstruct $|t|$ either. Instead they used the four-momentum transferred $\left(q^2\right)$ as the criterion for isolating coherent candidate events. In doing so, both analyses became model-dependent, given that q^2 is calculated using muon kinematics, which are obtained under a CCQE hypothesis (equation 2.3). Looking at equation 3.2 is clear that events with high q^2 can still have low $|t|$ values. In this case, the pion takes most of the momentum. So in rejecting events with high q^2 they got rid of some high-momentum pions, which tend to propagate in the forward direction. Because of these limitations, K2K and SciBooNE found NO evidence of the CC coherent pion production at energies ~ 1 GeV. Figures 3.9 and 3.10 show the reconstructed q^2 distribution reported by K2K and SciBooNE, where it can be seen that the data and the model do not match in the region where most of the signal lays according to the Rein-Sehgal model. The difference between the model and the data is almost equal to the whole predicted coherent pion contribution to the model.

The puzzle was finally solved in 2014 by the MINERvA collaboration [31], [7] using a carbon target, and neutrino and anti-neutrino beams with an average neutrino energy of ~ 3.5 GeV (known as the low energy "LE" beam), characteristics very similar to the K2K and SciBooNE experiments. Because of the containment capabilities of the MINERvA detector (chapter 5), the energy of the pions could be successfully reconstructed. This enabled $|t|$ reconstruction and therefore a model-independent analysis. Figure 3.11 shows the MINERvA $|t|$ distributions where at low values the data excess is consistent with the

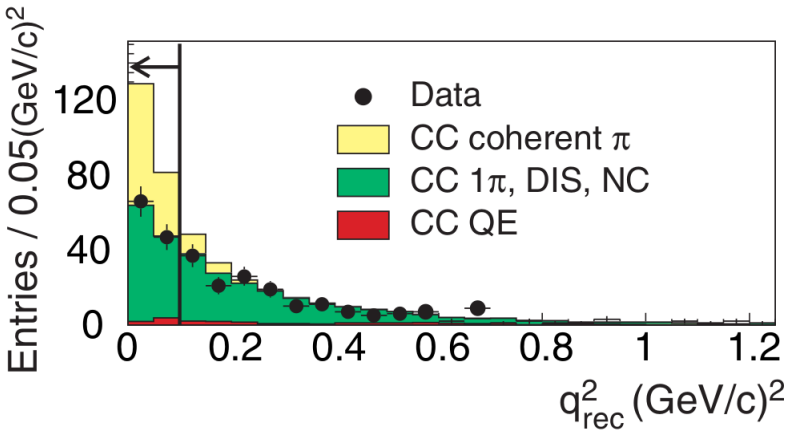

Figure 3.9: K2K reconstructed q^2 distribution, using a QE hypothesis to isolate CC coherent candidates. [Figure from [11].]

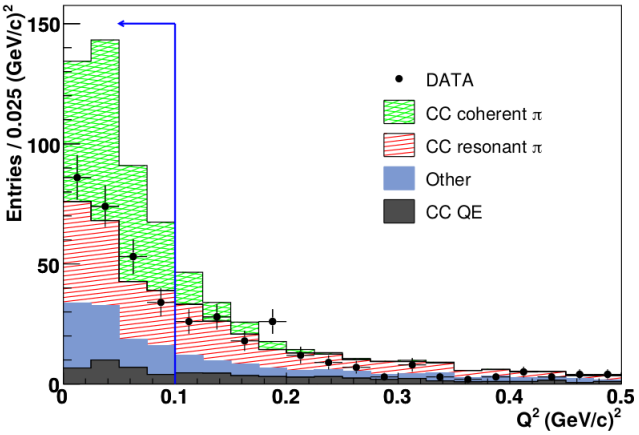

Figure 3.10: SciBooNE reconstruct Q^2 distribution, using a QE hypothesis to isolate CC coherent candidates. [Figure from [12].]

CC coherent prediction. With this result, coherent pions produced by muon neutrinos were finally observed in both neutrino and anti-neutrino modes, at both low and high neutrino energies, and at both neutral and charged currents.
The ArgoNeuT [32] and T2K [113] collaborations would later find evidence for the same reaction at $\sim$ 1 and $\sim$ 3.6 GeV neutrino energies, in neutrino and anti-neutrino mode, respectively, confirming the MINERvA result.

This thesis shows the measurements of CC coherent pions from ν_μ using the MINERvA detector in a more intense and energetic beam of E_ν = 6 GeV (known as the medium-energy "ME" beam), where CC coherent interactions off iron and lead targets

are shown for the first time. A carbon sample is also reported, with the highest statistics sample from a CC interaction up to date. All CC measurements, including this analysis, are summarized in table 3.2.

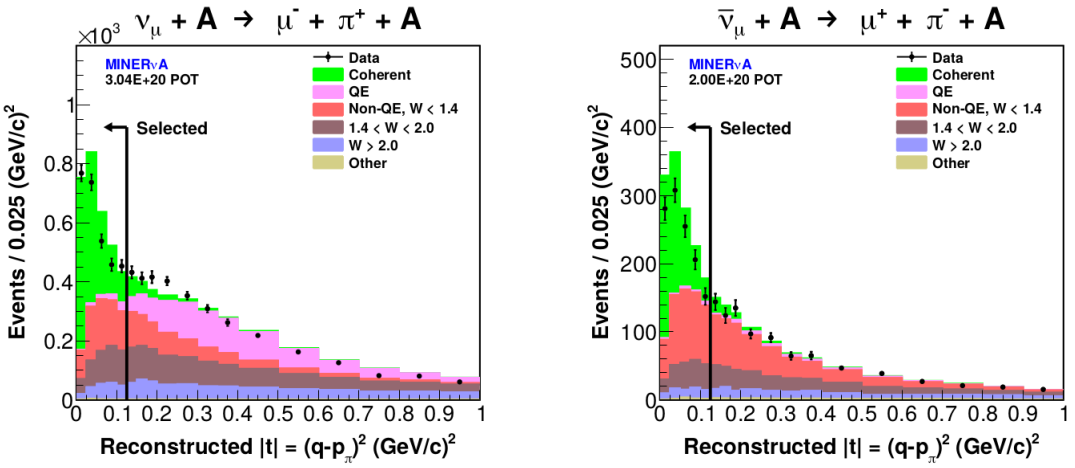

Figure 3.11: MINERvA's reconstructed $|t|$ distribution for neutrinos and anti-neutrinos, where the contribution from CC coherent pions in the data is clearly observed. [Figure from [7].]

EXPERIMENT	**YEAR**	**BEAM**	$< E_{\nu(\overline{\nu})} >$ **or range** $[GeV]$	**MATERIAL**	$< A >$
WA59	1984	$\overline{\nu}$	40	NeH_2	20
SKAT	1985	$\nu/\overline{\nu}$	7	CF_3Br (Freon)	36
BEBC WA59	1986	$\overline{\nu}$	5-150	Ne	20
E632	1988	$\nu/\overline{\nu}$	150 (110)	Ne	20
BEBC WA59	1989	ν	5-150	Ne	20
CHARM II	1993	$\nu/\overline{\nu}$	20	Glass	20.7
E632	1993	$\nu/\overline{\nu}$	80 (70)	Ne	20
K2K	2005	ν	1.3	C	12
SciBooNE	2009	ν	1.1	C	12
MINERvA (LE)	2014	$\nu/\overline{\nu}$	3.6	C	12
ArgoNeuT	2015	$\nu/\overline{\nu}$	9.6 (3.6)	Ar	40
T2K	2016	ν	< 1.5	C	12
MINERvA (ME)	2020	ν	6	C, Fe, Pb	12, 56, 207

Table 3.2: Summary of CC coherent pion production experiments. The neutrino beam energies go from ∼1 GeV to ∼150 GeV. Materials used are: carbon, glass, iron, neon, Freon, argon, and lead. Information is from [9], [22], [28], [10], [29], [11], [30], [31], [32], [33]

Chapter 4

The NuMI BEAM

The "Neutrinos at the Main Injector" (NuMI) beam is the world's most intense neutrino beam, located at the Fermi National Accelerator Laboratory "Fermilab". It was designed to serve the MINOS [114] oscillations experiment, but has also served other short and long baseline, neutrino experiments such as NOvA [115], as well as neutrino-nucleus experiments like ArgoNeuT [116] and MINERvA [16]. It is $\sim 99\%$ made of muon neutrinos, and the remaining 1% mostly of electron neutrinos.
Fermilab's chain of accelerators is used to achieve the energy needed for neutrino production, the process is described next. The MINERvA data taking covered two different configurations of the NuMI beam, the low-energy (LE), and medium-energy (ME) or NOvA configuration.

4.1 Fermilab Accelerator Complex

The Fermilab site hosts several particle physics experiments, including: neutrinos, dark matter and dark energy, muons, protons, quantum gravity, and accelerator science [117]. Such diversity demands a variety of state-of-the-art accelerators and technology to support the cutting-edge research carried at the lab. The majority of the budget of experiments at Fermilab rely on protons delivered by the Main Injector accelerator, which depending on the experiment, delivers protons at different energies and intensities. The beam starts its journey from a negative hydrogen ion source where ions are extracted and sent to a linear accelerator, which is connected to a circular accelerator, which ultimately feeds the Main Injector, as shown in figure 4.1.

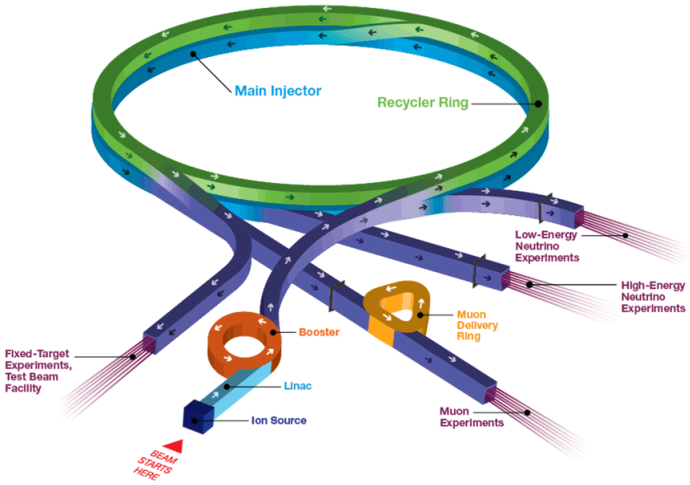

Figure 4.1: Fermilab accelerator complex. [Figure from [13].]

4.1.1 Radio Frequency Quadrupole Injection Line (RIL)

The protons that end up being fed to the different detectors and targets, start in the so called "Ion Source" [118], [119]. It consists of two twin direct-extraction magnetron hydrogen ion sources (one active, one for spare), where a high-voltage ionizes hydrogen gas creating a plasma. Electrons and negative ions in the plasma are drained, while the positive ones with an energy of 35 keV are transported towards a radio frequency quadrupole. Each of the two sources are kept to a pressure of $6 - 8\mu Torr$ for vacuum purposes.
The connection between the source and the quadrupole is called the low-energy beam transport (LEBT), and it consists of a series of magnets and vacuum devices in charge of focusing the beam coming from the source, with the collimation and acceptance needed by the quadrupole. The radio frequency quadrupole (RFQ) operates at 200 MHz, it accelerates the protons increasing the beam energy from 35 keV to 750 keV, it also provides further longitudinal and transverse collimation to the beam. After the quadrupole, the medium energy beam transport (MEBT) delivers the beam to the linear accelerator (LINAC), figure 4.1 [1]

4.1.2 Linear Accelerator (LINAC)

The beam enters the LINAC with an energy of 750 keV, where two radio frequency (RF) systems increase the beam energy. The first is a set of resonant tubes (Alvarez tubes) where its energy goes up to 116 MeV [120]. A set of high vacuum cavities additionally

[1] When not specified, figures in this chapter come from the reference in the same section.

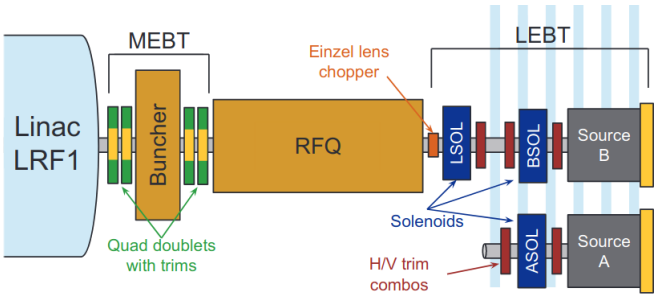

Figure 4.2: Pre-accelerator complex, also known as RIL.

accelerates the protons to reach 400 MeV. The LINAC increases the beam's momentum in 15-50 μs pulses, one per cycle, where every cycle lasts 66 ms, with an accelerating gradient of 7.5 MV/m. Its vacuum is $\sim 10^{-7} Torr$.
At the end of the line, a pulsed electrostatic deflector selects what portion of the line goes to the Booster accelerator (see next section). The width and length of the deflector determine the intensity of the beam [119]. There is a second LINAC under construction, meant to be used as the linear accelerator for the DUNE experiment [121].

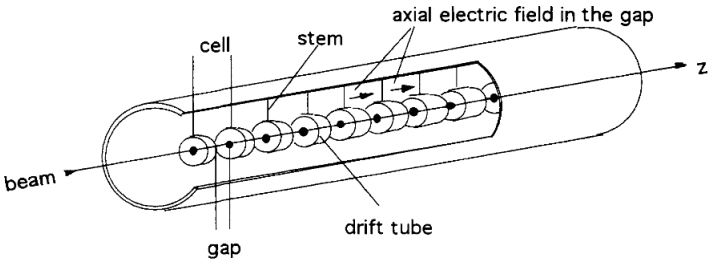

Figure 4.3: Components of a common Alvarez-type LINAC (not the one installed at FNAL.)

4.1.3 Booster

The FNAL booster is a 15 Hz, 75 m radius synchrotron that takes protons at 400 MeV from the LINAC. It delivers 8 GeV protons to either low-energy neutrino experiments or to the Main Injector. Ideally, a linear accelerator would feed the Main Injector, given the energy loss in synchrotrons due to synchrotron radiation, however such linear accelerator would need to be about 4 miles long, making it too expensive.
The booster also increases the beam intensity by stacking successive LINAC cycles. The extracted beam pulses from the booster are called "batches" (one batch per booster cycle),

and the Main Injector was designed to take six of these booster batches, as shown in figure 4.4.

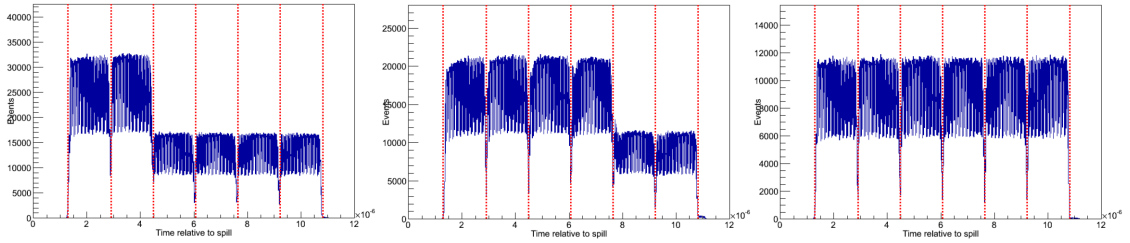

Figure 4.4: Protons on target per batch. The six Booster batches were increased their intensity in pairs. In the image can be seen how the first 2, 4 and all 6 batches increased their intensity.

4.1.4 Main Injector

The Main Injector (MI) was originally designed to replace the old "Main Ring" that supplied the anti-proton beam for the Tevatron (anti-proton mode), plus fixed target and collider injection modes. After the Tevatron shutdown, the MI is still the most committed machine in the accelerator complex, as shown in figures 4.1 and 4.5. It serves most of the experiments on site.

The batches coming from the booster have a length of a booster circumference, but the beam is not evenly spread, it is constrained in a region of the RF wave called a "bucket". The booster needs 84 buckets to fill its circumference, these buckets constitute a batch. With the batches injected into the MI, the energy of the protons ramps up at a steady pace to reach the 120 GeV. During 2012, the NOvA experiment required a most intense beam (4.9×10^{13} protons per pulse (ppp), $\sim 4 \times 10^{20}$ protons delivered to the target per year), for which the "Recycler", a ring installed below the MI, which was the one that actually supplied anti-protons to the Tevatron, was adapted to work as a "stacker" for the MI [122]. Increasing the intensity was done in stages, first slip-stacking two, then four to finish with all six batches (figure 4.4). The MINERvA data acquisition spanned during all fours intensity periods (to be considered in following chapters).

The fixed-target mode is the only one currently in operation from the three the MI was originally designed for. The beam is extracted from the MI in 10 μs "spills", that is the time structure in which the beam is sent towards the fixed target for the production of neutrinos.

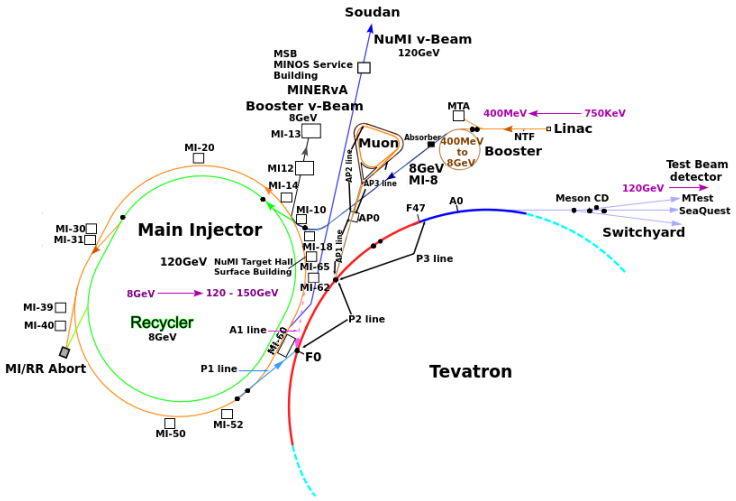

Figure 4.5: Fermilab accelerators chain [Figure taken from [14].]

4.2 Neutrino Production

Protons extracted from a hydrogen source are sent through a series of accelerators that increase the protons' energy in steps until they reach 120 GeV inside the "Main Injector", the protons are then fired to a target where hadrons (pions and kaons) are produced. The neutrinos come from the decay of the hadrons and muons, the latter coming from the decay of pions. Remnant charged particles are stopped in the underground rock, while neutrinos travel into the earth for around 1 km before reaching the near detectors "ND" and the neutrino-nucleus detectors. Neutrinos keep traveling through earth for about 700 and 900 km for the MINOS a NOvA long baseline experiments.

4.2.1 Target

The primary beam (Protons from the MI) is directed into the Earth at 58 mrad (3.34 °) downwards and focused onto a graphite production target $\sim$ 40 m underground, 350 m from the MI exit point, where the beam is approximately circular with a diameter of 1 mm (1.3 mm in the ME run) 4.6. It has a positioning accuracy of 1 cm longitudinally and 0.5 mm transversely. The target was originally designed to resist a power of 400 kW and after the NOvA upgrade, 700 kW without disintegrating, where the temperature and stress can reach 344 ° and 25.6M Pa. It is maintained in helium with a pressure above 1 atm, as it is easier and cheaper than operating it in vacuum. Its dimensions are 6.4×15×953.8 mm 4.7, segmented longitudinally into 47 fins. Such small transverse dimension is needed to minimize the number of undesired mesons and maximize the neutrino flux.

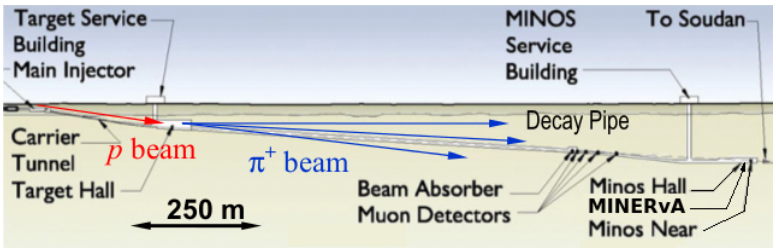

Figure 4.6: Side view of the NuMI beamline.

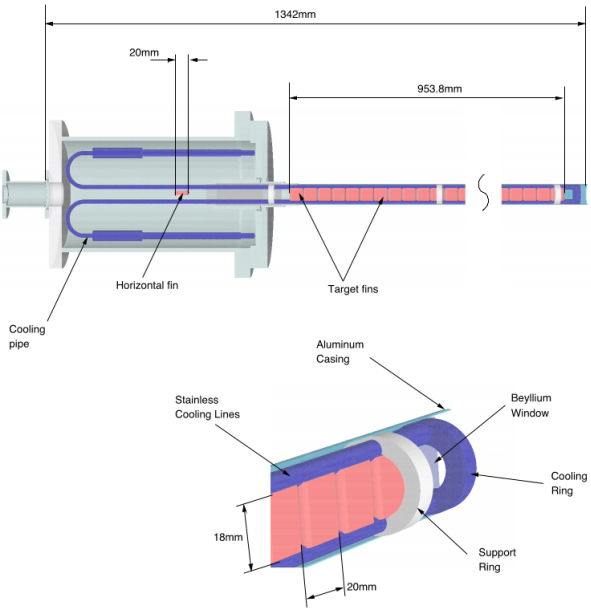

Figure 4.7: The NuMI target.

4.2.2 Focusing Horns

The mesons produced in the target are focused by two, 3-m long, aluminum magnetic "horns" 4.8. Their main purposes are to select the desired particles by their charge and energy, this is done by changing the relative placement of the two horns and the target, thereby the neutrino beam energy is also changed. Specifically, the second horn was moved further downstream from horn 1, and they are separated by 19.2 m now. Figure 4.9 shows how particles are focused depending on the angle at which they are produced. Particles along the beam axis are barely affected by the horns, the ones not focused in the first one can be focused in the second horn downstream.
The polarity of the applied voltage to the horns can be reversed to set them in anti-neutrino mode.

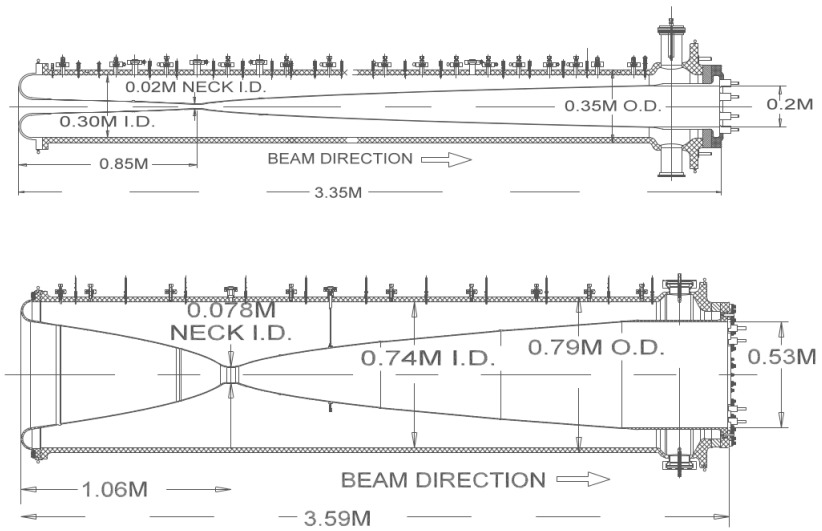

Figure 4.8: Focusing horns.

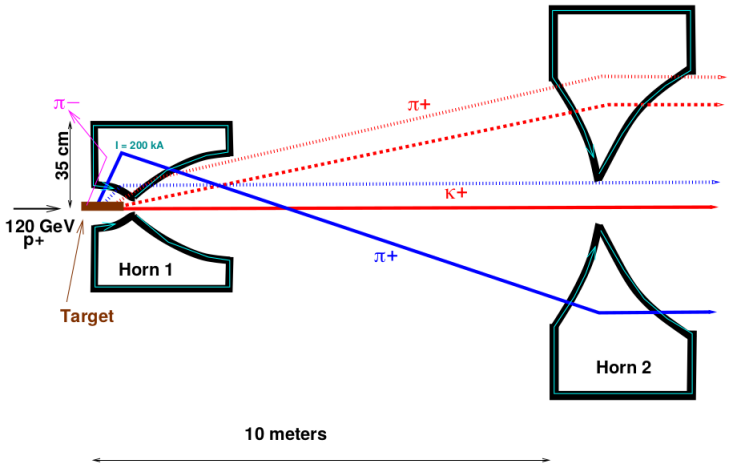

Figure 4.9: Side view of the NuMI horns.

4.2.3 Downstream Line

46 m downstream the target, starts a 675 m long, 2 m diameter steel decay pipe. The pipe was initially evacuated to ∼1 torr, but later filled with helium at a 13.2 PSIA to avoid corrosion at the entrance of the pipe. The focused particles leaving the horns (Pions and Kaons) decay inside the pipe, mostly into muons and muon neutrinos, it is there where the neutrino beam is born. The pipe length is approximately the decay length of a 10 GeV pion. The decay volume is surrounded by 2.5-3.5m of concrete, getting even thicker at the upstream end as it is closer to the surface.

At the end of the decay volume there are ionization chambers to count and characterize the remnant particles leaving the pipe, known as the hadron monitor. After the monitor, there is a beam absorber that consists of a $1.3m \times 1.3m \times 4.75m$ water-cooled aluminum core, a 1m layer of steel blocks surrounding the core, followed by a 1.5m layer of concrete blocks, to stop the charge particles that make it out of the pipe, this structure is known as the "absorber", where around a sixth of the initial beam particles surviving the decay pipe are stopped, most of it are protons that did not interact, mesons that did not decay and a small fraction of neutrons, gammas and electrons.
Three more ionization chambers, "the muon pits" are used to monitor the muons that escape the back of the hadron absorber, they are installed in between layers of dolomite rock where the muons are absorbed. To a good degree, the muon profile in the rock gives a good estimate of the neutrino profile, since both are created at the same hadron decay point. Figure 4.10 shows all the NuMI components, including the so called downstream line.

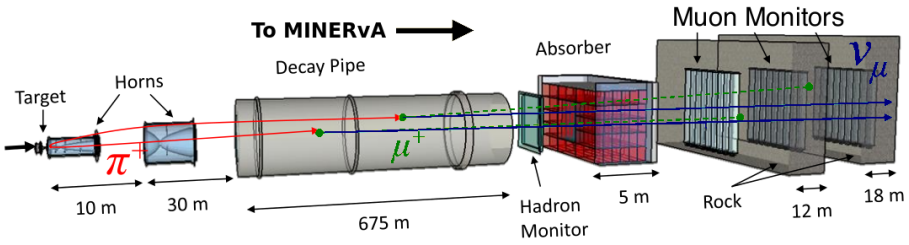

Figure 4.10: The NuMI beamline components.

4.2.4 Flux

All neutrino cross section measurements need a fairly good knowledge of the neutrino flux. The cross section formula: $\sigma = n/T\Phi$, where n is the number of events, T the number of targets (nuclei in this analysis), and Φ is the neutrino flux; depends on the flux, which is defined as the number of neutrinos per unit area (cm^2 in this analysis). The flux is usually normalized to exposure (POT normalized) 4.11. In order to get a very precise measurement of the flux, a large amount of secondary hadron interaction measurements would have to be carried in all parts where such particles interact with components of the beam line, plus a precise knowledge of all the parameters in the line. In complex systems like NuMI, this is not practical, instead, simulations for all those interactions have to be performed. There are extra cases when the lack of theoretical predictions make it harder to even get a good simulation. The best available approach is to tune those interactions in a simulation to existing data. Such data have been usually obtained under different circumstances, for

which corrections need to be done. The majority of interactions ($\sim 85\%$) per ν_μ produced in the beam are due to protons in the carbon target, followed by pions and kaons also in the target. Interactions in other materials have considerably low contributions [15]. Figure 4.12 shows the average number of interactions of the main interaction channels in the beamline per muon neutrino created, where the dominance of protons on target can be seen.

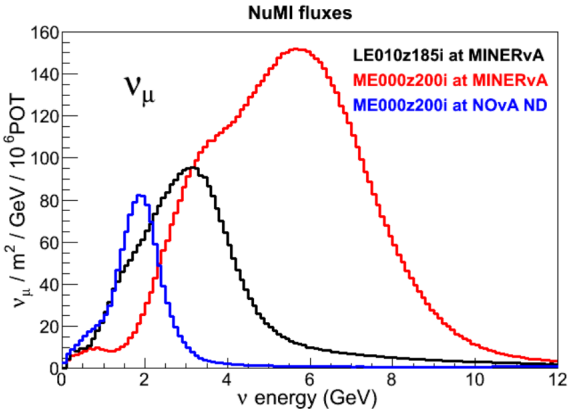

Figure 4.11: MINERvA's LE and ME simulated fluxes, along with NOvA's.

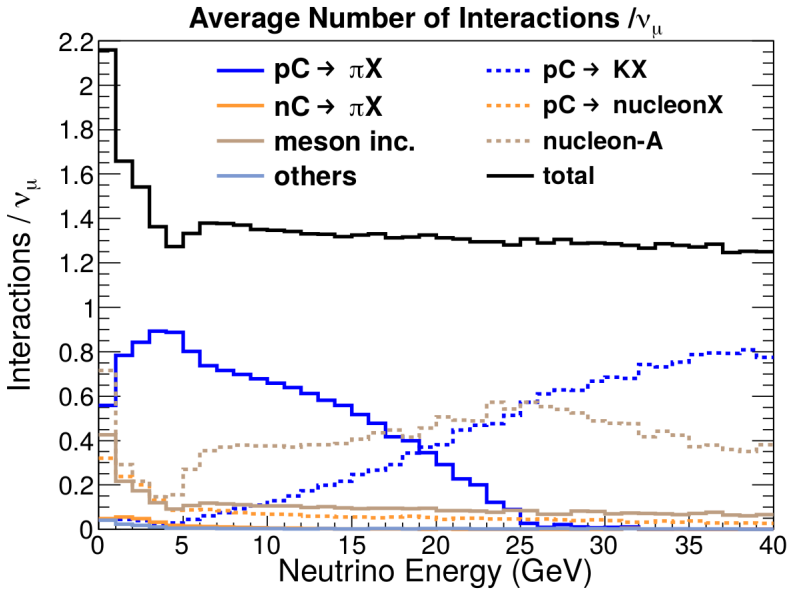

Figure 4.12: Average number of interactions in main channels, per muon neutrino created (LE configuration example).

For the MINERvA flux, two external datasets where used, one for constraining proton-

Carbon scattering, and one more for meson production. In the former, each hadron interaction producing neutrinos was weighted by

$$w\left(x_F, p_T, p_0^{MC}\right) = \frac{f_{data}\left(x_F, p_T, p_0^{data}\right)}{f_{MC}\left(x_F, p_T, p_0\right)} \times g\left(x_F, p_T, p\right) \tag{4.1}$$

Where p, and p_T are the incident proton's momentum and proton's transverse momentum, x_F the "Feynman" number (a scaling factor describing hadron production in $p+p$ interactions equals to $2p_L/\sqrt{s}$, where s is the momentum center squared), and g further scales the weight, based on Feynman scaling [123]. The main contribution to the MINERvA ME flux comes from the high precision region in figure 4.13, from the pion production from the "NA49" data [124].

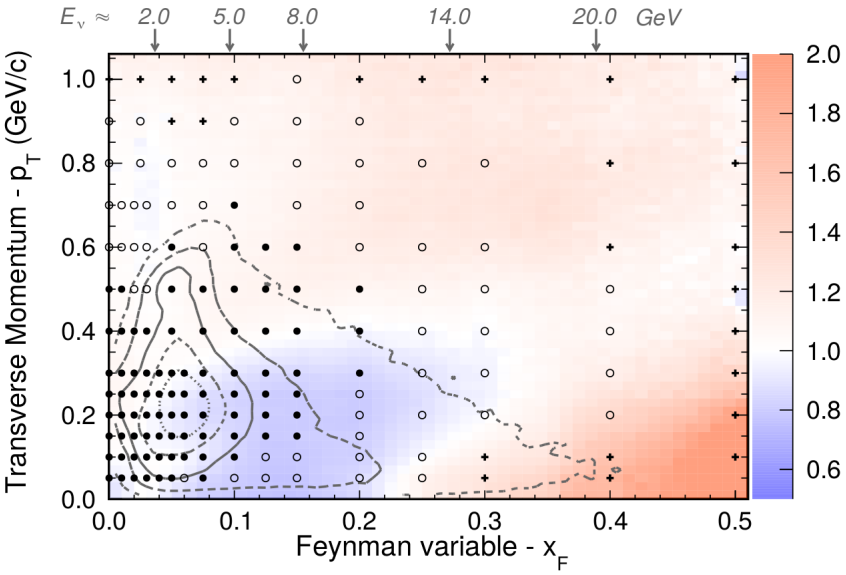

Figure 4.13: Hadron production data from the NA49 experiment. Filled data points show the high precision region (uncertainty $< 2.5\%$), the contour represents increasing contribution (from outer to inner contour) of the pion production to the creation of ν_μ in the MINERvA LE flux, while the upper energies are of the ν_μs from pions at the x_F value above [figure gotten from [15]].

There was no data to constraint meson interactions in the beam, for them an uncertainty of 40% was applied. This value comes from other uncertainties assigned based on the agreement of the data with the hadron models used in the simulation. The simulation of the beamline, starting from protons hitting the target until the creation of neutrinos, was

done using the Monte Carlo (MC) based simulation software, GEANT4 [125] and a full geometrical simulation of all beam components.
Additional constraint on the neutrino flux could be done by measuring the flux of muons, pions and kaons in the beamline, but the scarce knowledge of their backgrounds gives pour results. As a result of the constraint, it can be seen in figure 4.14 that the main peak of the flux gets weighted down, and the high energy tail is strengthened.

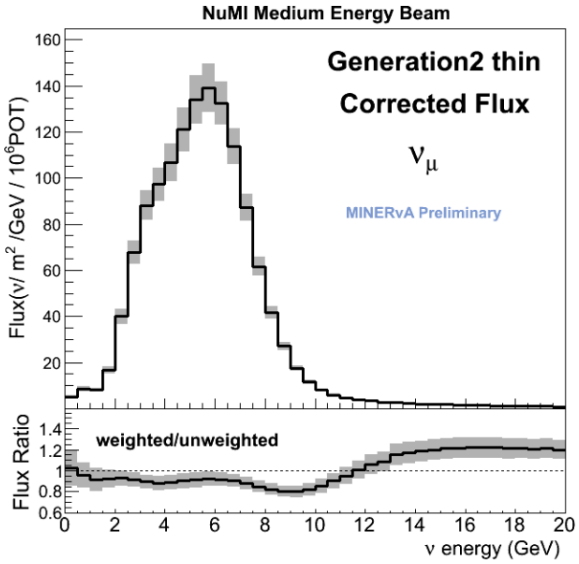

Figure 4.14: Comparison of the "hadron production" tuned and untuned ME flux predictions.

Flux Constraint With Neutrino-Electron Scattering

The MINERvA detector was able to collect 810 neutrino-electron scattering events ($\nu + e^- \rightarrow \nu + e^-$, mostly muon neutrinos through the NC channel) [126]. This interaction is a well known one, measured multiple times in different materials and with high precision. The ME measurement by MINERvA, however, is the most precise so far. It is used to further constraint the ME flux used in all MINERvA's ME cross section analyses. The technique consists on obtaining a probability distribution of the neutrino flux by weighting the initial flux probability distribution from the simulation with the likelihood of the data from the electron-neutrino sample, based on the Bayes' theorem. A series of simulations (universes) are generated by varying parameters of the neutrino flux (usually between some σ around their central value (CV)). The probability distribution is constructed by weighting the simulation in each universe with a χ^2 likelihood weight

$$W = \frac{1}{(2\pi)^{K/2}} \frac{1}{|\sum_N|^{1/2}} e^{\frac{1}{2}(\mathbf{N}-\mathbf{M})^T \sum_N^{-1} (\mathbf{N}-\mathbf{M})} \tag{4.2}$$

where K is the number of bins, $\mathbf{N}$ a vector of the data content in the bins, $\mathbf{M}$ a vector of the content of the simulation in each universe, and $\sum_N$ a covariance matrix with all data uncertainties in $\mathbf{N}$. Figure 4.15 shows the fractional uncertainty of the neutrino flux with the constraint compared against the unconstrained flux. The normalization uncertainty from 2-20 GeV gets reduced from 7.5% to 3.9%.

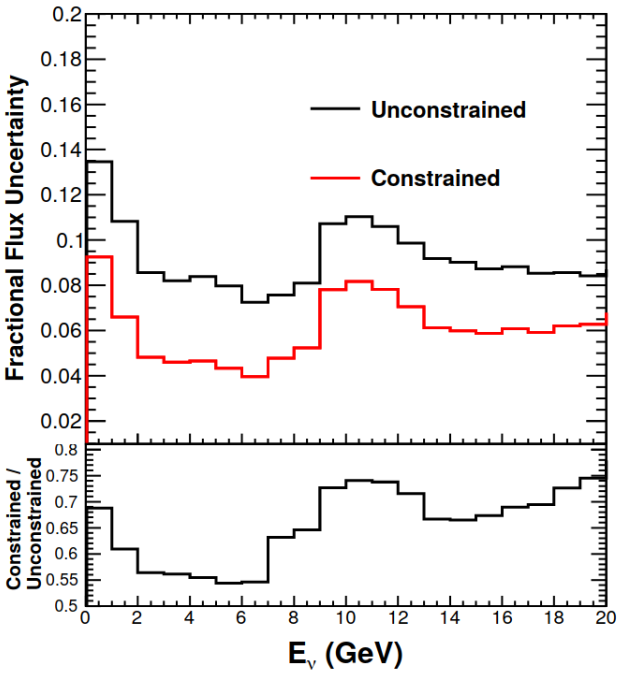

Figure 4.15: Uncertainty of the ME constrained and unconstrained ν_μ flux in neutrino energy bins.

Chapter 5

The MINERvA EXPERIMENT

MINERvA is a cross section experiment, focused on the interactions of neutrinos with electrons, nucleons and nuclei. Its name stands for "Main Injector ExpeRiment for ν-A". It was designed and proposed in the early 2000's to better understand such interactions, as the data collected so far was statistically limited and mostly available in heavy (high "A") nuclei. It is also designed to help neutrino oscillation experiments reduce their uncertainties on different neutrino reactions, both by testing and improving the models of such interactions, and by constraining the beam's flux-related systematic uncertainties.
It is noteworthy that even though the major source of systematic uncertainties in neutrino oscillation experiments comes from neutrino-nucleus and neutrino-nucleon scattering, a major undertaking had not been pushed in order to reduce it.
The MINERvA detector has targets with six different materials (chemical elements), and it was placed in the high intensity NuMI beam line at Fermilab, the man-made world's most intense neutrino beam, which allows for both nuclear effects probing, and high statistics even in rare processes.

5.1 The MINERvA Detector

The detector was composed of the following subdetectors: the passive target subdetector also known as the "target region"; the fully active inner detector (ID); side and downstream electromagnetic calorimeters; and the side and downstream hadronic calorimeters (figure 5.1). It was located at the NuMI hall, 105 m underground in the Fermilab site, 2 m upstream the MINOS near detector. Detectors were placed deep underground to reduced cosmic ray interactions as much as possible. MINERvA was 5 m long (from the front of

the nuclear target region to the back end of the hadronic calorimeter), 3.45 m tall, and weighted ∼175 tons adding the mass of all subdetectors.
Building of the planes began off-site in 2006, mounting of the first plane in 2007, and commissioning in 2009. It started taking data in November 2009 (with just a few of the back planes installed), running for more than two years in the NuMI low-energy (LE) configuration ($\langle E_\nu \rangle$ ∼3.5 GeV), and almost six more in the medium-energy (ME) configuration ($\langle E_\nu \rangle$ ∼6.0 GeV). It recorded its last neutrino event in February 2019, reaching a total of $\sim 3 \times 10^{20}$ protons on target in both neutrino and anti-neutrino mode. It was finally decommissioned and dismantled by the end of that year and the first few of 2020.

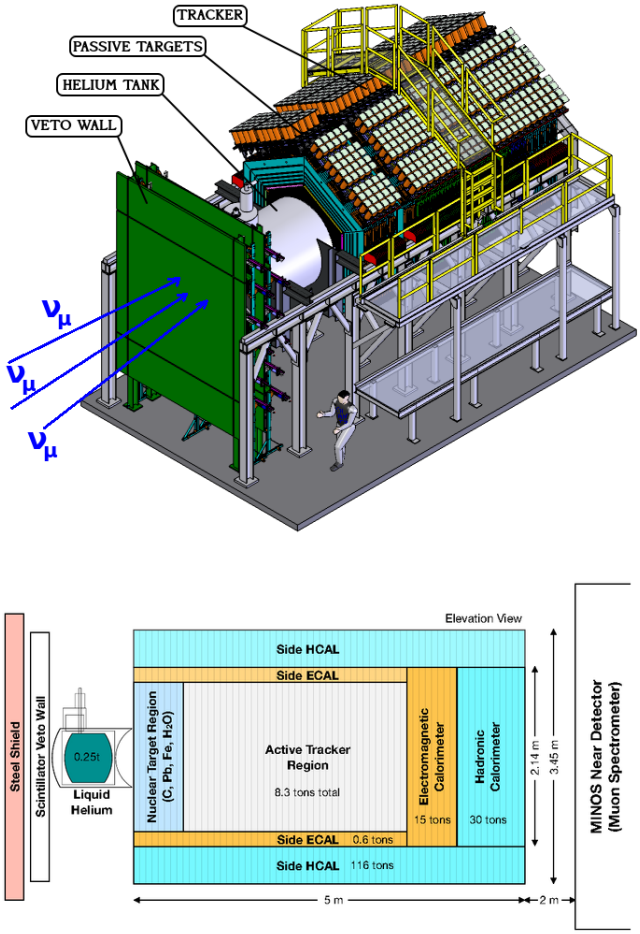

Figure 5.1: Isometric and side view of the MINERvA detector. [Figure from [16].]

5.1.1 Coordinate System and System of Units

All data analyses in MINERvA use a right-handed Cartesian Coordinate system with origin $(x = 0, y = 0)$ located at the center of gravity of the ID, 3.29±0.01 m above the floor, with the y axis pointing upwards and the z axis pointing into the detector parallel to the floor; the origin $(z = 0)$ is at the front end of the detector (front face of the detector stand). The neutrino beam points downwards approximately at 3.34 ° with regards to the z axis. More details and info about MINOS coordinate system can be found here [127]. The unit system used, is the same one used by the Gaudi framework [128], and it is broken down in table 5.1.

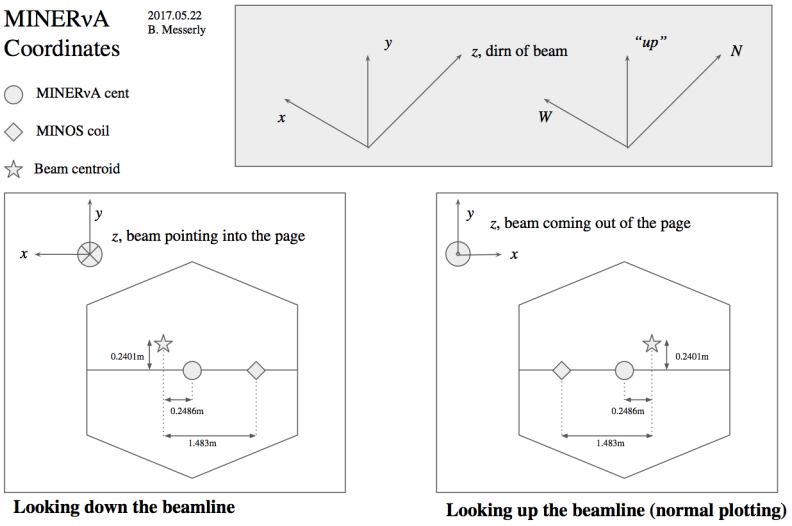

Figure 5.2: MINERvA's coordinate system. [Figure from [**?**].]

Quantity	**Unit**
Length	millimeter
Time	nanosecond
Energy	MeV
Plane Angle	radian
Electric Charge	positron charge
Temperature	Kelvin
Amount of Substance	mole

Table 5.1: System of units used in this analysis.

5.1.2 The Inner Tracker Detector

Also known just as the "tracker", it is a fully active region, with 8.3 tons of fine-grained plastic scintillator, designed for detailed tracking and vertexing. It is made of polystyrene strips with 92% Carbon, 7.6% Hydrogen, and smaller amounts of other elements (see table 6.10). It was arranged in 62 modules with two planes each. 127 pyramidal strips were stacked as in figure 5.7 in each plane. The base of the strips are perpendicular to the beam, and half of the base's length determines the vertexing resolution due to the stacking arrangement. The planes are aligned in the "X", "U" and "V" views to enable 3-D tracking reconstruction, the first one with the strips axes perpendicular to the x-axis allows to determine position along the x-axis, the other two are rotated 60° clockwise and counterclockwise with respect to the first one, respectively. The planes followed the sequence "XUXV" and so on, in which each plane had an X-plane downstream one of the other two. The hexagonal shape of the detector symmetrically accommodates the three views.
It was in the ID where most of the analyses published by the collaboration took place, because of its high statistics and good energy, timing and position resolution.

5.1.3 The Inner Passive-Targets Detector

The upstream region of the ID included passive material for A-dependence measurements. Five hexagonal modules (with the same transverse dimensions of the inner tracker detector) with carbon (C), iron (Fe) and lead (Pb) in different configurations; a water (H_2O) target; and a liquid helium (He) target. They covered a pretty large range of the "mass number" or nucleon number (A) scale. The positioning and mass of the materials under analysis were chosen taking into account the following aspects:

- Statistics - The bigger the amount of mass the bigger the probability of neutrinos interacting with the passive material.
- Containment - Particles created in the passive material should have a similar containment as particles created in the tracker, in order to have good energy resolution.
- Mass Equalizing - Each material should have the same amount of mass installed to try to get the same number of neutrino events from each.
- Energy Threshold - The thinner the target the more low-energy particles can get out of the passive material and get tracked.

- Vertex Resolution - The thinner the target the better the interaction vertex position resolution.
- Track Resolution - The region needed enough active material for the tracking algorithm to be able to reconstruct multiple charged particle events.
- Space - Ideally there would have been as much planes as possible in between passive materials for better tracking, but the underground hall dimensions limitations, put a maximum limit of nine modules.

It is obvious that some of the requirements are mutually exclusive. The perfect configuration would have been a long passive-target region with several targets with different thicknesses of the same material for each of the materials installed and separated by several scintillator planes for a highly efficient tracking. Given the space and cost limitations, a final design was agreed trying to fulfill the requirements in order of importance. Figures 5.3 and 5.4 show a side view of the passive-target region showing the final thickness and position of all five targets, and the front view (beam pointing into the page) with the areal separation of the materials in the targets. Thinner targets were put downstream close to the tracker so that low-energy events produced inside them would benefit from all the active region in the tracker. Thicker targets located upstream would have the highest neutrino-energy events and the highest statistics (higher mass) utilizing the downstream targets as calorimeters.

Configuration of C/Fe/Pb Targets

Targets 1 and 2 were made of Fe and Pb in almost equal masses, iron occupying 60% of the area due to its lower density. Target 2 was rotated 60° counterclockwise so both materials had similar acceptance in the tracker and MINOS detector.
Target 3 allowed for comparison of the three materials at the same "z" coordinate. Although the hydrocarbon target already contained enough neutrino-carbon interactions, a region of pure carbon in target 3 was installed to extract hydrogen contribution in DIS, resonant pions and $\overline{\nu}_\mu$ quasi-elastic interactions. Carbon in target 3 had a dominant area (50%), mass ($\sim$40%) and thickness of $\sim$76 mm. The lead portion of that target, occupied the lowest sixth of the hexagon area, as lead in other targets was mostly in the upper half. The remaining third was occupied by iron. Both iron and lead had a thickness of $\sim$25 mm.
Target 4 served both as an EM calorimeter for π^0 (photon) detection, and as the thinnest lead target for low-energy lead neutrino interactions.

Finally, target 5 included a thinner version of target 1, to also include iron and lead low energy events. Their areal distribution was such that allowed uniform areal presence of each material. Table 5.2 shows a detailed summary of the masses, thicknesses and location of the passive targets (besides helium), extracted from [16], with updated values.

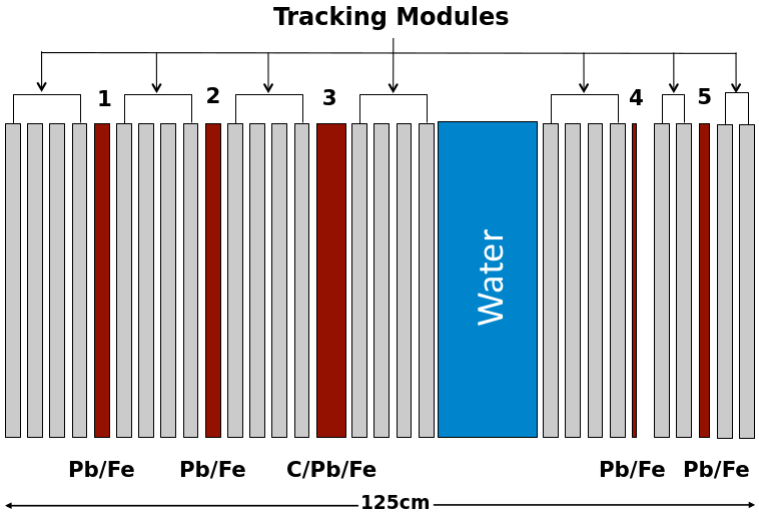

Figure 5.3: Positioning of targets in the passive targets region. [Figure from [16].]

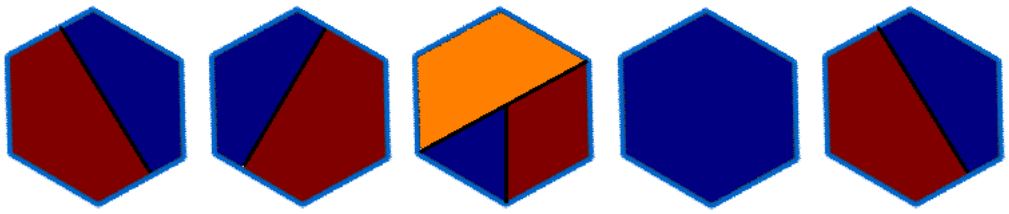

Figure 5.4: Configuration (front view) of each of the passive targets. Blue=Lead, Red=Iron, Orange=Carbon [Figure from [16].]

The Helium Target & Veto Wall

The target consisted of a vessel filled with 2300 l of cryogenic helium. It was placed upstream the scintillator planes at the beginning of the target region. Its design criteria were similar to the ones for the five targets downstream: maximize the probability of interaction with the incoming neutrinos, minimize the material with which the secondary particles could interact before reaching the tracking planes, and a good acceptance. The vessel was a cylinder 100 cm long, and 152 cm of radius which was surrounded by a vacuum for thermal isolation. This target presents the biggest reconstruction challenges because of

Target	z-Location of Center (cm)	Thickness (cm)	Fiducial Area (cm^2)	Fiducial Mass (kg)	Total Mass (kg)
1-Fe	448.2	2.567 ± 0.006	15999	322	492
1-Pb	448.2	2.578 ± 0.012	9029	263	437
2-Fe	470.2	2.563 ± 0.006	15999	321	492
2-Pb	470.2	2.581 ± 0.016	9029	263	437
3-C	494.6	7.620 ± 0.005	12027	158	238
3-Fe	492.1	2.573 ± 0.004	7858	107	170
3-Pb	492.1	2.563 ± 0.004	3694	160	258
H_2O	528.4	17-24	25028	452	627
4-Pb	564.5	0.795 ± 0.005	25028	225	340
5-Fe	577.8	1.289 ± 0.006	15999	162	227
5-Pb	577.8	1.317 ± 0.007	9029	134	204

Table 5.2: Position, mass, thickness and areas of the passive targets.

its poor acceptance, and being the only one with no tracking planes upstream. It greatly relied in the veto wall to discard background events.
In order to differentiate events coming from the rock from actual neutrino events happening in the first module in the target region, a veto wall was installed in front of the detector to identify the incoming muons 5.1. The veto wall had two steel shield plates (5 cm and 2.5 cm thick) that helped stopping some of the incoming muons, interspersed with two scintillator planes (1.9 cm thick) that recorded their trajectory and timing.

The Water Target

Figure 5.5 shows a lateral and frontal view of the water target, it was installed in between targets 3 and 4, with four scintillator modules of separation between targets. Its composition was ∼88.5% oxygen, ∼11.5% hydrogen, plus carbon and nitrogen in small amounts. When filled with water, the targets expanded more at the bottom, but given the not easy access to it, its shape and mass were determined using a finite analysis and weighting the water when emptied. It was centered in the axis joining the geometrical center of the hexagonal modules, and had a radius slightly larger than the hexagons' apothem. Its dimensions and mass are included in table 5.2.

5.1.4 Calorimeters

The electromagnetic calorimeter (ECAL) served the purpose of electromagnetic showers containment. It surrounded the sides and back of the hexagonal inner tracker detector as

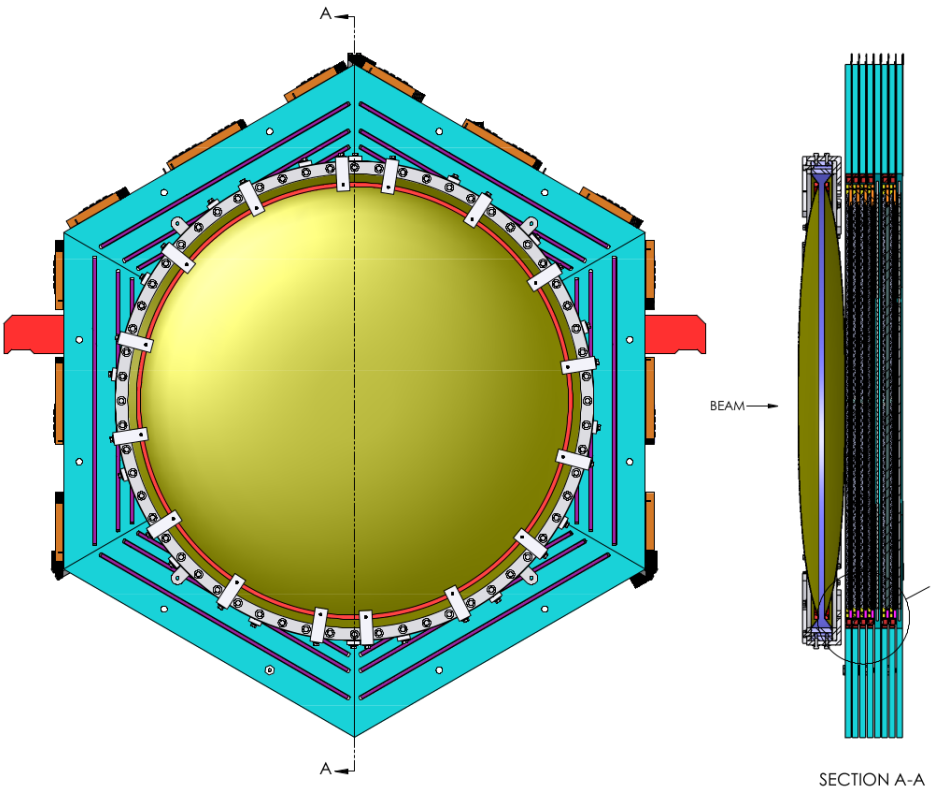

Figure 5.5: Water Target, front and side view. [Figure from [16].]

shown in figure 5.6. The side ECAL consisted of a 0.2 cm thick, 15 cm wide collar of lead, with the purpose of containment, and electron and photo conversion in the transverse direction. The downstream ECAL was a region ∼42.2 cm long after the tracker, with ten modules made of a plane with a standard scintillator, followed by a 0.2 cm thick downstream plane made of only lead 5.1.

Installed in the most outer (outer detector or OD) and downstream region of the detector, was the hadron calorimeter (HCAL). The side region was sectioned in six parts (towers) 26 cm wide extending outwards, ∼10 cm from the edge of the tracker. It counted with four $15mm \times 19mm$ squared scintillator strips inserted in the steel in each tower, for tracking particles moving transverse to the direction of the beam. The downstream HCAL was made of twenty modules of 2.54 cm steel planes with a standard scintillator plane downstream. Both side and downstream HCAL served as the container of hadronic showers and more energetic particles escaping the inner and ECAL detectors.

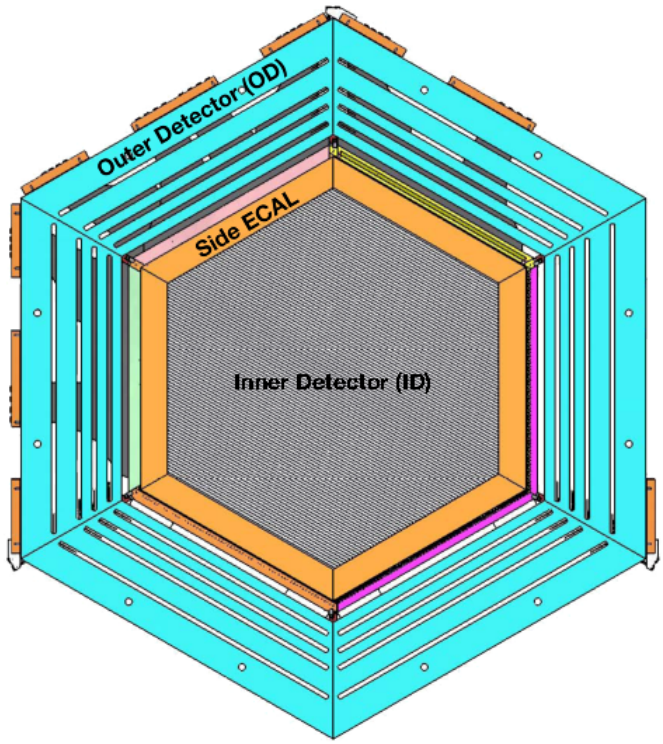

Figure 5.6: Front view of a MINERvA module. The inner part shows the fiducial active region. Next two layers are the side electromagnetic and side hadronic calorimeters. [Figure from [16].]

5.1.5 Optical System

All reconstructed quantities in the MINERvA detector were obtained through the processing of the light that charged particles yielded in the plastic scintillator. Plastic scintillator absorbs part of the particle's energy and re-emits it in the form of photons (usually a few nanoseconds after absorption) giving information about the timing and energy of the particles. In order to have an accurate reconstruction, the optical system had to deliver the greatest possible amount of photons created by the charged particles traveling in the plastic, to the electronic system.

Considering all subdetectors, there were 32000 scintillator strips, they constituted the first element in the optical system. They were made of extruded plastic scintillator (C_8H_8 polystyrene) doped with small amounts of other substances for maximizing light yield, and covered with a white reflective coating of TiO_2. Strips in the ID had a triangular cross section with a base of 33±0.5 mm, a height of 17±0.5 mm, and a varying length depending on their position in the planes. Strips in the side OD where rectan-

gular ($19 \pm .5mm \times 16.6 \pm .5mm$, and a few millimeter thicker in the downstream OD to fit the thicker steel). For very energetic particles there is a saturation in the light output of the plastic, the proper correction implemented by MINERvA was included in a MINERvA publication [129]

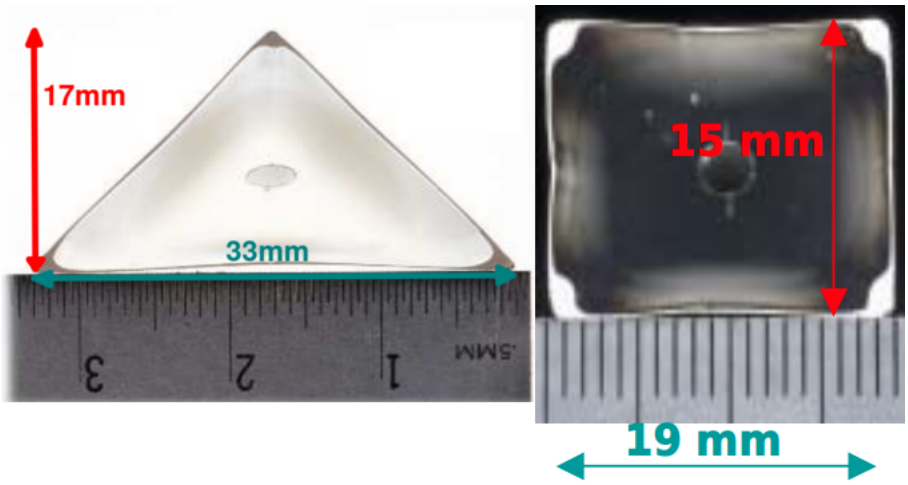

Figure 5.7: Cross section of the plastic scintillator strips in the ID (left) and OD (right). [Figure from [16].]

At $8.5 \pm 0.25mm$ from the base of the ID strips there is a $2.6 \pm 0.2mm$ radius hole along the length of every ID strip; and a similar (3.5∼0.2 mm) hole in the OD strips. Inside the wholes there is a 1.2 mm diameter, 32 cm long wavelength shifting fiber (WLS) that collects the light created by the scintillator and carries it to a set of "optical connectors" where the WLS met clear fibers (from 1.08 m up to 6 m long) that ultimately carry the light into the photomultiplier tubes (PMT). Due to cost constraints just one end of the fiber was read, while the other was mirrored by polishing and adding an aluminum coating to help gathering more light (see figure 5.8). The purpose of shifting the light's wavelength is to deliver the light at the PMT's most efficient wavelength. The clear fibers are used for lowering operation costs, since the WLS is not needed once the wavelength has been shifted. The WLS absorption and emission peaks are 430 nm and 476 nm (see figure 5.9).

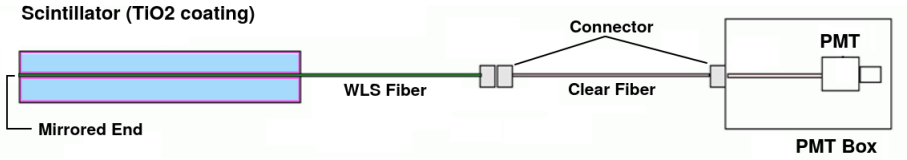

Figure 5.8: Path of light produced in scintillators to the PMTs. [Figure from [16].]

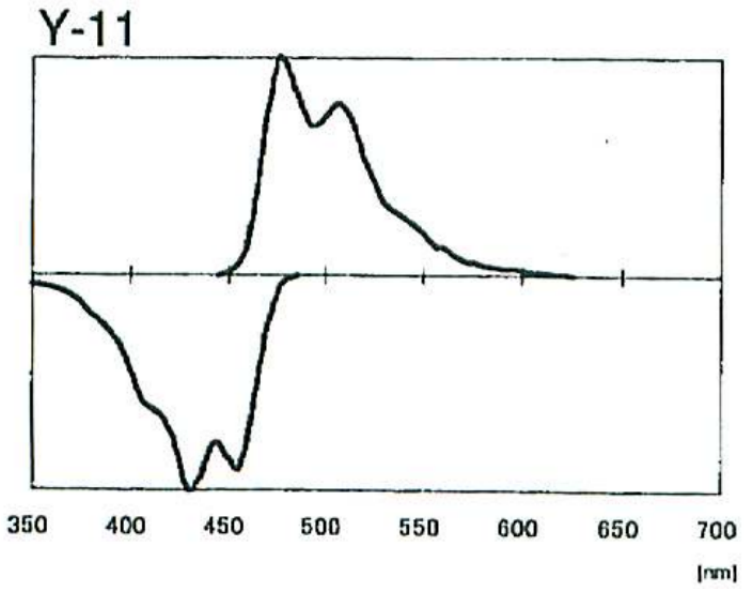

Figure 5.9: Absorption (bottom wave) and emission (top wave) peaks for the wavelength shifting fiber.

5.1.6 Electronics & DAQ System

Timing and energy information of the physics events in the detector was obtained by the processing of the light delivered by the optical system and processed by the electronic and DAQ system, which created the raw data that would latter go into the calibration and reconstruction stages.

Photomultiplier Tubes

The system begins with the 507 installed PMTs by Hamamatsu, model H8804MOD-2 with 64 channels each. These were mounted on top of the two upper towers of the OD. The input light hitting the photocathode of the PMTs produced photoelectrons (electrons release by means of the photoelectric effect), the number of photoelectrons is multiplied in the PMT by means of a high voltage. The electron multiplication factor is called the "gain" of the PMT. Each tube is inside a box for mechanical protection, ease of installation, and magnetic shielding (specially for the ones closest to MINOS), see figure 5.10. Inside the box, the tube gets connected to the fibers at one end and to a "front end board" (FEB) at the other.

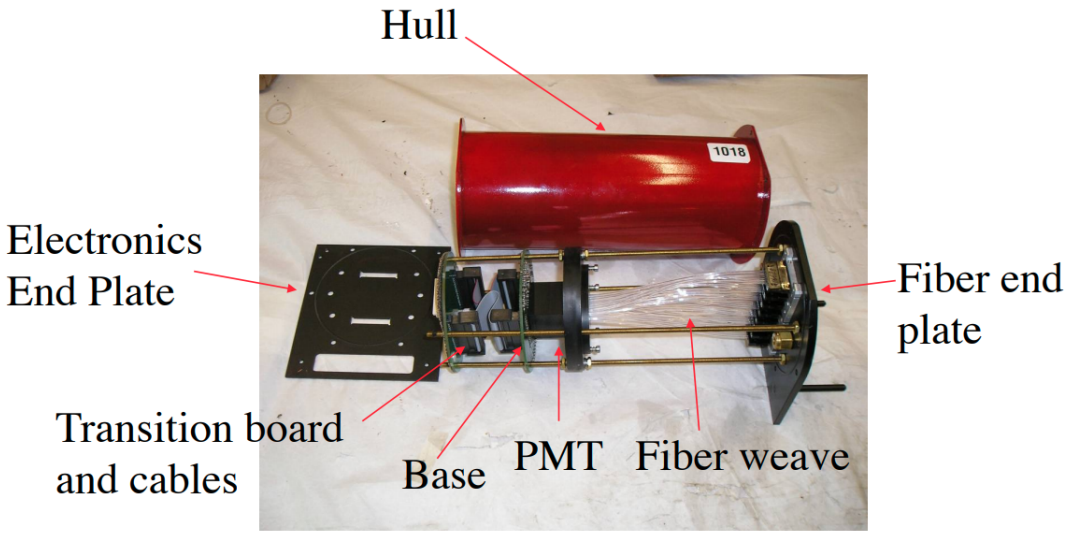

Figure 5.10: PMT box with all internal components. [Figure from [16].]

Front End Boards

The FEB performed three tasks, it controlled a Cockcroft-Walton generator at the base of the box to produce the high voltage needed by the PMT. It also had four 16-channel and two 32-channel chips (TriP chips) that recorded the electronic pulses from the anode. The former took care of the medium and high gain events and the latter processed low gain events (see figure 5.11). When the discriminator of any channel was triggered (time T_0) all channels in the chip start digitizing and recording the charge from the incoming hits (even the channels that got no hits at all) during 150 ns, and stay off (in reset state) for 18.8 ns. During the "reset state", charge can still be recorded but with a wrong timing information (see figure 5.12).

The chips kept repeating that process and collecting several hits for 16μs, time during which the integration "gate" of the analog-to-digital converters (ADC) modules stayed open. The gate opened 0.5μs after the start of the spill sent by the accelerator division (AD) to make sure no neutrino events were missed, the spill lasted 10μs but the gate remained opened 5.5μs more to record activity of delayed interactions, such as Michel electrons [130]. See figures 5.13 and 5.14.

Lastly, each FEB was the interface communicating with the readout controller. Groups of ten FEBs were connected in series (for cable handling issues) in a chain, and four of these chains were connected in a "CROCE" (Chain Readout Controller); Eight CROCEs were controlled by a "CROCE Interface Module" (CRIM) that fed the CROCES with trigger

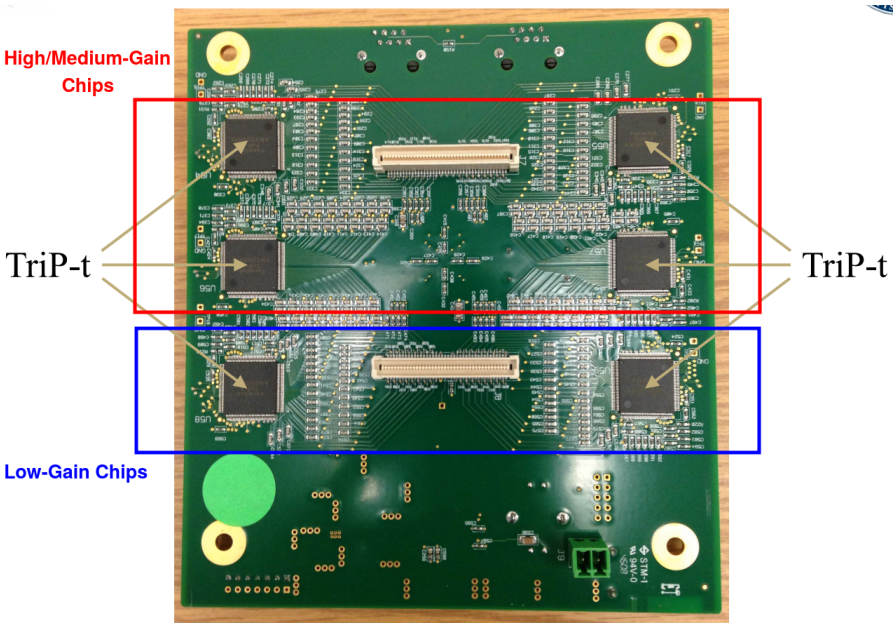

Figure 5.11: Front End Board. Four top chips are the medium/high gain chips, and bottom chips are the low-gain chips. [Figure from [16].]

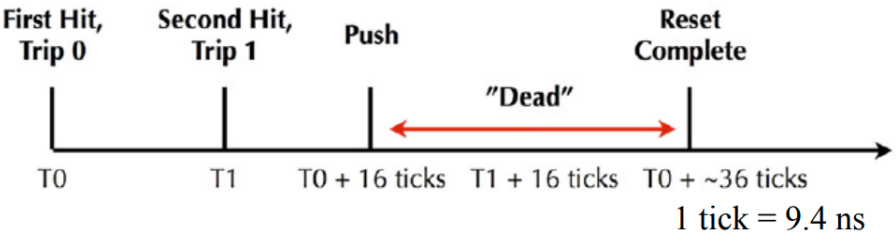

Figure 5.12: Digitizing and reset (dead) time of the TriP chips. [Taken from [17].]

and timing commands. Finally the CRIMs received commands from the MINOS timing system for event matching, and to receive the status of the MI neutrino pulse through a MINERvA timing module. Further and detailed information about MINERvA's and MINOS' DAQ can be found at [17].

5.2 Simulation

Every serious experiment needs to have, to some degree, predictions on the expected outcome(s) of the measurement(s) to be performed. Previous knowledge of related parameters or similar experiments help to constraint and focus the effort, optimize resources, skip triv-

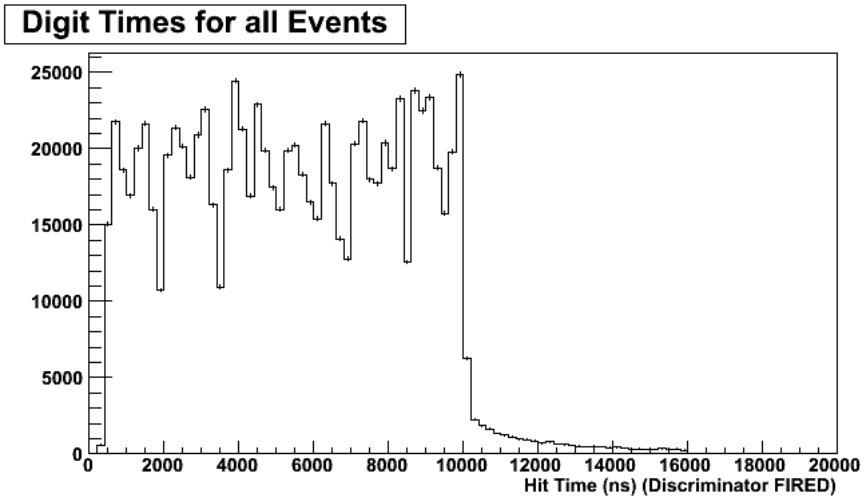

Figure 5.13: MI spill duration. The gate remains open the last 5.5μs to record late activity such as Michel electrons.

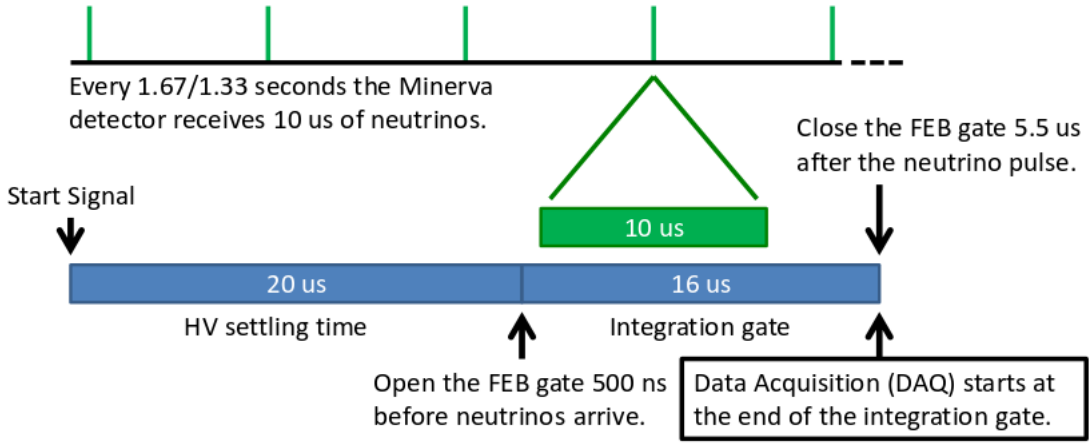

Figure 5.14: Integration gate structure. [Figure by Geoff Savage, FNAL.]

ial parts of the measurement and to even obtain any useful result(s). Whenever is possible and reliable to use, simulation is a powerful tool, specially in low-statistics and complex fields like neutrino physics. Simulation also helps in the comparison of new results against theoretical models. In some cases it is the only source and best estimate of parameters that are unavailable at the moment and without which is impossible to make any prediction. MINERvA compares its data to theoretical models by constructing a Monte Carlo (MC) simulation of the physics of the interactions under study including backgrounds, and all the detector components. A different MC is generated to incorporate the conditions

of each data set, like variations in the beam intensity or hardware replacements. The simulation is divided in three main branches.

5.2.1 Simulation of Neutrino Interactions

MINERvA uses the GENIE neutrino Monte Carlo generator [131], [132] as its base generator to simulate the interaction of neutrinos with nuclei and nucleons in different nuclear environments (different materials), as well as the interaction of neutrinos with electrons. Final cross section results are also usually compared against generators like NuWro [133], NEUT [134], and GiBUU [64]. Simulation of neutrino interactions in MINERvA starts by using the neutrinos from the GEANT4 and FLUKA [135] simulation of the NuMI beam, which delivers a neutrino energy distribution of the ME flux (see section 4.2.4), that together with the information about the geometry of the detector are used as the input information in GENIE. The probability that a neutrino interacts with a given scattering process is determined by the neutrino's incoming energy, the target material and from probabilities of existing cross sections.
All dominant scattering channels in the MINERvA's ME regime are built into GENIE and are explained in more detail in section 2.1: Quasi-Elastic Scattering, the dominant interaction at E_ν <2.0 GeV, is implemented using the Llewellyn-Smith model. Resonance Pion Production is slightly dominant in the $2 \lesssim E_\nu \lesssim$10GeV region, and uses the Rein-Sehgal model. Shallow and Deep Inelastic Scattering greatly overcomes all other channels after $10GeV$, and it is implemented using the model of Bodek and Yang. Coherent pion production is built into GENIE through the model of Rein and Sehgal. Neutrino-electron cross sections are calculated using the Marciano-Parsa theory [136]. As can be seen in figure 5.16, there exist overlap regions where two or more kind of interactions are present, GENIE approximates the total cross section of the overlapping zones as $\sigma^{total} = \sigma^{QE} \oplus \sigma^{RES} \oplus \sigma^{DIS}$ [137]

It is not possible to obtain realistic data-MC comparisons if nuclear effects are not taken into account. The modeling of the nucleus plays an important role, specially in heavier nuclei. Previous versions of GENIE modeled the nucleus as a relativistic Fermi gas (RFG) of protons and neutrons in the nucleus (including Fermi motion and Pauli blocking), where the average energy $\langle\epsilon\rangle$ is used to get the binding effects [58], but lacking a proper treatment of nucleon correlations. This analysis uses GENIE version 2.12.6 that already includes processes like the long range correlations of nucleons inside the nucleus, present in the random phase approximation model (RPA) [62], short-range correlations of nucleons, where the scattering is from correlated pairs of nucleons (proton-neutron,

proton-proton or neutron-neutron pairs), treated by one of the "two-particle two-hole" (2p2h) models available in the field [61]. These modifications have the effect (among others) of suppressing and enhancing the event rate in different Q^2 regions.
The particles created in the neutrino interaction, usually re-interact with the nucleons within the nucleus with the possibility of undergoing different processes, like pion absorption and pion production, elastic or inelastic scattering, or charge exchange. The reconstruction in MINERvA is done by looking at the particles after these final state interactions (FSI), which disguise the original interaction (see figure 5.15). GENIE simulates final state interactions with the "Intranuclear Cascade Model" [63], the model propagates particles inside the nucleus in steps, for each step a probability of no-interaction is calculated, which depends on the nuclear density and in the cross section of the particular interaction (charge exchange, pion absorption, and so on), such cross sections are obtained from previous data or by extrapolation from different nuclei.

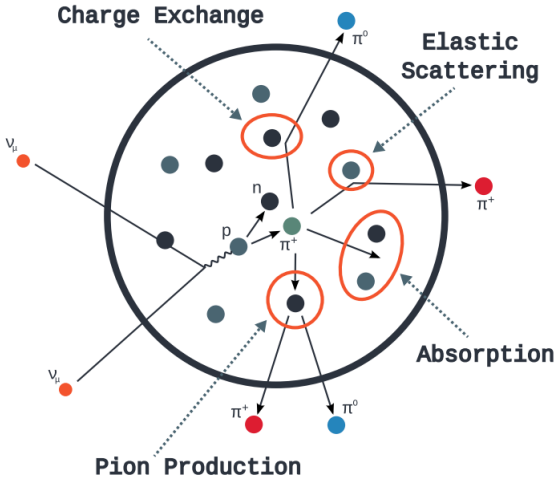

Figure 5.15: Possible final state interactions (FSI) undergone inside the nucleus by the primary interaction particles. [Figure by Tomasz Golan, MINERvA collaboration.]

GENIE's final state particles have all the initial kinematic information that will be used when particles are propagated through the detector.

5.2.2 Simulation of Particles Through Mater

All materials and geometry of the MINERvA subdetectors are included in a very detailed GEANT4 simulation 5.17. Particles exiting the nucleus (from the GENIE simulation) are propagated through the detector. GEANT4 basically decides the fate of the outgoing particles, based on probabilities of the different possible interactions, like particle decays,

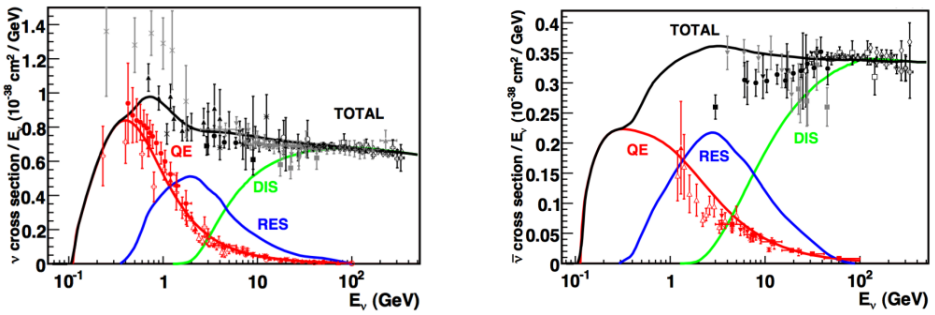

Figure 5.16: Dominant ν_μ (left) and $\overline{\nu}_\mu$ (right) scattering channels in MINERvA interaction particles. [Figure by G.P. Zeller, Fermilab.]

scattering and absorption, these probabilities are provided by the GEANT4's physics list [138]. The list includes interactions of hadrons, ions, standard electromagnetic processes, stopping particles and decays. Given the amount of particles created and due to the big number of possible interactions, it is basically impossible (or at least unpractical) to get a full theoretical prediction of the energy loss by all the particles involved in an interaction. GEANT4 simulates an interaction in 1 mm steps where the interaction is modeled depending on its momentum, if it is below 10 GeV/c, the Bertini cascade model is used [139], and for higher momenta the QSGP model [140]. However it is not practical, in terms of computing resources, to save all the 1-mm step information for every particle in the detector. Instead, MINERvA saves "trajectories", where a trajectory represents a particle. Each trajectory has trajectory points, where each of these points corresponds to the steps mentioned above. Only the initial and final points of the primary particles (particles from the main neutrino interaction) are saved. Additional points are saved whenever the particle goes into a different material, energy loss changed more than 5%, the path length is larger than 20 cm or an elastic interaction happens. If required, special samples can be generated saving either all points of the primary trajectories, all trajectories, or even all trajectories with all points.

5.2.3 Readout Simulation

The optical, electronic and DAQ systems are included in the readout simulation. The readout is simulated with only one neutrino interaction happening in each gate (no pile-up). The light yielded in the plastic scintillator simulated by GEANT4 is translated to photoelectrons (PE) in the PMTs using an optical model, by means of the Birk's law [129]. The gain of the photoelectrons as they travel through the dynodes in the PMT, is simulated

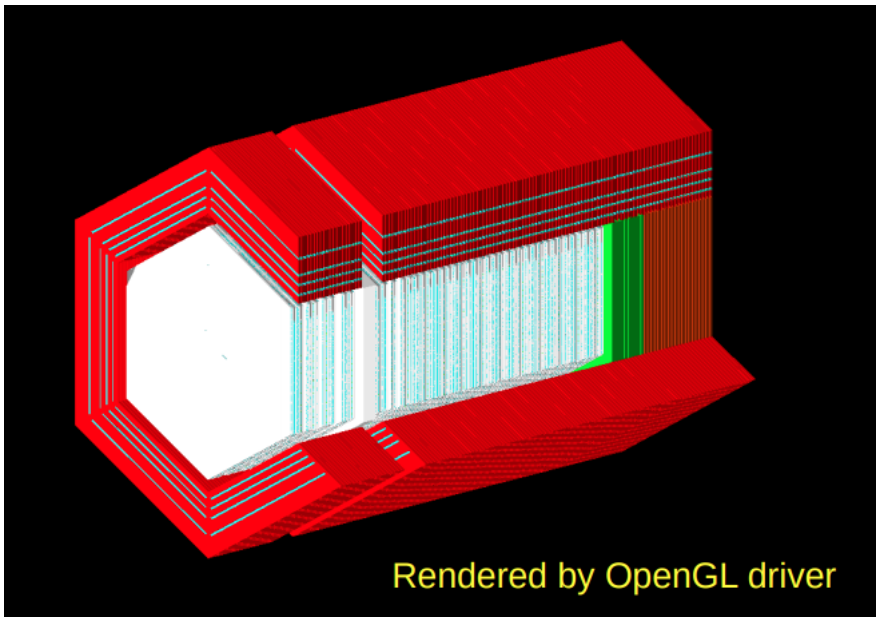

Figure 5.17: Detailed simulation of the detector geometry. Simulation was done using OpenGL and written in XML. [Figure by Jaewon Park, MINERvA collaboration.]

using a statistical model. Neighbor fibers getting into the PMT usually leak light to each other, this feature is known as "cross talk", and is also simulated using information from cross talk created by "rock muons" (muons created by the interaction of neutrinos in the rock upstream the detector, see section 5.3). The gain and cross talk simulated charge coming out of the PMTs is treated by a model of the FEBs, that simulates the low, medium and high gain chips, taking care of the amplification and integration of the charge that then is passed to and ADC for digitization at the end of the gate. Reset time (also known as dead time) in the TriP chips is also simulated in the FEB model.

5.2.4 Data Driven Simulation

Even though MINERvA is a neutrino experiment, it had to deal with pile-up due to the NUMI's high intensity. This means that more than one neutrino event got into the same readout gate. The pile-up is simulated by overlaying a random data gate in a MC gate (see figure 5.18). All dead time hits are hidden, whether they are data or simulated hits.

The time distribution for MC hits is much narrower than that of the data, this means that pile-up and dead time have a more significant contribution in data than in MC. MINERvA simulates this effect by looking at "rock muons" in the data and data-driven particle simulation for the MC, then a fit is done to get a random smearing that will be

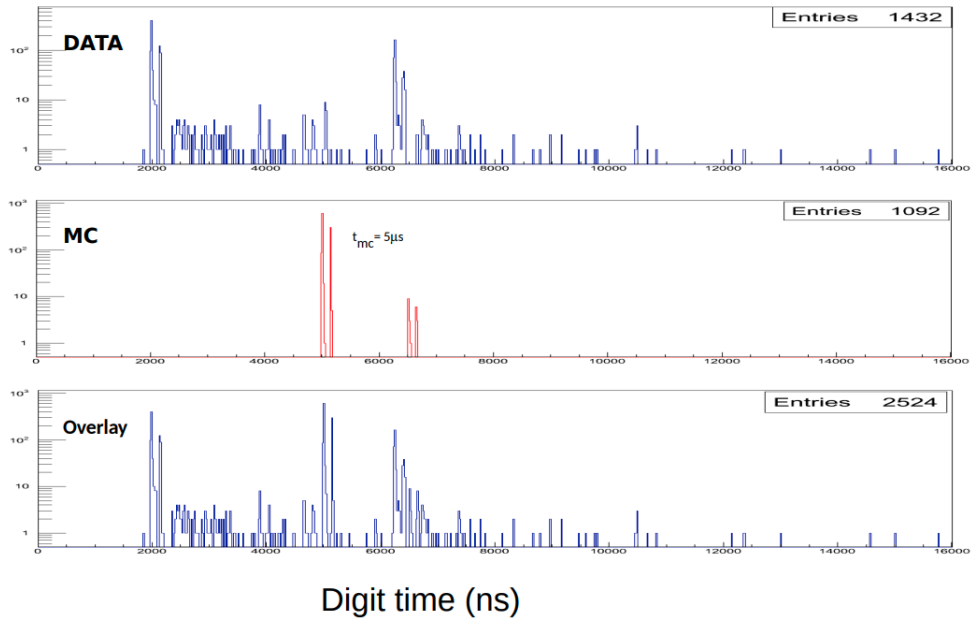

Figure 5.18: Data readout gate overlaid with a MC gate for pile-up simulation. [Figure by Trung Le, MINERvA collaboration.]

used to correct the hits timing. Then a random number is added to the raw hit time to account for timing calibration corrections.

5.3 Calibration

MINERvA uses the raw digits from ADCs and TDCs (time-to-digital conversion), processes them through a series of steps to ultimately get calibrated energy and time that is later used for reconstruction purposes. Figure 5.19 shows the overall calibration process (some steps are omitted in this section).

5.3.1 Energy Calibration

The process of energy calibration involves taking the ADC counts and taking them all the way to energy expressed in MeV, available for doing physics analysis. The expression to get the calibrated energy is as follows

$$E = PE\left(c,t\right) \times Att\left(s\right) \times S2S\left(s,t\right) \times F_{MEU}\left(t\right) \tag{5.1}$$

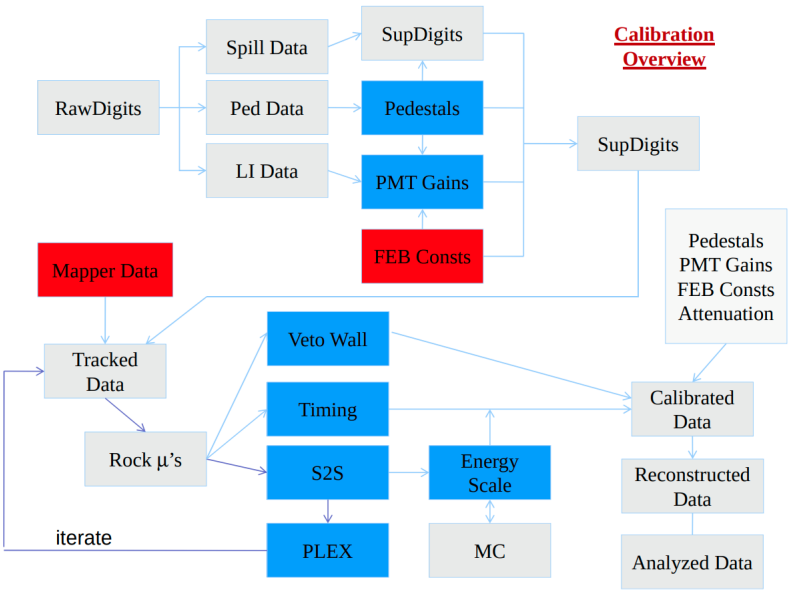

Figure 5.19: Overall calibration flow diagram [Figure by Dan Ruterbories (U. of Rochester).]

where PE, Att, $S2S$ and F_{MEU}, are the number of photoelectrons, the attenuation, the "strip to strip" correction, and the "muon energy unit", respectively. They are explained next.

Photoelectrons

The first step in getting the calibrated energy is to convert ADC counts to number of photoelectrons, these are calculated as follows

$$PE\,(c,t) = ADC \times FEB\,(c)\,/Gain\,(c,t) \tag{5.2}$$

"ADC" are the ADC counts obtained when the beam is present but subtracting the electronic noise always present in the ADC module, this noise is known as pedestals and it was determined by measuring the ADC counts in mixed beam/no-beam runs. After removing outliers, the pedestal subtracted is the mean of the distribution in the channel, see figure 5.20

the "$FEB\,(c)$" gives the low, medium and high response of each of the ADC channels (TriP chips) in the FEBs. The response curve for each is obtained by comparing a known input charge against the output charge of the channels (see figure 5.21).

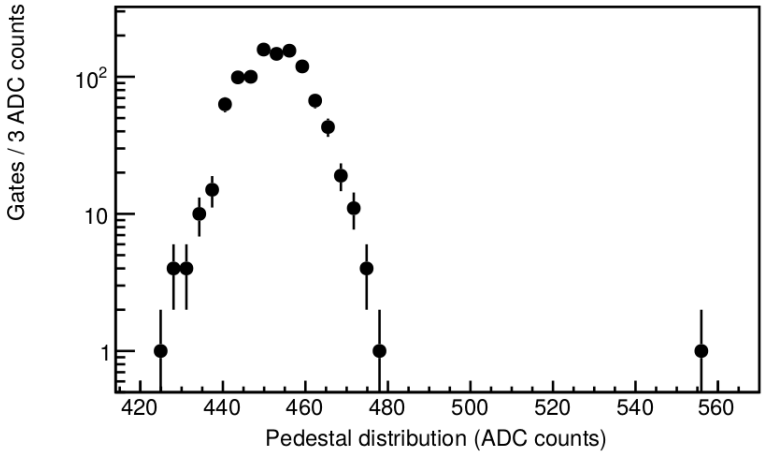

Figure 5.20: Pedestal distribution in a channel, for the duration of a readout gate. [Figure from [18].]

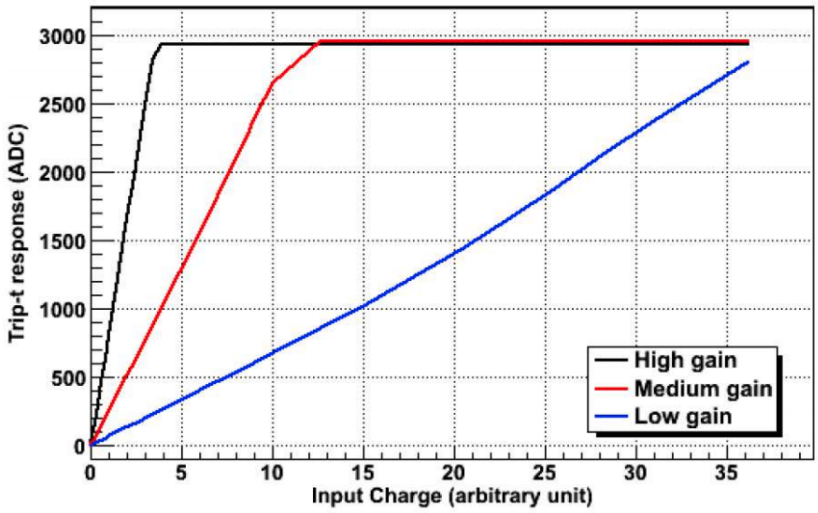

Figure 5.21: Response of the low, medium and high gain ADC channels (TriP chips) in FEBs. [Figure from [16].]

The "$Gain\,(c,t)$" term is the ratio of the output (anode) over the input (photocathode) charge in the PMT. It is gotten by doing light injection into the PMTs, this was done through special runs, or once after each beam spill, using ∼30 ns long pulses of blue light from LEDs, a diffuser is used to spread the light evenly through the photocathode. The gain is time dependent due to factors like aging of the PMTs, voltages variations (sags), or FEB swaps. The data from the light injection (LI) is combined with a photostatistics

model of the PMTs to extract the final gain (see figure 5.22).

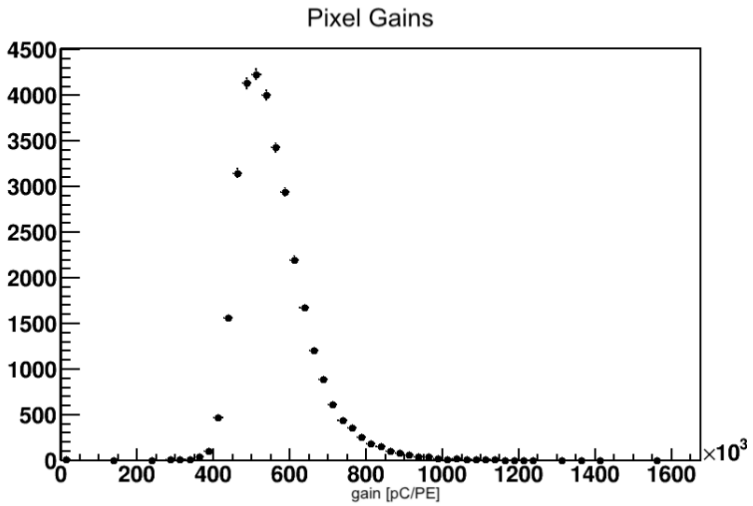

Figure 5.22: Gain distribution off all PMTs installed in the MINERvA ME run. [Figure from [19].]

Attenuation

The "Att" term is the attenuation of the scintillation light in each channel. The total attenuation in a channel is determined as the product of the attenuation in the fibers times the attenuation of the strip in that channel, and $Att\,(s)$ is the inverse of the total attenuation. Before installation, each module was scanned with a $Cs - 137$ source, and the light response of all the strips as a function of transverse and longitudinal position was measured. Figure 5.23 shows the longitudinal measurement versus the attenuation in one of the strips.

S2S Correction

The S2S factor consists of the alignment correction plus the strip to strip correction and has the purpose of uniforming the detector response. The firs step is the alignment of the strips to have a good estimate of the path length. Strips can be misaligned basically in each direction but the more significant are the transverse shift of the strips on the XY plane, and the rotation planes around the Z axis, other displacements are relatively small. The transverse misalignment is measured using the reconstructed tracks of rock muons (see section 5.4), the track makes an angle (θ) at the point where it intersects the base

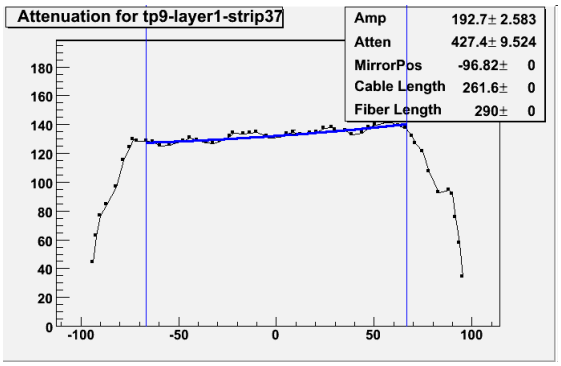

Figure 5.23: Longitudinal attenuation of the plastic scintillator in one of the strips.

of the strip, with the normal to the base of the strip, the hit energy is multiplied by the $\cos\theta$, and this way the energy is corrected to normal incidence. The average energy from all the rock muon hits in a strip is plotted against the hits base position and fitted with the strip shape. The position of the fit's maximum shows the transverse displacement of that strip (see figure 5.24).
The rotation of the planes is measured by selecting the transverse displacement of all the strips in the plane in bins and plotting them against longitudinal position along the strips, where the longitudinal position is determined also by the rock muon track. The transverse displacement is fit again, but now as a function of the longitudinal position. The rotation of the plane is taken as the slope of the line from the fit (see figure 5.25). Displacements and rotations are measured in every plane, and corrections are applied during the reconstruction stage.

After the alignment, strip response across all planes is measured, the variation comes mainly from aging effects in the scintillator and from different amounts of leakage across all optical connectors, imperfections in the sealing epoxy, etc. Using rock muons' peak energy deposition along their track, a first iteration of the channel energy is obtained by considering the S2S corrections as unity and using a truncated mean energy deposition ($\frac{dE}{dx}$), using a truncated mean reduces the number of rock muons required which in turns reduces the time interval between samples (given that rock muons are statistically limited). For the next iterations (up to four are used before converging), events with $\pm 50\%$ of the initial mean are used to calculate the new mean. When a hardware swap takes place, the process must start over. The constant in each strip is normalized to 1.0 to preserve the detector energy scale (later in this section) and is calculated as

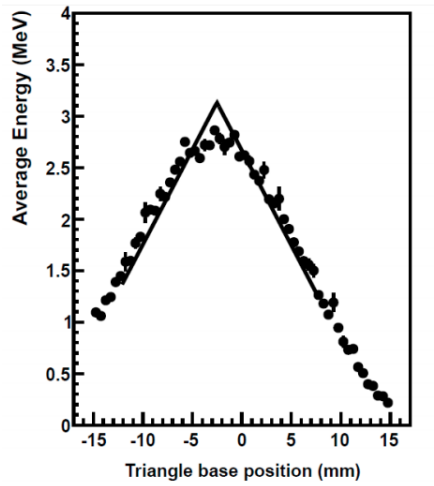

Figure 5.24: Transverse displacement of a strip. Module 50, plane 2 in the CH target, are used as an example.

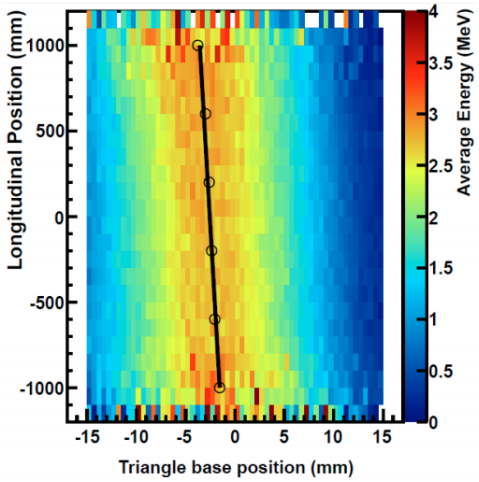

Figure 5.25: Fit for plane rotation around the Z axis (module 50, plane 2 in the CH target is used as an example). [Figure from [16].]

$$c_i^{strip} = \frac{\frac{1}{x_i}}{\frac{1}{N}\sum_k \frac{1}{x_k}} \tag{5.3}$$

where x_i is the truncated mean of the strip, N is the number of good channels, and k is the sum over all good channels.

A similar correction factor (c_i^{plane}) is obtained for each plane, and the overall correction

is $c_i^{plane} \times c_i^{strip}$. Finally a second iteration of both the alignment procedure and strip to strip calibration is done, improving the results from the first iteration.

Detector Energy Scale

The last term in equation 5.1 is the detector energy scale or "muon energy unit" (MEU). This calibration comes after the corrections for uniforming strips and planes have been applied, therefore an overall MEU correction is calculated for all the strips in all planes. The position and momentum of a data sample of rock muons matched in the MINOS detector is used to guide a simulated sample of rock muons (data-driven simulation). An energy of the rock muon clusters (see section 5.4) is obtained using a preliminary MEU value in both data and MC. The peak reconstructed energy is used as the expected muon energy deposition per plane. The MC reconstructed cluster energy is corrected to the true cluster energy, using the slope of the reconstructed versus true cluster energy in the MC. The MEU is calculated as

$$MEU = MEU_{preliminary} \frac{E_{Peak}^{MC}}{a} \frac{1}{E_{Peak}^{Data}} \tag{5.4}$$

where E_{Peak}^{MC} and E_{Peak}^{Data} are the MC and data "peak" reconstructed cluster energy; and a is the slope of the reconstructed vs true cluster energy in the MC. The light yield L_Y is calculated in a similar fashion, but in this case, clusters PE along the rock muon tracks in the MC are match to data to be sure statistical fluctuations on the photocathode for both data and MC are identical. The calibrated light yield factors is calculated as

$$L_Y = L_{Y preliminary} \frac{PE_{Peak}^{Data}}{PE_{Peak}^{MC}} \tag{5.5}$$

Figures 5.26 and 5.27 show the peak cluster PE and the peak cluster calibrated energy (MEU) for all the time the MINERvA detector took data.

5.3.2 Time Calibration

Raw TDC counts are calibrated by correcting for time slewing T_{Slew}, channel-to-channel time offset T_{CtC} and transport time in the optical fiber T_{Trans}. The calibrated time T_{Cal} is calculated as

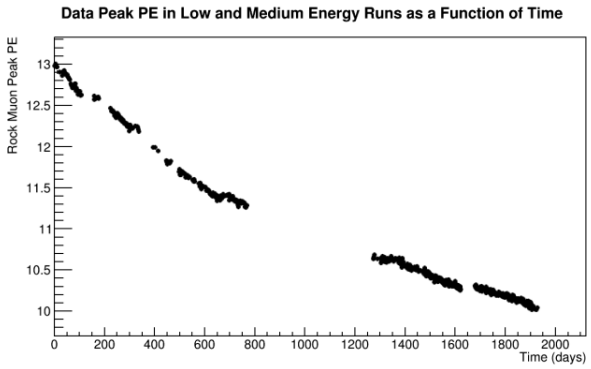

Figure 5.26: Peak cluster PE during all MINERvA data taking for both the LE (left side of the transition period gap) and ME (right side of the transition period gap) configurations. [Figure from [16].]

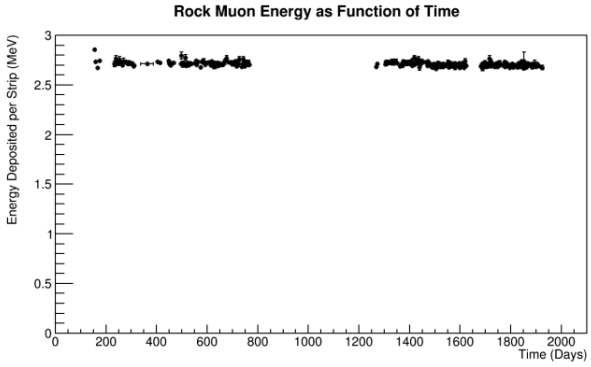

Figure 5.27: Peak cluster MEU during all MINERvA data taking for both the LE (left side of the transition period gap) and ME (right side of the transition period gap) configurations. [Figure from [16].]

$$T_{Cal} = T_{Raw} - T_{Trans}\,(c) - T_{CtC}\,(c) - T_{Slew}\,(PE) \tag{5.6}$$

$T_{Trans}\,(c)$ is the transport time of the light in the optical fiber to the PMT's photocathode, it is measured as the distance from the center of the strip to the photocathode divided by the speed of light in the fibers (156 mm/ns). When the hit position is known during the reconstruction, the time is recalculated using the updated distance. $T_{CtC}\,(c)$ includes cable delays between individual FEBs and FEB chains, and time offsets between chains. $T_{Slew}\,(PE)$ is caused by scintillator decay times and is a function of the number of photoelectrons yielded in a strip (see figure 5.28). Both channel-to-channel and time slew are

measured simultaneously in an iterative process that uses rock muon tracks, both times for each hit in a muon track are corrected for muon time-of-flight, transport time in the optical fiber, time slewing and channel-to-channel offsets from the previous iteration (up to eight iterations are performed).
All channels read by the same TriP chip get the same measured time offset. Timing calibration needs to be done after each hardware swap since it changes the channel-to-channel time offset.

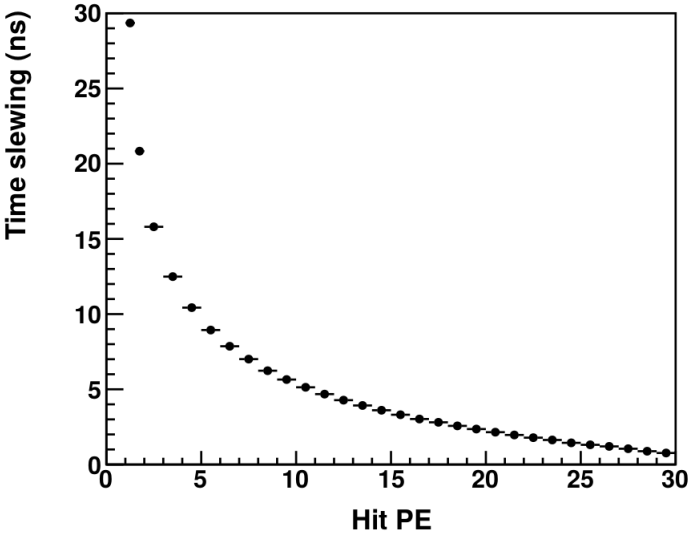

Figure 5.28: Time slew as a function of the PE yield in the muon track.

Before the first iteration T_{Slew} and T_{CtC} are set to 0, in the i^{th} iteration a time corrected, T_{Corr} and a time average, T_{Avg} are calculated as

$$T_{Corr} = T_{Raw} - T_{Trans} - T_{Slew} - T_{CtC} - T_{TOF} \tag{5.7}$$

$$T_{Avg} = \frac{\sum_{i=1}^{i=8} T_{Corr_i}}{8} \tag{5.8}$$

And the final expressions for the channel-to-channel and time slew are

$$T_{CtC} = T_{Raw} - T_{Trans} - T_{CtC} - T_{TOF} - T_{Avg} \tag{5.9}$$

$$T_{Slew} = T_{Raw} - T_{Trans} - T_{CtC} - T_{TOF} - T_{Avg} \tag{5.10}$$

5.4 Reconstruction

Reconstruction begins after hit times and hit energies have been calibrated. Hits close in time in the same strip are grouped into digits, a digit per strip. Digits are grouped into different kinds of "clusters", one or more clusters per plane. Clusters are the basis of most of the reconstructed objects. Examples of which, are vertices, tracks and blobs which determine the start and end points of the particles, the trajectories they followed, and how they interacted in the detector. With them, other reconstructed quantities can be derived, such as angles, ranges, etc. These object together with their energy and timing information will be later used to determine the physical quantities used to extract physics results from the detector.

5.4.1 Time Slicing

Time slicing separates neutrino events within the same readout gate using hit timing information, by grouping hits close in time that fired the discriminator. Slices are formed if they contain enough energy. The slicing is done by an algorithm called "chronobuncher", which considers a window backward and forward in time from the hit under study where other hits are gathered. It is crucial in separating events from different neutrino interactions that are very close in time, specially in the ME beam, where the intensity increased and so did the pile-up compared to the LE beam, and a more aggressive slicing had to be performed where the window time was varied to optimize event separation. During the 16μs of the readout gate, hits from different events accumulate. The new slicing algorithm groups interactions as shown in figure 5.29, where a random data gate is shown as example to visualize the slicing of neutrino events. The piled-up events in that same gate are shown in figure 5.30. [1]

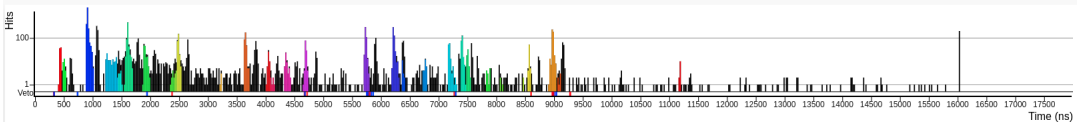

Figure 5.29: Hits grouped in time slices within a readout gate for real data.

After slicing, different interactions are available for analysis. Figures 5.31 and 5.32 show a zoom and event display of only slice 3 in the gate shown above. This particular slice has a width of ∼100 ns.

[1] event comes from the MINERvA event display software, Arachne [141].

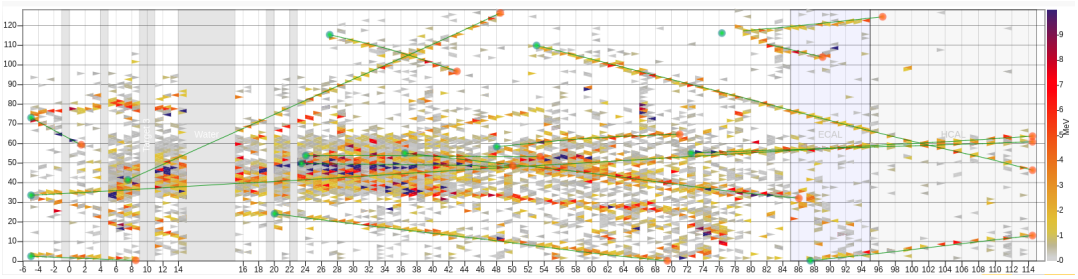

Figure 5.30: Reconstructed objects in a full standard readout gate for real data.

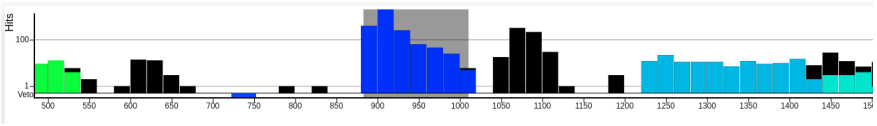

Figure 5.31: Zoom of slice number 3 in the readout gate shown in figure 5.29.

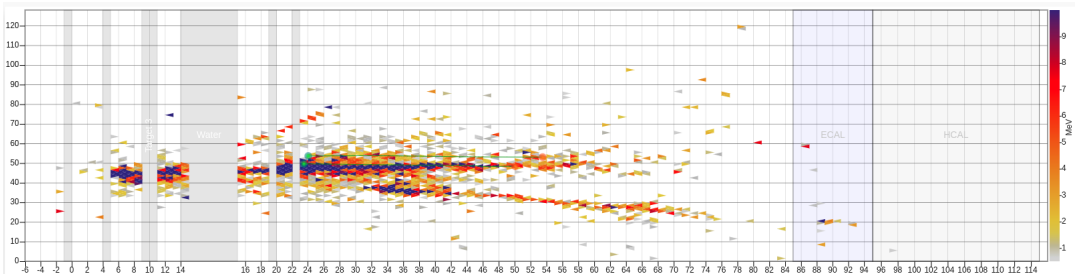

Figure 5.32: Event display corresponding to slice number 3, isolated from the readout gate shown in figure 5.30.

5.4.2 Cluster Formation

From now on, reconstructed objects are supposed to be in the same time slice, unless otherwise stated. All the hits in a strip are grouped to form a "digit". There are "ID Digits" and "OD Digits" for strips located in the inner and outer detector. Neighbors strips in the same plane form "clusters", which are categorized depending on their energy and size (see figure 5.31).

- Low activity - Clusters with low total energy.
- Cross Talk - The ones that include activity identified as cross talk by the cross talk algorithm (light leaked between neighbor fibers in the PMT).
- Trackable - Energy in the range 1-8 MeV per hit and less than 12 MeV in total. These clusters are compatible with minimum ionizing particles.

- Heavy Ionizing - Very energetic clusters, with energies larger than 12 MeV (usually way larger than that). No limits in the upper energy bound. These clusters are typically narrow in their energy distribution.
- Super Clusters - Show a broader energy distribution. Usually present in electromagnetic and hadronic showers.

It is during the cluster formation that cross talk as well as low activity hits are removed and not considered to be part of clusters.

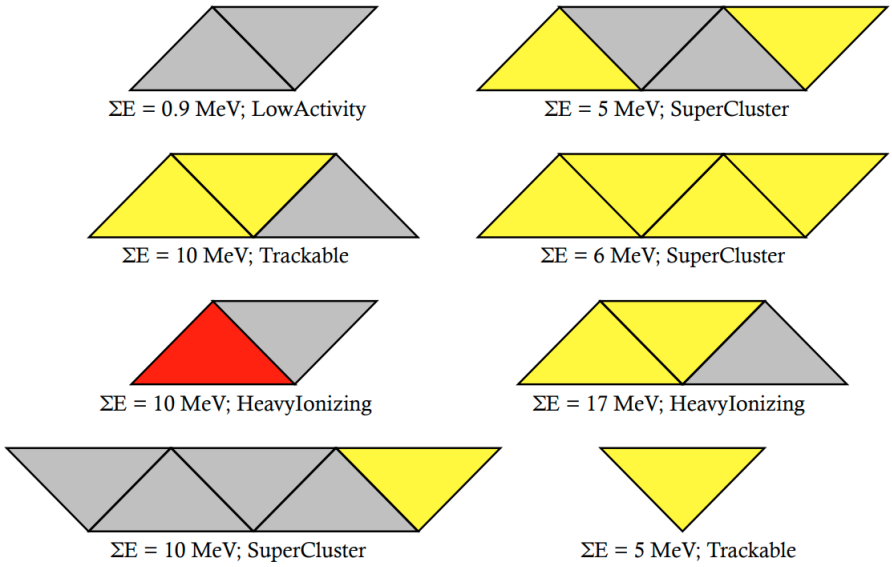

Figure 5.33: Types of clusters in the MINERvA detector. [Figure by Gabriel Perdue, Fermilab.]

Each cluster has a five-vector associated to it which includes the calibrated time (of the most energetic hit), energy and the three spatial coordinates. The Z coordinate is the plane's center, while the X,Y position is the energy weighted average transverse position.

5.4.3 Track Formation

Two main tracking algorithms are used in MINERvA, the long and short tracking algorithms. The former is relatively easier to work with, as it has more planes to form. It uses the heavy-ionizing and trackable clusters. 2-D seeds are formed in each view (X, U and V) which requires a minimum of eleven planes to then form 3-D tracks. Finally a Kalman Filter technique [142], considers the multiple scattering of the entire track, multiple Coulomb

scattering makes peculiar curved tracks. The algorithm searches clusters starting from the back end of the detector and going in the direction opposite to the beam. Going in that direction, makes it easier for the algorithm to tell between tracks, as they have larger opening angles than when they are closer to their common vertex upstream. Tracks can have planes with no clusters, this often happens in planes with dead channels or in planes affected by dead time. Each plane in the track is called a "node" of the track, even if there are no clusters in that plane. Tracks are constrained to angles less than 70° with regards to the Z axis, angle above which, the number of planes is not enough to construct the track.
Short tracks are very important for short-lived and low energy particles which usually travel just a few planes in MINERvA, even when their angle with regards to the z axis is small (forward particles). At least four planes are needed in order to have a short track (an XUXV-view configuration). It uses two different algorithms: one that looks for short segments overlapping (similar to the long-tracking algorithm), and another one that looks for peaks around a point in order to find a track candidate.

A sample of rock muons is selected to measure the tracking angle and tracking position resolution. Their track is divided into an upstream and downstream section, a track is reconstructed in both sections and the angle and position are compared in the boundary between sections, the differences in their angle and 3-D positions are the reported resolution: ∼0.02 rad and ∼3 mm, respectively.
Muon tracks are passed through a "cleaning" algorithm that removes energy assigned to them that is not likely due to a minimum ionizing particle (MIP), that energy is freed and made available for further hadronic energy reconstruction.

The track efficiency is defined as the number of reconstructed target over the number of "trackable" true simulated particles. Particles are considered trackable when they span more than the number of required planes to form a short or a long track, and their angle is less than 70° with regards to the Z axis. Figures 5.34 and 5.35 show the tracking efficiency obtained with a MC sample of CC coherent pion events, in C, CH, Fe and Pb targets. The former uses "long tracks" only, while the latter also includes "short tracks".

Although using short tracks increases the efficiency in CC coherent pion events (signal events), it also increases the number of background events. Therefore events with reconstructed short tracks are rejected in this analysis.

5.4.4 Vertex Reconstruction

Vertices are also categorized depending on the tracks associated to them

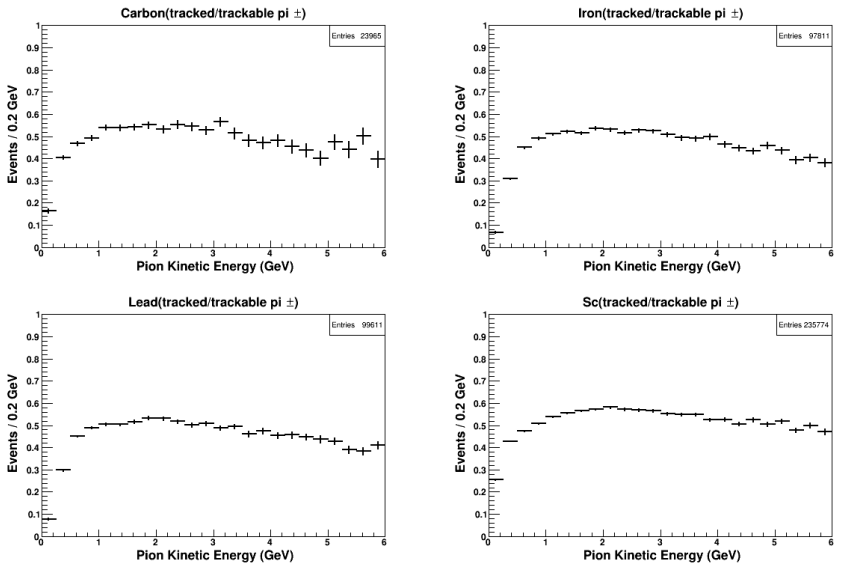

Figure 5.34: Track efficiency for a ME sample with more than 1 track in the main neutrino interaction vertex, using long tracks only. The same data set was used to select and compare events from the plastic scintillator, carbon (graphite), all iron and all lead targets. Pion energy refers to the hadronic (non-muon energy).

- Starter - No incoming tracks. More than one outgoing track.
- Kinked - One incoming and one outgoing track.
- Forked - One incoming track and more than one outgoing tracks.
- Stopper - One incoming and no outgoing tracks.
- Exceptional - More than one incoming and any number of outgoing tracks.

The primary vertex (anchor vertex) is usually chosen as the muon most upstream node (the muon upstream vertex), and is actually the primary vertex used in this analysis (see chapter 6). Vertices close to the primary vertex are added to it depending on the result of the fit procedure. When the extra vertices are added to the primary, the vertex is redefined as the point of closest approach of the tracks. This method works acceptably well for events with opening angles between the tracks considerably large. For events with small opening angles the fit delivers a poor resolution, where the vertex is predicted way upstream or way downstream the truth vertex in the simulation. Most recent analyses in the ME era of the experiment have used “machine learning” (ML) techniques to better

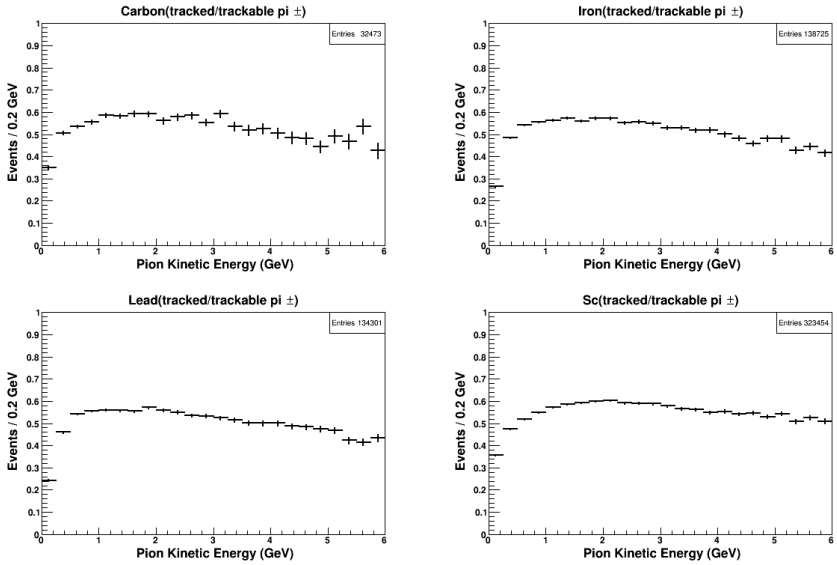

Figure 5.35: Track efficiency for a ME sample with more than 1 track in the main neutrino interaction vertex, using long and short tracks. The same data set was used to select and compare events from the plastic scintillator, carbon (graphite), all iron and all lead targets. Pion energy refers to the hadronic (non-muon energy).

predict the interaction or primary vertex [143].
Whether the fiducial volume of interest of a particular analysis is in the tracker or in the passive targets region, affects the definition of the vertex for analyses not using ML. For instance one-track analyses like CCQE in the passive target region, where there is a muon and a neutron as the observables, there is only one tracked particle, the muon. In those events the primary vertex is also selected as the first node of the muon track. In the target region, the muon vertex is always in the first plane downstream the passive material.

5.4.5 Energy Reconstruction

This is divided in muon energy and hadron energy reconstruction. Since all analyses in MINERvA so far use only one muon, the muon energy reconstruction involves just one particle. Besides that, in the majority of the analyses the muon is required to enter the MINOS detector [2], meaning that in those cases the muon traverses the detector from the point of the neutrino interaction until the back end of MINERvA, and looses energy basically only through ionization, a well understood mechanism.

[2] the CC kaon analyses were the exception due to statistical limitations [144], [145].

There is a big difference with the recoil or hadronic energy, where frequently, multiple particles are present, these particles deposit their energy in many different ways, creating secondary particles with different detector response. Neutral particles are also created and their energy deposition has to be inferred from models. When the hadrons escape the detector their energy is also lost and cannot be measured.
Particles originated outside the detector continuously entered the OD and ID, depositing energy in both. Particles like muons from cosmic ray origin, or other non-beam related particles are hard to predict, and very little is done to get rid of them. Rock muons as useful as a tool they are, can enter the detector during the same time the readout gate is open, depositing energy along the main neutrino interaction originated inside MINERvA. These events make the reconstruction algorithms to overestimate the energy of the events under study or misidentify the topology of the interaction. Rock muons have the signature of starting in the first module of the detector. A "rock-muon-removal" algorithm subtracts their energy from the overestimated energy of the neutrino event without getting rid of the event.

Muon Energy Reconstruction

The total energy of the muon is the sum of the energy lost in the MINERvA detector plus the energy lost or calculated in the MINOS detector. The energy lost in MINERvA is calculated using the Bethe-Bloch equation [20] (equation 5.11), updating the energy in each possible layer of the detector, as the energy deposited depends on the energy of the incoming particle.

$$-\frac{dE}{dx} = Kz^2\frac{Z}{A}\frac{1}{\beta^2}\left[\frac{1}{2}ln\frac{2m_ec^2\beta^2\gamma^2T_{max}}{I^2} - \beta^2 - \frac{\delta}{2}\right] \tag{5.11}$$

The energy in MINOS is obtained by either one of two methods, by range or by curvature. To count a muon in MINOS as a valid muon that was created in MINERvA, a matching procedure is done where the downstream end of the MINERvA track is compared to the upstream end of the MINOS track, they have to be less than 200 ns apart and less than 40 cm separated from each other. After a good match, if the muon stops inside the MINOS detector, its momentum is determine by range, which is a more precise and certain method (momentum resolution $\sim$ 5%, compared to $\sim$ 10% for the curvature method). When the muon also escapes the MINOS detector, the by-curvature method is used, and the momentum P is calculated using the radius of curvature of the particle R in cm, and the MINOS magnetic field B in kGauss, as follows:

$$\frac{1}{R} = \frac{0.3 \times B}{P} \tag{5.12}$$

Recoil Energy Reconstruction

The recoil energy is defined as all the energy deposited in the detector and not used by the muon track, or electron in neutrino-electron scattering. The first step in the procedure consists in correcting the "visible" energy in the active material by the energy lost in passive materials, where a calorimetric scale factor is obtained for each subdetector

$$C^{SF} = \frac{E^{vis}_{module} + E^{pass}_{module}}{f \times E^{vis}_{module}} \tag{5.13}$$

where E^{vis}_{module} is the visible energy deposited in the plastic scintillator of a module, E^{pass}_{module} is the energy deposited in passive materials in the module, and $f \simeq 0.8127$ is the active fraction of the scintillator plane. The energy lost in the passive materials is supposed to be due to a minimum ionizing particle, which is a good estimate for sufficiently high energy but not for low-energy particles (see energy loss curve in figure 5.36). After the passive material correction, the energy is compared with the truth energy from the model, and an additional scale factor is applied to the sample to match it to the truth energy. This correction factor is meant to compensate for all the neutral and escaping particles that do not show up as visible energy in the detector, as well as for the extra energy lost by low-energy particles in the passive material.

$$E_{recoil} = \alpha \times \sum_i C^{SF}_i E^{vis}_i \tag{5.14}$$

where α is the "calorimetric" scale factor, obtained by matching the passive material corrected to the true energy; C^{SF}_i and E^{vis}_i are the passive material scale factor and the visible energy in subdetector i.

The performance of the calorimetric energy reconstruction and an extra energy dependent correction are detailed in section (6.4).

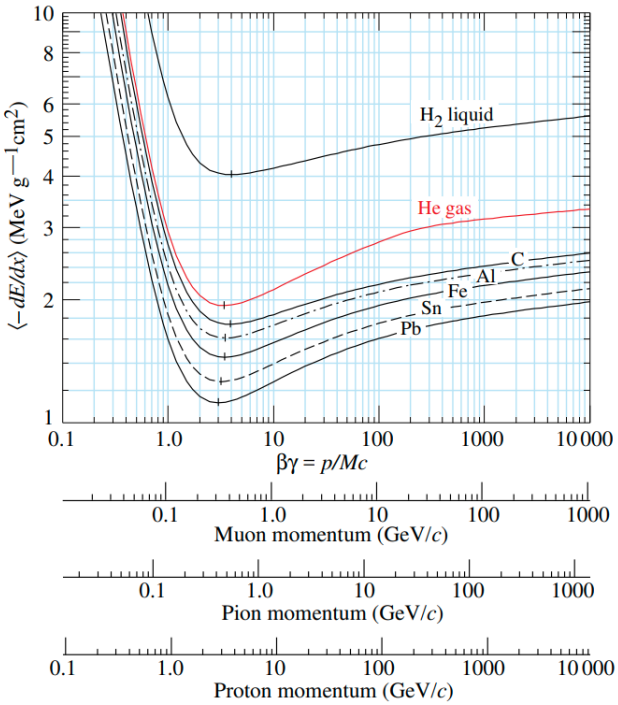

Figure 5.36: Mean energy loss rate by different particles in different materials, from the Bethe-Bloch equation [20]. [Figure from [20].]

Chapter 6

CC COHERENT π^+ PRODUCTION Off C, CH, Fe And Pb At MINERνA

In this chapter, the ν_μ beam described in chapter 4, is used to search for the CC coherent production of positive-charge pions from C (graphite), CH (hydrocarbon), Fe and Pb targets, in the MINERvA detector described in chapter 5. This work represents the largest statistical sample from carbon, and the first reported measurement from iron and lead. It is also the first simultaneous measurement of the interaction in different materials.

The experimental signature consists of a forward muon (μ^-) and a forward charged pion (π^+) originated from a common vertex. The energy of the vertex is consistent with the energy deposited by only the muon and the pion, both considered minimum-ionizing particles. These are all detector-independent and model-independent topologies. A sub sample of the MINERvA ν_μ dataset with these characteristics has been isolated. Measurements of the total cross section $\sigma\left(E_\nu\right)$, and differential cross sections $d\sigma/dE_\pi$, $d\sigma/d\theta_\pi$ and $d\sigma/dQ^2$, were obtained from C, CH, Fe and Pb targets. All results are compared against the Rein-Sehgal model [5].

Unlike the previous MINERvA low-energy (LE) measurement [31], [7], this analysis does not use anti-neutrino data. Besides just recently becoming available, the statistics of the medium-energy (ME) $\overline{\nu}_\mu$ dataset are a small fraction of the ν_μ sample, making the $\overline{\nu}_\mu$ analysis in C, Fe and Pb, statistically limited.

The NC process is not pursued, because as mentioned in chapter 3, it is model-dependent.

6.1 Dataset

All results shown in this chapter correspond to the "neutrino"data taken in the so called "medium-energy" (ME) era of the MINERvA full run. It spanned for almost three and a half years, from September 2013 to February 2017, reaching $\sim 10.6\times10^{20}$ protons on target (POT) (figure 6.1). POT is a parameter that allows neutrino experiments to have an idea on the number of neutrinos that were sent to the detector, since most of them do not interact with it. The data was separated into "playlists", according to important changes in accelerator, beamline and detector configuration, like changes in intensity, resuming data taking after long accelerator shutdown periods, or after filling or emptying the water and helium targets (see table 6.1). The water target does have an impact in this analysis, since it is downstream three of the targets used (see section 6.2). The helium target is upstream all the regions analyzed, and therefore it has not been included in table 6.1.

Monte Carlo (MC) samples were generated, simulating the beamline and detector configuration in each playlist. A sample 4 times the data POT was simulated for events in the tracker (CH target), while for the passive target region (C, Fe and Pb target) 10 times the number of data POT was needed due to the reduced statistics. The size of the MC samples is increased until the statistical uncertainty in the simulation is not significant compared to the other sources of errors. It is typically maintained below a few percent.

A special MC sample of CC coherent π^+ events was generated to measure the selection efficiency, resolution of reconstructed variables and migration matrices (see sections 6.4, 6.5 and 6.9). Because CC coherent π^+ events represent $\sim 1\%$ of the overall neutrino events [18], the sample was made 100 times the data POT.
All events in the MC samples were generated inside the inner detector (ID). Events were allowed to develop and interact in all the detector, but none was generated in the outer detector (OD) calorimeters.

The beam intensity was increased in three different occasions while MINERvA was running in the ME neutrino mode. The four intensity configurations shown in table 6.1 reflect these changes, which correspond to the changes in the proton stacking patterns of the booster batches (see figure 4.4).

Playlist	Data POT ($\times 10^{20}$)	MC POT CH - C/Fe/Pb - Signal Only ($\times 10^{20}$)			Intensity	Period (approx. days)	H_2O Target
ME1A	0.896	3.935	9.992	93.534	6+0	124	Empty
ME1B	0.186	1.084	2.011	18.306	6+0	23	Empty
ME1C	0.429	1.931	4.358	42.320	6+0	61	Empty
ME1D	1.433	5.749	14.327	136.510	6+0	150	Empty
ME1E	1.026	4.997	10.951	141.278	6+0	105	Empty
ME1F	1.660	6.739	17.011	160.473	6+2	124	Empty
ME1G	1.371	5.423	14.266	131.369	6+2	122	Empty
ME1L	0.132	0.572	1.470	11.601	6+4	8	Filled
ME1M	1.567	8.445	21.105		6+4	118	Filled
ME1N	1.063	4.993	11.253	49.146	6+4	66	Filled
ME1O	0.297	1.542	3.285	28.530	6+6	12	Filled
ME1P	0.462	1.976	4.749	42.715	6+6	20	Filled
TOTAL	10.521	45.998	114.778	855.782		933	

Table 6.1: All ME ν_μ data samples (known as playlists). The MC simulation in the passive materials (C, Fe and Pb) needs more protons on target (POT) due to their reduced mass compared to the tracker region (CH). Intensity is shown in terms of the slip stacking of the batches in the booster (see chapter 4). The water target was filled just for the last 5 playlists.

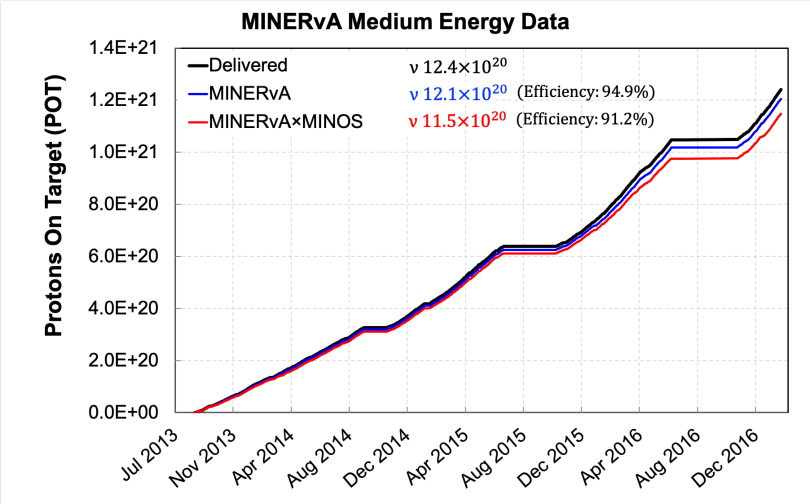

Figure 6.1: Number of protons on target (POT) vs time for the MINERvA ME data taking. The plateaus correspond to beam downtime. The loss in efficiency in MINOS and MINERvA, is due to issues with the data acquisition system DAQ, and due to hardware failures and replacements. [Figure by Nuruzzaman, MINERvA collaboration.]

6.1.1 MC Samples Reweighing

Most of the neutrino interactions in the MINERvA MC are built into the GENIE MC generator version 2.8.4. [132]. The MINERvA collaboration has made modifications to some of this interactions in the standard GENIE MC, based on data from previous MINERvA analysis or from other experiments. Based on new available models, the collaboration has also added other interactions previously not considered by generators. Such changes make the MC prediction better agree with the data.
Further corrections to the MC were applied to the flux prediction and the tracking efficiency of muons in the MINOS detector.

CCQE

MINERvA's definition of CCQE-like scattering includes low energy protons and any number of neutrons in the final state [146]. Since the scattering of neutrinos off correlated pairs of nucleons, in medium (2p2h) and long range (RPA) (section 2.2.1) fall in this definition, corrections to the CCQE event rate due to 2p2h and RPA processes are included in the MC simulation. The magnitude of the correction depends on the energy and three-momentum transferred.

Non-Resonant Single Pion Production

Re-analyzed data from the ANL and BNL neutrino-deuterium interactions [147], [148] allowed to make constraints to the production of non-resonant pions. A scale factor of 0.43 ± 0.04 was applied to all non-resonant single pion events in GENIE, based on a fit obtained from the deuterium data in those experiments.

Resonant Single Pion Production

From the same neutrino-deuterium data fit, an overall normalization of 1.15 ± 0.07 was obtained for single resonant pion events. A correction to the axial vector mass for resonant pion production (similar parameter to the one used in section 3.3.1), changed its best estimate and reduced its fractional uncertainty from $\sim 20\%$ to $\sim 5\%$ ($1.12 \pm 0.22 \rightarrow 0.94 \pm 0.05$). A recent analysis [149] has been used to simultaneously tune GENIE to the neutrino-deuterium data and to the CC pion production data from hydrocarbon at MINERvA [130] [150] [151]. From this analysis a further "ad hoc" correction for resonant pion events with $Q^2 < 0.7$ GeV is obtained. The correction tries to match the MC prediction to the data suppressed in this region, due to collective nuclear effects (figure 6.2)

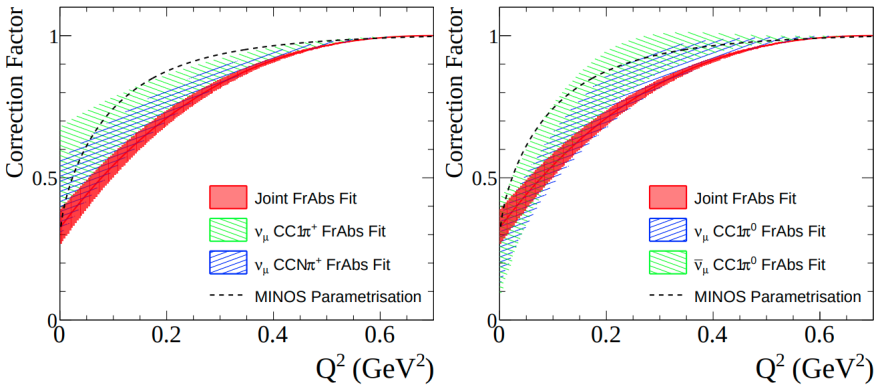

Figure 6.2: Correction to resonant pions with $Q^2 < 0.7$ GeV. The data in that region is believed to be suppressed due to collective nuclear effects. The "joint" correction was obtained by tuning GENIE using all the CC pion production data in MINERvA. The $CC1\pi^+$ and $CCN\pi^+$ corrections were obtained by tuning GENIE using the CC single and N pion production data in MINERvA. The ν_μ $CC1\pi^0$ and $\overline{\nu}_\mu$ $CC1\pi^0$ corrections were obtained in a similar fashion.

Flux

The flux prediction by FLUKA [135] and GEANT4 [125] has large uncertainties specially due to some of the secondary hadron interactions in the beamline. A recent measurement by MINERvA of neutrino-electron scattering [126] and data from hadron interactions from other experiments [152] have helped constraining the flux prediction. A correction factor is applied to account for the difference between the original and constrained predictions.

MINOS Tracking Efficiency

A correction factor is applied to the MC to account for the difference in the efficiency of tracking muons in the MINOS detector, compared to the data. The efficiency in the MC is a few percent larger than the efficiency seen in real data events. The difference is due to the non-simulation of pileup events in the MINOS detector. When more than two muons enter the MINOS detector in the same time slice (see section 5.4.1), the data event is rejected. Since no multiple events are considered in the MINOS simulation, the MC efficiency is larger. The difference in efficiency and therefore the correction factor depend on the muon momentum, as seen in figure 6.3. A curve is fitted to the data to correct events with momentum in between measured values. There is a curve for low and one for high intensity playlists.

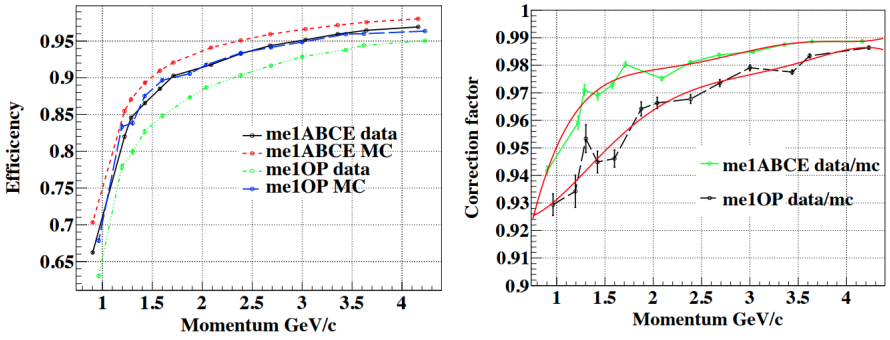

Figure 6.3: Momentum dependent tracking efficiency (left) and correction factor (right) of the muons entering the MINOS detector. Black and red (green and blue) curves correspond to the data and MC efficiencies in the low (high) intensity playlists. The right plot shows the correction functions for the low (green) and high (black) intensity playlists. [Figure by Anushree Gosh (MINERvA collaboration).]

6.2 Signal

A proper signal definition is needed in order to isolate CC coherent-pion candidates from the dataset. The signal definition is the same used in the LE analysis [18], the only difference being the addition of three more targets. CC coherent-pion events are defined as those with the following features:

- A CC coherent interaction induced by a muon neutrino scattering off a C, CH, Fe or Pb nucleus. Creating a positive pion and a negative muon from a common interaction vertex.
- The interaction vertex must be inside an hexagonal prism centered in the MINERvA detector with an apothem of 850 mm and a height dependent on the material under study.
- The neutrino energy must be $2.0 \lesssim E_\nu \lesssim < 20.0$ GeV. Neutrinos with energy below that range do not create muons energetic enough to enter the MINOS detector, so their energy cannot be reconstructed. Events from neutrinos with more than 20 GeV have large systematic errors associated to the flux.
- Events happening on other nuclei, but inside the fiducial volume, are considered signal, to avoid a dependence of the background on the signal model. This basically concerns only events in hydrocarbon and iron, where the percentage of events scattering from other a different material is $\sim 4\%$ and $\sim 2\%$, respectively.

6.2.1 CH Fiducial Volume

The fiducial volume for the hydrocarbon (CH) target is defined as an hexagonal prism centered in the MINERvA detector with an apothem of 850 mm and a height of 108 planes ($\sim$ 2.42 m), being contained completely in the ID, plastic scintillator region. The reconstructed interaction vertex is defined as the vertex of the muon track. This is due to the poor resolution of the standard algorithm in signal events, which uses the point of closest approach between the pion and muon tracks (see sections 5.4.4 and 6.5). The vertex of the muon track then must be inside the fiducial volume, to select the event[1]

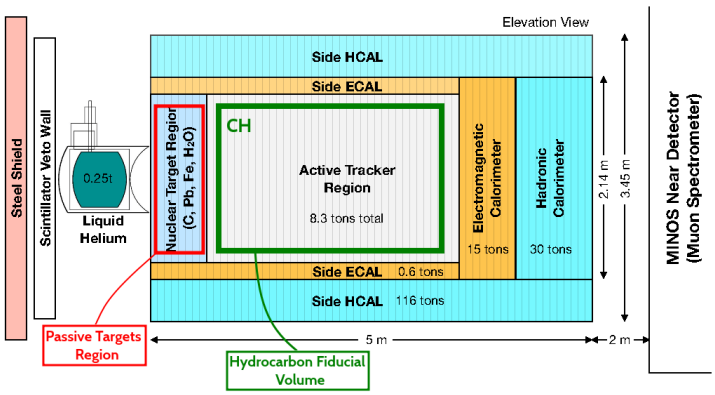

Figure 6.4: Side view of the MINERvA detector, showing the fiducial volume of the CH target (in green). The passive targets region (in red) does not represent the fiducial volume for those materials.

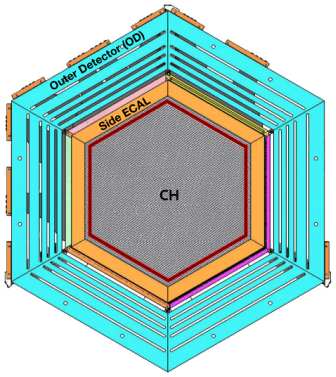

Figure 6.5: Front view of the fiducial volume for the CH target.

[1]From now on the expressions "muon vertex" and "reconstructed vertex" will be used interchangeably.

6.2.2 C/Fe/Pb Fiducial Volume

The passive targets region in the MINERvA detector is somewhat complicated. But as explained in chapter 5, the material distribution through it, was meant to maximize the statistics of some interactions, and equalize the acceptance and mass of iron and lead. The installed iron and lead mass, were distributed in 4 iron and 5 lead targets across the passive targets region. The overall fiducial volume for iron and lead consists then in the addition of four and five independent fiducial volumes, respectively. As carbon was already present in the tracker region, just a single pure carbon target was installed to extract hydrogen contributions from CH interactions. A guiding drawing is shown in figure 6.7 depicting the position and configuration of the passive targets.

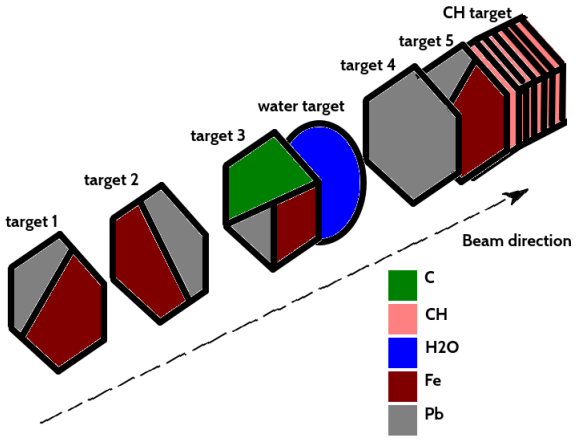

Figure 6.6: Isometric drawing of the passive targets configuration and arrangement in the passive material region. In reality there are plastic scintillator planes in between the passive targets, used for tracking. Targets 1 and 5 have the same material configuration.

Unlike the CH target, the passive targets only span one module, and have all different thicknesses, as shown in table 6.2. And because no light is deposited in them by the passage of a charged particle, the fiducial volume for each of the targets, is defined as the area of the plane immediately downstream and in front of each material times the thickness of the plane (figures 6.7 and 6.8). Figures 6.9 and 6.10 show a simulated signal event in the CH and Fe target 1 fiducial volumes.

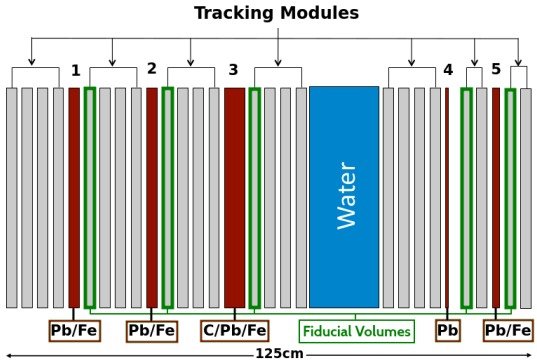

Figure 6.7: Side view of the target region, with the fiducial volume of each target in green. This figure is a zoom of the red target region in figure 6.4.

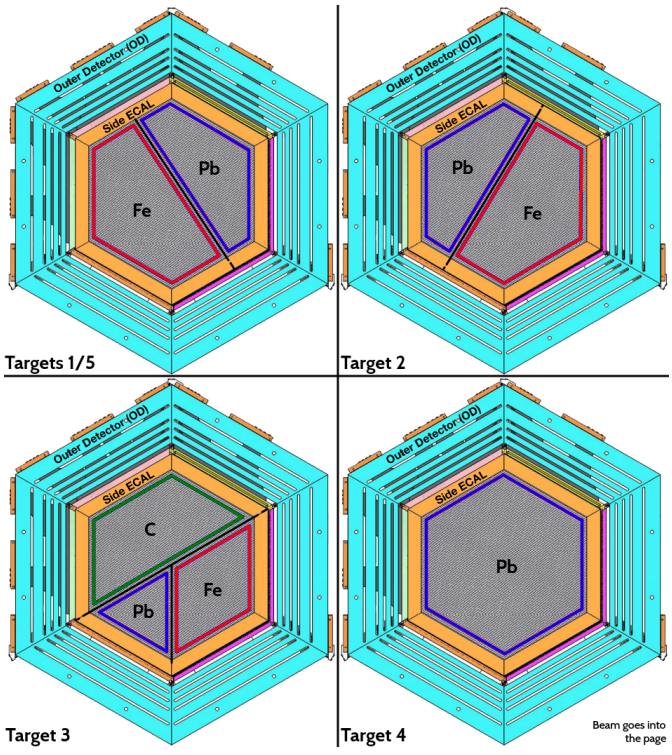

Figure 6.8: Front view of the fiducial volume in the passive targets. All have an apothem of 850 mm. The buffer region separation between fiducial volumes is 25 mm.

Target/Material	Fiducial Area (m^2)	Thickness (cm)	Fiducial Volume (cm^3)	Fiducial Mass (kg)	No. of Fiducial Nuclei (E27)
Fe target 1	1.557	2.567	3.998E4	313.193	3.38
Fe target 2	1.557	2.563	3.992E4	312.705	3.37
Fe target 3	0.786	2.873	2.258E4	158.397	1.71
Fe target 5	1.557	1.289	2.008E4	157.267	1.70
Pb target 1	0.860	2.578	2.218E4	250.427	0.73
Pb target 2	0.860	2.581	2.221E4	250.718	0.73
Pb target 3	0.369	2.563	9.467E4	106.879	0.31
Pb target 4	2.503	0.795	1.990E4	224.641	0.65
Pb target 5	0.860	1.317	1.133E4	127.933	0.37
C Total	1.203	7.62	9.165E4	159.371	7.99
Fe Total			12.256E4	941.562	10.16
Pb Total			17.029E4	960.598	2.79
CH Total	2.503	242.0	605.681E4	4754.3	238.38

Table 6.2: Characteristics of the fiducial regions in all targets used in this analysis. Individual and total contributions from iron and lead targets are shown.

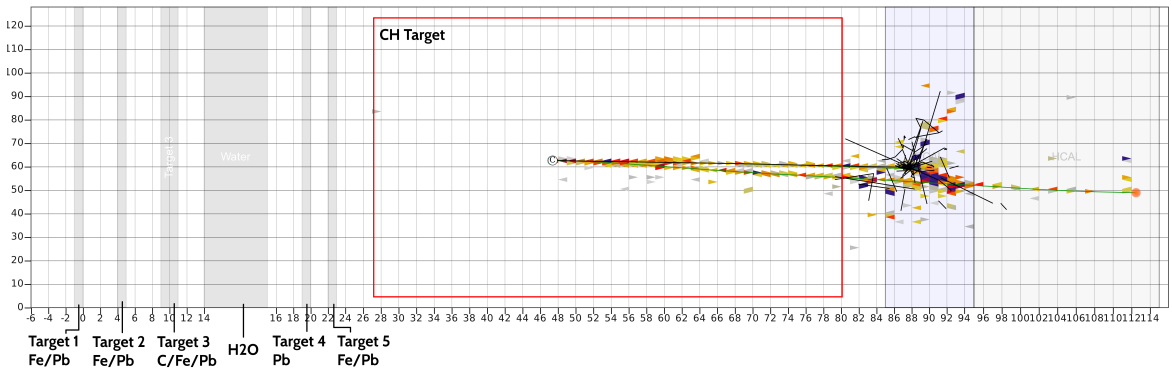

Figure 6.9: Top view of a simulated signal event in the CH target. A scale version of the inner part of the detector can be observed. The muon and the pion tracks go close to each other and then separate. The pion is seen interacting in the ECAL, while the muon leaves the back of MINERvA to enter MINOS. The red region is the fiducial volume of the CH target. Each colored triangle corresponds to a scintillator strip, and the color indicates the energy deposited in the strip according to the scale in the right-hand side of the plot.

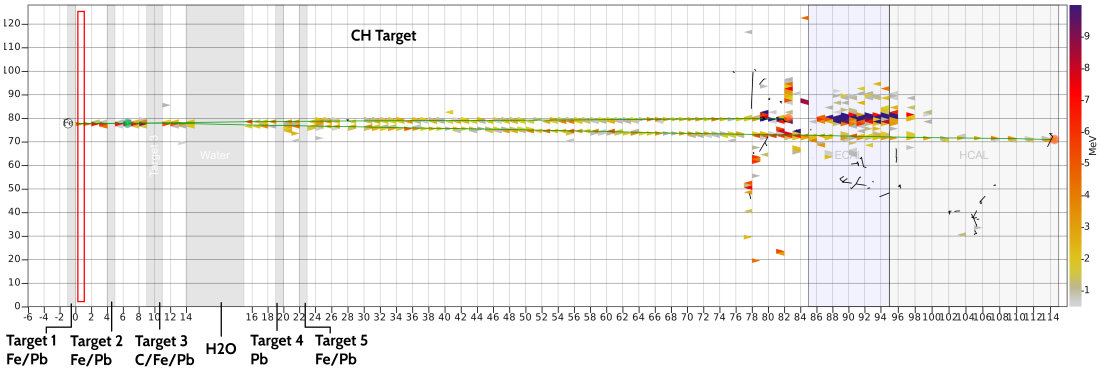

Figure 6.10: Top view of a simulated signal event in Fe target 1. A scale version of the inner part of the detector can be observed. The muon and the pion tracks go close to each other and then separate. The pion is seen interacting in the ECAL, while the muon leaves the back of MINERvA to enter MINOS. The red region is the fiducial volume of Fe in target 1. Each colored triangle corresponds to a scintillator strip, and the color indicates the energy deposited in the strip according to the scale in the right-hand side of the plot.

6.3 Background

The background consists of events that mimic the topology of the signal. Different interactions can have the same final state of a muon (μ^-) plus a pion (π^+) and no apparent activity near the vertex. A correct understanding of the backgrounds is as important as understanding the signal. They have a direct impact on the final cross section results. The background classification for this analysis also uses the classification from the LE analysis [18], plus the addition of the "plastic background" for the passive material targets. All background events come from the same fiducial volumes defined in section 6.2. The background classification goes as follows:

- CH (Plastic Background) - Because of the location of the fiducial volume of the passive targets, there are selected events that actually occurred in the plastic scintillator planes in between. Most of these plastic interactions occurred in the fiducial volume. Some others, because of the small opening angle between the muon and the pion, happened in the plastic upstream or downstream the fiducial volume. All "plastic" events are considered background.

- $\nu_\mu + n \rightarrow \mu^- + p^+$ (CCQE) - In a CC quasi-elastic scattering, the final state proton can be mistaken as a positive pion. Although the proton and pion usually have different energy deposition patterns, they often are very similar and hard to distinguish. The small contribution from the scattering off correlated pairs (2p2h) described in chapter 2, is included here.

- $\nu_\mu + N \rightarrow \mu^- + \pi^+ + N$ (W<1.4 GeV)- This includes all single pion production from resonant (the π^+ may be produced by a delta resonance) or non-resonant origin. These events are limited by the invariant mass of the hadronic system ($W < 1.4$ GeV). The signature of these events is the same as the signal when there is small activity near the vertex.

- $\nu_\mu + N \rightarrow \mu^- + X$ ($1.4 < W < 2.0$ GeV) - The multiplicity of final state hadrons increases. This is known as the transition region or "shallow" inelastic scattering (SIS). Usually the most energetic of the final state hadrons mimics the pion, while the rest might escape detection.

- $\nu_\mu + N \rightarrow \mu^- + X$ ($W > 2.0$ GeV) - This is the deep inelastic scattering (DIS) region, with higher multiplicity. Pions from the re-hadronization from the neutrino-quark interaction can look like signal-like events.

- Other - Events not coming from a CC ν_μ interaction. Including NC, wrong neutrino flavor and muon anti-neutrinos. Any of these could create a lepton and a hadron imitating the signal.

6.4 Analysis-Specific Reconstruction

The reconstructed objects obtained from the general reconstruction of the data and MC, with improvements and specifics for the ME sample (section 5.4), such as muon energy, vertices and tracks, are used in this analysis. Further reconstruction stages are needed in order to isolate the desired sample. All variables in this analysis follow basically the same reconstruction procedure as in the LE era, with adjustments to the CH sample in order to be consistent with the passive targets which demand new considerations.

The MC samples include the simulation of most of the processes involved, based on the most accepted physics models available (section 5.2). This is called the truth Monte Carlo, or "MC truth". The MC, is also taken through the same reconstruction steps as the data, in order to validate the reconstruction of the latter. This is called the reconstructed Monte Carlo, or "MC reco". Every analysis in MINERvA validates its reconstructed variables by looking at the comparison of the reco against the truth. This gives a "resolution" for each of the reconstructed variables, which is an indicator of how good the real data is being reconstructed.

In summary, this analysis searches for: events with only two tracks originated from a common neutrino interaction vertex; energy near the vertex consistent with the energy deposited by those two tracks only; and a low squared four-momentum transfer to the nucleus, $|t|$ (chapter 3). Expressing equation 3.8 explicitly

$$\begin{aligned} |t| = \Big| &-2\left(E_\mu + E_\pi\right)\left(E_\mu - P_\mu \cos\theta_{\nu\mu}\right) + m_\mu^2 \\ &-2\left(E_\pi^2 - \left(E_\mu + E_\pi\right) P_\pi \cos\theta_{\nu\pi} + P_\mu P_\pi \cos\theta_{\mu\pi}\right) + m_\pi^2 \Big| \end{aligned} \tag{6.1}$$

It is clear that the fundamental reconstructed variables needed to isolate signal events are: Vtx_{reco}, E_μ, E_π, $\theta_{\nu\mu}$ and $\theta_{\nu\pi}$, which are the interaction vertex, muon and pion total energy, and the angle of the muon and pion with regards to the neutrino. [2] The vertex energy E_{Vtx} is just the contribution of the muon and pion energy in the vertex region.

[2] All neutrinos are considered to travel in the direction of the simulated neutrino beam (see section 6.8).

6.4.1 Vertex Reconstruction

As mentioned in section 6.2.1, the reconstructed interaction vertex is the first node of the muon track candidate, which is always placed at the center of the plane where the vertex happens to be. This implies an uncertainty on the Z coordinate of half the width of the plane (∼8.5 mm) for events happening in the CH target.

For the passive materials, the uncertainty is larger in all three coordinates (X, Y and Z). Figure 6.11 shows the already explained separation between the Z position of the truth and reconstructed vertices. It can also be seen how the muon track is projected into the center of the passive material to assigned the reconstructed X and Y positions.

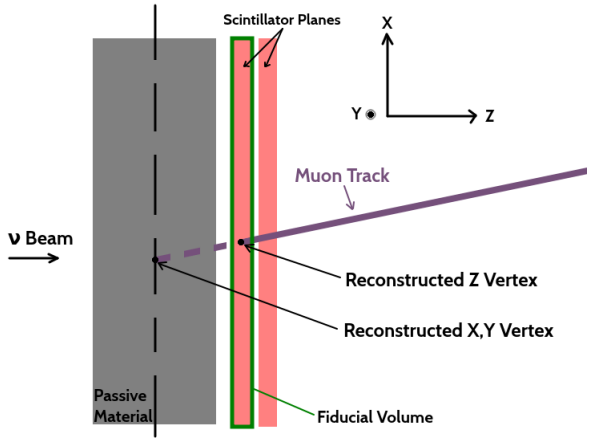

Figure 6.11: View from above the detector, showing the passive material to the left and the first active plane downstream to the right. The muon vertex is located at the center of the downstream plane. The muon track is projected into the passive material to assign the X and Y coordinates of the reconstructed vertex. This last part is important to determine the material in targets having more than one.

Figures 6.12 to 6.22 show the resolution of the X, Y and Z vertices for the CH, C and all Fe and Pb targets. The resolution is defined as the reconstructed minus the truth vertices in mm.

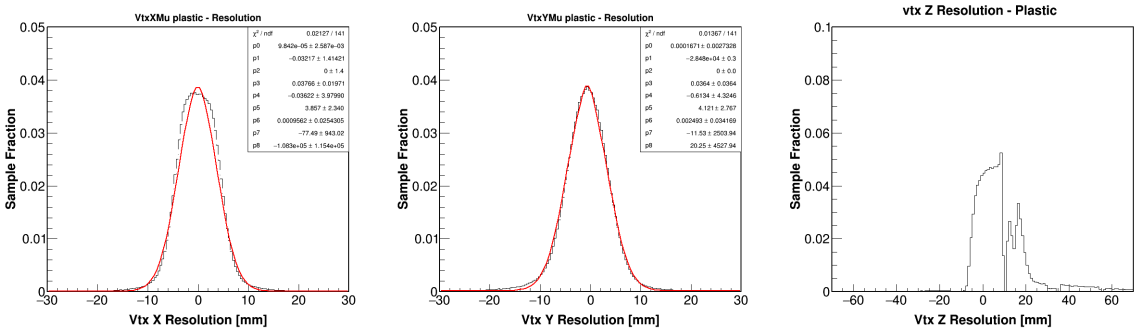

Figure 6.12: Vertex resolution in all coordinates in the CH target. The gap in the Z vertex resolution corresponds to the gap between the plane where the true vertex and reco vertex are.

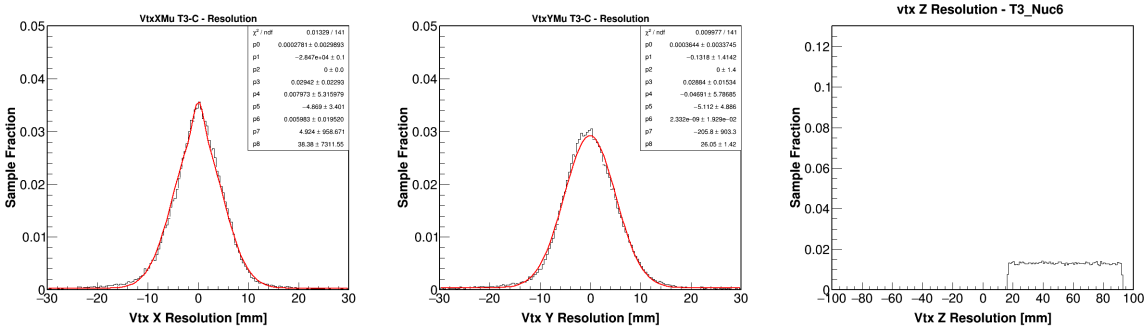

Figure 6.13: Vertex resolution in all coordinates in the C target. The shifted and wider range in the Z vertex resolution, correspond to the distance between any point inside the passive material (true vertex) and the center of the downstream plane (reco vertex).

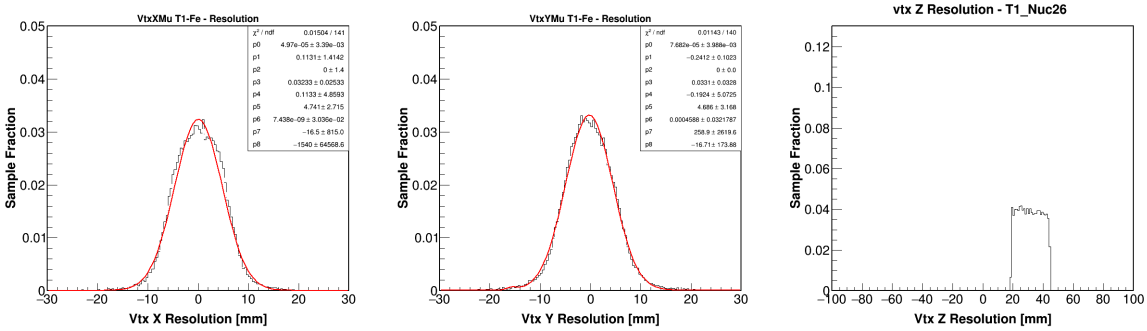

Figure 6.14: Vertex resolution in all coordinates in Fe target 1. The shifted and wider range in the Z vertex resolution, correspond to the distance between any point inside the passive material (true vertex) and the center of the downstream plane (reco vertex).

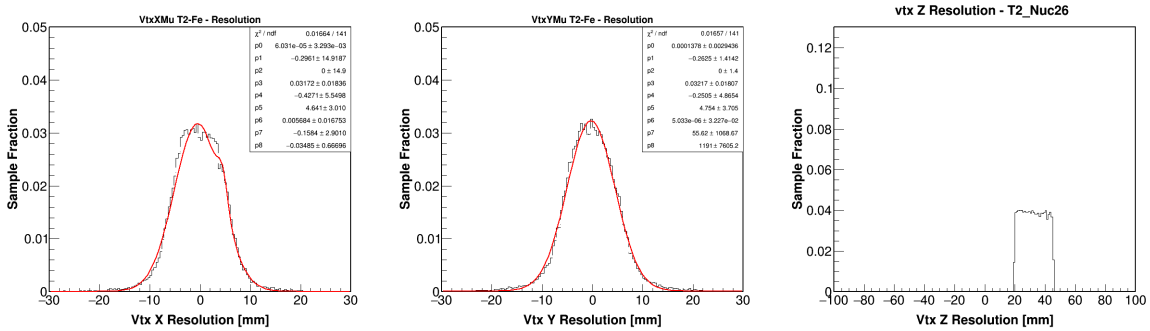

Figure 6.15: Vertex resolution in all coordinates in Fe target 2. The shifted and wider range in the Z vertex resolution, correspond to the distance between any point inside the passive material (true vertex) and the center of the downstream plane (reco vertex).

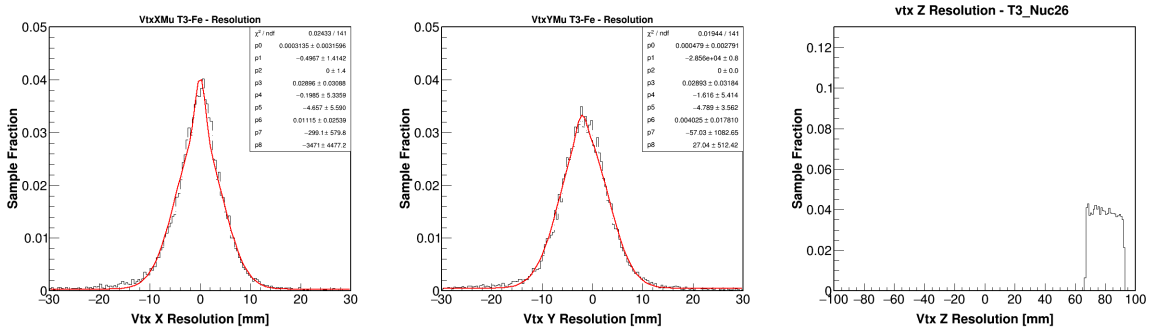

Figure 6.16: Vertex resolution in all coordinates in Fe target 3. The shifted and wider range in the Z vertex resolution, correspond to the distance between any point inside the passive material (true vertex) and the center of the downstream plane (reco vertex).

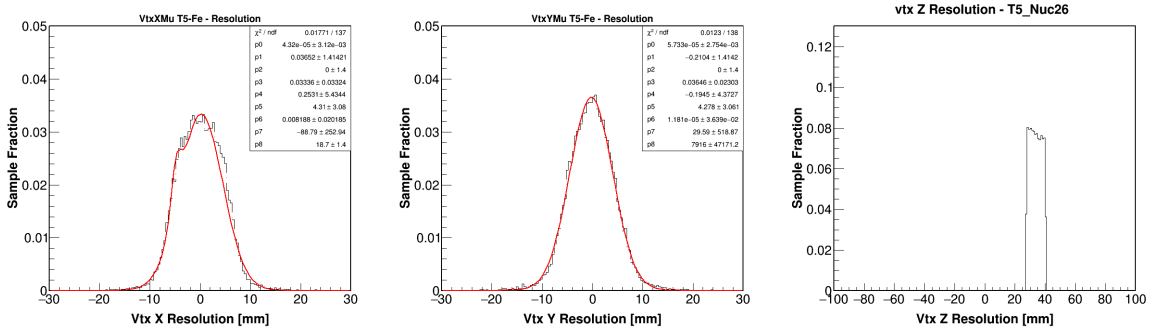

Figure 6.17: Vertex resolution in all coordinates in Fe target 5. The shifted and wider range in the Z vertex resolution, correspond to the distance between any point inside the passive material (true vertex) and the center of the downstream plane (reco vertex).

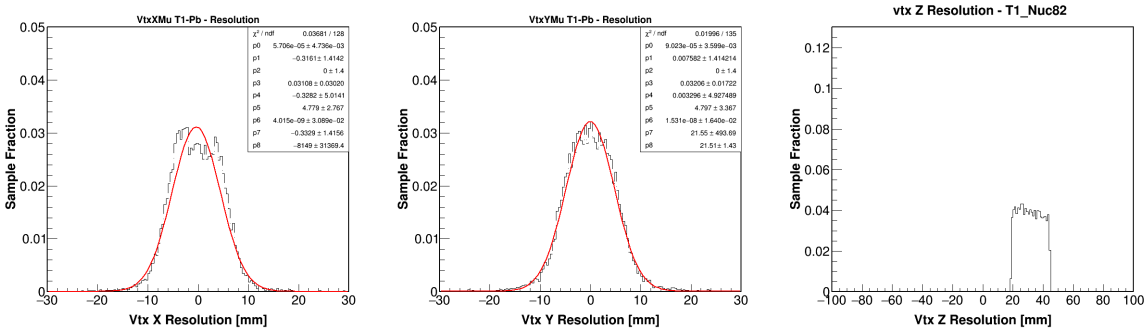

Figure 6.18: Vertex resolution in all coordinates in Pb target 1. The shifted and wider range in the Z vertex resolution, correspond to the distance between any point inside the passive material (true vertex) and the center of the downstream plane (reco vertex).

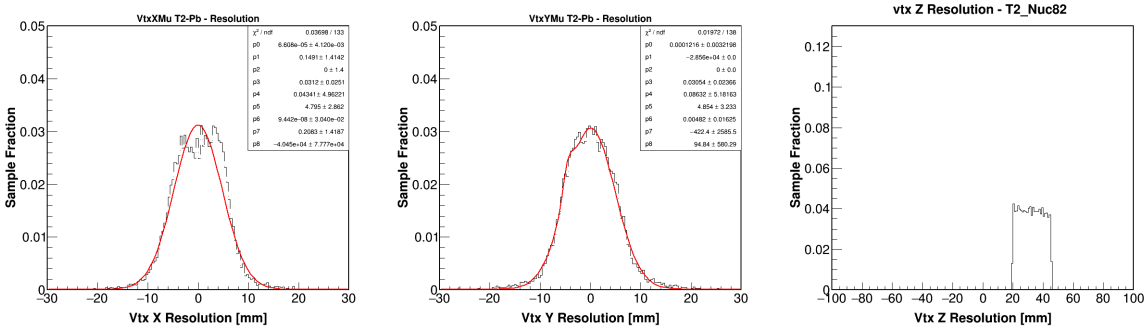

Figure 6.19: Vertex resolution in all coordinates in Pb target 2. The shifted and wider range in the Z vertex resolution, correspond to the distance between any point inside the passive material (true vertex) and the center of the downstream plane (reco vertex).

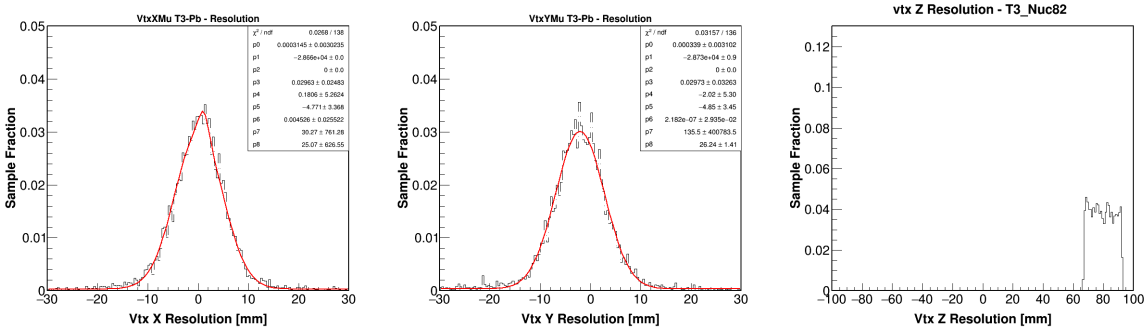

Figure 6.20: Vertex resolution in all coordinates in Pb target 3. The shifted and wider range in the Z vertex resolution, correspond to the distance between any point inside the passive material (true vertex) and the center of the downstream plane (reco vertex).

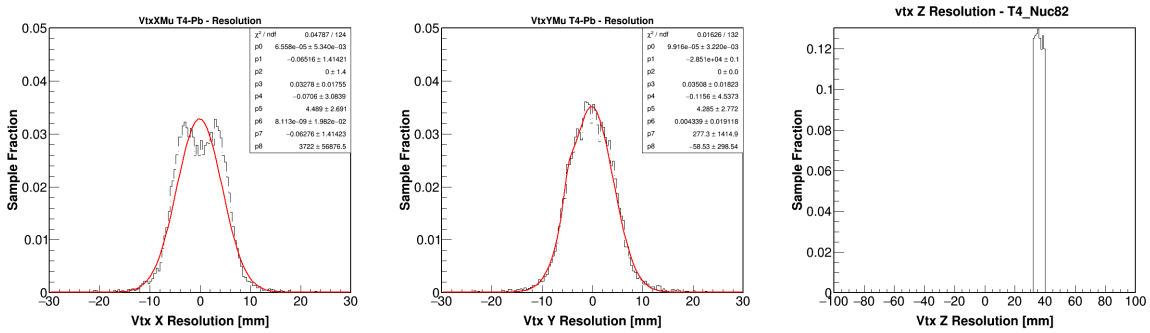

Figure 6.21: Vertex resolution in all coordinates in Pb target 4. The shifted and wider range in the Z vertex resolution, correspond to the distance between any point inside the passive material (true vertex) and the center of the downstream plane (reco vertex).

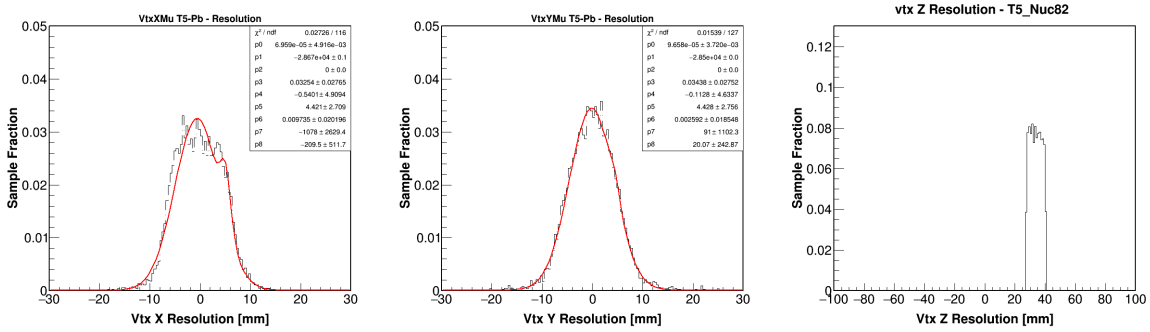

Figure 6.22: Vertex resolution in all coordinates in Pb target 5. The shifted and wider range in the Z vertex resolution, correspond to the distance between any point inside the passive material (true vertex) and the center of the downstream plane (reco vertex).

6.4.2 θ_μ Reconstruction

The direction of the muon is determined by the long-tracking algorithm. The direction vector of the first node in the track determines the reconstructed muon direction. It is reconstructed during the general MINERvA reconstruction (5.4.3). The resolution of the muon angle with regards to the neutrino beam for the CH, C and all Fe and Pb targets, is shown from figures 6.23 to 6.33. The resolution is defined as the reconstructed minus the truth angle, in degrees.

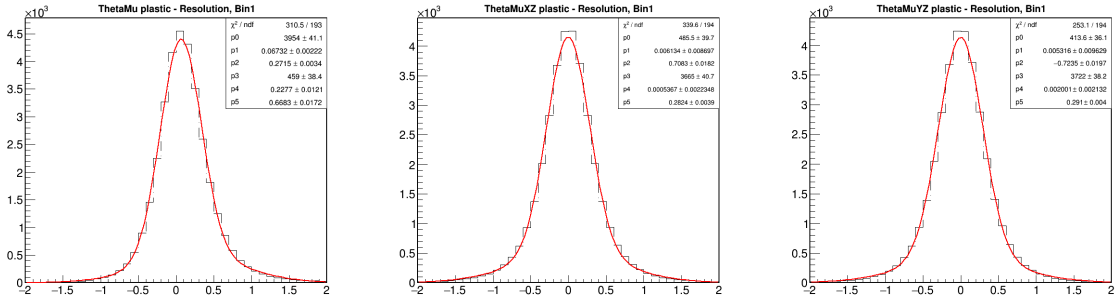

Figure 6.23: Absolute, XZ-Plane and YZ-Plane muon angle resolution in the CH target.

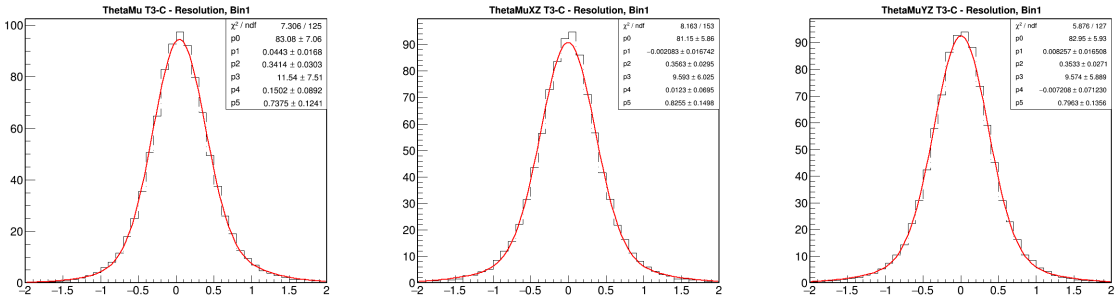

Figure 6.24: Absolute, XZ-Plane and YZ-Plane muon angle resolution in the C target.

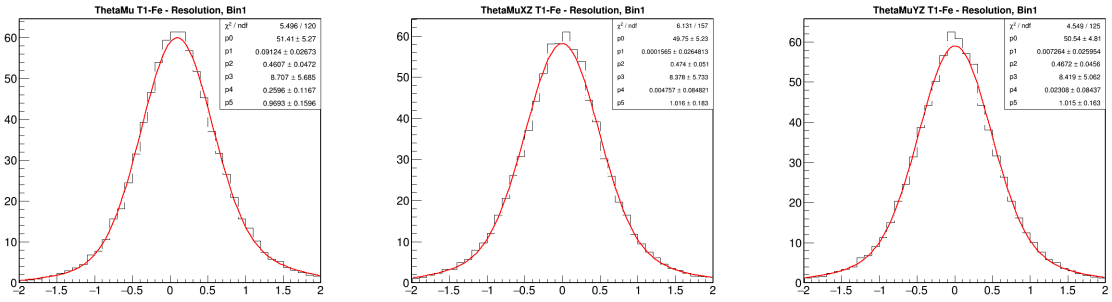

Figure 6.25: Absolute, XZ-Plane and YZ-Plane muon angle resolution in Fe target 1.

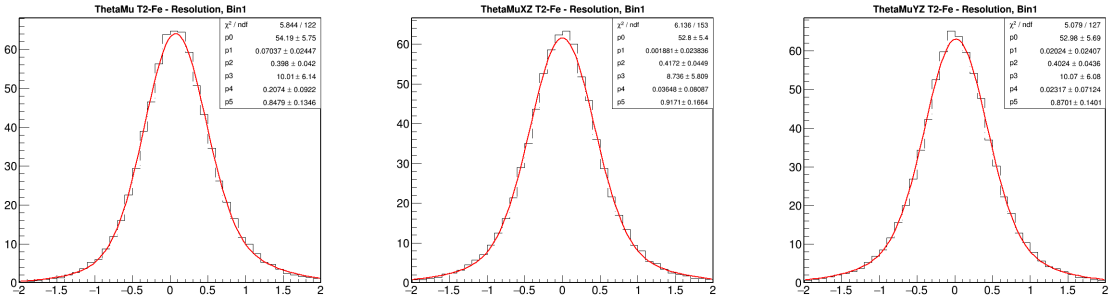

Figure 6.26: Absolute, XZ-Plane and YZ-Plane muon angle resolution in Fe target 2.

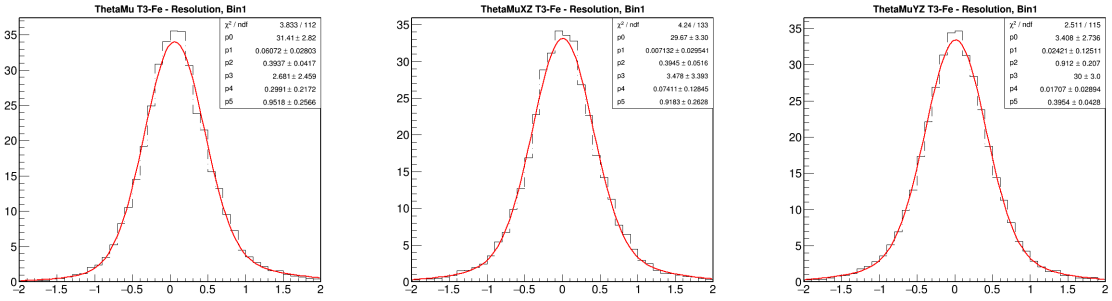

Figure 6.27: Absolute, XZ-Plane and YZ-Plane muon angle resolution in Fe target 3.

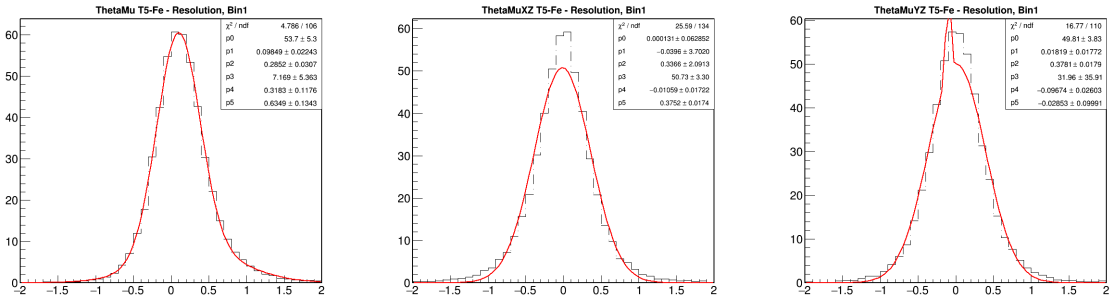

Figure 6.28: Absolute, XZ-Plane and YZ-Plane muon angle resolution in Fe target 5.

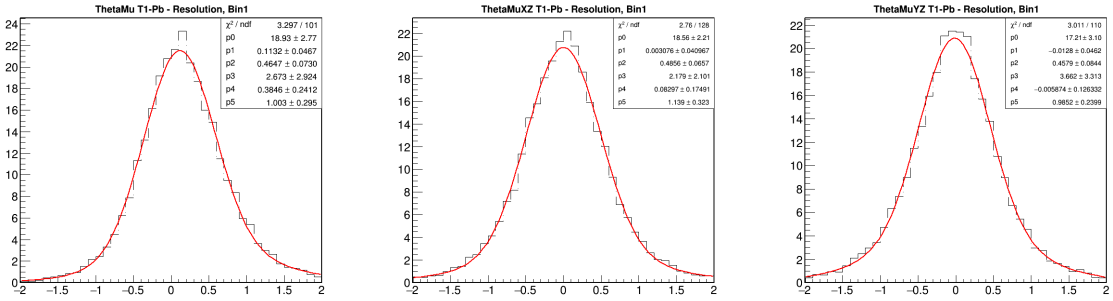

Figure 6.29: Absolute, XZ-Plane and YZ-Plane muon angle resolution in Pb target 1.

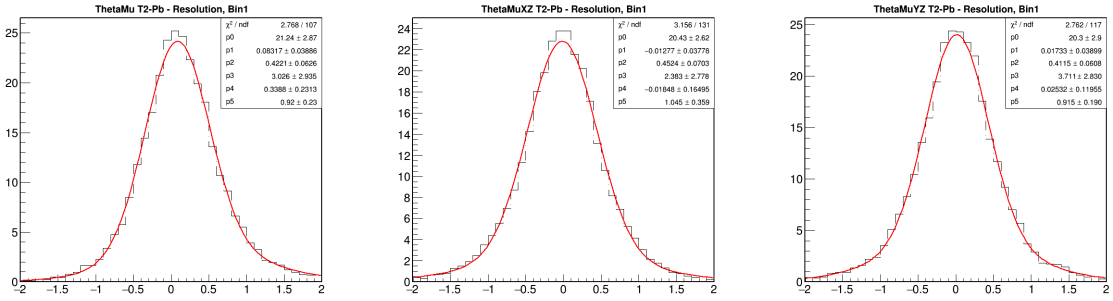

Figure 6.30: Absolute, XZ-Plane and YZ-Plane muon angle resolution in Pb target 2.

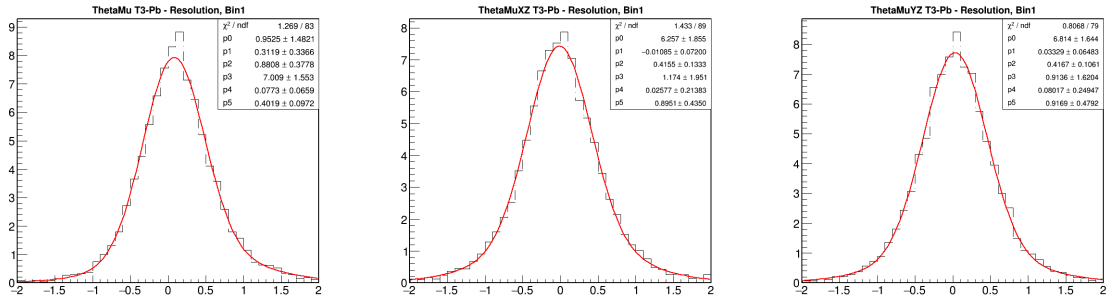

Figure 6.31: Absolute, XZ-Plane and YZ-Plane muon angle resolution in Pb target 3.

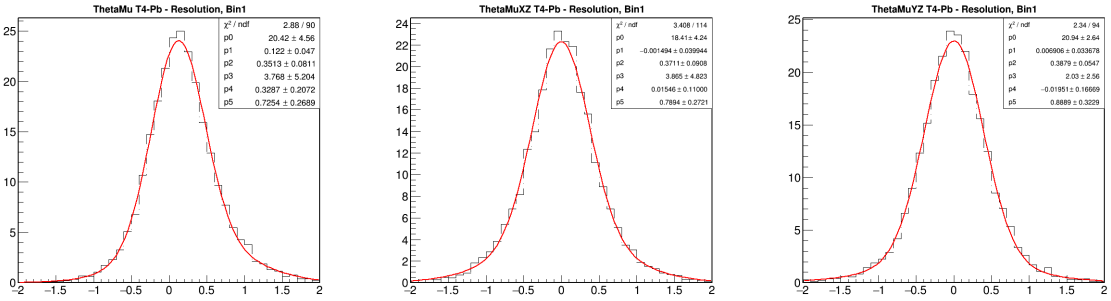

Figure 6.32: Absolute, XZ-Plane and YZ-Plane muon angle resolution in Pb target 4.

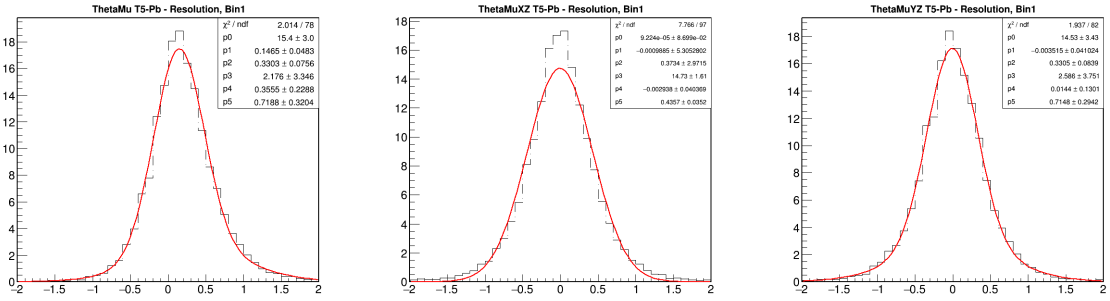

Figure 6.33: Absolute, XZ-Plane and YZ-Plane muon angle resolution in Pb target 5.

6.4.3 θ_π Reconstruction

The pion direction is also determined by the long-tracking algorithm. It can be reconstructed by the short-tracking algorithm when it spans from 4 to $\sim$ 11 planes. The short-tracking algorithm is successful in reconstructing signal events where the pion has low-energy. Unfortunately it reconstructs more low-energy resonant pions, reason why events reconstructed by the short-tracking algorithm are not used in this analysis. Pion tracks with angles larger than 70° are not reconstructed, as the number of planes is not enough to form a track. Like the muon track, the direction vector of the first node in the track determines the reconstructed pion direction. It is also reconstructed during the general MINERvA reconstruction (5.4.3). The resolution of the pion angle with regards to the neutrino beam for the CH, C and all Fe and Pb targets, is shown from figures 6.34 to 6.44. The resolution is defined as the reconstructed minus the truth angle, in degrees.

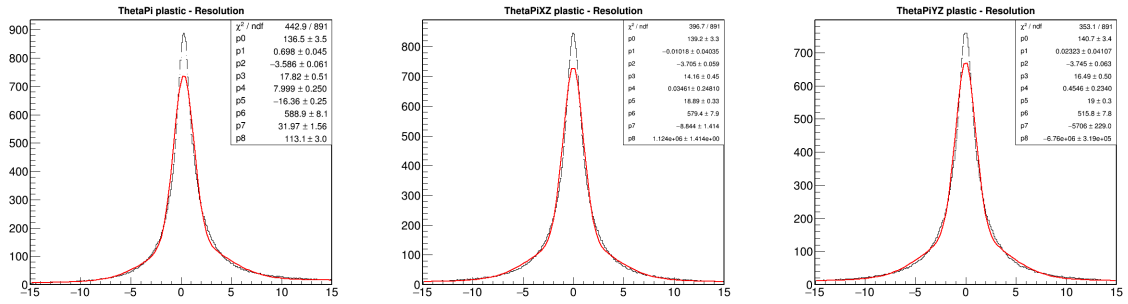

Figure 6.34: Absolute, XZ-Plane and YZ-Plane pion angle resolution in the CH target.

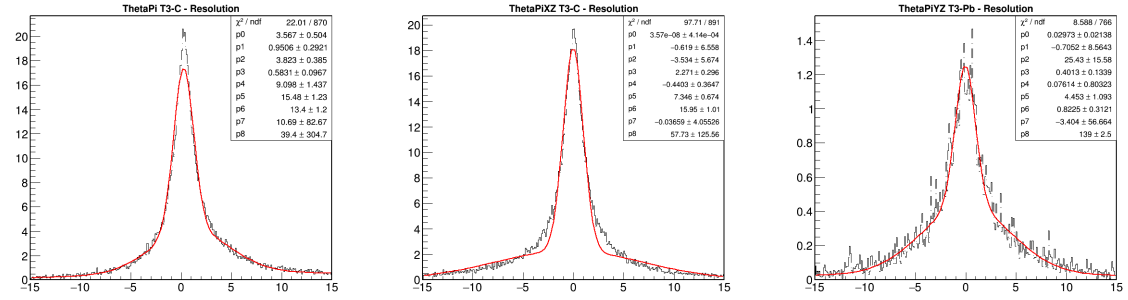

Figure 6.35: Absolute, XZ-Plane and YZ-Plane pion angle resolution in the C target.

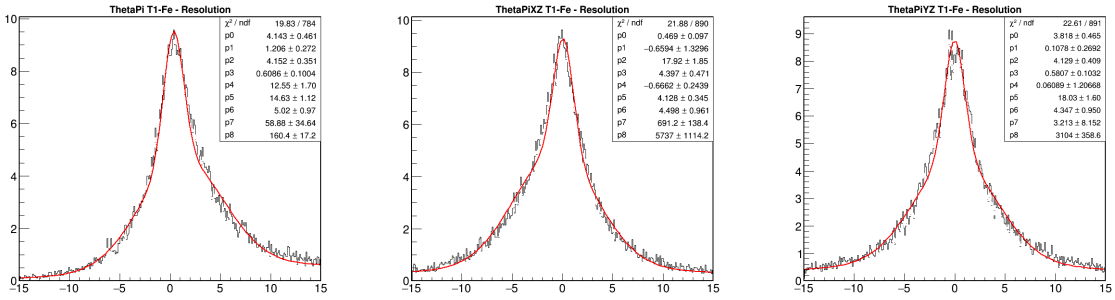

Figure 6.36: Absolute, XZ-Plane and YZ-Plane pion angle resolution in Fe target 1.

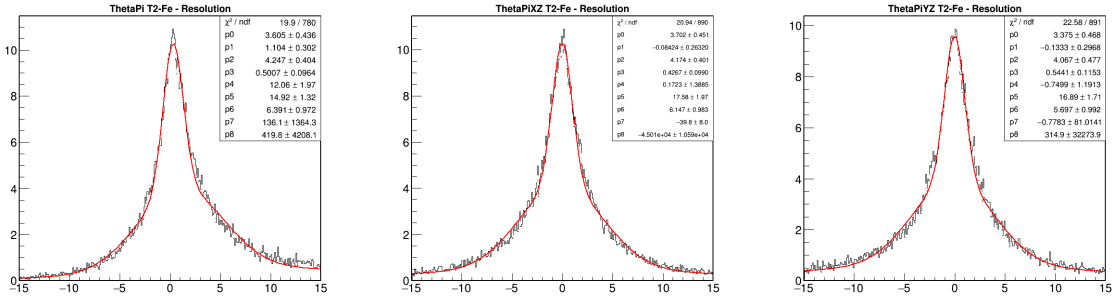

Figure 6.37: Absolute, XZ-Plane and YZ-Plane pion angle resolution in Fe target 2.

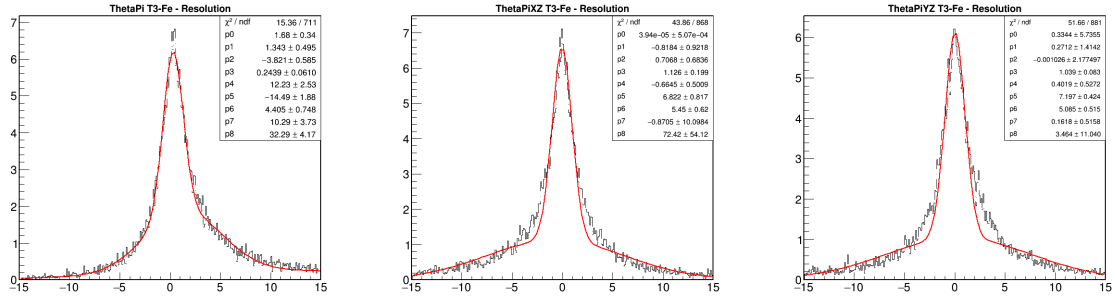

Figure 6.38: Absolute, XZ-Plane and YZ-Plane pion angle resolution in Fe target 3.

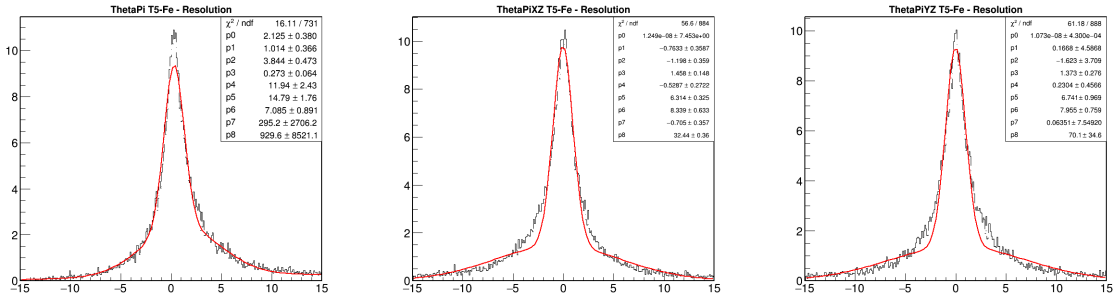

Figure 6.39: Absolute, XZ-Plane and YZ-Plane pion angle resolution in Fe target 5.

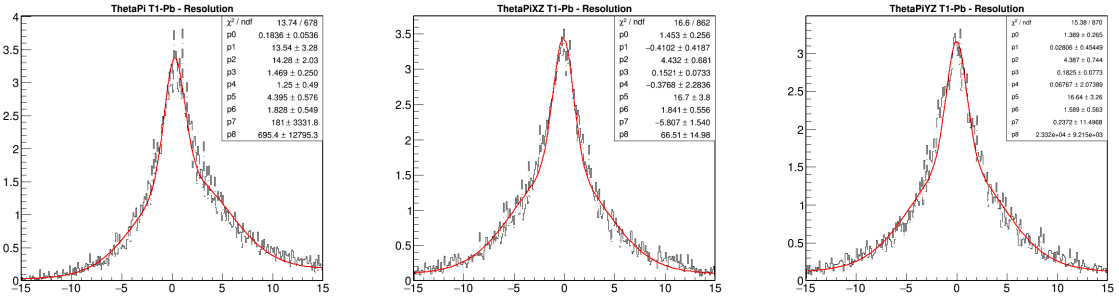

Figure 6.40: Absolute, XZ-Plane and YZ-Plane pion angle resolution in Pb target 1.

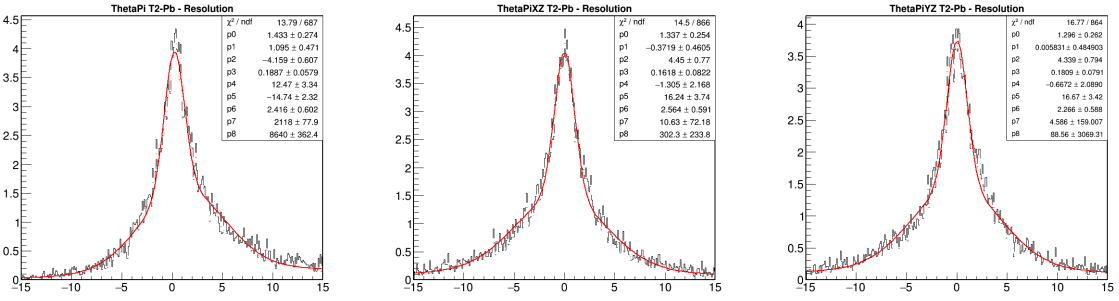

Figure 6.41: Absolute, XZ-Plane and YZ-Plane pion angle resolution in Pb target 2.

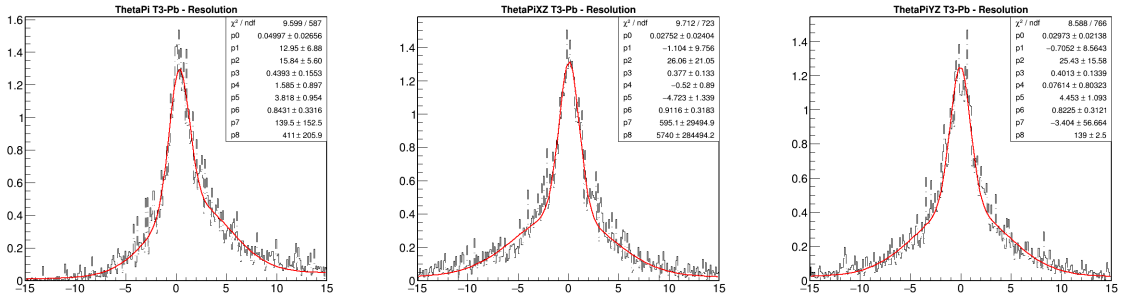

Figure 6.42: Absolute, XZ-Plane and YZ-Plane pion angle resolution in Pb target 3.

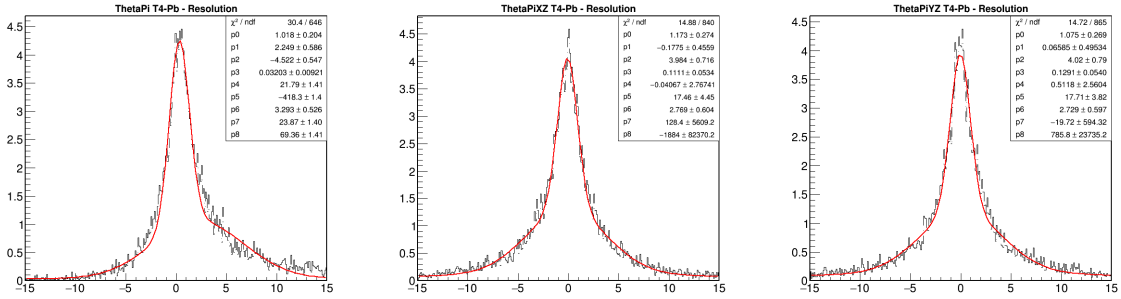

Figure 6.43: Absolute, XZ-Plane and YZ-Plane pion angle resolution in Pb target 4.

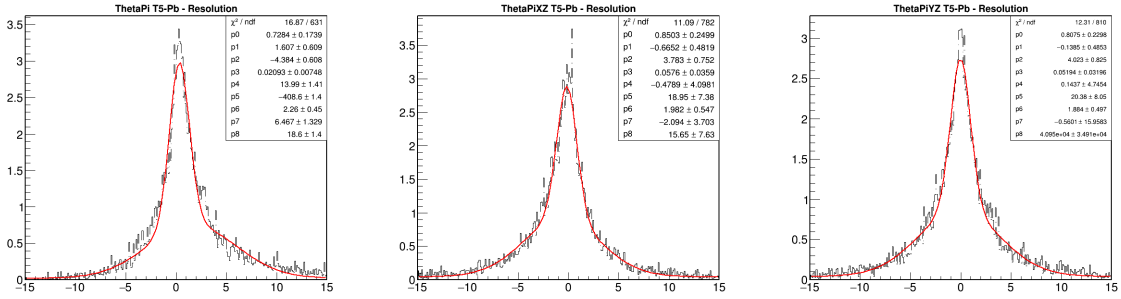

Figure 6.44: Absolute, XZ-Plane and YZ-Plane pion angle resolution in Pb target 5.

6.4.4 E_μ Reconstruction

The reconstructed total energy of the muon is measured in both MINERvA and MINOS detectors. The energy measured by ionization inside MINERvA is added to the energy measured by either range or curvature in the MINOS detector (section 5.4.5). It is mandatory in this analysis to have the muons entering the MINOS detector, given that the energy measured inside MINERvA is not enough to assess the muons' total energy, nor the signal of their electric charge (to know whether it is a muon or an anti-muon). An additional correction is added to muons created inside and traversing passive materials. Muons with vertex immediately downstream a passive material, are considered to come from the center of the passive target (projected vertex in figure 6.11). The passive material correction is

$$C_i = \frac{1}{f_{active} * M_{sc} * dEdx_{sc}} \sum_{i}^{mat} (M_i * dEdx_i) \tag{6.2}$$

where dE/dx_i and dE/dx_{sc} are the energy loss in the passive materials and in the plastic scintillator in MeV $g^{-1}cm^2$; $f_{active} = 0.8127$ is the fraction of active material in a scintillator strip; M_{sc} is the number of MEU per g/cm^2 (section 5.3.1); and M_i is the mass of the ith material in gcm^{-2}. Table 6.3 shows the value of C_i in equation 6.2 for a strip in different subdetectors.

Sub-detector	Correction Factor (C_i)
Tracker (CH)	1.197
Side ECAL (X-view strips)	2.696
Side ECAL (U and V-view strips)	4.339
Downstream ECAL	1.998
Downstream HCAL	10.441
OD (stories 1-3)	24.232
OD (story 4)	42.660
Passive Targets Region	Depends on target near the strip

Table 6.3: Passive material correction factor (C) in all sub-detectors.

The calibrated energy of each strip (section 5.3), also called "visible energy" or E_{vis}, is then multiplied by the appropriate C. The total muon energy, without the passive material correction, is also reconstructed during the general MINERvA reconstruction stage. The energy resolution, unlike for the other variables, is a fractional resolution, defined as

$$E_{\mu}^{resolution} = \frac{E_{\mu}^{recostructed} - E_{\mu}^{truth}}{E_{\mu}^{truth}} \tag{6.3}$$

This definition is used for variables where the absolute resolution is meaningless, as the truth value at which the resolution is obtained, is important. From figures 6.45 to 6.55, the fractional resolution as a function of the truth muon energy is shown. The fit of each of the one-dimensional muon energy fractional resolution histograms in the right-hand side plots, are shown in appendix A.

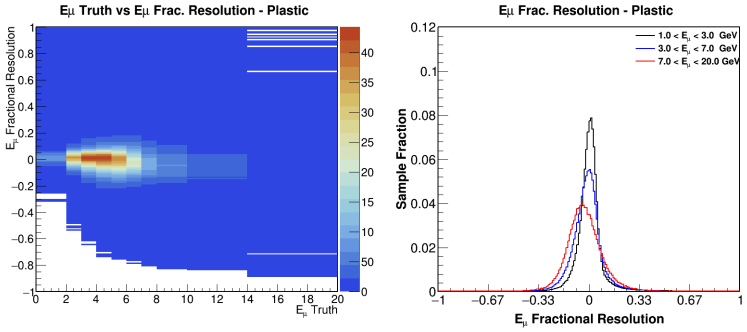

Figure 6.45: Fractional muon energy resolution vs true muon energy (left). The Y-axis in the left is projected into three 1-D histograms corresponding to three energy ranges in the X-axis, to see the difference in energy resolution at different muon energies in more detail (right). CH target.

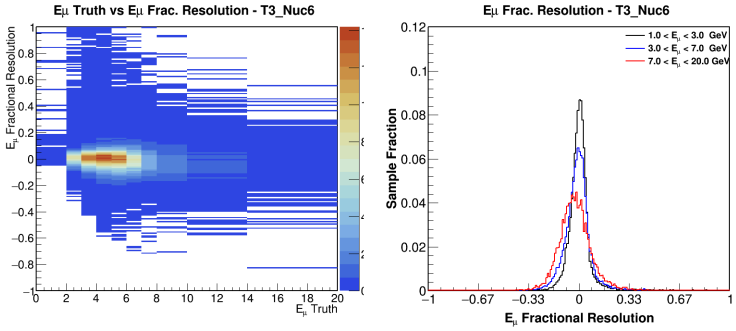

Figure 6.46: Fractional muon energy resolution vs true muon energy (left). The Y-axis in the left is projected into three 1-D histograms corresponding to three energy ranges in the X-axis, to see the difference in energy resolution at different muon energies in more detail (right). C target.

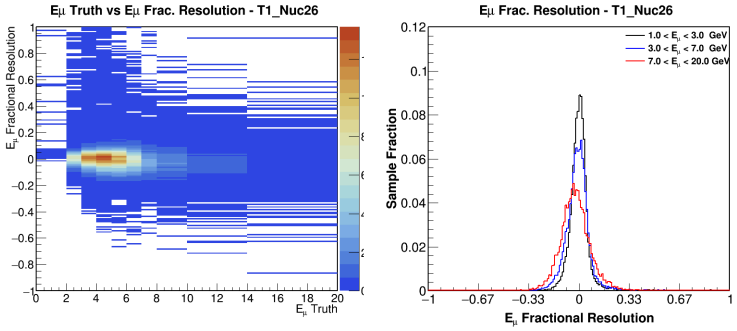

Figure 6.47: Fractional muon energy resolution vs true muon energy (left). The Y-axis in the left is projected into three 1-D histograms corresponding to three energy ranges in the X-axis, to see the difference in energy resolution at different muon energies in more detail (right). Fe in target 1.

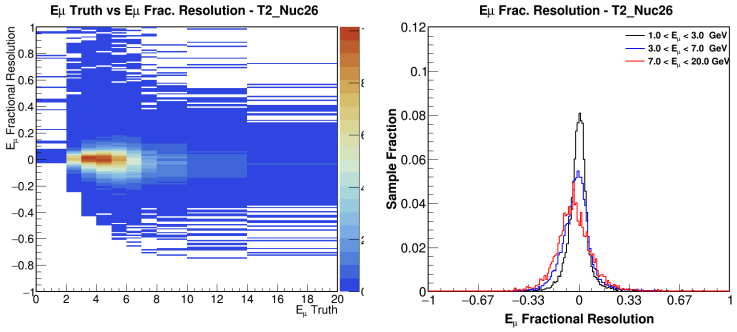

Figure 6.48: Fractional muon energy resolution vs true muon energy (left). The Y-axis in the left is projected into three 1-D histograms corresponding to three energy ranges in the X-axis, to see the difference in energy resolution at different muon energies in more detail (right). Fe in target 2.

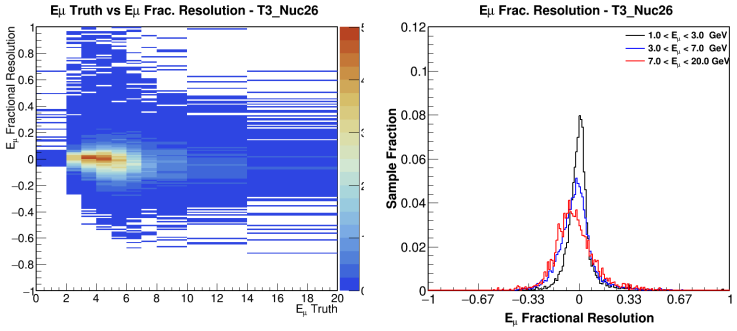

Figure 6.49: Fractional muon energy resolution vs true muon energy (left). The Y-axis in the left is projected into three 1-D histograms corresponding to three energy ranges in the X-axis, to see the difference in energy resolution at different muon energies in more detail (right). Fe in target 3.

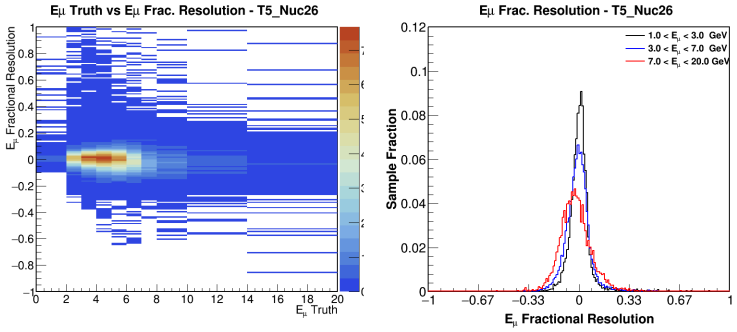

Figure 6.50: Fractional muon energy resolution vs true muon energy (left). The Y-axis in the left is projected into three 1-D histograms corresponding to three energy ranges in the X-axis, to see the difference in energy resolution at different muon energies in more detail (right). Fe in target 5.

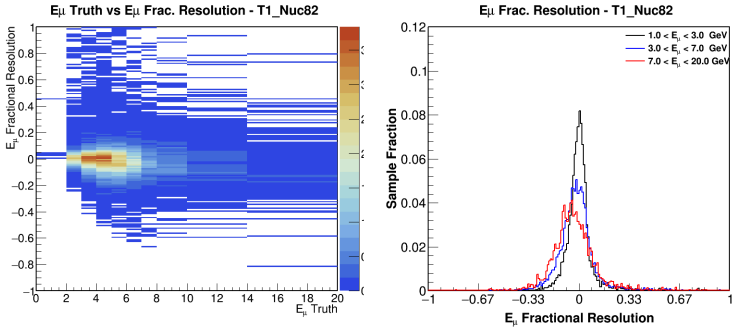

Figure 6.51: Fractional muon energy resolution vs true muon energy (left). The Y-axis in the left is projected into three 1-D histograms corresponding to three energy ranges in the X-axis, to see the difference in energy resolution at different muon energies in more detail (right). Pb in target 1.

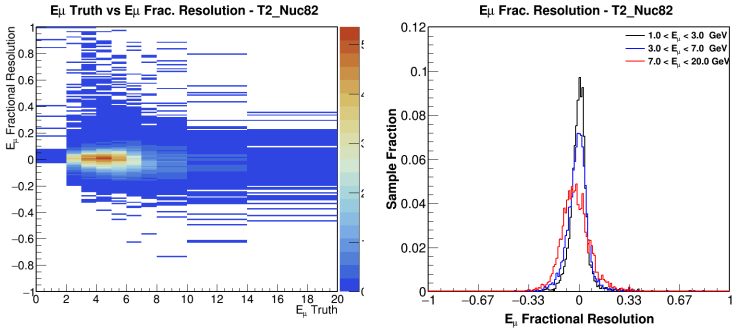

Figure 6.52: Fractional muon energy resolution vs true muon energy (left). The Y-axis in the left is projected into three 1-D histograms corresponding to three energy ranges in the X-axis, to see the difference in energy resolution at different muon energies in more detail (right). Pb in target 2.

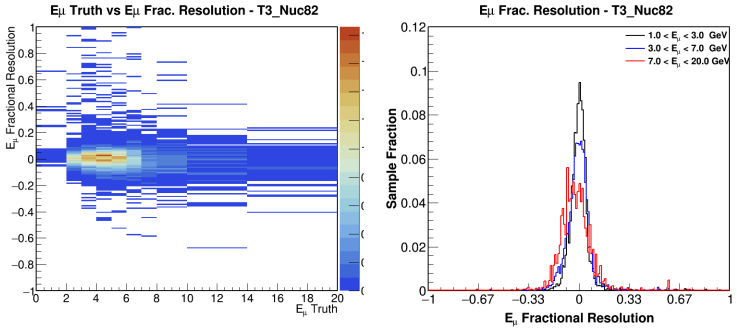

Figure 6.53: Fractional muon energy resolution vs true muon energy (left). The Y-axis in the left is projected into three 1-D histograms corresponding to three energy ranges in the X-axis, to see the difference in energy resolution at different muon energies in more detail (right). Pb in target 3.

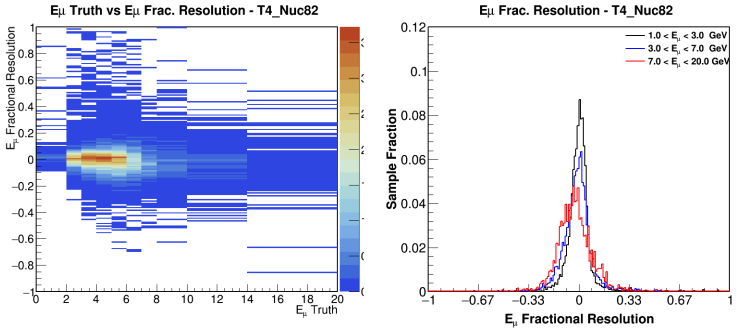

Figure 6.54: Fractional muon energy resolution vs true muon energy (left). The Y-axis in the left is projected into three 1-D histograms corresponding to three energy ranges in the X-axis, to see the difference in energy resolution at different muon energies in more detail (right). Pb in target 4.

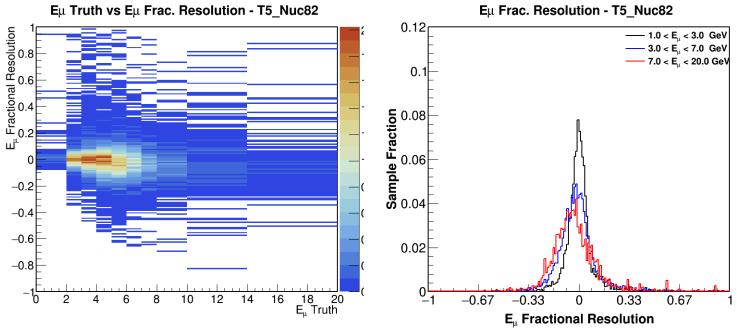

Figure 6.55: Fractional muon energy resolution vs true muon energy (left). The Y-axis in the left is projected into three 1-D histograms corresponding to three energy ranges in the X-axis, to see the difference in energy resolution at different muon energies in more detail (right). Pb in target 5.

6.4.5 E_π Reconstruction

In signal events, the pion energy is defined as all energy deposited in the MINERvA detector during the neutrino interaction, that is not associated to the muon. All the clusters not used by the algorithm when reconstructing the muon track are included in the pion energy reconstruction. The pion visible energy E_{vis}, is first corrected by passive material loss using equation 6.2

$$E_\pi^{pass} = \frac{E_\pi^{vis}}{f_{active} * M_{sc} * dEdx_{sc}} \sum_i^{mat} (M_i * dEdx_i) \tag{6.4}$$

where E_π^{pass} is the pion energy with the passive material correction. However, after this correction, the reconstructed energy is still systematically lower than the true pion energy. The missing energy can be due to some of the following:

- The pion candidate develops hadronic interaction in its passage through the detector, and it often creates secondary neutral and charged particles below the detection threshold which do not create light in the scintillator.
- The passive material correction factors assume minimum-ionizing particles, but if the particles have low energy, the energy loss is larger (figure 5.36).
- When the opening angle between the pion and muon is small enough, the tracking algorithm will assign some of the shared clusters to the muon energy only.

To compensate for the energy lost and achieve a good energy resolution, an overall scale factor called "α" is obtained by calorimetry depending on the subdetector where the interaction takes place, and applied to the passive material corrected energy. These calorimetric corrections were obtained using the "signal-only" MC described in section 6.1.

$$E_{cal} = \alpha * E_{pass} \tag{6.5}$$

The set of calorimetric corrections for every detector is shown in table 6.4.

An energy-dependent correction is applied to the calorimetry-corrected energy E_{cal}. By looking at the residuals of E_{cal} $\left([E_\pi^{reco} - E_\pi^{true}]/E_\pi^{true}\right)$ in bins of E_π^{true}, and applying a different correction to each bin.

Sub-detector	Calorimetric Correction, α (error ~ 0.03 in all cases).
Fe target 1	1.74
Fe target 2	1.75
Fe target 3	1.80
Fe target 5	1.69
Pb target 1	1.68
Pb target 2	1.63
Pb target 3	1.81
Pb target 4	1.61
Pb target 5	1.62
C target	1.69
CH target	1.72

Table 6.4: Calorimetric scale factors α, in all sub-detectors. The error in determining α is similar in all cases (~ 0.03)

When applying the series of corrections to the pion visible energy, all clusters inside a 10 cm radius sphere centered at the vertex are excluded and replaced by the energy deposited by a minimum-ionizing pion. This is done because the vertex activity is not well understood in the background models. The same procedure was adopted in the LE analysis [18] in the CH target. In order to validate the same procedure in the passive targets, a special MC sample of pions created inside each of the passive materials was generated with different initial pion momenta. Figures 6.56 to 6.59, show the energy loss in iron and lead compared to the particles path length, where it can be seen how the energy loss pattern deviates from a MIP depending on the particle's initial momentum.

It is evident that from ~ 200 MeV the hypothesis of using the energy loss patern inside iron and lead is justified.

After the passive material, calorimetric and the energy-dependent corrections are applied, the pion energy fractional resolution as defined in equation 6.2, in all targets is shown from figure 6.60 to 6.70. The fit of each of the one-dimensional pion energy fractional resolution histograms are shown in appendix A.

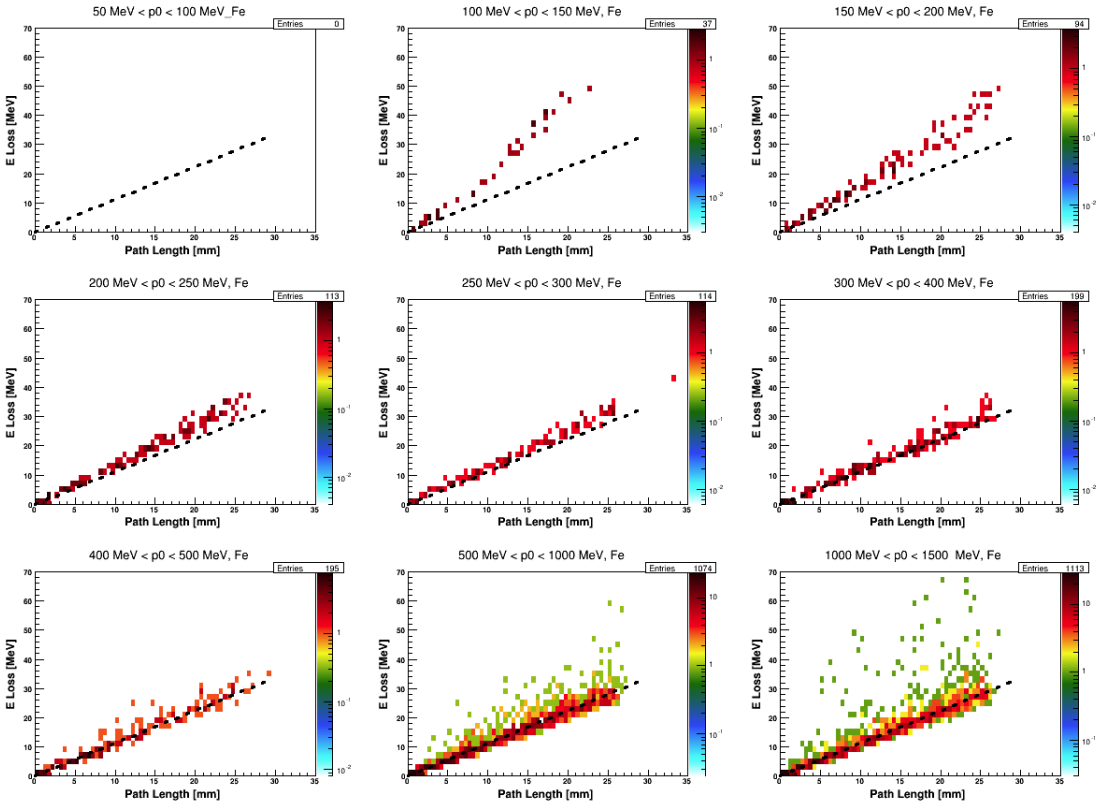

Figure 6.56: Path length of pions created inside one of the Fe targets versus the energy loss. Pions with different initial momenta were generated from 50 to 1500 MeV. The dashed line corresponds to the energy deposited by a minimum-ionizing pion of initial momentum in the range shown, simulated inside iron of target 1 [20].

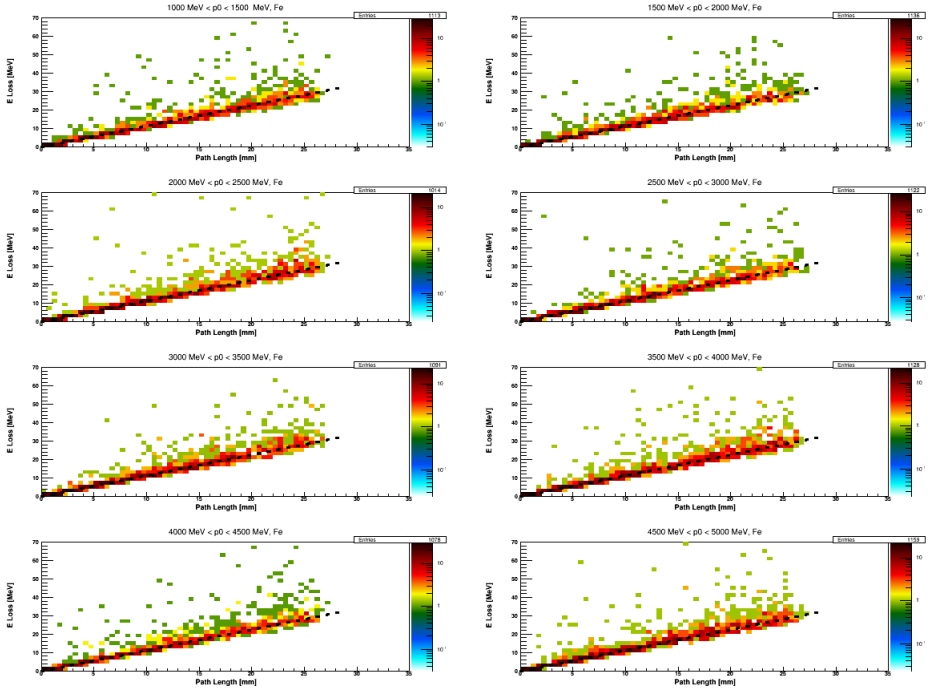

Figure 6.57: Path length of pions created inside one of the Fe targets versus the energy loss. Pions with different initial momenta were generated from 1000 to 5000 MeV. The dashed line corresponds to the energy deposited by a minimum-ionizing pion of initial momentum in the range shown, simulated inside iron of target 1 [20].

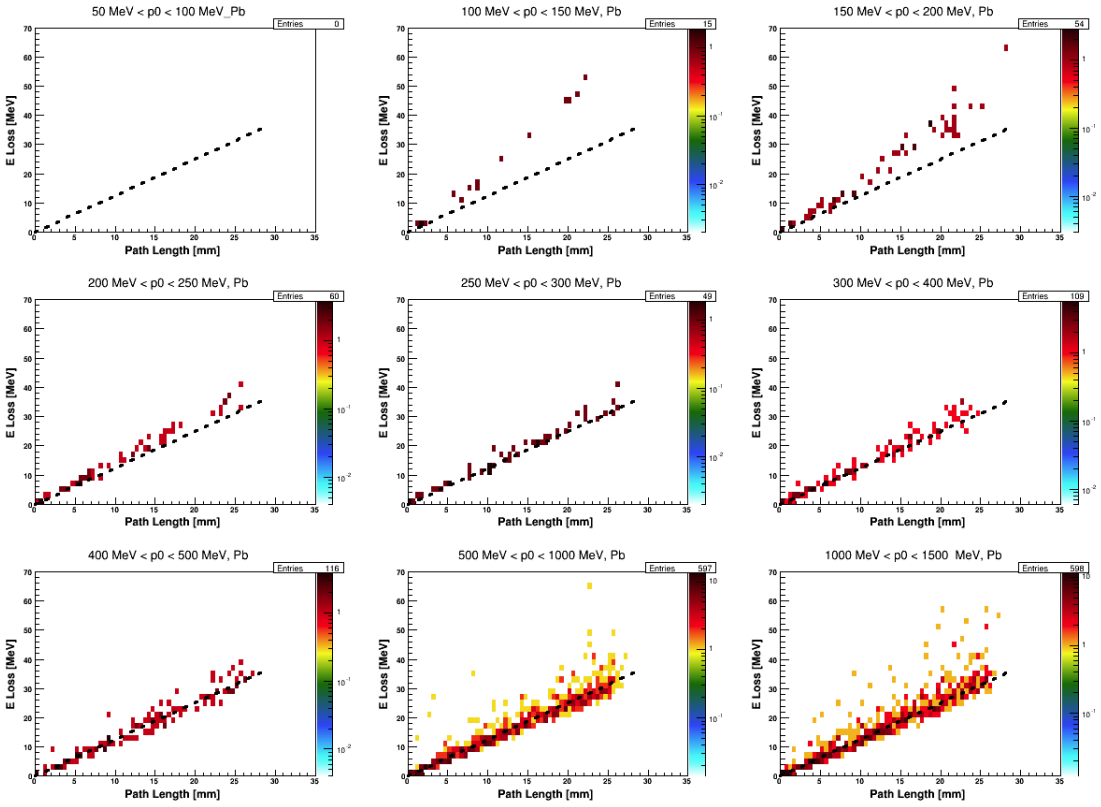

Figure 6.58: Path length of pions created inside one of the Fe targets versus the energy loss. Pions with different initial momenta were generated from 50 to 1500 MeV. The dashed line corresponds to the energy deposited by a minimum-ionizing pion of initial momentum in the range shown, simulated inside lead of target 1 [20].

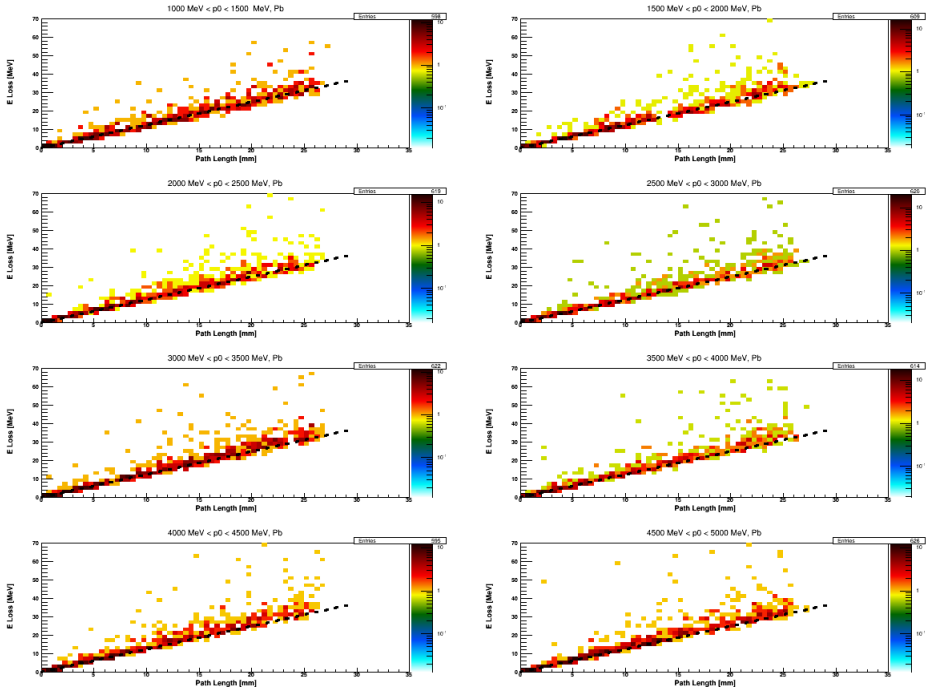

Figure 6.59: Path length of pions created inside one of the Fe targets versus the energy loss. Pions with different initial momenta were generated from 1000 to 5000 MeV. The dashed line corresponds to the energy deposited by a minimum-ionizing pion of initial momentum in the range shown, simulated inside lead of target 1 [20].

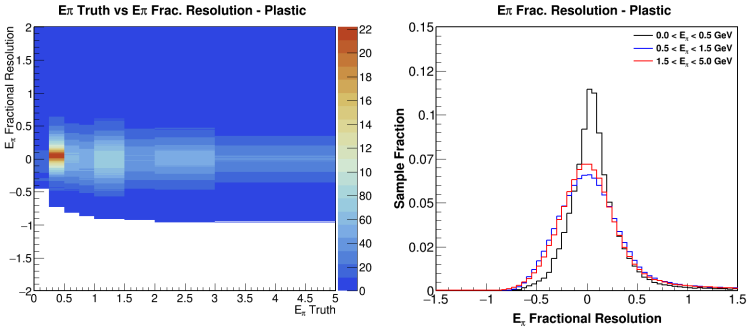

Figure 6.60: Fractional pion energy resolution vs true pion energy (left). Three energy ranges are chosen to see the difference in energy resolution at different pion energies in more detail (right). CH target.

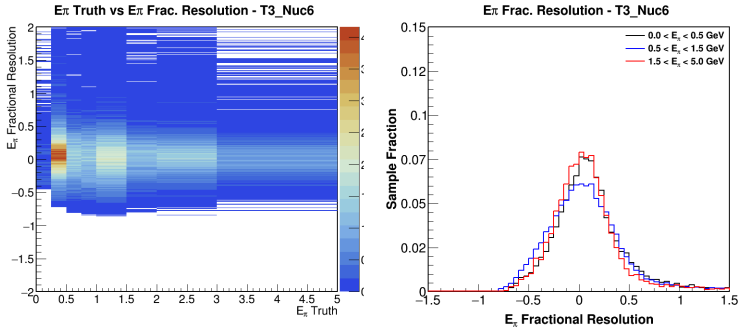

Figure 6.61: Fractional pion energy resolution vs true pion energy (left). Three energy ranges are chosen to see the difference in energy resolution at different pion energies in more detail (right). C target.

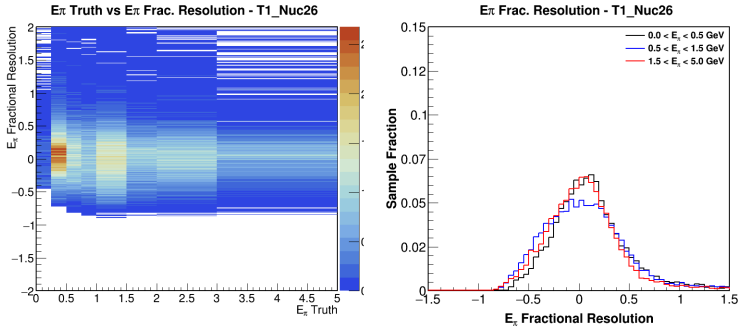

Figure 6.62: Fractional pion energy resolution vs true pion energy (left). Three energy ranges are chosen to see the difference in energy resolution at different pion energies in more detail (right). Fe in target 1.

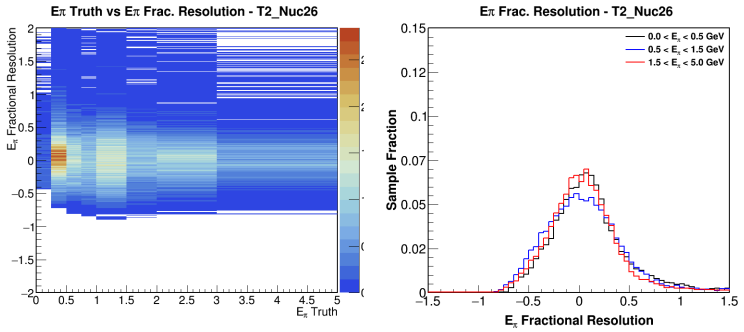

Figure 6.63: Fractional pion energy resolution vs true pion energy (left). Three energy ranges are chosen to see the difference in energy resolution at different pion energies in more detail (right). Fe in target 2.

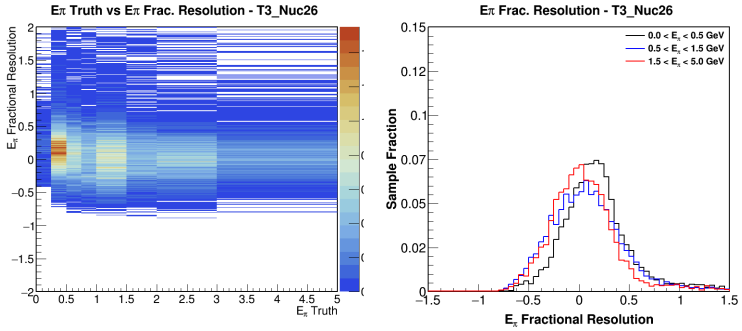

Figure 6.64: Fractional pion energy resolution vs true pion energy (left). Three energy ranges are chosen to see the difference in energy resolution at different pion energies in more detail (right). Fe in target 3.

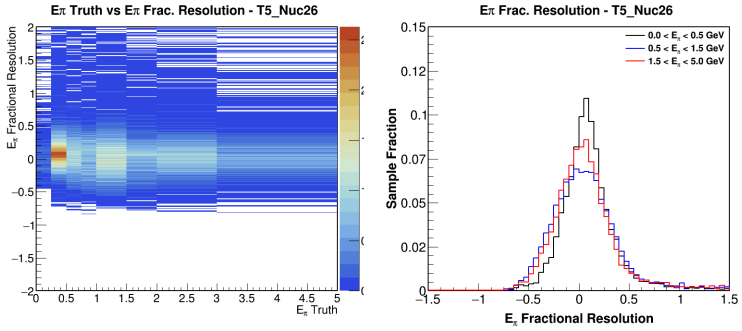

Figure 6.65: Fractional pion energy resolution vs true pion energy (left). Three energy ranges are chosen to see the difference in energy resolution at different pion energies in more detail (right). Fe in target 5.

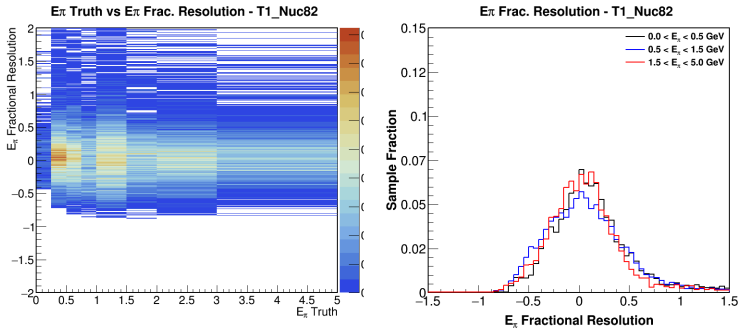

Figure 6.66: Fractional pion energy resolution vs true pion energy (left). Three energy ranges are chosen to see the difference in energy resolution at different pion energies in more detail (right). Pb in target 1.

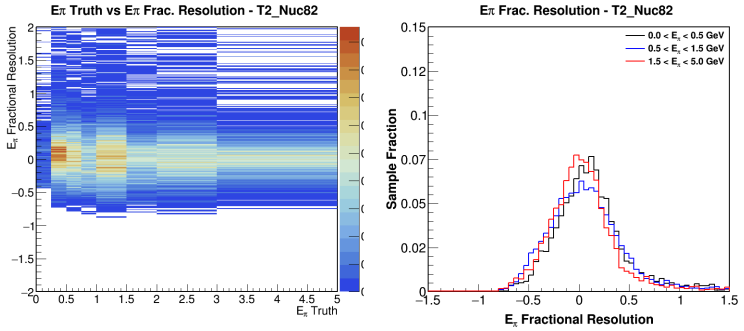

Figure 6.67: Fractional pion energy resolution vs true pion energy (left). Three energy ranges are chosen to see the difference in energy resolution at different pion energies in more detail (right). Pb in target 2.

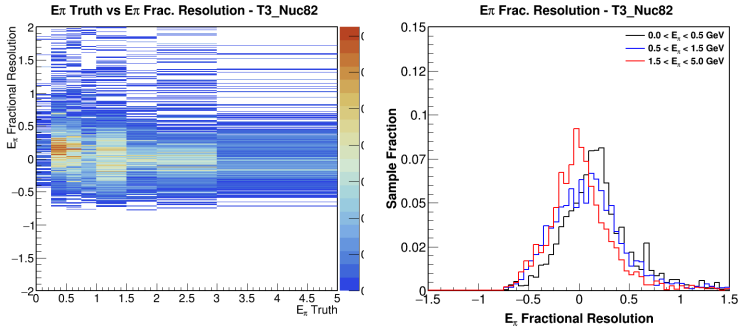

Figure 6.68: Fractional pion energy resolution vs true pion energy (left). Three energy ranges are chosen to see the difference in energy resolution at different pion energies in more detail (right). Pb in target 3.

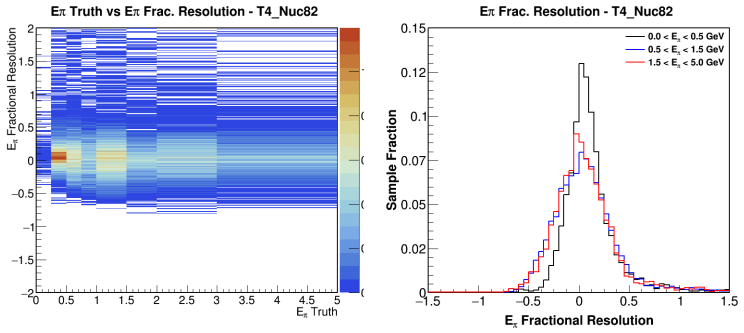

Figure 6.69: Fractional pion energy resolution vs true pion energy (left). Three energy ranges are chosen to see the difference in energy resolution at different pion energies in more detail (right). Pb in target 4.

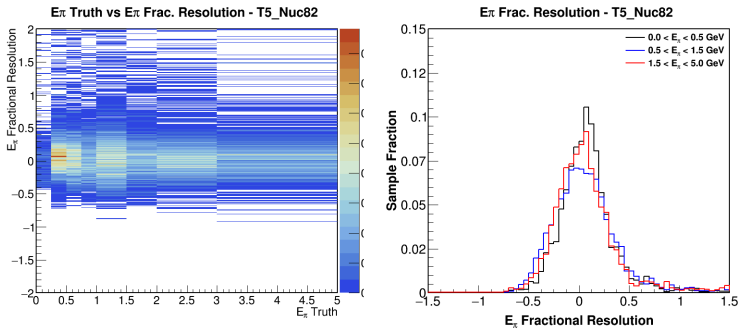

Figure 6.70: Fractional pion energy resolution vs true pion energy (left). Three energy ranges are chosen to see the difference in energy resolution at different pion energies in more detail (right). Pb in target 5.

6.4.6 E_ν Reconstruction

The reconstructed neutrino energy E_ν, is affected by both the muon and pion energy (see equation 3.7). No special treatment is given to reconstruct this variable, other than adding the reconstructed E_μ and E_π. The fractional neutrino energy resolution is shown from figure 6.71 to 6.81, for each of the targets under study. The fit of each of the one-dimensional neutrino energy fractional resolution histograms are shown in appendix A

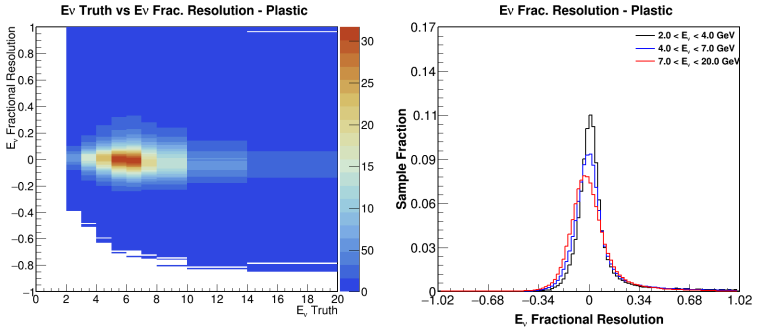

Figure 6.71: Fractional neutrino energy resolution vs true neutrino energy (left). Three energy ranges are chosen to see the difference in energy resolution at different neutrino energies in more detail (right). CH target.

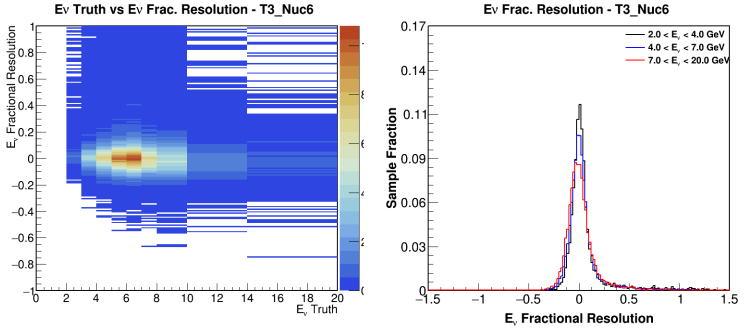

Figure 6.72: Fractional neutrino energy resolution vs true neutrino energy (left). Three energy ranges are chosen to see the difference in energy resolution at different neutrino energies in more detail (right). C target.

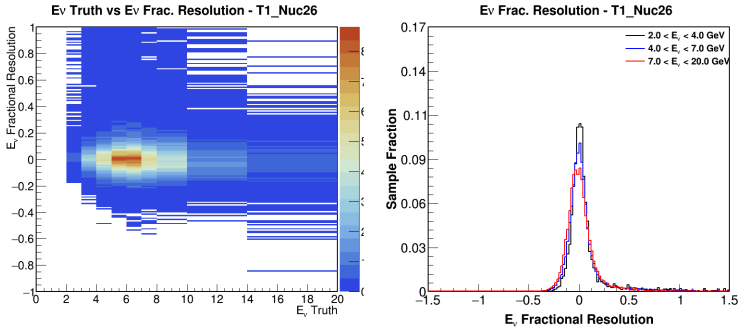

Figure 6.73: Fractional neutrino energy resolution vs true neutrino energy (left). Three energy ranges are chosen to see the difference in energy resolution at different neutrino energies in more detail (right). Fe in target 1.

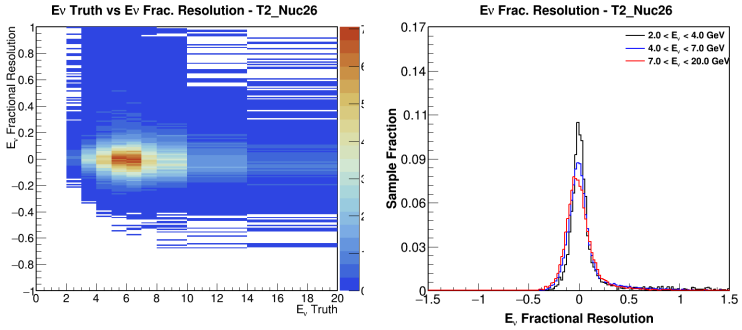

Figure 6.74: Fractional neutrino energy resolution vs true neutrino energy (left). Three energy ranges are chosen to see the difference in energy resolution at different neutrino energies in more detail (right). Fe in target 2.

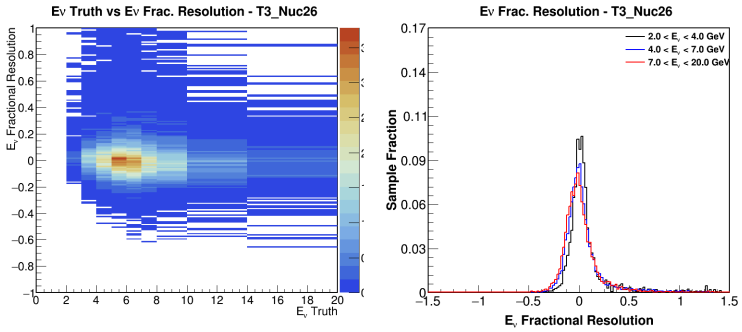

Figure 6.75: Fractional neutrino energy resolution vs true neutrino energy (left). Three energy ranges are chosen to see the difference in energy resolution at different neutrino energies in more detail (right). Fe in target 3.

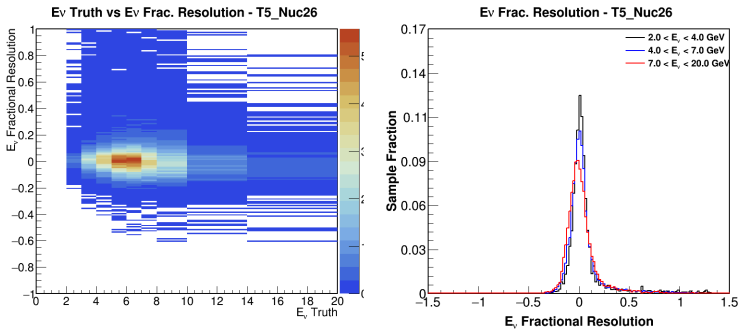

Figure 6.76: Fractional neutrino energy resolution vs true neutrino energy (left). Three energy ranges are chosen to see the difference in energy resolution at different neutrino energies in more detail (right). Fe in target 5.

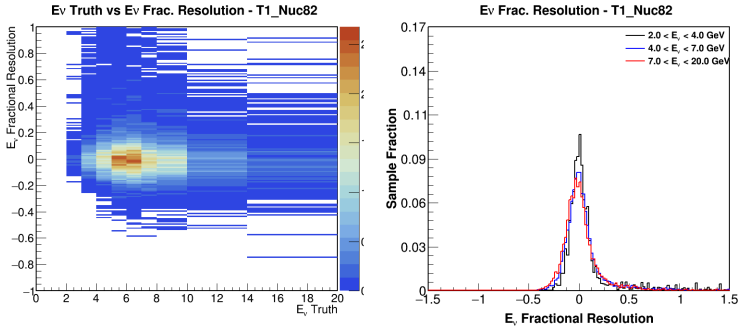

Figure 6.77: Fractional neutrino energy resolution vs true neutrino energy (left). Three energy ranges are chosen to see the difference in energy resolution at different neutrino energies in more detail (right). Pb in target 1.

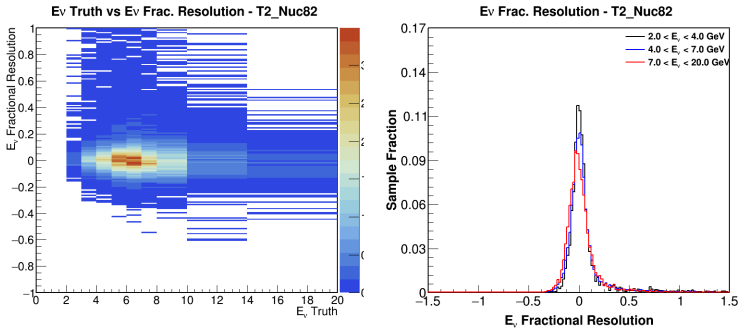

Figure 6.78: Fractional neutrino energy resolution vs true neutrino energy (left). Three energy ranges are chosen to see the difference in energy resolution at different neutrino energies in more detail (right). Pb in target 2.

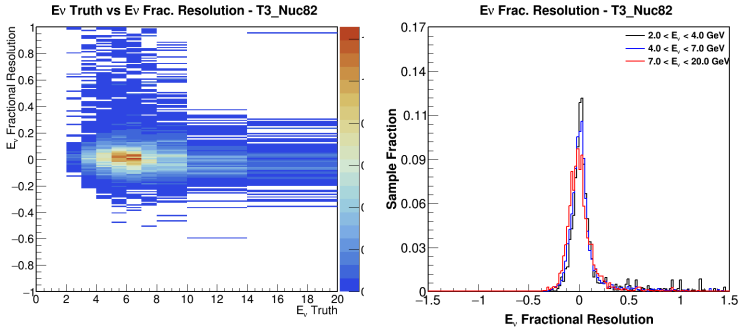

Figure 6.79: Fractional neutrino energy resolution vs true neutrino energy (left). Three energy ranges are chosen to see the difference in energy resolution at different neutrino energies in more detail (right). Pb in target 3.

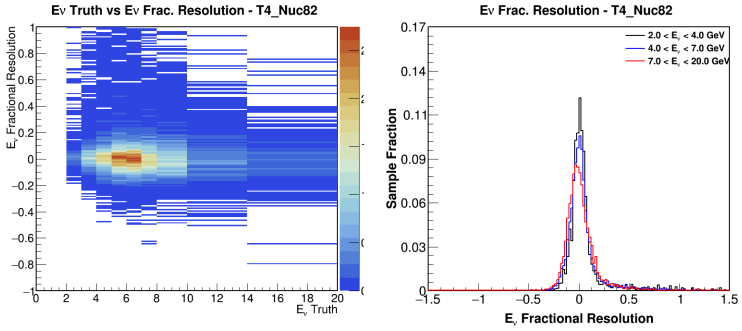

Figure 6.80: Fractional neutrino energy resolution vs true neutrino energy (left). Three energy ranges are chosen to see the difference in energy resolution at different neutrino energies in more detail (right). Pb in target 4.

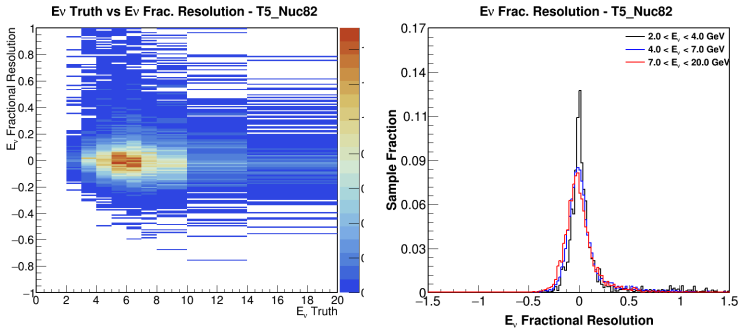

Figure 6.81: Fractional neutrino energy resolution vs true neutrino energy (left). Three energy ranges are chosen to see the difference in energy resolution at different neutrino energies in more detail (right). Pb in target 5.

6.4.7 Q^2 Reconstruction

An expression for Q^2 can be derived from equation 3.2 as follows

$$Q^2 = 2E_\nu \left(E_\mu - P_\mu \cos\theta_{\nu\mu}\right) - m_\mu^2 \tag{6.6}$$

And so the reconstructed Q^2 is obtained from those variables and the measured value of the muon mass [20]. Figures 6.82 to 6.92 show the fractional Q^2 resolution. The fits for the one-dimensional histograms of Q^2 fractional resolution are shown in appendix A. Q^2 completes the reconstruction of the kinematic variables used in this analysis.

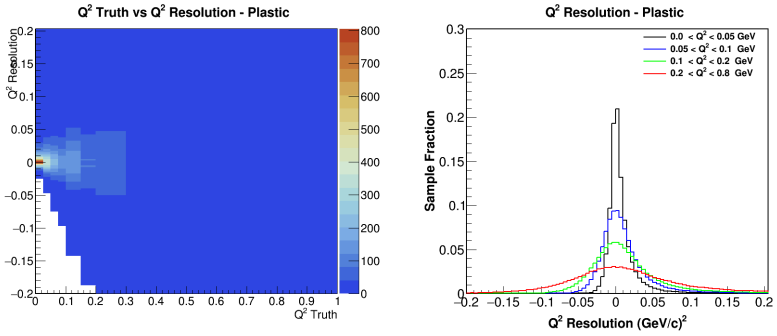

Figure 6.82: Fractional Q^2 resolution vs true Q^2 (left). Three momentum ranges are chosen to see the difference in Q^2 resolution at different momentum transfer in more detail (right). CH target.

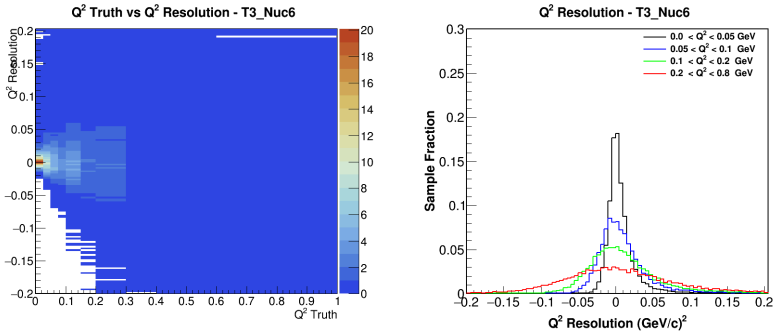

Figure 6.83: Fractional Q^2 resolution vs true Q^2 (left). Three momentum ranges are chosen to see the difference in Q^2 resolution at different momentum transfer in more detail (right). C target.

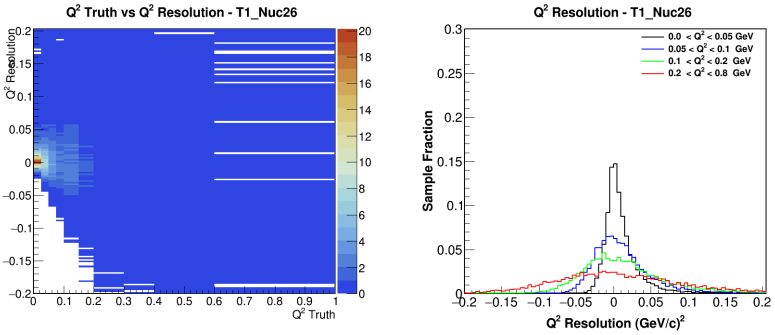

Figure 6.84: Fractional Q^2 resolution vs true Q^2 (left). Three momentum ranges are chosen to see the difference in Q^2 resolution at different momentum transfer in more detail (right). Fe in target 1.

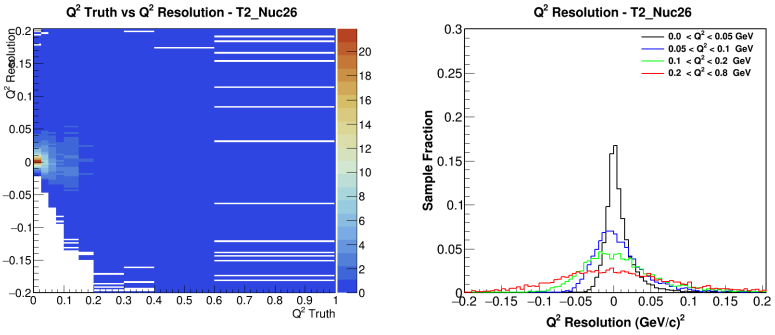

Figure 6.85: Fractional Q^2 resolution vs true Q^2 (left). Three momentum ranges are chosen to see the difference in Q^2 resolution at different momentum transfer in more detail (right). Fe in target 2.

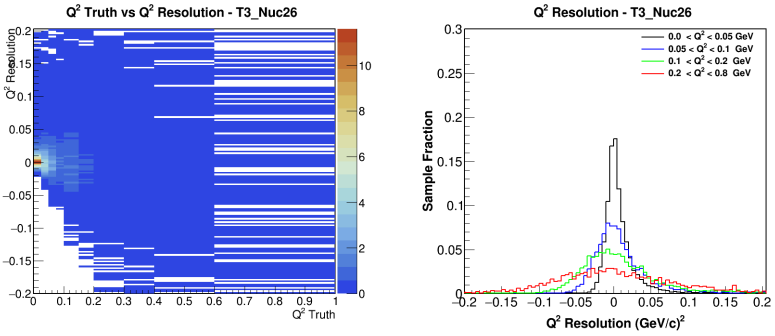

Figure 6.86: Fractional Q^2 resolution vs true Q^2 (left). Three momentum ranges are chosen to see the difference in Q^2 resolution at different momentum transfer in more detail (right). Fe in target 3.

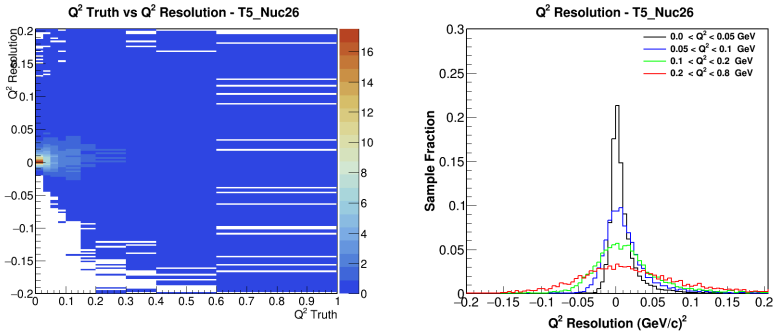

Figure 6.87: Fractional Q^2 resolution vs true Q^2 (left). Three momentum ranges are chosen to see the difference in Q^2 resolution at different momentum transfer in more detail (right). Fe in target 5.

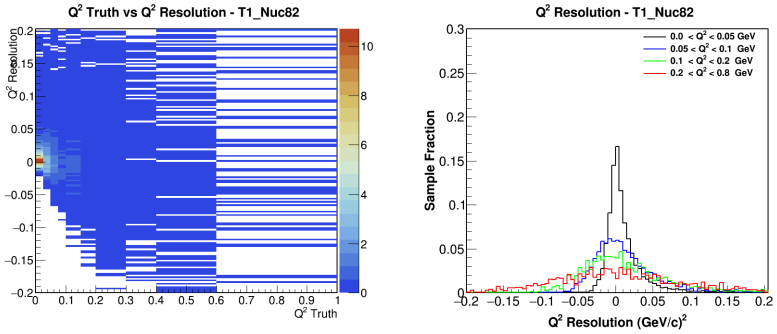

Figure 6.88: Fractional Q^2 resolution vs true Q^2 (left). Three momentum ranges are chosen to see the difference in Q^2 resolution at different momentum transfer in more detail (right). Pb in target 1.

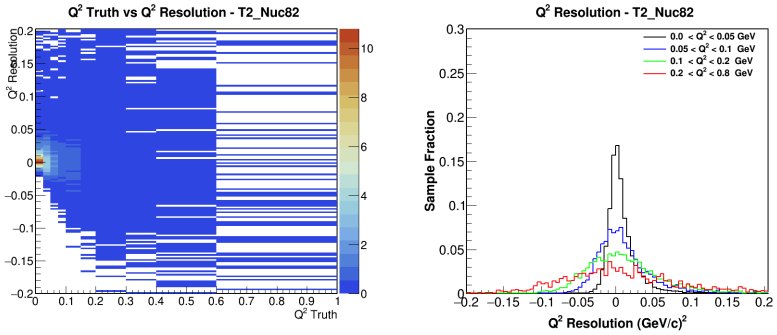

Figure 6.89: Fractional Q^2 resolution vs true Q^2 (left). Three momentum ranges are chosen to see the difference in Q^2 resolution at different momentum transfer in more detail (right). Pb in target 2.

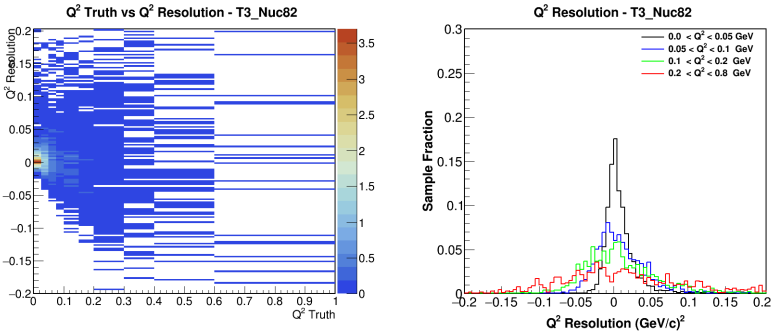

Figure 6.90: Fractional Q^2 resolution vs true Q^2 (left). Three momentum ranges are chosen to see the difference in Q^2 resolution at different momentum transfer in more detail (right). Pb in target 3.

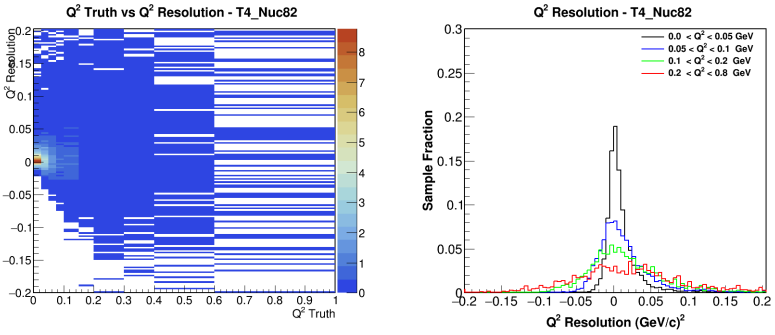

Figure 6.91: Fractional Q^2 resolution vs true Q^2 (left). Three momentum ranges are chosen to see the difference in Q^2 resolution at different momentum transfer in more detail (right). Pb in target 4.

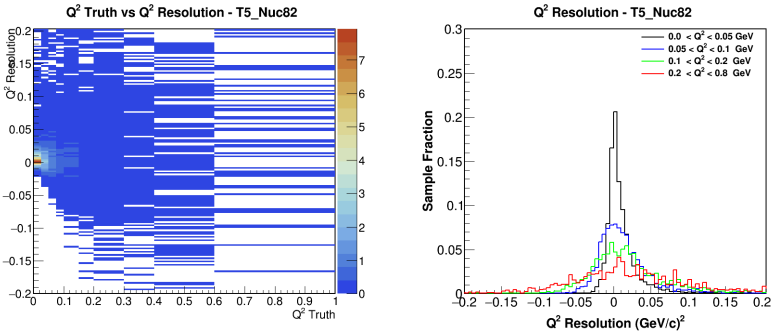

Figure 6.92: Fractional Q^2 resolution vs true Q^2 (left). Three momentum ranges are chosen to see the difference in Q^2 resolution at different momentum transfer in more detail (right). Pb in target 5.

6.4.8 $|t|$ Resolution

The resolution in $|t|$ depends on the resolution of all the variables involved in the expression 6.1

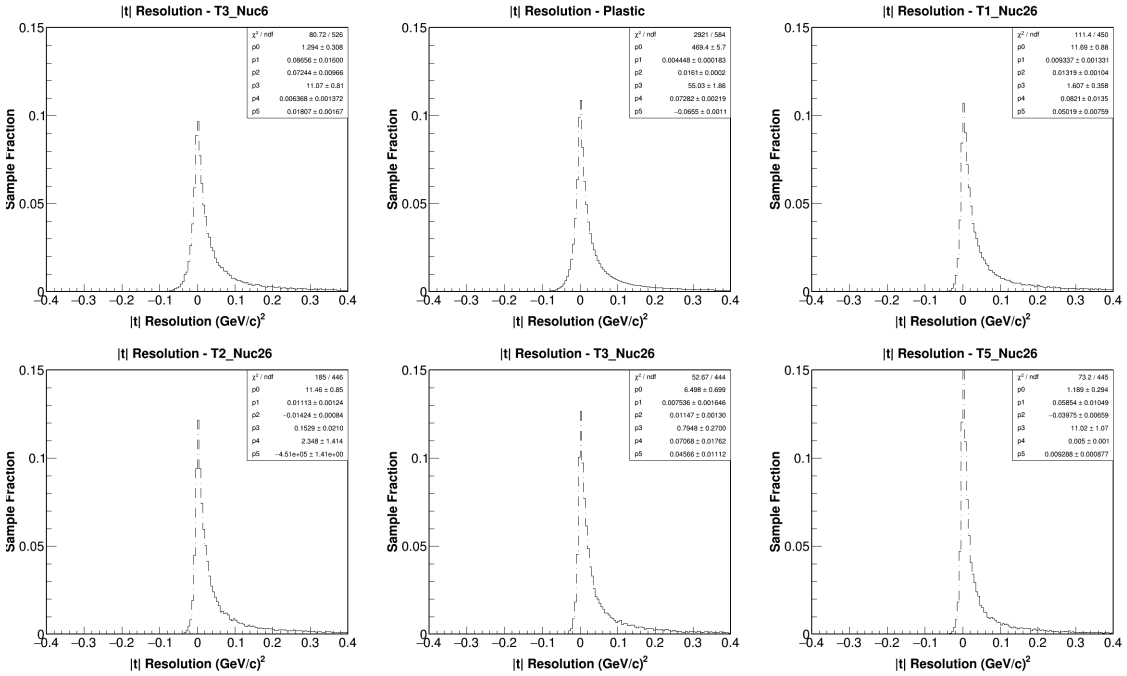

Figure 6.93: Resolution in $|t|$ in the C, CH and Fe targets. Resolution is defined as $|t|_{reco} - |t|_{true}$.

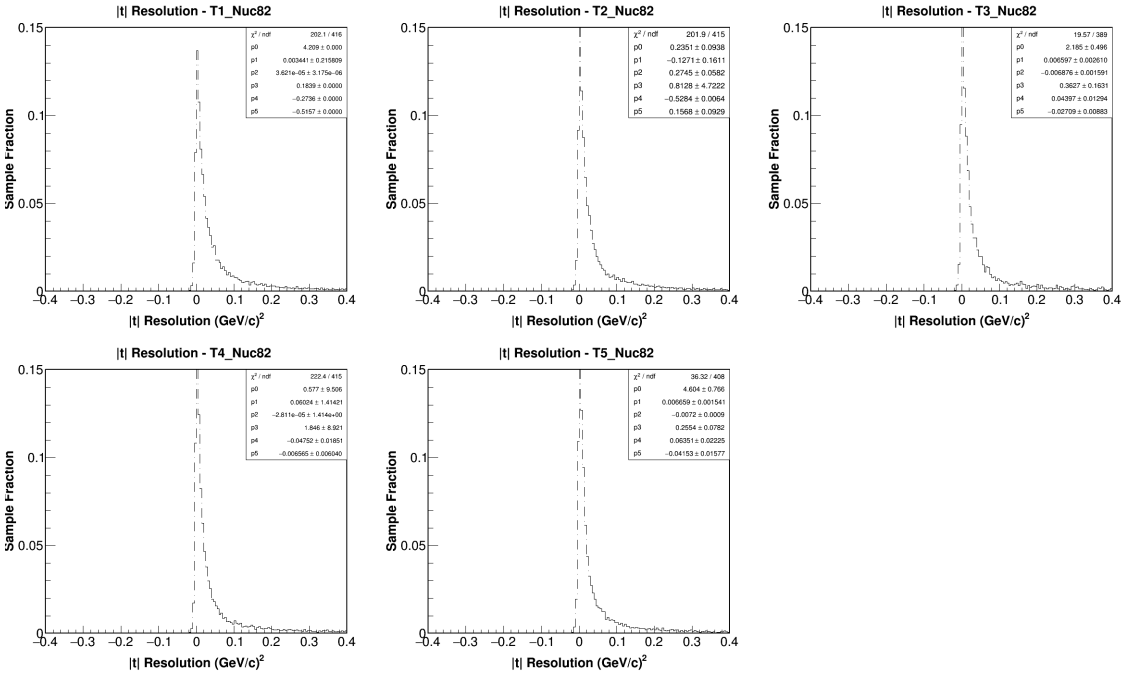

Figure 6.94: Resolution in $|t|$ in the Pb targets. Resolution is defined as $|t|_{reco} - |t|_{true}$.

6.5 Event Selection

After the successful reconstruction of the variables of interest for the analysis, events with the topology of neutrino-induced coherent pion are isolated from the rest of events in the MINERvA data set. The separation of events is performed in steps, where a particular characteristic of the interaction is looked for. These steps are called "cuts", and are applied to both the data and MC samples. There is not a particular order in which the cuts have to be applied. A total of 12 (13) cuts are used in events originated at the CH (C, Fe, Pb) target(s). However they are presented in groups of similar cuts.
Most of the cuts are determined by the MC predictions of the signal and background, trying to maximize the efficiency and purity of the sample after each cut. Arrows in the relevant plots show the parts of the distribution kept and rejected after the cut.

$$Efficiency = \frac{No.\ of\ signal\ events\ after\ cut}{Total\ number\ of\ signal\ events} \tag{6.7}$$

$$Purity = \frac{No.\ of\ signal\ events}{Total\ No.\ of\ events\,(signal\ +\ background)} \tag{6.8}$$

The set of cuts is essentially the same used in the LE analysis, with just a few additions or modifications, specially for the passive material sample. The full set of cuts is explained next

6.5.1 Fiducial Volume and MINOS Acceptance Selection

It is important to define a fiducial volume for each of the materials of interest. They are all located in the inner detector (any calorimeter region is excluded from the fiducial volume). The edge of the hexagonal prism defining each fiducial volume (shown in section 6.2.2) is 20 mm separated from the edge of the inner detector in all six faces of the prism. Such separation allows a larger containment of the pion candidates, as well as certainty that the event comes from the material of interest.
Most of the energy loss and charge of the muon candidate are measured in the MINOS detector, that is why every event is required to have one and just one muon matched inside the MINOS detector. The muon track originated in MINERvA is matched if it gets a reconstructed track inside MINOS, and both are within the same time slice (chapter 5). Two more cuts are performed in this first set, trying to eliminate events happening outside

the fiducial volume. Some events occur during the reset time of the electronics (section 5.1), this causes that part of the event is not seen, and in some cases the events might seem to be originated inside the fiducial volume, even though they were not. These kind of events and those with particles whose vertex starts at the very front of the detector, are rejected.

6.5.2 Neutrino Mode Selection

With the use of the MINOS detector, it is possible to assign a sign to the muon charge, which allows identifying whether the event comes from a ν_μ or from a $\overline{\nu}_\mu$. The cut is applied by looking at the quantity q/p divided by the error on that quantity, called the significance of q/p, where q and p are the charge and momentum of the muon track originated in MINERvA and measured in MINOS. Figures 6.95 to 6.97 show the significance ratio in all targets. The MC contribution called "other" includes events coming from NC processes, other neutrino flavor and anti-neutrinos. The cut rejects most of those events.

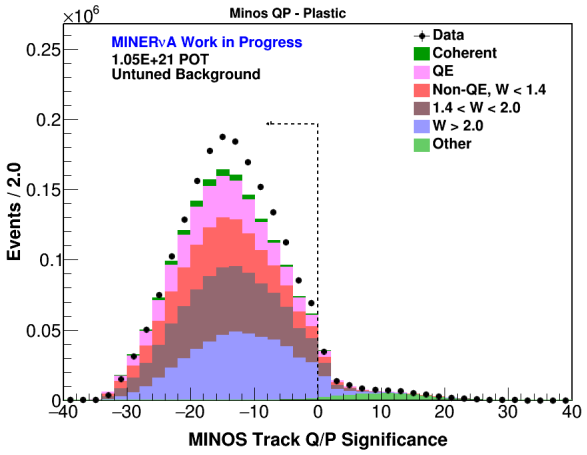

Figure 6.95: MINOS QP significance in the CH target.

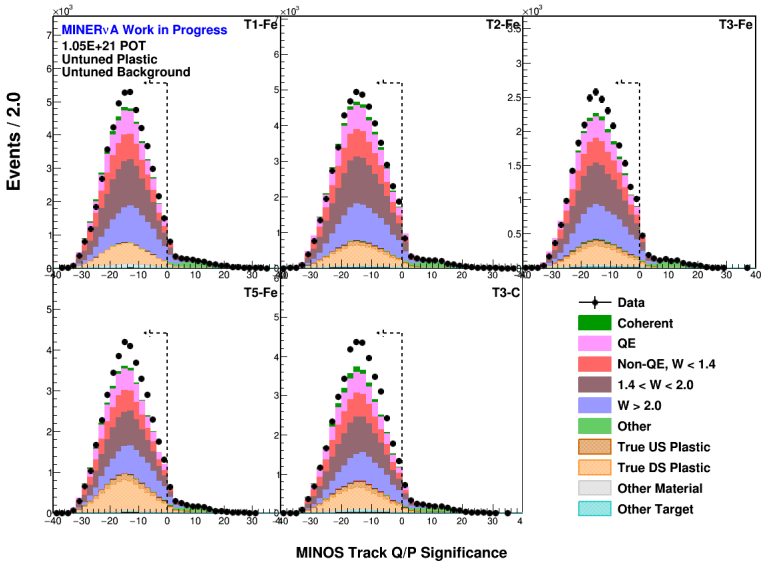

Figure 6.96: MINOS QP significance in the C and Fe targets.

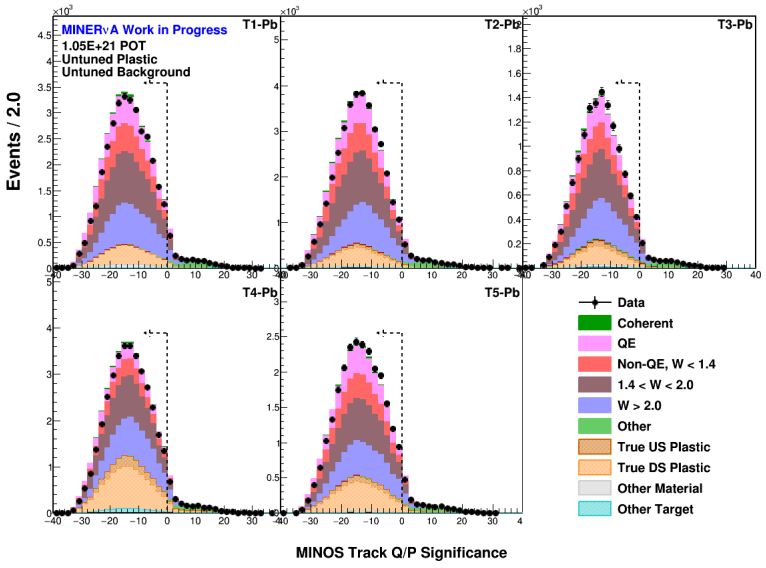

Figure 6.97: MINOS QP significance in the Pb targets.

6.5.3 Hadron Containment Selection

To achieve a better pion energy reconstruction it is necessary to contain the pions inside the inner detector (ID). Escaping pions will deposit energy in the OD, where passive material corrections represent a large fraction, and given that these corrections considered a minimum-ionizing pion, the energy resolution is generally worse. A set of cuts are applied to avoid those escaping pions.
The pion track candidate must not be matched in the MINOS detector. The pion track candidate must not enter the outer detector (OD), and not even leave the ID. Pion tracks candidates going backward in the detector are also rejected in this set of cuts. Although pions in signal events can hit a particle and change its trajectory to even travel backwards, these events are rejected as the purity of the sample increases significantly without a big loss in efficiency.

6.5.4 Neutrino Energy Selection

Figures 6.98 to 6.100 show the neutrino energy distributions in all targets, after the neutrino mode selection cut. As explained before, only muons from events with neutrino energies larger than $\sim$ 2 GeV make it into MINOS. Events getting matched in MINOS with reconstructed energy less than $\sim$ 2 GeV indicate reconstruction failure.
The upper cut rejects events where the neutrino was originated from a kaon decay ($K^+ \rightarrow \mu^+ + \nu_\mu$) or ($K^0 \rightarrow \pi^\pm + \mu^\mp + \nu_\mu$). These events have usually large uncertainties related to the flux (process poorly understood due to the lack of data).

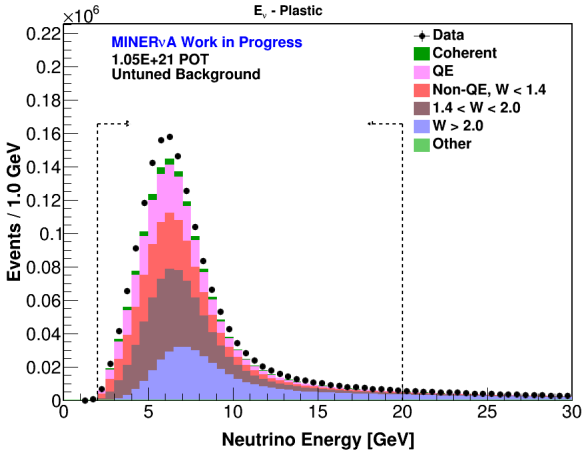

Figure 6.98: E_ν distribution after applying the neutrino mode cut, in the CH target.

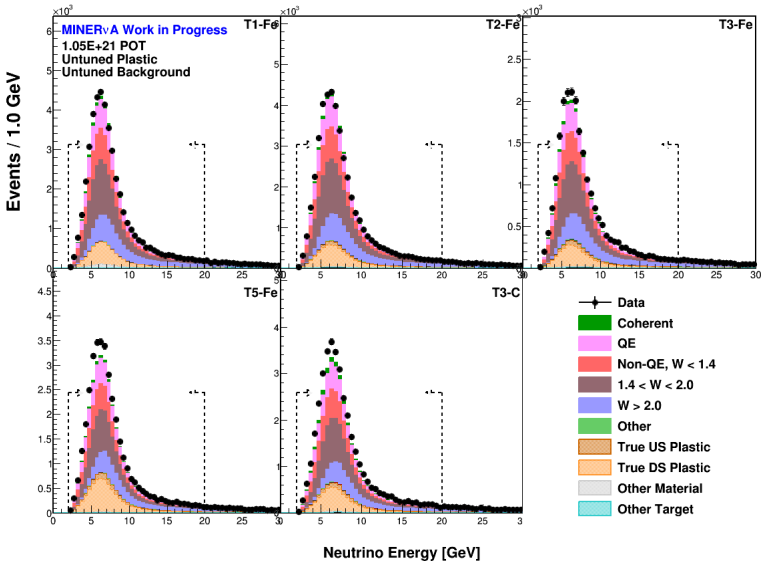

Figure 6.99: E_ν distribution after applying the neutrino mode cut, in the C and Fe targets.

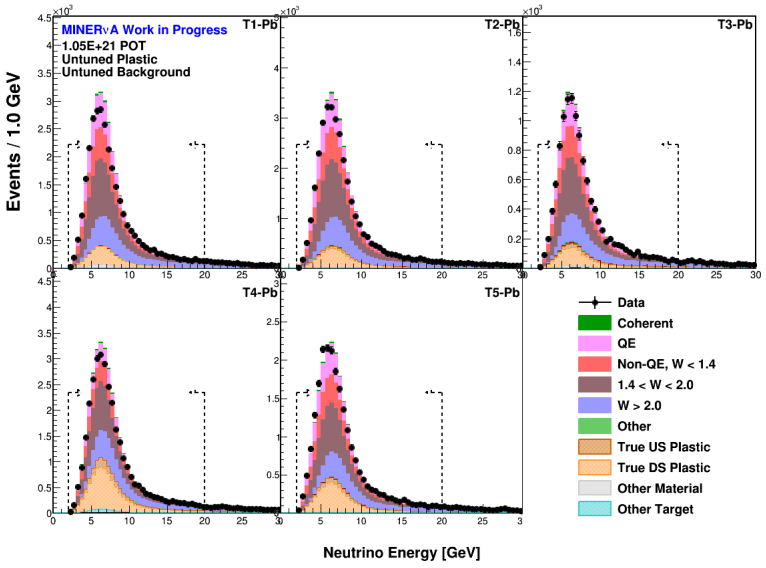

Figure 6.100: E_ν distribution after applying the neutrino mode cut, in the Pb targets.

6.5.5 Particle ID Selection

Pions and protons have usually similar energy pattern depositions. However, based on the Bethe-Bloch formula [20], an energy deposition (dE/dx) hypothesis can be built for each (one for pions, one for protons), in order to reject proton events, coming from CCQE and resonant interactions. Equation 6.9 shows the pion and proton hypotheses

$$\begin{aligned} \mathcal{L}_{\pi} &= \prod_{nodes} P\left(E_{node}|\pi\right) \\ \mathcal{L}_{p^+} &= \prod_{nodes} P\left(E_{node}|p^+\right) \end{aligned} \tag{6.9}$$

where $\mathcal{L}$ is the likelihood that the track is due to a pion or a proton, $P\left(E_{node}|a\right)$ is the probability the energy deposition in a given track's node, is due to particle a (pion or proton)

The hypotheses are built as follows. From each node in figure 6.101, a histogram of the energy deposition is obtained. The pion and proton histograms in each node, are fit to a Landau distribution (figure 6.102). A pion and a proton hypothesis is assigned to each node, based on the energy deposited by an event. The likelihood for each particle is finally the product of all node hypothesis in the track

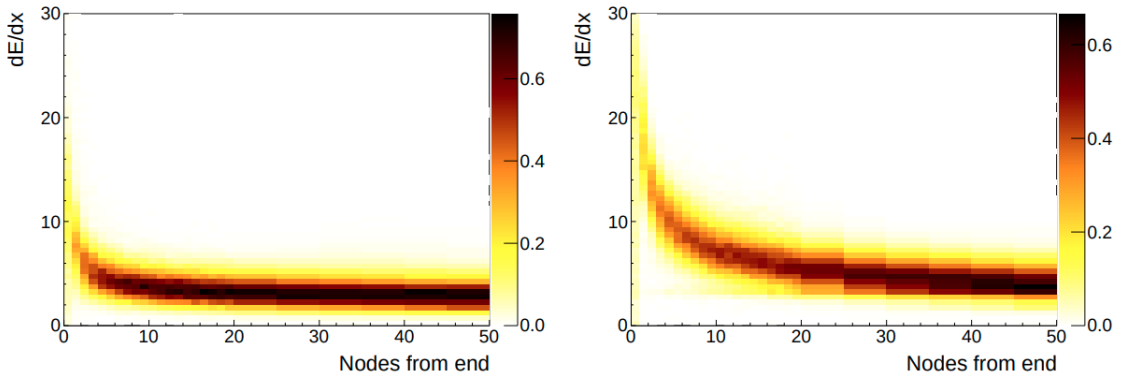

Figure 6.101: Energy loss (dE/dx) in each of the nodes of pions and proton tracks, from a simulation based on the Bethe-Bloch equation [20], of events in the CH target. [Figure by Phil Rodrigues (MINERvA collaboration).]

The Neyman-Pearson lemma [153] says that the most efficient way to test a hypothesis is by looking at the likelihood ratio. And using the properties of logarithms, the ratio between the pion and proton likelihood in equation 6.9 can be written like

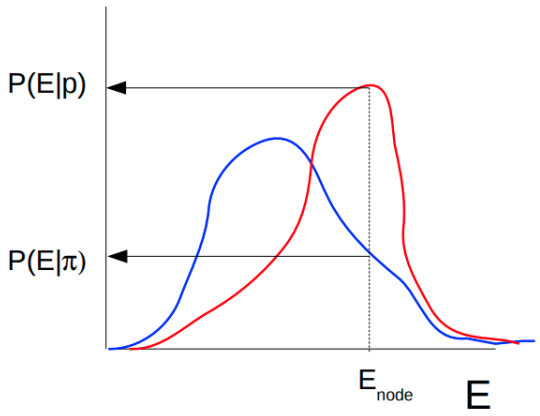

Figure 6.102: Pion (blue) and proton (red) probability distributions in a given node. The probability for each is assigned according to the energy in that node in a given event. [Figure by Phil Rodrigues (MINERvA collaboration).]

$$LLR = \sum_{nodes} \left[logP\left(E_{node}|p^{+}\right) - logP\left(E_{node}|\pi\right) \right] \tag{6.10}$$

where LLR is the log likelihood ratio. Data and MC distributions can be constructed using the LLR. Such distributions are shown from figure 6.103 to 6.105, for all targets, after the neutrino energy cut. A clear separation of pions from protons can be observed around $LLR = 0$, where the cut is applied, getting rid of a large fraction of the protons (in blue).

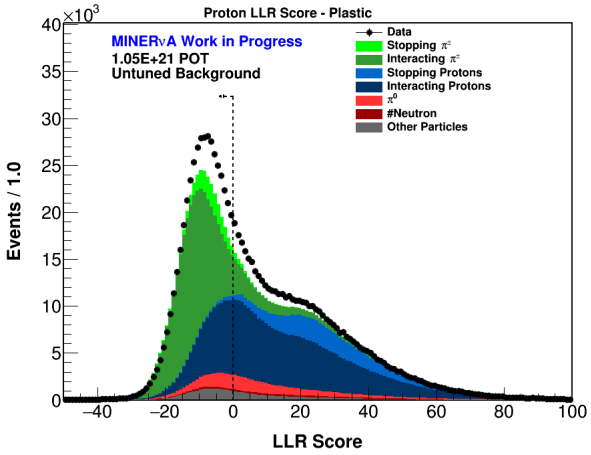

Figure 6.103: Proton LLR distribution after the E_ν cut, in the CH target.

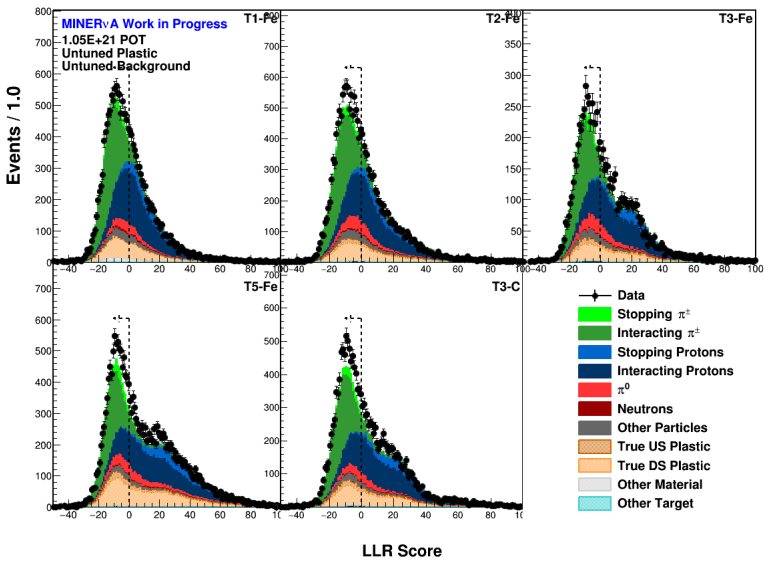

Figure 6.104: Proton LLR distribution after the E_ν cut, in the C and Fe targets.

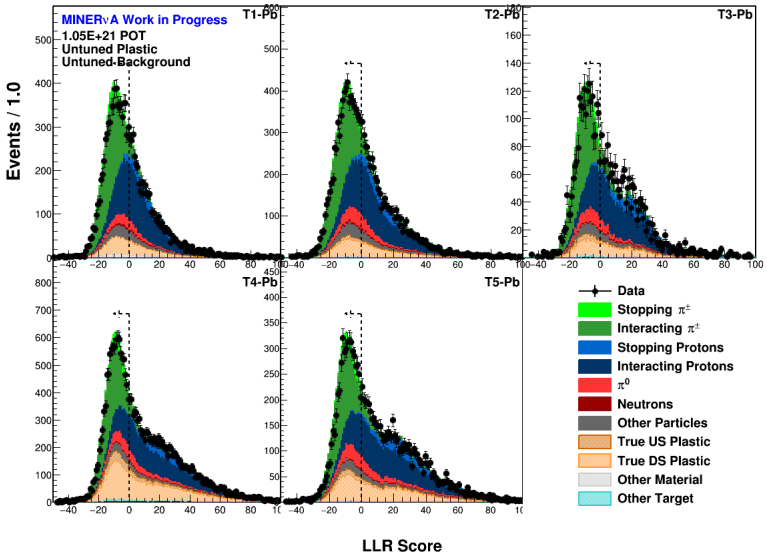

Figure 6.105: Proton LLR distribution after the E_ν cut, in the Pb targets.

6.5.6 Vertex Energy Selection

It is not obvious how to delimit the vertex region. A very large region would include signal events where the pion interacts creating hadronic showers, this mimics the behavior of some background events (like DIS). A very small region would not allow the pion to propagate enough to measure its energy deposition (specially in the passive targets). The vertex region is defined as a cylinder surrounding the muon vertex. This cylinder has radius of 200 mm and a height of seven planes (three downstream, three upstream and the vertex plane). The number of planes is limited by the separation between targets in the passive targets region (figures 6.9 and 6.10). The width or transverse span of the vertex region (200 mm), is the distance between the edge of the fiducial volume to the end of the inner detector (edge of plastic scintillator) in order to still have room for the development of hadronic showers for events occurring near the edge of the fiducial volume. In figure 6.106, the top view of the vertex region in one of the passive materials is shown.

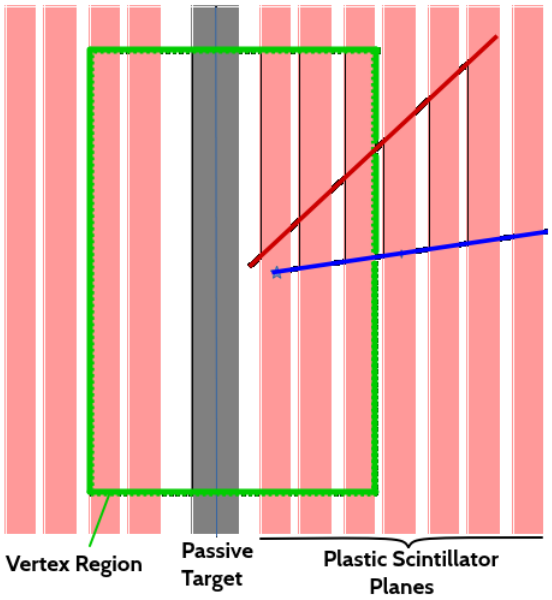

Figure 6.106: Delimitation of the vertex region (in green). It consists of a cylinder of 200 mm radius and seven planes of height, centered at the muon vertex in both the longitudinal and transverse direction.

To select events with vertex energy E_{Vtx} consistent with minimum-ionizing muon and pion, the reconstructed signal-only sample was used. Figures 6.107 and 6.108 show the distributions of the energy deposited by signal events in the vertex region. The cut is defined as the mean of the fit to the distribution $\pm$ 1 sigma from the mean.

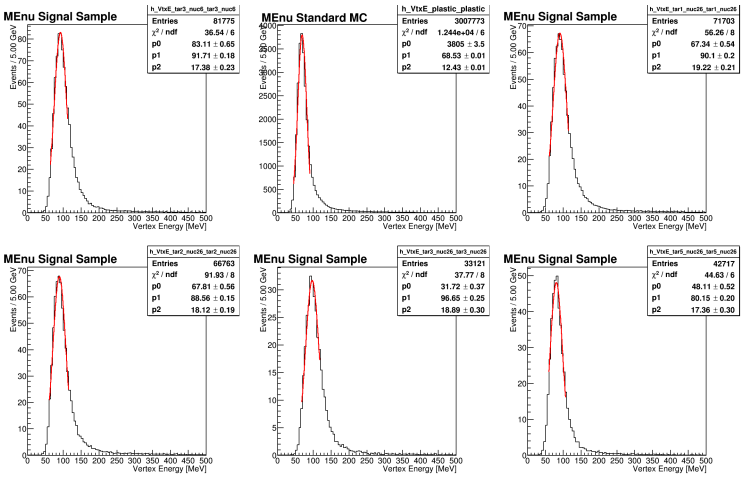

Figure 6.107: Fits to the distributions of the energy deposited by signal events in the vertex region (C, CH and Fe targets).

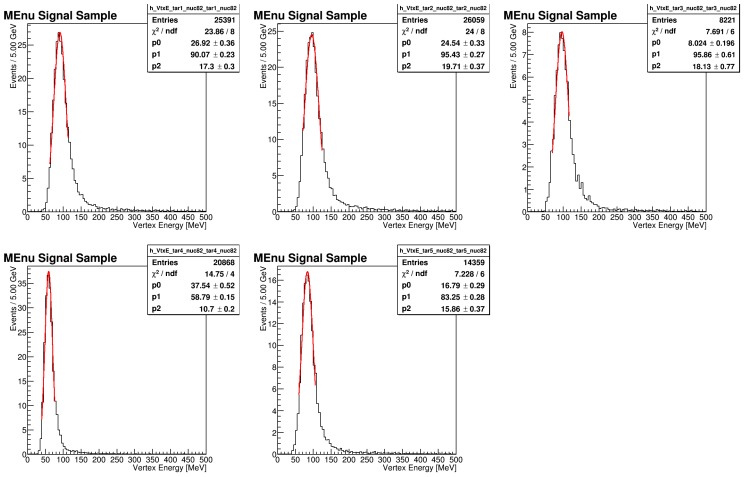

Figure 6.108: Fits to the distributions of the energy deposited by signal events in the vertex region (Pb targets).

The upper cut obviously gets rid of events with nuclear breakup, while the lower cut removes events where one of the gammas from the decay of a π^0 gets tracked. These have less energy than track pions. Unlike previous cuts, this one does not have the same lower and upper limits in all targets, due to the different widths of the passive materials. Different amounts of energy is deposited in different materials, and more energy is deposited in thicker targets of the same material. Figures 6.109 to 6.111 show the reconstructed vertex energy distributions for all the targets, after the PID cut.

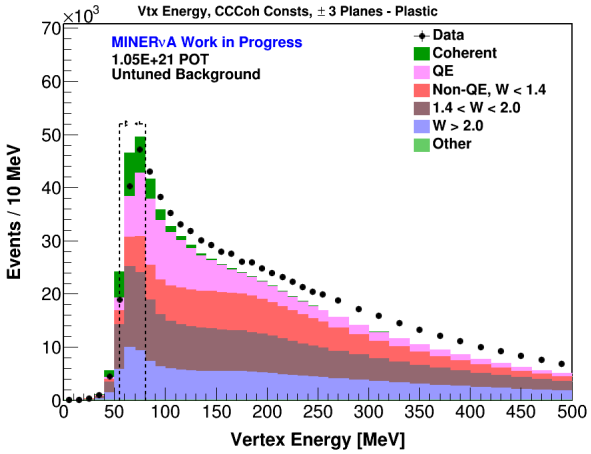

Figure 6.109: Vertex energy distribution after the PID cut including background events, in the CH target.

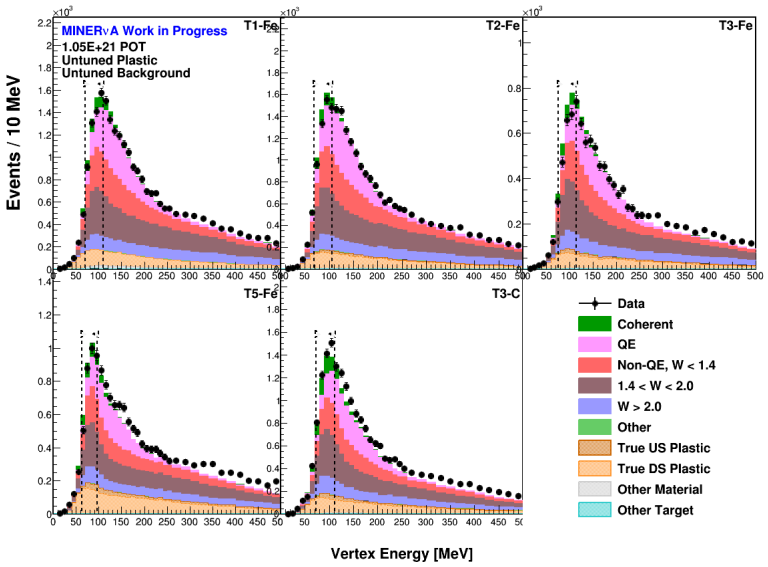

Figure 6.110: Vertex energy distribution after the PID cut including background events, in the C and Fe targets.

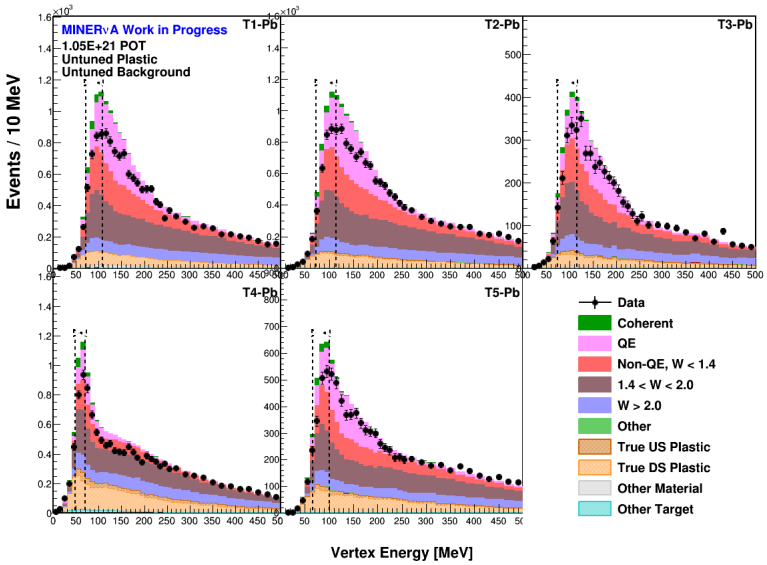

Figure 6.111: Vertex energy distribution after the PID cut including background events, in the Pb targets.

6.5.7 $|t|$ Selection

The $|t|$ cut removes events with nuclear breakup that survived the vertex energy cut. Some of these events correspond to single pions that happen to not interact inside the vertex region. The value for the cut in the CH was determined in the LE analysis. Events with $|t| > 0.125\,(GeV/c)^2$ were rejected, since $\gtrsim 99\%$ of the true coherent events fall below that value. A similar cut is used in the C (graphite) target.
In section 3.3.1 a dependence of the CC coherent pion cross section on $|t|$ is introduced from the elastic pion-nucleus interaction, which depends on $|t|$ through the expression $\left(e^{-b|t|}\right)$. b is the slope of the exponential, the larger its value the faster the reduction of the pion-nucleus cross section. From equation 3.16, it can be shown that b is larger for bigger nuclei $(\sim 40, \sim 110, \sim 270)\,(GeV/c)^2$ for C, Fe and Pb, respectively. This means that the $|t|$ distributions for Fe and Pb fall faster than in C. This is evident in the $|t|$ distributions in figures 6.112 to 6.114. Iron (lead) events are required to be less than 0.075 (0.05) $(GeV/c)^2$.

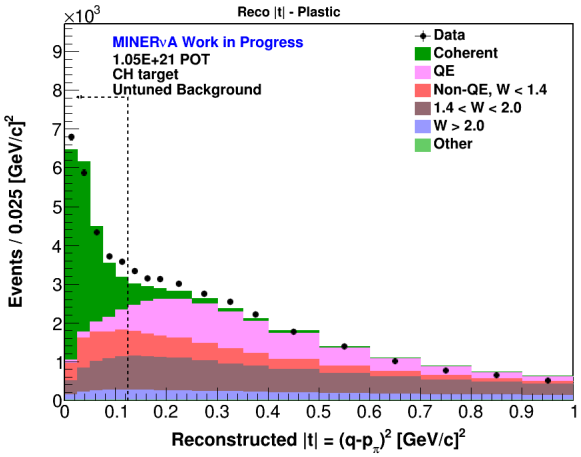

Figure 6.112: $|t|$ distribution after the vertex energy cut, in the CH target.

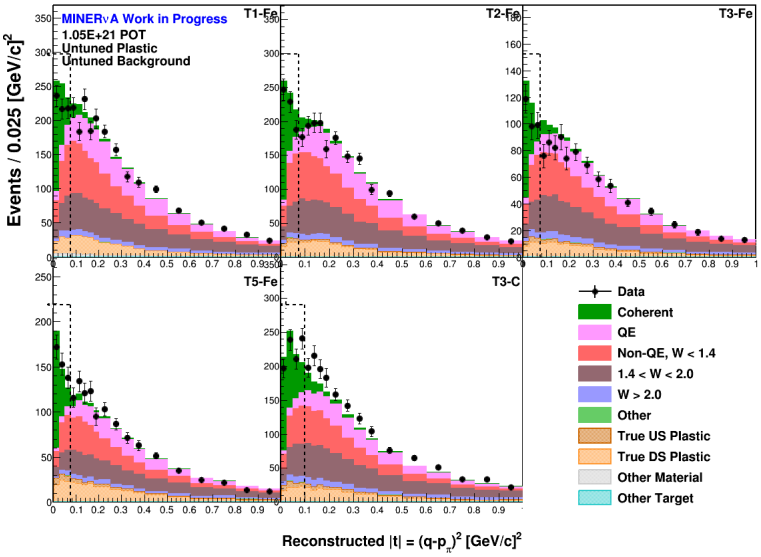

Figure 6.113: $|t|$ distribution after the vertex energy cut, in the C and Fe targets.

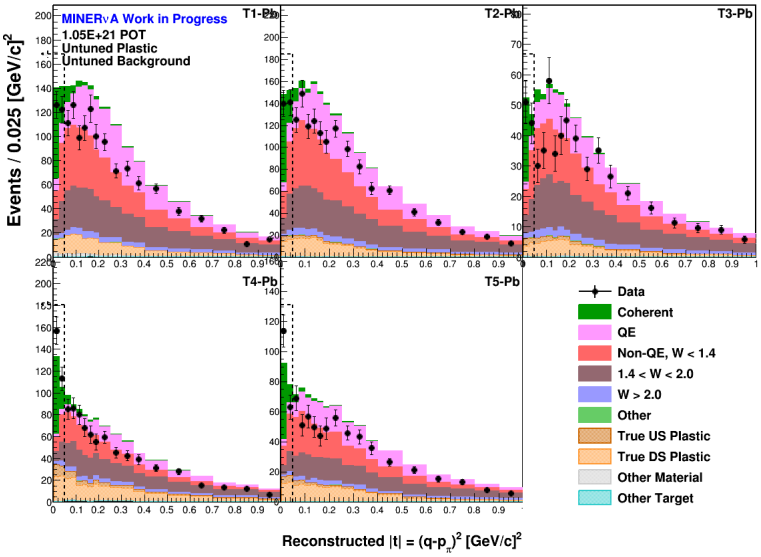

Figure 6.114: $|t|$ distribution after the vertex energy cut, in the Pb targets.

6.5.8 Final Event Rates, Efficiency and Purity

The event rates in the MC and data samples after the $|t|$ cut, are shown in tables 6.5 and 6.6, for all targets and per material (respectively). Final efficiency and purity of the sample (after the $|t|$ cut) are also included.

	C	CH	Fe 1	Fe 2	Fe 3	Fe 5	Pb 1	Pb 2	Pb 3	Pb 4	Pb 5
Total MC Events	11610	89592	10026	9695	4650	5636	3870	4064	1355	2611	2101
Efficiency (%)	33.34	29.01	30.94	34.99	31.51	36.11	31.15	32.65	30.36	33.41	33.52
Purity	38.92	65.88	36.77	38.90	37.94	45.37	34.24	33.81	32.10	44.16	37.55
Total Data Events	807	15542	597	604	291	406	229	253	87	238	160

Table 6.5: MC and Data events after the $|t|$ cut, per target. Efficiency and purity are also shown, in each target. Background not subtracted yet.

	C	CH	Fe	Pb
Total MC Events	11610	89592	30007	14001
Efficiency (%)	33.34	29.01	33.30	32.33
Purity	38.92	65.88	39.25	36.26
Total Data Events	807	15542	1898	967

Table 6.6: MC and Data events after the $|t|$ cut, per material. Efficiency and purity are also shown. Background not subtracted yet.

6.6 Plastic Background Tuning

Up to now, all distributions in the passive targets have a contribution from the events being originated truly in plastic scintillator. A small contribution is from the plastic upstream the passive material, where the tracking and vertex algorithms fail to reconstruct the most upstream part of the track. The majority of the plastic background is located downstream the passive material, mostly from the fiducial volume (first plane downstream the passive target) (see figure 6.11). The plastic background needs to be subtracted from the passive material contribution, in order to extract physics information from the latter.
To subtract the "plastic background", it has to be tuned first. The tuning consists in adjusting the plastic scintillator prediction in the MC, according to the data event rate in a region dominated by plastic background. This region is called a "sideband". And it comprises all the planes in between passive targets, excluding the two planes closest to each passive target (figure 6.115). A sideband is constructed for each of the three passive materials (C, Fe and Pb), using the plastic in front of each target material (figures 6.6 and 6.8).

A χ^2 hypothesis is constructed (equation 6.11) for each passive material, and minimized by applying scaling parameters to the "upstream" and "downstream" plastic MC contribution, while keeping constant the signal (carbon, iron or lead) and the "other" (interactions from other targets and materials) MC contributions. These MC contributions are kept constant since their contribution in the sideband is negligible. During the minimization procedure for the obtainment of the upstream plastic scale factor, the downstream plastic contribution remains constant, and vice versa (figures 6.116 to 6.121 are the sidebands in each material, before and after tuning the "us" and "ds" plastic background).

$$\chi^2 = \sum_i \left[\frac{MC^i_{signal} + MC^i_{other} + \alpha_{us} MC^i_{us} + \alpha_{ds} MC^i_{ds} - Data^i}{\sqrt{Data^i}} \right]^2 \tag{6.11}$$

where MC_{signal}, MC_{us}, MC_{ds} and MC_{other} are the signal (carbon, iron or lead), upstream plastic, downstream plastic, and other MC contribution to the total MC in the sideband. $Data$ is the data in the sideband. The sum is over all the bins in the sideband. α_{us} and α_{ds} are the upstream and downstream scale factors obtained during the minimization routine. Pairs of α_{us} and α_{ds} scale factors are gotten for each passive material, and are summarized in table 6.7. After tuning the plastic, most of the data/MC ratios from 6.116 to 6.121, are close to 1, which means there is a reasonable good agreement between the data and the tuned simulation. The only region with a huge disagreement is the downstream

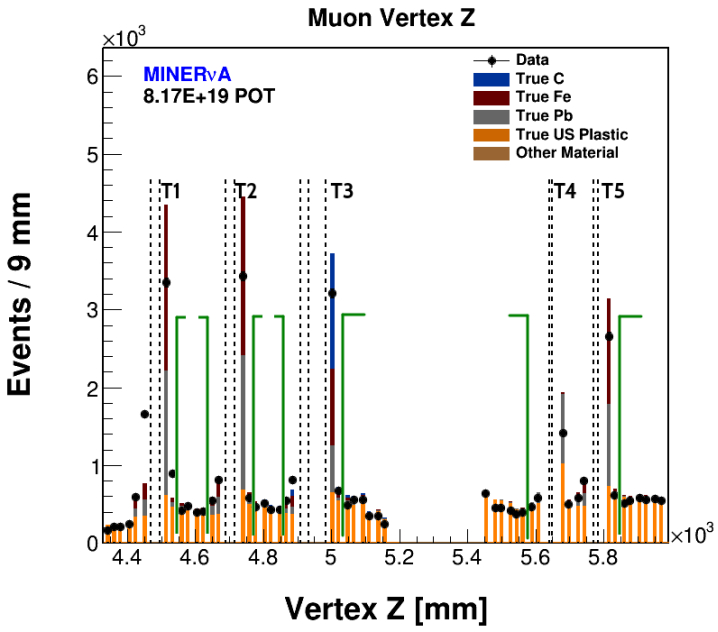

Figure 6.115: Zoomed out view of the passive target region. The histogram represents the reconstructed muon vertex in that region. The bins in between the green lines represent the sidebands for the tuning of the plastic background. The dashed lines are the passive targets. The plastic upstream target 1 is not used, due to the high rock muon contribution (section 5.3). The number of events in this plot is just a small sample of the total used. It was generated just to illustrate the passive target region.

sidebands for all materials in target 3. This is believed to be caused by the presence of the water target, which is installed downstream target 3. The water target somehow causes a reduction of data events in the upstream bins close to it, perhaps due to the absorption of a fraction of the events.

Material	α_{us}	α_{ds}	$\frac{\chi^2}{ndf}_{us}$	$\frac{\chi^2}{ndf}_{ds}$
C	1.152 ± 0.009	1.111 ± 0.008	1.70	11.83
Fe	1.170 ± 0.004	1.039 ± 0.005	4.62	6.10
Pb	1.16 ± 0.005	1.165 ± 0.005	7.88	3.49

Table 6.7: Upstream and downstream scale factors obtained during the minimization of the χ^2 functions. The χ^2/ndf value after the minimization, is also shown for all materials, for the US and DS sidebands.

The α_{us} and α_{ds} scale factors are applied to the plastic background in the fiducial volume

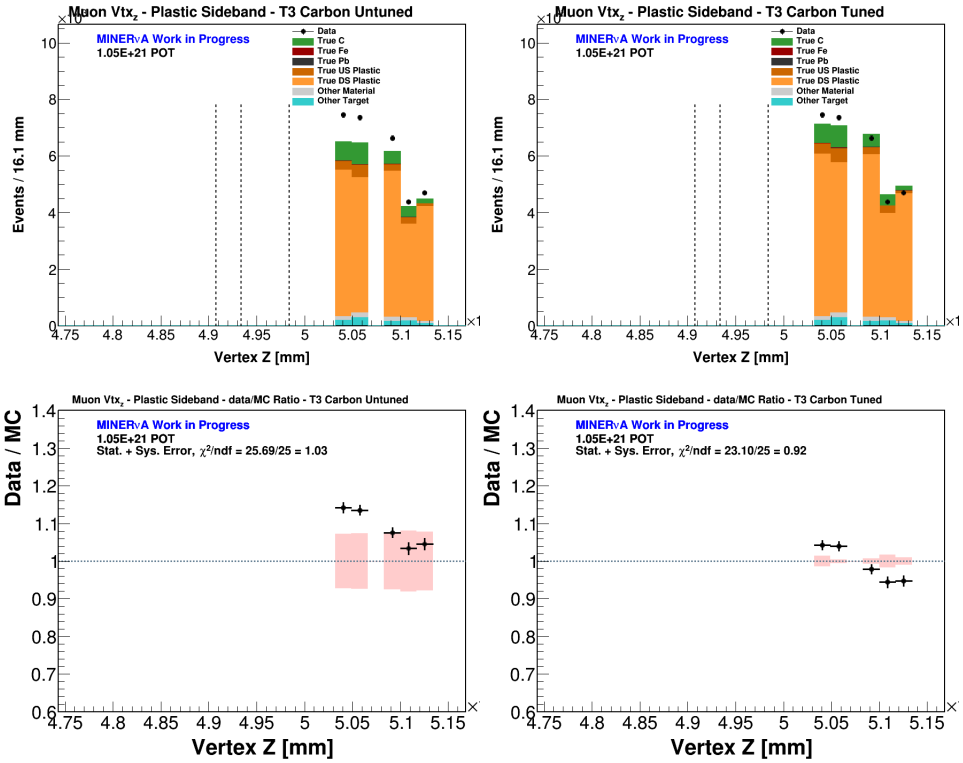

Figure 6.116: The top left (right) plot is the C sideband before (after) tuning the DS plastic background. The bottom left (right) plot is the data/MC ratio before (after) tuning the DS plastic background. The error bands in pink-like color are related to the systematic uncertainties, explained in section 6.8.

for each of the passive targets. The tuned MC plastic is the best estimate for the plastic contamination in the data in the fiducial volume. The tuned MC plastic is then subtracted from both the MC and data samples.

After this, the targets with the same material (Fe and Pb) are merged to gather more statistics for each. Figures 6.122 to 6.124 show the $|t|$ distribution in each passive material with the plastic background before and after the tuning, and with the plastic background subtracted.

It is important to highlight the importance of the $|t|$ distributions above. The CH sample represents the largest statistical sample of CC neutrino-induced coherent pion production until now. The Fe and Pb samples are the first evidence of the same interaction in these materials, Pb being the largest nuclei from which the interaction has been observed. The signal contribution is evident at low $|t|$ in all materials.

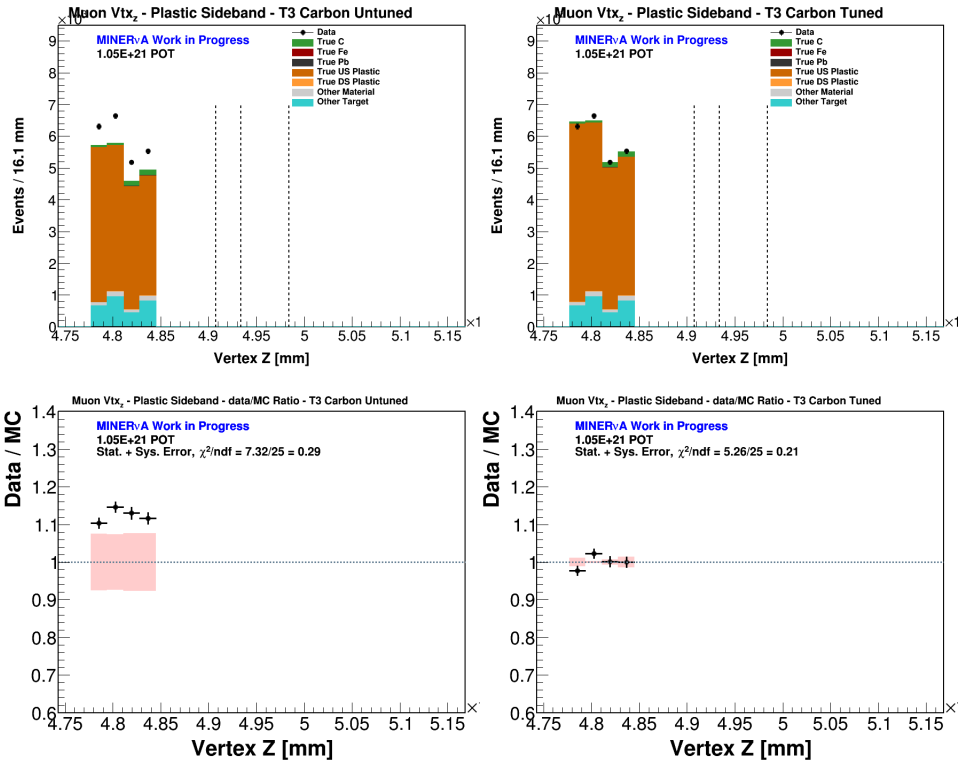

Figure 6.117: The top left (right) plot is the C sideband before (after) tuning the US plastic background. The bottom left (right) plot is the data/MC ratio before (after) tuning the US plastic background. The error bands in pink-like color are related to the systematic uncertainties, explained in section 6.8.

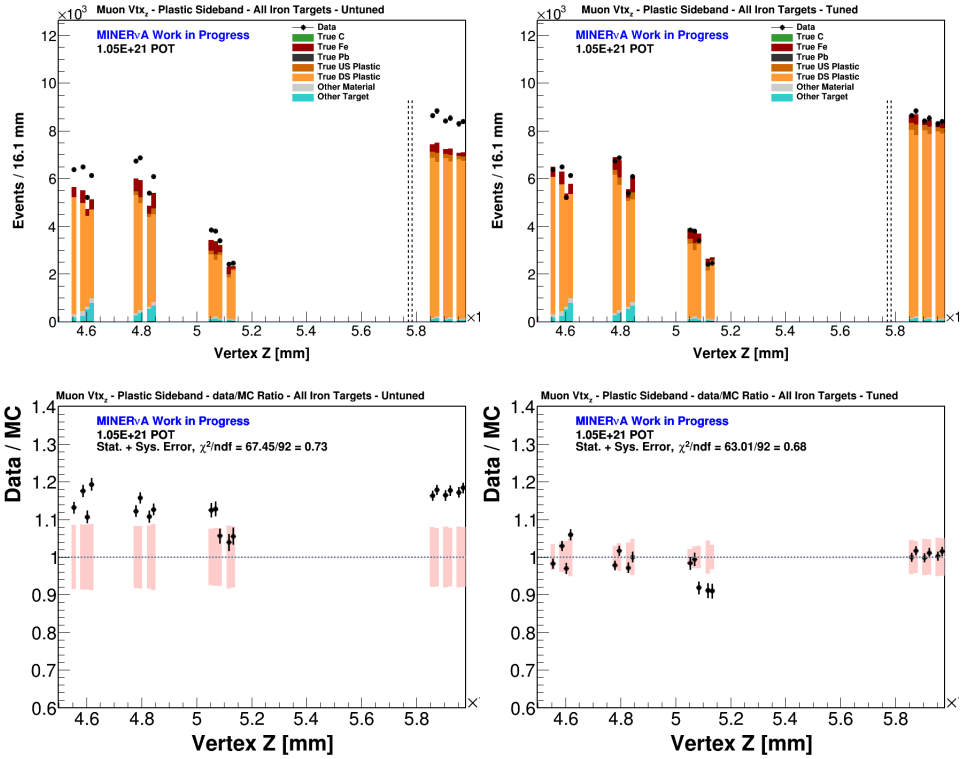

Figure 6.118: The top left (right) plot is the Fe sideband before (after) tuning the DS plastic background. The bottom left (right) plot is the data/MC ratio before (after) tuning the DS plastic background. The error bands in pink-like color are related to the systematic uncertainties, explained in section 6.8.

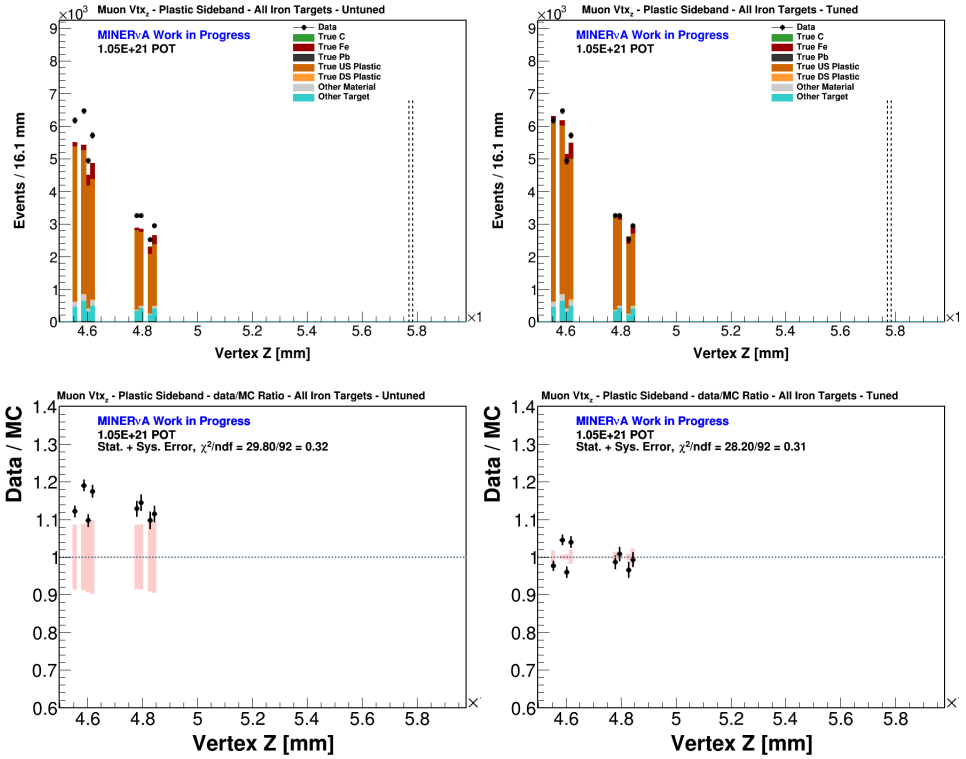

Figure 6.119: The top left (right) plot is the Fe sideband before (after) tuning the US plastic background. The bottom left (right) plot is the data/MC ratio before (after) tuning the US plastic background. The error bands in pink-like color are related to the systematic uncertainties, explained in section 6.8.

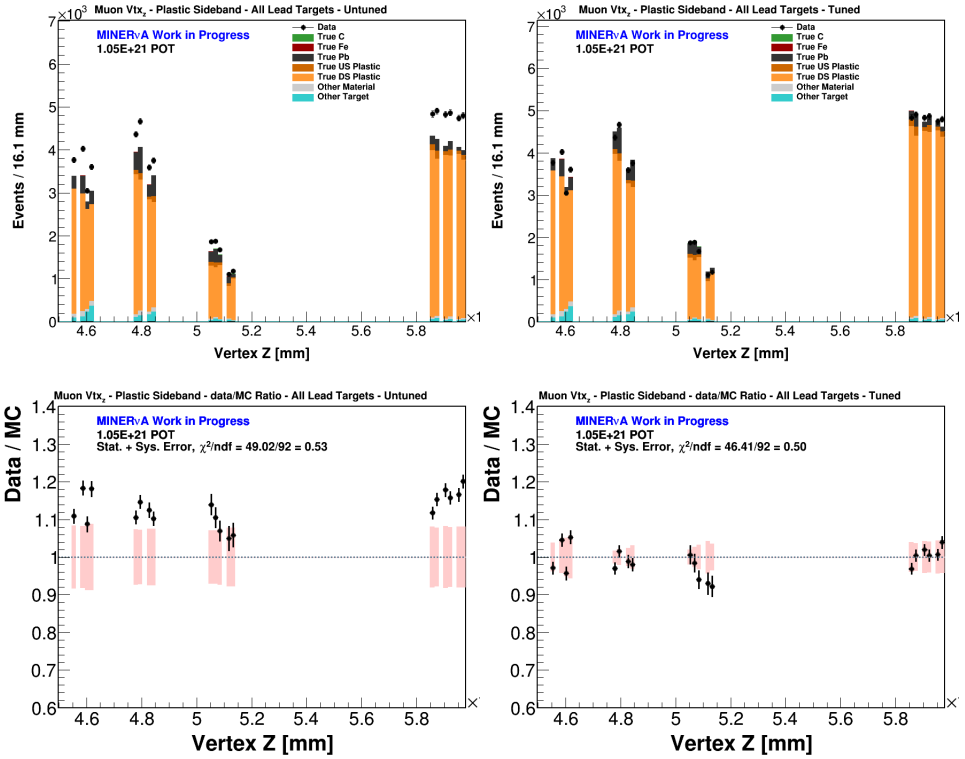

Figure 6.120: The top left (right) plot is the Pb sideband before (after) tuning the DS plastic background. The bottom left (right) plot is the data/MC ratio before (after) tuning the DS plastic background. The error bands in pink-like color are related to the systematic uncertainties, explained in section 6.8.

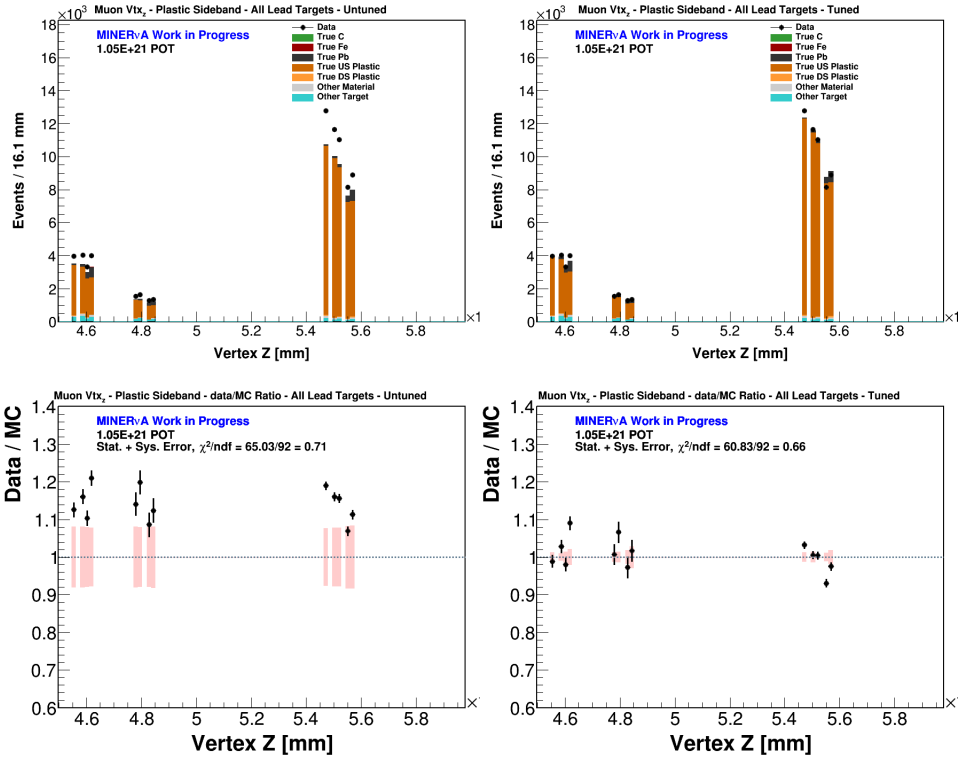

Figure 6.121: The top left (right) plot is the Pb sideband before (after) tuning the US plastic background. The bottom left (right) plot is the data/MC ratio before (after) tuning the US plastic background. The error bands in pink-like color are related to the systematic uncertainties, explained in section 6.8.

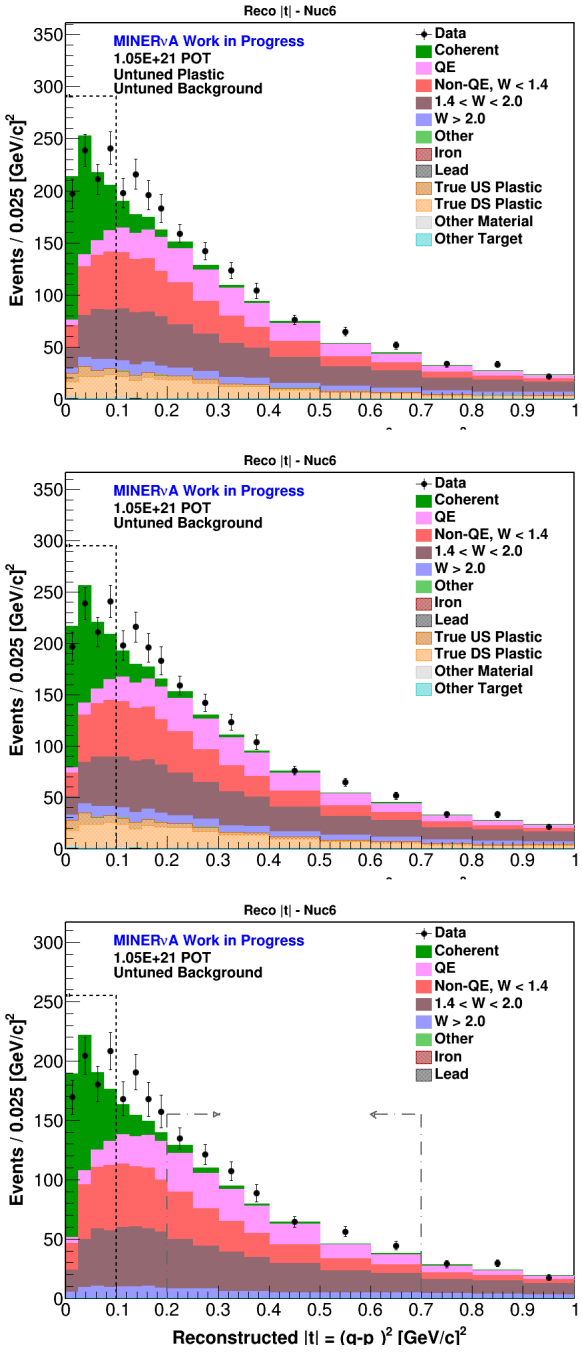

Figure 6.122: Carbon $|t|$ distribution before tuning (top), after tuning (middle), and after subtracting the plastic background (bottom). The larger arrow is the cut applied to the $|t|$ distribution. The shorter arrows in the bottom plot are explained in the next section.

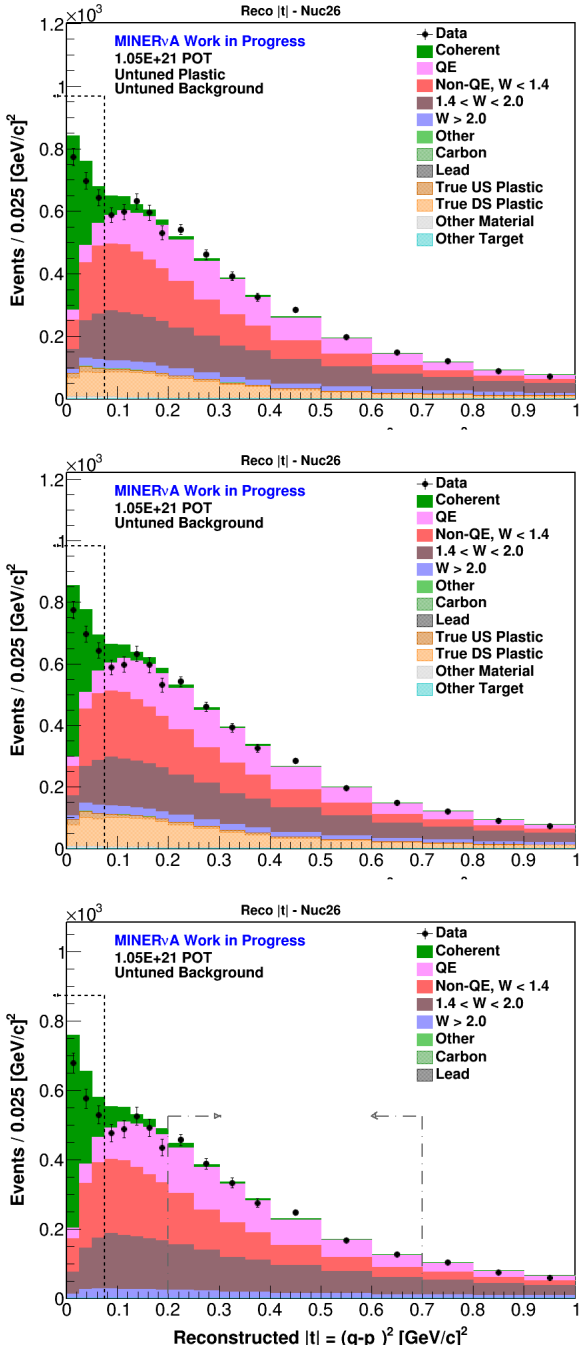

Figure 6.123: Iron $|t|$ distribution before tuning (top), after tuning (middle), and after subtracting the plastic background (bottom). The larger arrow is the cut applied to the $|t|$ distribution. The shorter arrows in the bottom plot are explained in the next section.

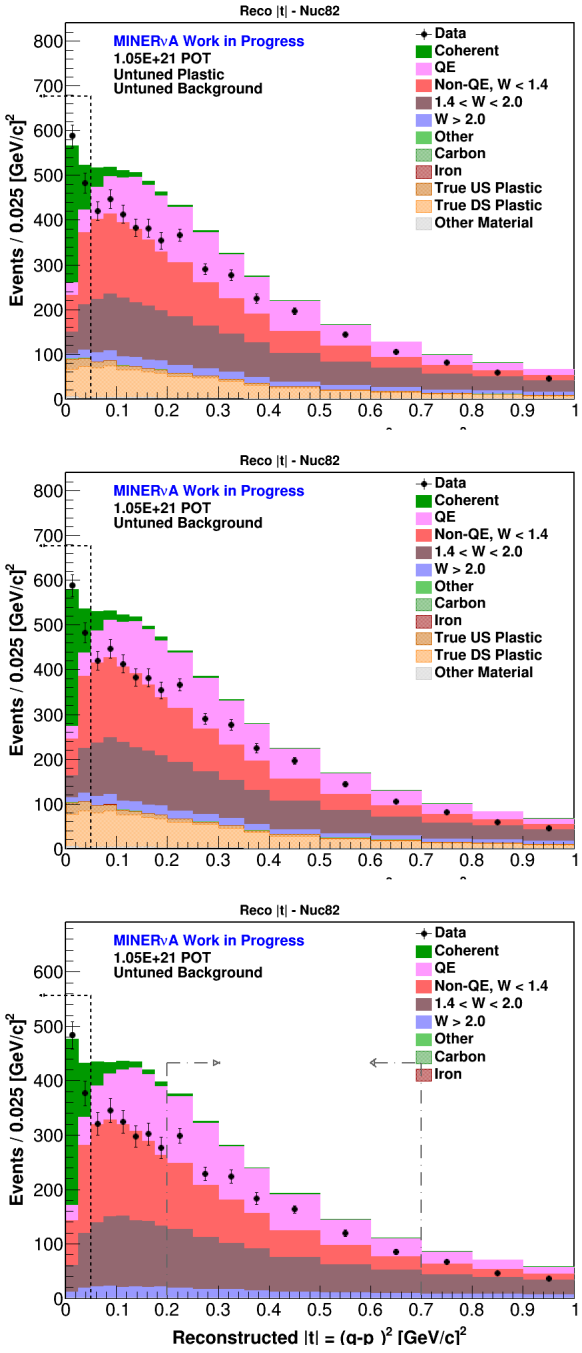

Figure 6.124: Lead $|t|$ distribution before tuning (top), after tuning (middle), and after subtracting the plastic background (bottom). The larger arrow is the cut applied to the $|t|$ distribution. The shorter arrows in the bottom plot are explained in the next section.

6.7 Non-Coherent Background Tuning

The event rates in the models used by GENIE [131,132] are usually over or underestimated, due to large uncertainties in some of the models used by the generator and in the flux itself. And therefore, the overall normalization of the kinematic distributions is neither reliable nor quite meaningful. The normalization of each background needs to be tuned so the correct amount from each background can be subtracted from the data. The tuning is done in a fashion similar to the plastic background tuning. A sideband that is background dominated, with appreciable separation between backgrounds and with negligible signal contribution is used in the tuning procedure. The tuning is done after applying the vertex energy cut because of the poor performance of the background models predicting the activity near the interaction vertex. During the tuning the signal and the "other" MC, remain constant as their contribution is negligible. Each physics background gets a scale factor during the tuning.
The bottom plot in figures 6.122 to 6.124 includes the sideband region from $0.2 < |t| < 0.7\,(GeV/c)^2$ (region in between the shorter arrows). The E_π and Q^2 distributions of events inside the sideband provide the needed separation between the QE and resonant, and between the DIS/transition regions from the resonant backgrounds, respectively. The E_π and Q^2 samples in the sideband for each material before tuning the background, are presented in figures 6.125 and 6.128.

A χ^2 is also minimized during the tuning procedure, where the tuning is performed simultaneously in both variables and it is built as follows:

$$\chi^2 = \sum_i \sum_j \frac{\left[N_{ij}^{Data} - \sum_k \alpha_k N_{ijk}^{MC}\right]^2}{\sum_k \alpha_k N_{ijk}^{MC}} \tag{6.12}$$

where N^{Data} is the number of data events in the ij bin; N^{MC} is the number of MC events from the k background, in the ij bin; and α_k is the scale factor for each background. From the tuning procedure, the α scale factors are obtained for all backgrounds. Table 6.8 shows the scale factors in all four materials.

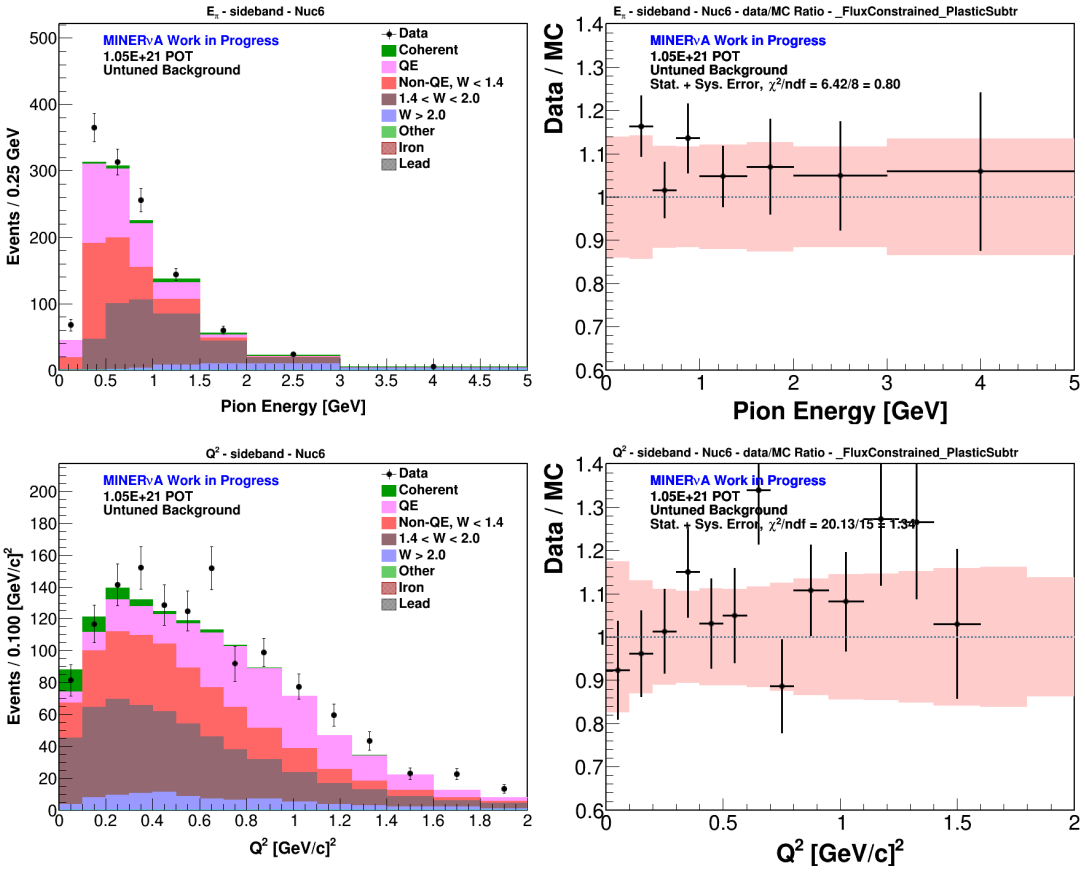

Figure 6.125: E_π and Q^2 distribution in the $0.2 < |t| < 0.7\,(GeV/c)^2$ sideband before tuning the background in C. The right-hand side plot is the data/MC ratio. The pink-like error band includes the systematic errors, explained in section 6.8.

Target	α_{QE}	α_{RES}	α_{INE}	α_{DIS}	χ^2/ndf
C	1.447 ± 0.139	1.3398 ± 0.165	0.66 ± 0.098	1.518 ± 0.224	2.32
CH	1.146 ± 0.015	1.344 ± 0.045	0.733 ± 0.019	0.877 ± 0.035	10.66
Fe	1.300 ± 0.063	1.181 ± 0.087	0.563 ± 0.059	1.092 ± 0.137	2.99
Pb	1.021 ± 0.052	0.752 ± 0.073	0.540 ± 0.057	1.036 ± 0.153	3.84

Table 6.8: Scale Factors for each of the non-coherent backgrounds in each target.

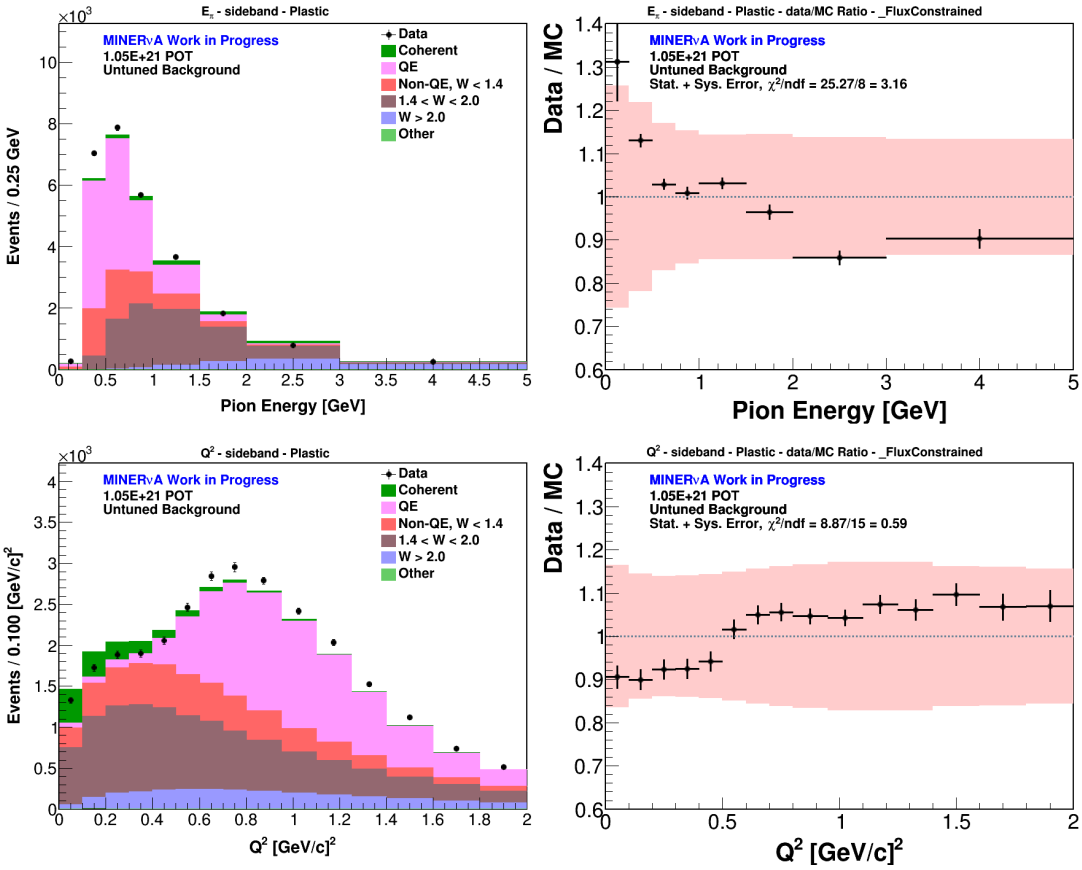

Figure 6.126: E_π and Q^2 distribution in the $0.2 < |t| < 0.7\,(GeV/c)^2$ sideband before tuning the background in CH. The right-hand side plot is the data/MC ratio. The pink-like error band includes the systematic errors, explained in section 6.8.

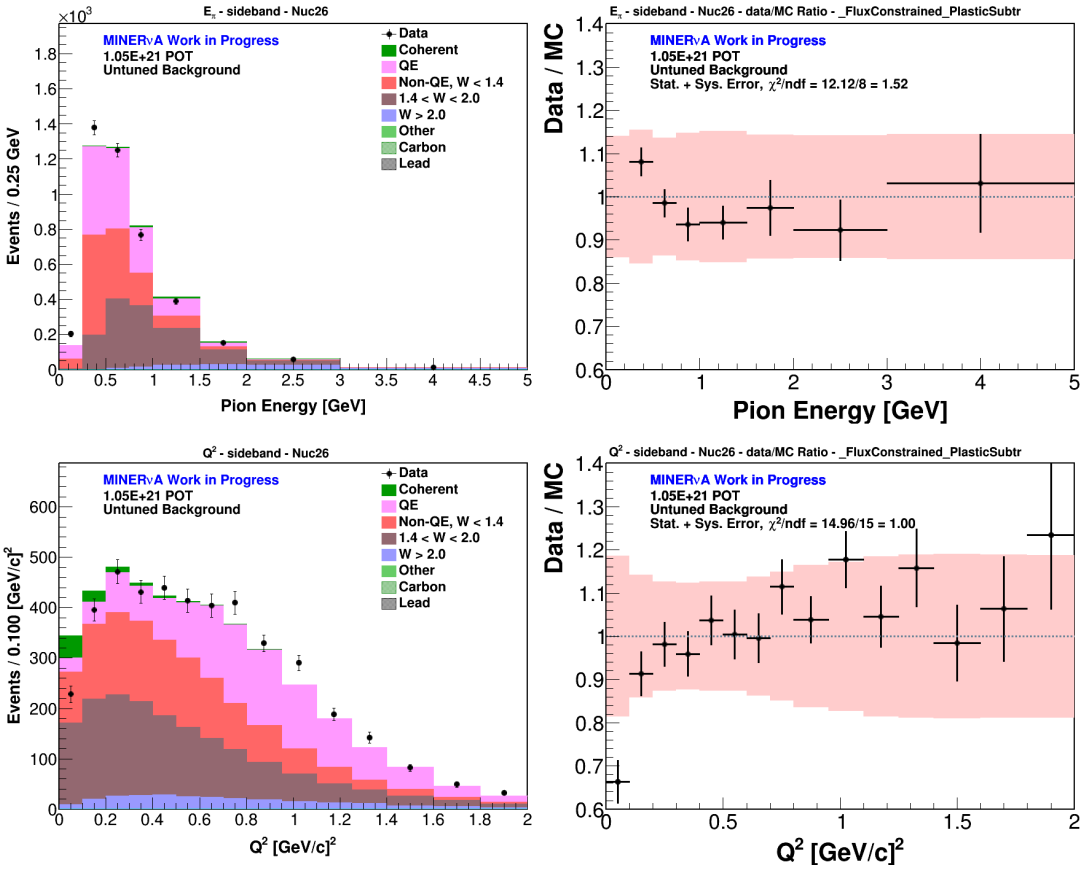

Figure 6.127: E_π and Q^2 distribution in the $0.2 < |t| < 0.7\,(GeV/c)^2$ sideband before tuning the background in Fe. The right-hand side plot is the data/MC ratio. The pink-like error band includes the systematic errors, explained in section 6.8.

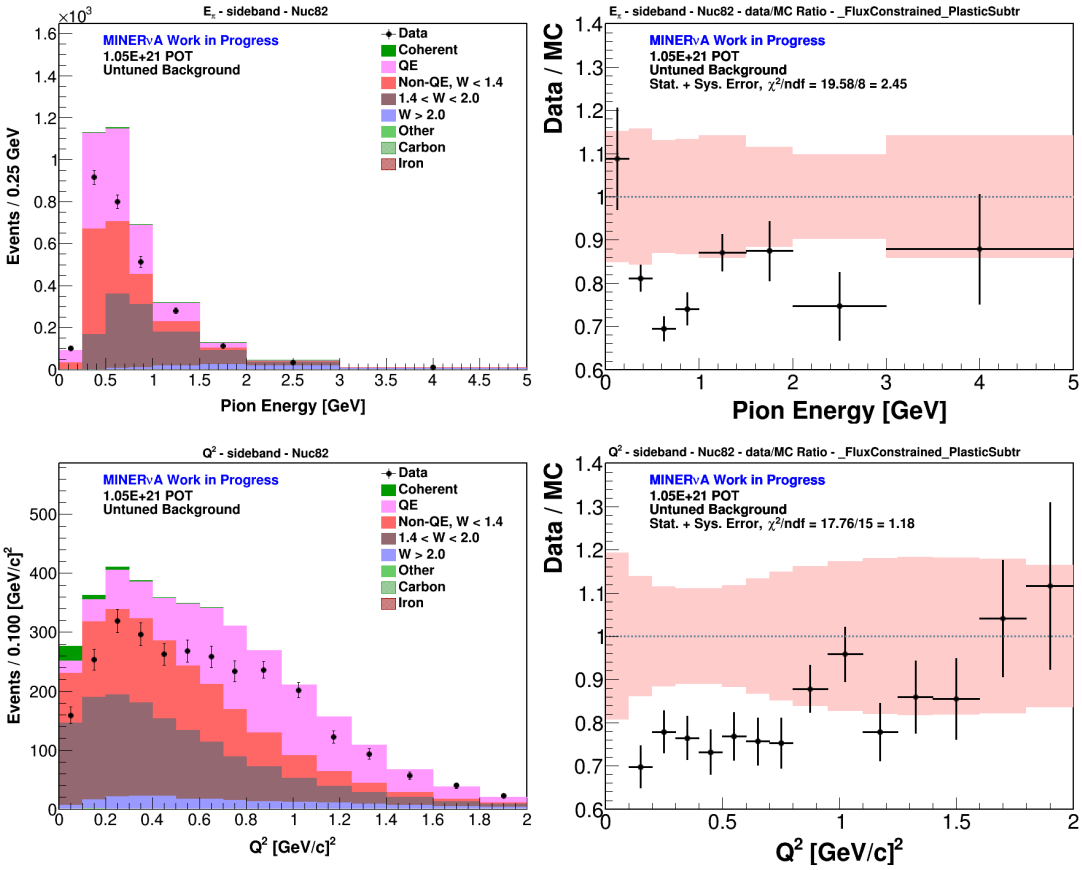

Figure 6.128: E_π and Q^2 distribution in the $0.2 < |t| < 0.7\,(GeV/c)^2$ sideband before tuning the background in Pb. The right-hand side plot is the data/MC ratio. The pink-like error band includes the systematic errors, explained in section 6.8.

After applying the appropriate scale factor to each background, the E_π and Q^2 distributions in the sideband show a better agreement between the MC and data. Figures 6.129 and 6.132 are the sideband samples after tuning the background. It is worth noting that the Q^2 distribution in the sideband in the CH target a very good match is achieved between data and MC, at $Q^2 < 0.7 GeV/c^2$, region where the suppression to resonant pions is applied (see figure 6.2). For the Fe and Pb targets, it can be seen the data is more suppresed compared to the suppression provided by the MC in the same $Q^2 < 0.7 GeV/c^2$ region. This suggest an A-dependent suppression in that region.

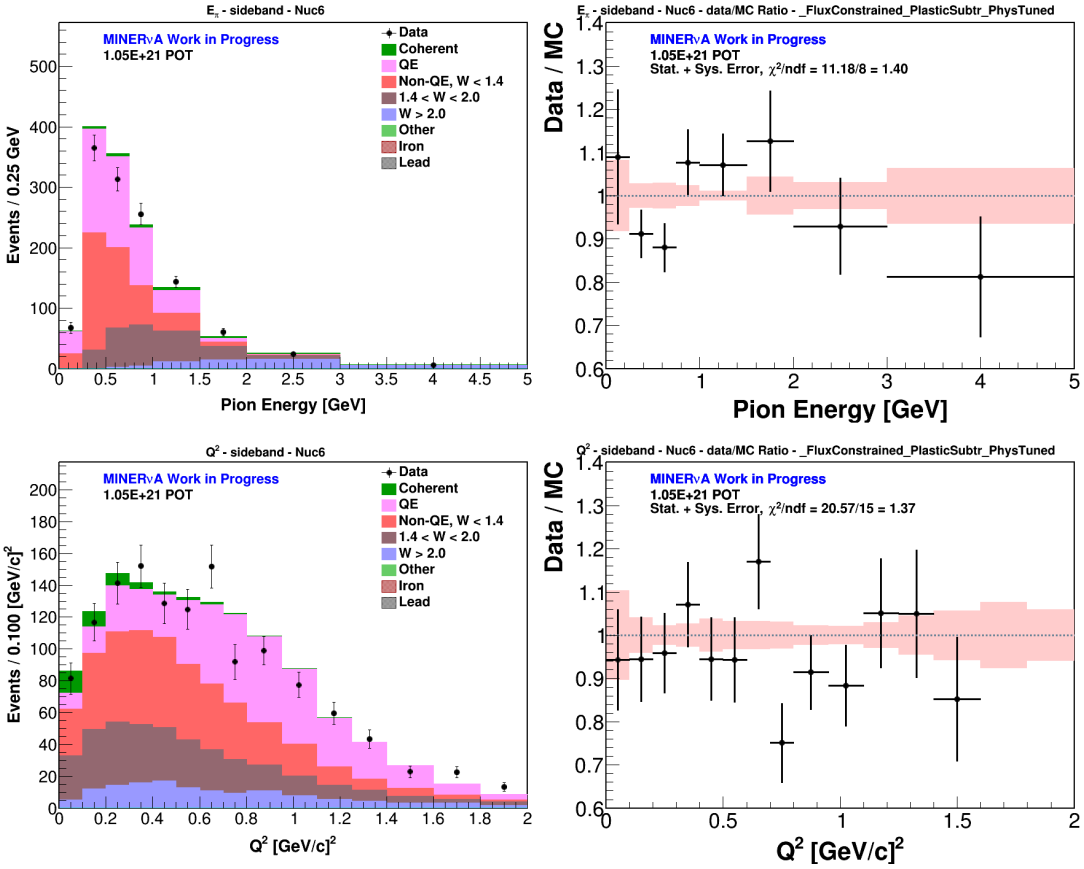

Figure 6.129: E_π and Q^2 distribution in the $0.2 < |t| < 0.7\,(GeV/c)^2$ sideband after tuning the background in C. The right-hand side plot is the data/MC ratio. The pink-like error band includes the systematic errors, explained in section 6.8.

After tuning the non-coherent background, the $|t|$ distributions in all targets, are shown in figures 6.133 to 6.136

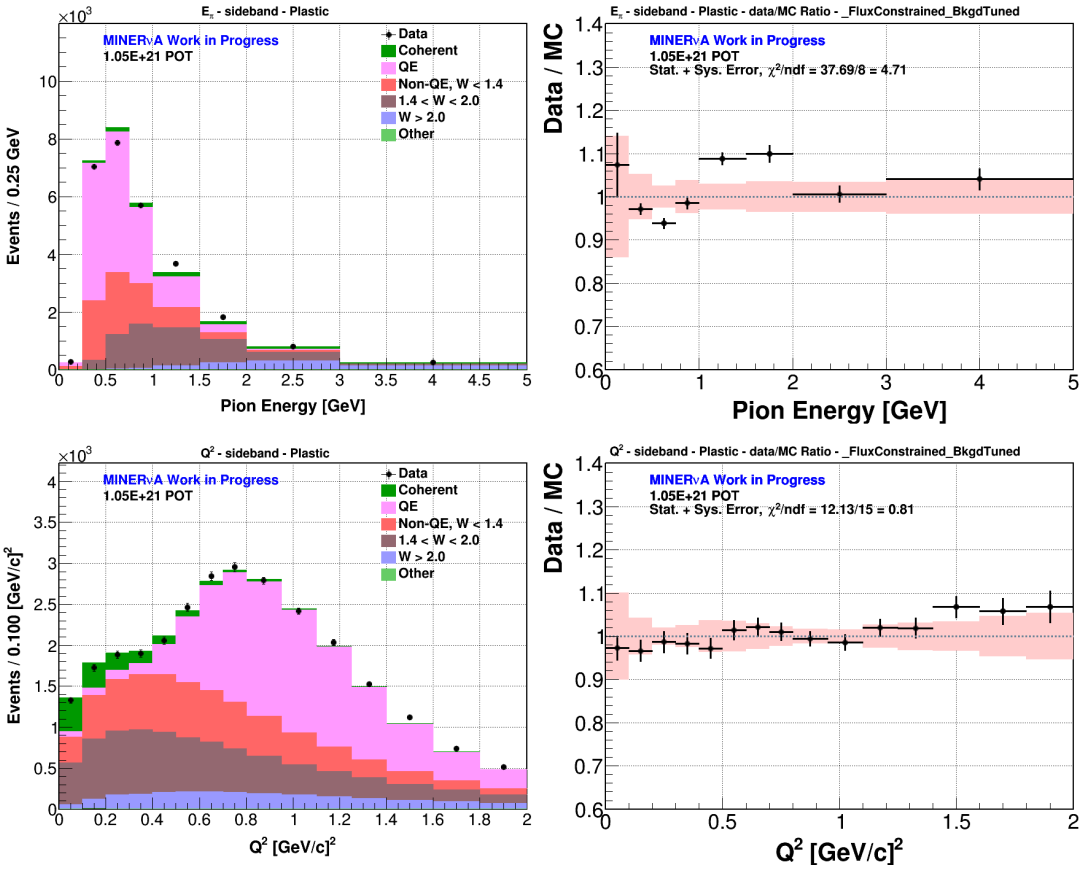

Figure 6.130: E_π and Q^2 distribution in the $0.2 < |t| < 0.7\,(GeV/c)^2$ sideband after tuning the background in CH. The right-hand side plot is the data/MC ratio. The pink-like error band includes the systematic errors, explained in section 6.8.

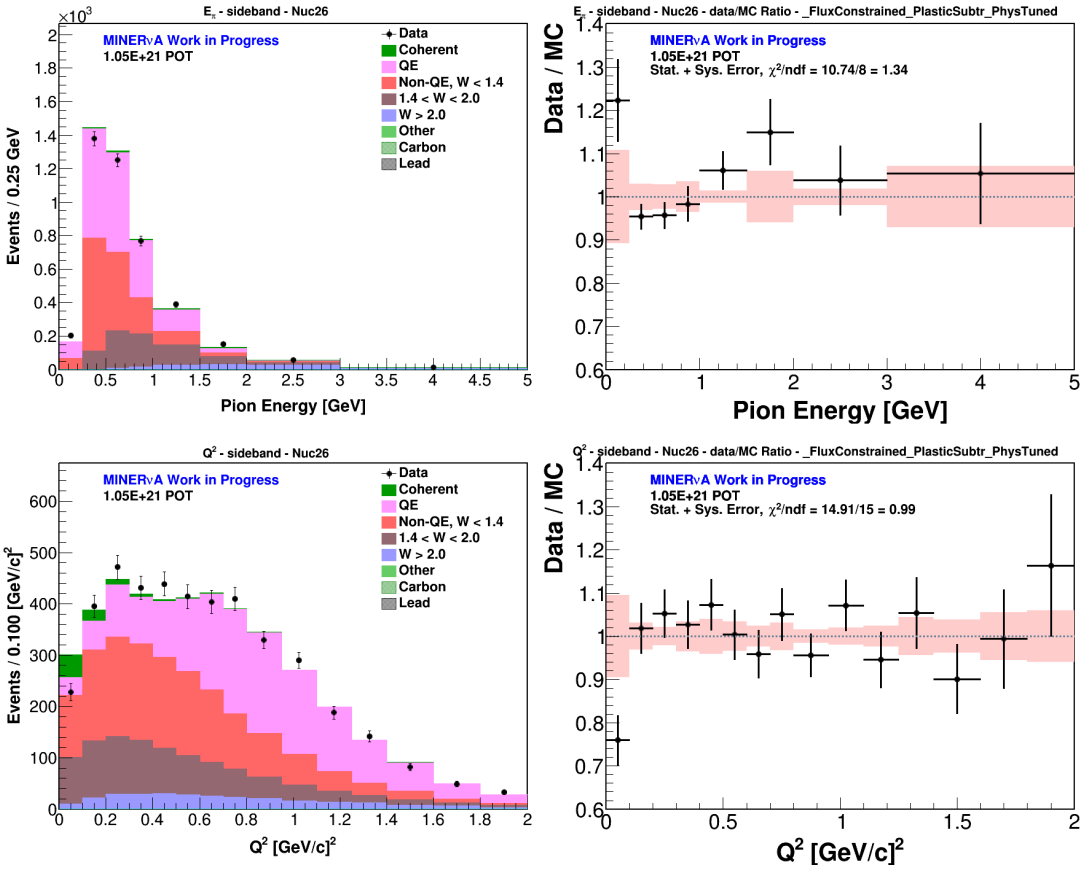

Figure 6.131: E_π and Q^2 distribution in the $0.2 < |t| < 0.7\,(GeV/c)^2$ sideband after tuning the background in Fe. The right-hand side plot is the data/MC ratio. The pink-like error band includes the systematic errors, explained in section 6.8.

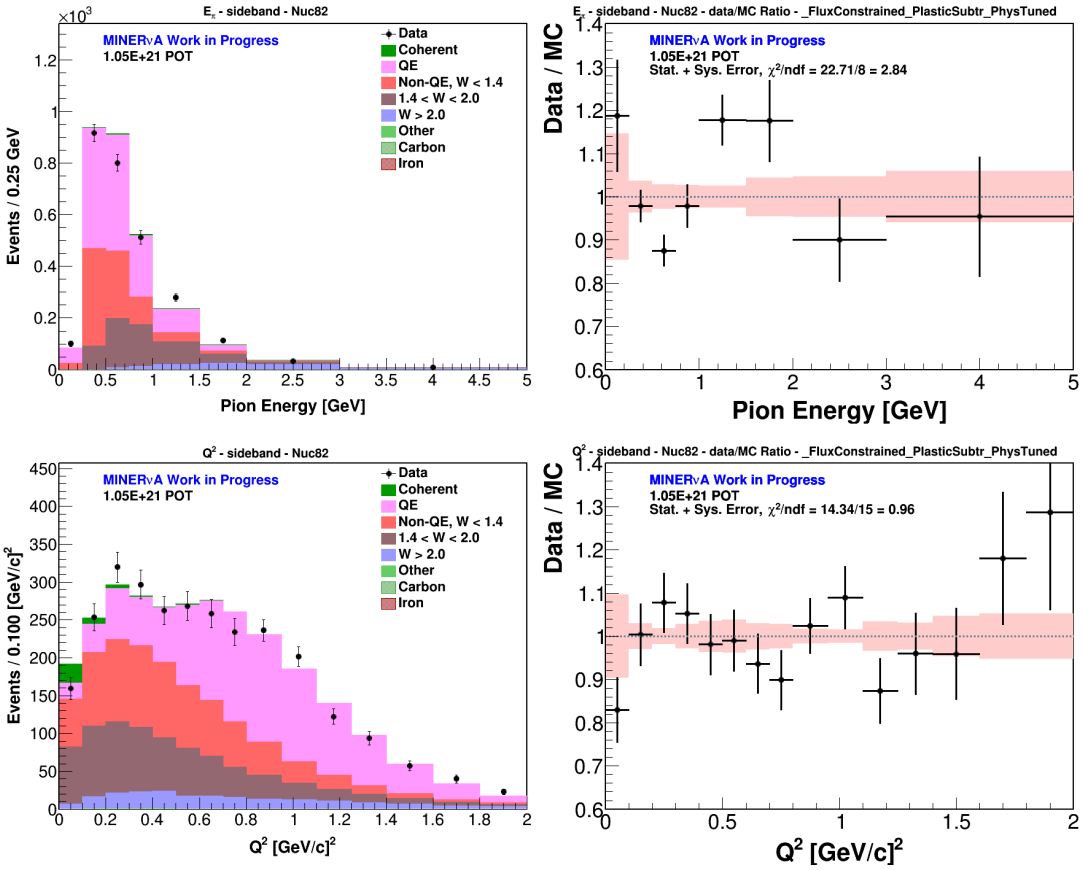

Figure 6.132: E_π and Q^2 distribution in the $0.2 < |t| < 0.7\,(GeV/c)^2$ sideband after tuning the background in Pb. The right-hand side plot is the data/MC ratio. The pink-like error band includes the systematic errors, explained in section 6.8.

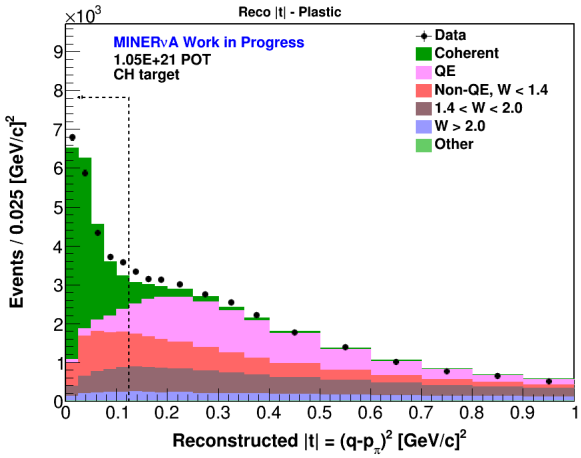

Figure 6.133: Hydrocarbon $|t|$ distribution after tuning the non-coherent background. The shorter arrows in the bottom plot delimit the used $|t|$ sideband.

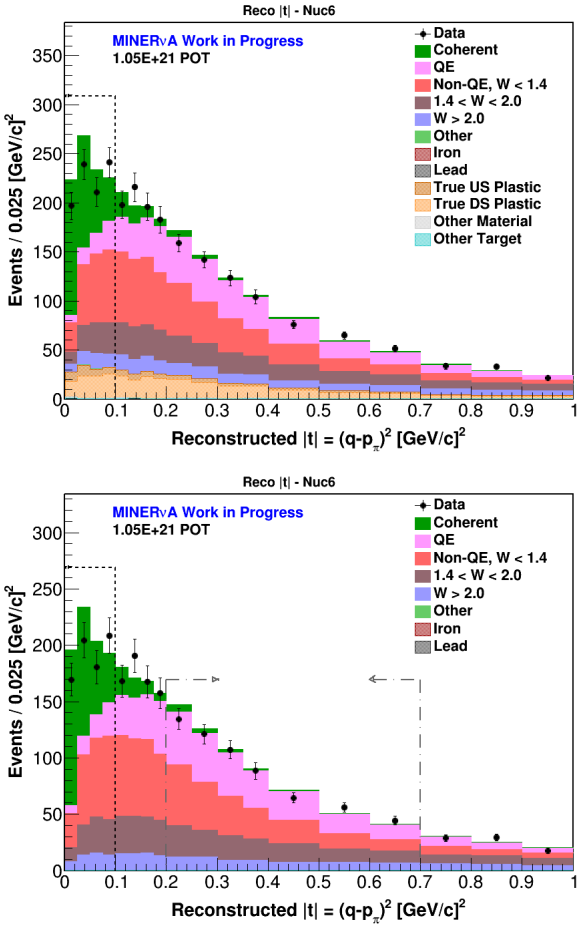

Figure 6.134: Carbon $|t|$ distribution after tuning the plastic and non-coherent background (top), after subtracting the tuned plastic background from both data and MC(bottom). The shorter arrows in the bottom plot delimit the used $|t|$ sideband.

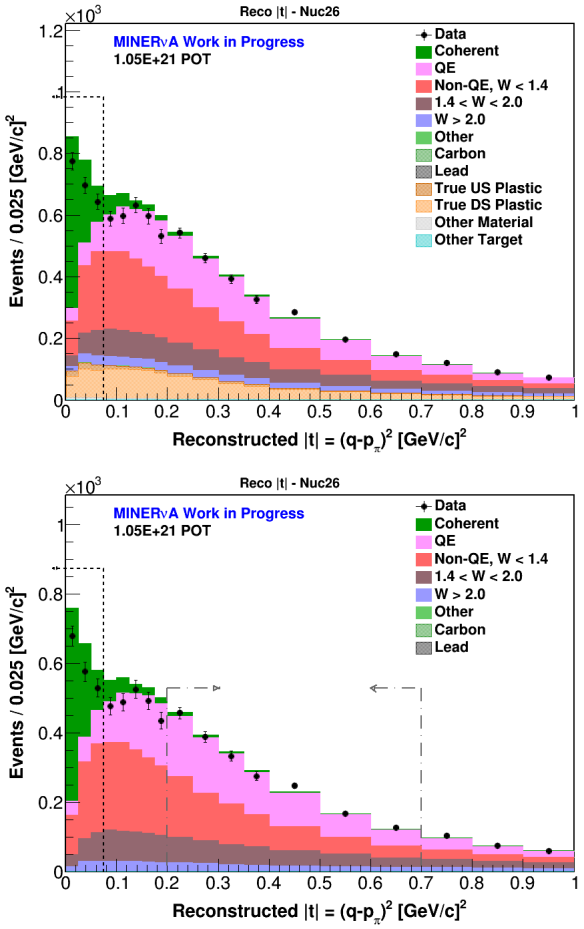

Figure 6.135: Iron $|t|$ distribution after tuning the plastic and non-coherent background (top), after subtracting the tuned plastic background from both data and MC(bottom). The shorter arrows in the bottom plot delimit the used $|t|$ sideband.

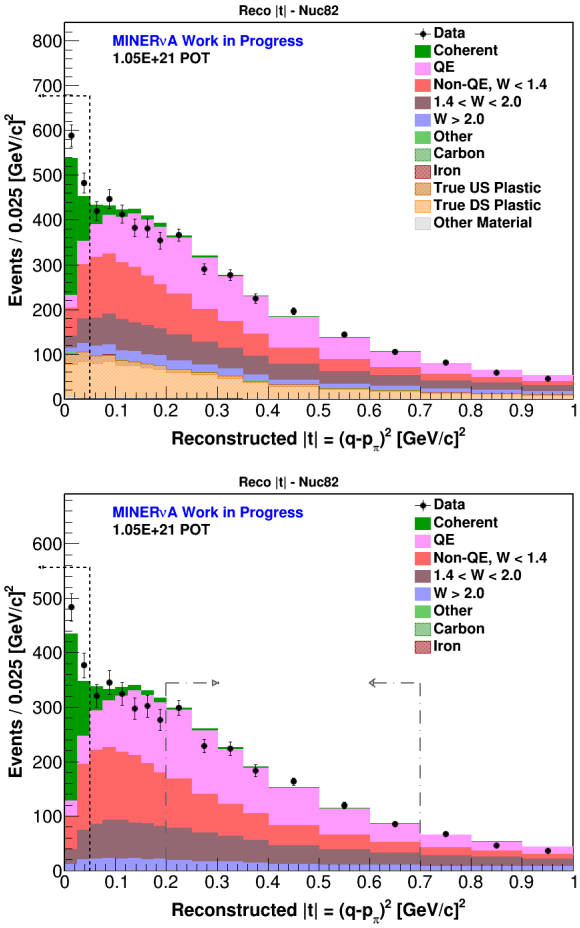

Figure 6.136: Lead $|t|$ distribution after tuning the plastic and non-coherent background (top), after subtracting the tuned plastic background from both data and MC(bottom). The shorter arrows in the bottom plot delimit the used $|t|$ sideband.

6.8 Systematic Errors

To give any meaningful result from any measurement, it is important to understand the errors associated to it. Measurements can be statistical or systematic limited, or even both. This chapter defines the sources of errors reported in the cross section for each of the four variables: E_ν, E_π, θ_π and Q^2, for all the materials under study: C, CH, Fe and Pb. The errors are obtained by applying a variation to all the error sources affecting the cross section uncertainty (see section 6.9). The variation is equal to a number of standard deviations from the best estimate (also known as central value or "cv"). In each of these variations, called "universes", the cross section and all intermediate steps involving the propagation of errors, are re-calculated (in other words, there is a cross section calculation per universe). In some universes, the overall normalization of the distributions is weighted up and down around the central value, which means that there is an uncertainty on the normalization of a distribution around the best estimate. Other universes make some events migrate to neighbor bins in the distribution, shifting the distribution left and right. All errors presented are added in quadrature, where the total fractional uncertainty δ is expressed as

$$\frac{\delta x}{|x_{best}|} = \sqrt{\sum_i \left(\frac{\delta u_i}{u_i}\right)^2} \tag{6.13}$$

where δx is the uncertainty in the x quantity, and $|x_{best}|$ is the best estimate for the measured quantity; u_i are the independent sources of error contributing to the total. The systematic uncertainties are estimated from the MC, and propagated to data when subtracting the background from it, based on the MC prediction of the background.
The errors are calculated from an error matrix called covariance matrix, defined as

$$cov_{i,j} = \frac{1}{N}\sum_k^N \left(x_{ki} - \overline{x}_i\right)\left(x_{kj} - \overline{x}_j\right) \tag{6.14}$$

where N is the number of universes, x is the variation from the central value in bin i, j due to the variation k. The error is expressed as

$$\sigma_i = \sqrt{cov_{i,j}} \tag{6.15}$$

The error can be interpreted as the average difference between each universe prediction and the central value.
To show the errors contributing to this measurement, the error summary of the Pb distribution in the $|t|$ sideband, is shown (figures 6.137 and 6.138). The error summary for all the variables in the cross sections for all materials under study, are presented in section 6.9

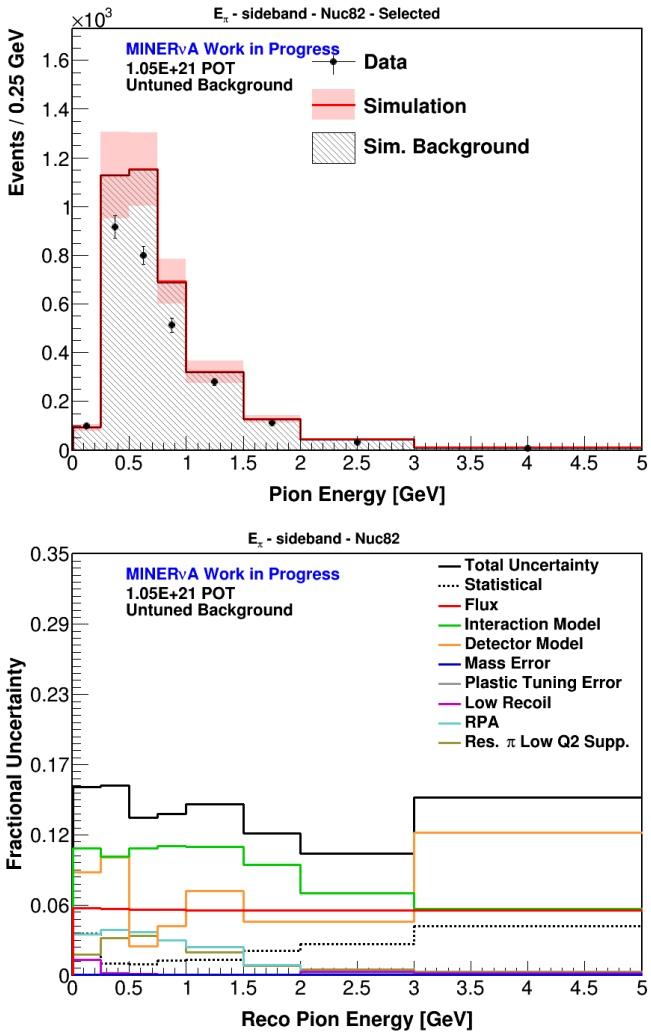

Figure 6.137: Total and fractional error summary of the E_π distribution in the $0.2 < |t| < 0.7\,(GeV/c)^2$ sideband in Pb, before tuning the background. The upper plot shows (pink-like) error band, which corresponds to the total error in each bin. Dividing the error over the best estimate (red line) in each bin, one obtains the total fractional error in the bottom plot.

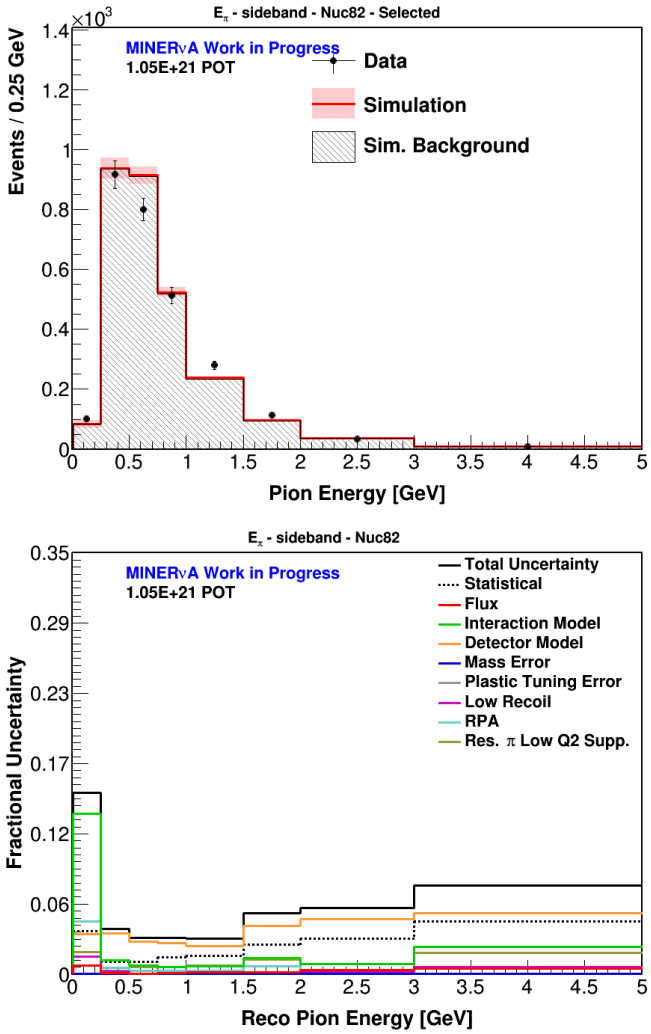

Figure 6.138: Total and fractional error summary of the Q^2 distribution in the $0.2 < |t| < 0.7\,(GeV/c)^2$ sideband in Pb, after tuning the background. The upper plot shows (pink-like) error band, which corresponds to the total error in each bin. Dividing the error over the best estimate (red line) in each bin, one obtains the total fractional error in the bottom plot.

Figure 6.139 summarizes the classification of errors relevant to this analysis. Some of them are further classified. All are explained in the next section.

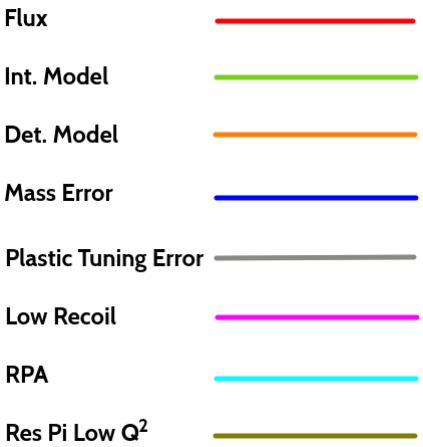

Figure 6.139: Classification of systematic errors relevant to this thesis.

6.8.1 Flux

The uncertainty on the flux of neutrinos comes from the uncertainty on the beamline parameters, which comes primarily from the uncertainty on the position of the magnets focusing the hadrons produced in the beam target, and other components of the downstream beamline (section 4.2). The other important source of uncertainty corresponds to the hadron interactions happening in the beamline, from the hadrons produced in the proton-target collision to the decay of particles producing the neutrinos. Some of those hadronic interactions have large uncertainties, and data for constraining them are scarce. The flux uncertainty is obtained using the covariance matrix in equations 6.14 and 6.15, using 100 universes. In each universe, all parameters adding up to the flux uncertainty are varied randomly and simultaneously.

6.8.2 Interaction Model

The systematic uncertainties in this group correspond to the uncertainties in the models built into GENIE version 2.12.6 [132]. The errors in this case are obtained by weighting some of the parameters used in calculating the cross section of the neutrino interactions, like the axial vector mass in QE and resonance pion production (see sections 6.1 and 3.3), and the overall normalization of the interaction. The parameters are varied also randomly $\pm 1\sigma$ around the best estimate of the parameter.

6.8.3 Detector Model

The detector model uncertainty group includes errors dependent on the detector geometry and on the interaction of the particles with the detector. These include the following uncertainties.

Muon Energy

Muon Energy. It corresponds to the uncertainty on the energy deposition by the muon track, in both MINERvA and MINOS. The uncertainty is defined as the addition in quadrature of the MINOS momentum by range uncertainty, MINOS momentum by curvature uncertainty, and the uncertainty in the energy loss inside MINERvA.

Hadron Response

Hadron Response. A test beam experiment using a downscale replica of the MINERvA detector, was used to evaluate the response to protons, pions, kaons and electrons. The hadron beamline allowed the use of particles of the desired energy, which in turn allowed to measure the response, defined like the visible energy measured in the detector divided by the energy of the incoming particle [129]. This analysis uses the uncertainty in the response to pions and protons. The error is defined as the fractional difference between the response measured and the response obtained from a GEANT4 simulation (5% for pions, 3% for protons).

Pion Inel σ, Proton Inel σ, and Neutron PathLength

These systematic uncertainties are related to the uncertainty on the interaction rate in each of the particles. It was evaluated by varying the interaction rate for each particle. For neutrons, their mean free path was varied according to their kinetic energy. The variations were determined by comparing the model predictions to hadron scattering data. For pions and protons the variations depend on the material where the interaction takes place, the particle's total path length, and the energy of the particle. The elastic part of the pion and proton cross section was not modeled.

Muon Tracking Efficiency

Muon Tracking Efficiency. This error is associated to the correction applied to account for the difference in the data and MC efficiency of the muon tracks being reconstructed

into MINOS. The correction applied is a function of the muon momentum, for which a function was obtained by fitting the ratio of the data efficiency over the MC efficiency to a 5 degree polynomial. This systematic is evaluated by adding in quadrature the error on the parameters of that function (see section 6.1).

Beam Direction

The "nominal" direction of the NuMI beam as predicted by the simulation, is going downwards at an angle of 3.4 degrees (59 mrad) with respect to the detector $\vec{z}$ axis. Given that the direction of the neutrinos cannot be directly measured, the direction of high energy muons (> 30 GeV) with low $\nu\,(E_\nu - E_\mu)$ and low Q^2 is taken as a good approximation, as in those events, the muon created are assumed to travel almost parallel to the incoming neutrino direction.
Using a sample with those characteristics, with a maximum muon energy of 120 GeV, the deviation from the nominal angle is obtained for both data and Monte Carlo. The sample is additionally divided in regions of ν, for each of these regions the mean and the sigma of the residuals are obtained. A linear fit is obtained for data and MC, and the uncertainty is defined as the difference between the data and MC fits, which is around 3 mrad [126].

6.8.4 Mass & Plastic Tuning Errors

The error due to the detector mass comes from the discrepancy between the weighted mass and the mass obtained from the model (section 5.2). The model overestimates the mass by $\sim 1\%$.
A systematic error is obtained for the tuning of the background. It is evaluated as the error on the plastic scale factors. From table 6.7, it can be seen that the errors in all three materials are below 1%.

6.8.5 Low Recoil & RPA

The systematic errors due to these weights are estimated by accounting for the difference between the central value of best estimate and one of the alternative cases where the interaction can take place, like proton and neutron combination in 2p2h processes or RPA at low or high Q^2 values.

6.8.6 Res Pi Low Q^2

The error on the suppression applied to resonant pion interactions with $Q^2 < 0.7\ (GeV/c)^2$, is defined as the difference between the best estimate for the $CC1\pi^+$ weight and its error, divided by the best estimate (see green error band in the left-hand side of figure 6.2).

6.9 Cross Section Extraction

After tuning the background, the sample is ready to start the cross section extraction. The cross section of a process, although is given in units of area, it represents the probability for the interaction to happen. This chapter presents the steps the background-tuned data sample is taken through, to obtain the total cross section of the CC ν_μ-induced coherent π^+ production, and differential cross sections for the pion energy, pion angle and the squared of the four-momentum transferred to the hadronic system (Q^2); using carbon, hydrocarbon, iron and lead targets.
The tuned background is subtracted from the selected sample; the remaining signal candidate events are unfolded (events reconstructed in the wrong bin are moved back to their true bin according to the model); the unfolded distributions are then corrected for efficiency, flux and by number of target nuclei in each material.
The total cross section is calculated as

$$\sigma_i = \beta \frac{\sum_j U_{ij} \left(N_j^{DATA} - N_j^{BKGD} \right)}{\epsilon_i \phi_i T} \tag{6.16}$$

where β is a correction factor for interactions happening on other nuclei, different than the material under study; U_{ij} is the ij element of the unfolding matrix; N_j^{DATA} is the number of data events in the reconstructed bin j, after applying all the selection cuts; N_j^{BKGD} is the number of tuned background events in the reconstructed bin j after applying all the selection cuts; ϵ is the efficiency in the true bin i after applying all the cuts; ϕ_i is the neutrino flux (number of neutrinos per cm^2) in bin i; and T is the number of target nuclei in the fiducial volume.

The differential cross section is calculated like

$$\left(\frac{d\sigma}{dx} \right)_i = \beta \frac{\sum_j U_{ij} \left(N_j^{DATA} - N_j^{BKGD} \right)}{\epsilon_i \Phi T \left(\Delta x \right)_i} \tag{6.17}$$

where Φ is the flux integrated (from 2-20 GeV), and $(\Delta x)_i$ is the width of the i^{th} bin.

6.9.1 Background-Tuned Selected Sample

The selected sample in the four variables, and four materials of interest, is shown after all background has been tuned (plastic and non-coherent in the passive targets, and non-coherent only in the hydrocarbon target).

In some bins, in some distributions, the predicted tuned background is higher than the data. This happens in the θ_π distribution in all four materials, which points to a defect in the Rein-Sehgal model, in the prediction of θ_π larger than $\sim 40°$. In other variables, this issue seems to be material-dependent. This is very likely due to the fact that eve though some of the weights applied during the MC reweighing process (section 6.1.1) are based in $\nu - C$ interactions, are also applied to $\nu - Fe$ and $\nu - Pb$ interactions. Unfortunately, there are no similar studies available for Fe and Pb. The possibility of using ad-hoc weights for this materials, using an extrapolation process, has been considered (see chapter 7).

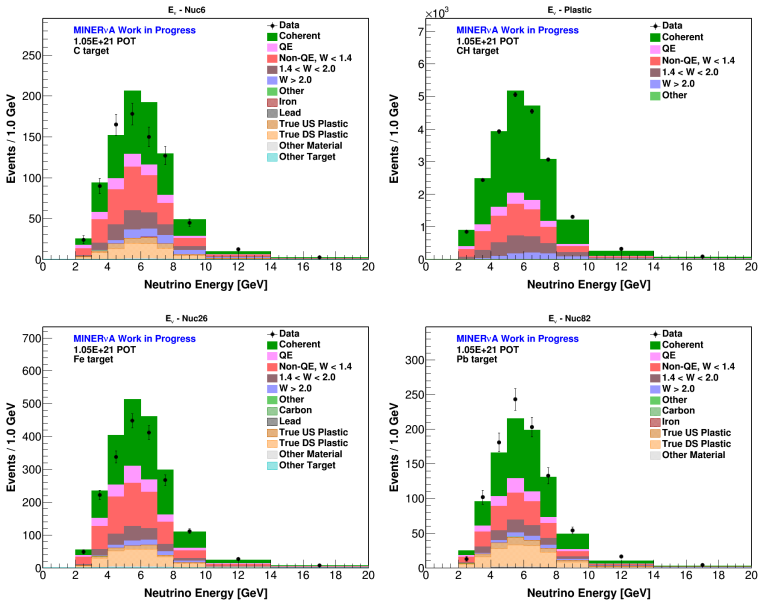

Figure 6.140: E_ν distribution in all four targets with all backgrounds tuned.

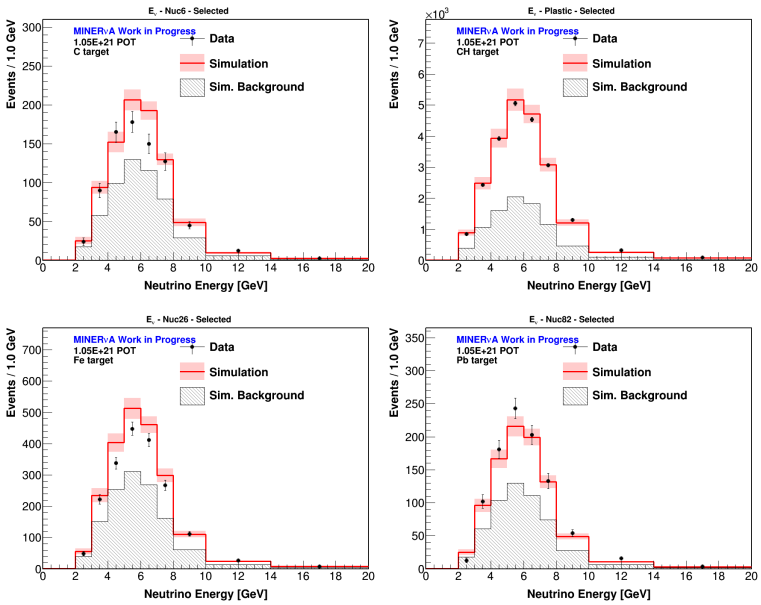

Figure 6.141: E_ν distribution in all four targets with all backgrounds tuned, and systematic error band in the MC.

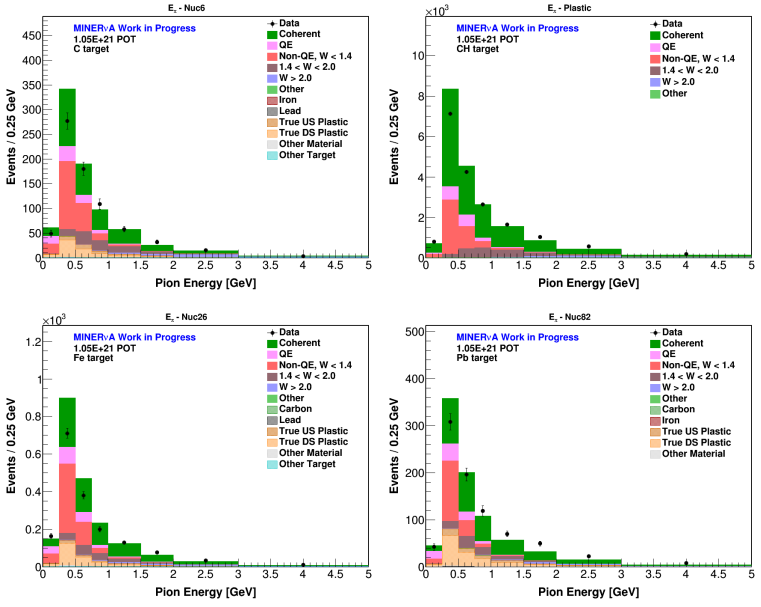

Figure 6.142: E_π distribution in all four targets with all backgrounds tuned.

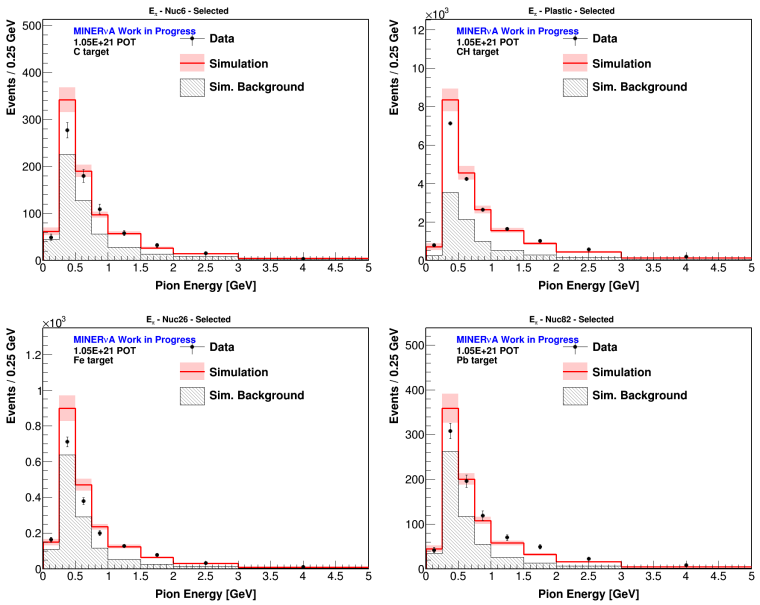

Figure 6.143: E_π distribution in all four targets with all backgrounds tuned, and systematic error band in the MC.

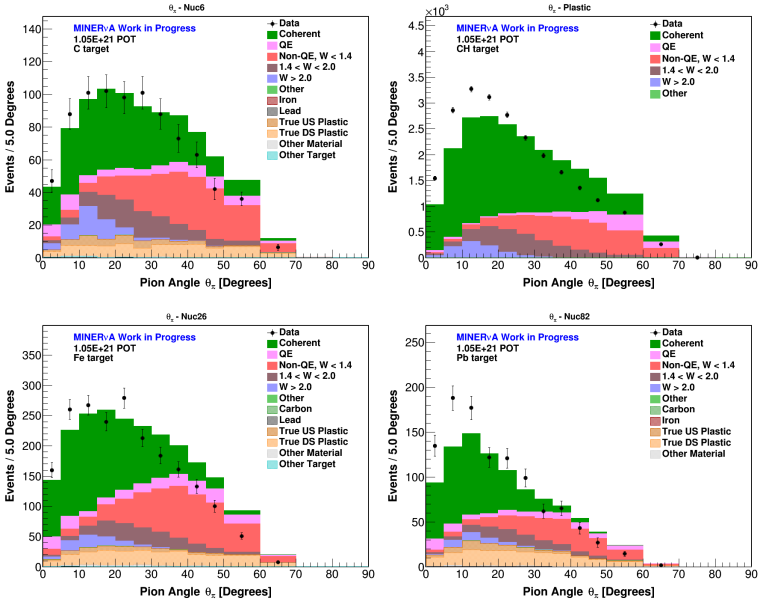

Figure 6.144: θ_π distribution in all four targets with all backgrounds tuned.

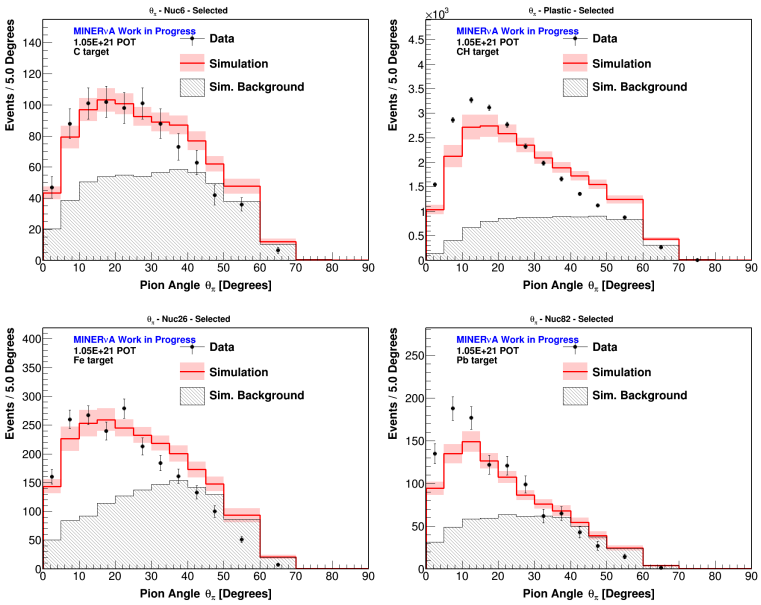

Figure 6.145: θ_π distribution in all four targets with all backgrounds tuned, and systematic error band in the MC.

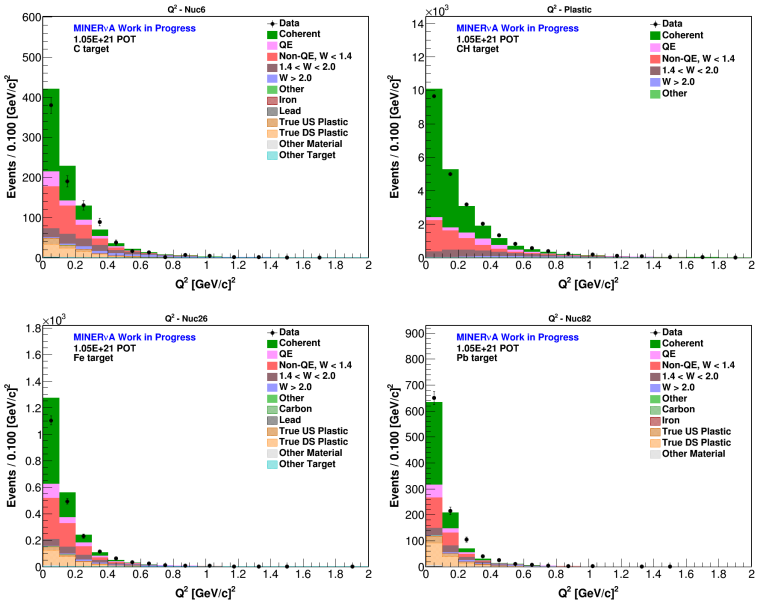

Figure 6.146: Q^2 distribution in all four targets with all backgrounds tuned.

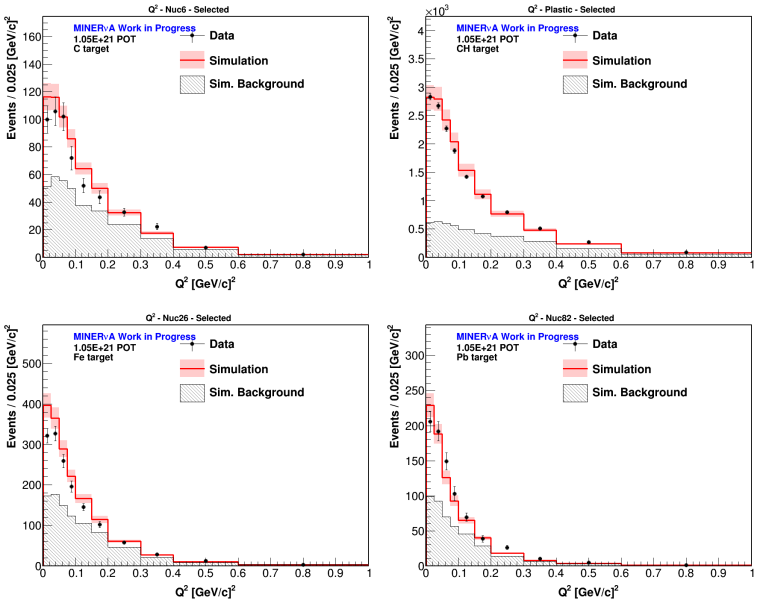

Figure 6.147: Q^2 distribution in all four targets with all backgrounds tuned, and systematic error band in the MC.

6.9.2 Background-Subtracted Sample

All the tuned background in section 6.9.1 is subtracted from the selected sample. The non-coherent background is subtracted from the CH target, while both the plastic and non-coherent backgrounds are subtracted from the C, Fe and Pb targets. Using equation 6.16, the background is subtracted bin by bin using the expression $N_j^{DATA} - N_j^{BKGD}$. Where N_j^{BKGD} includes plastic and non-coherent, as the case may be

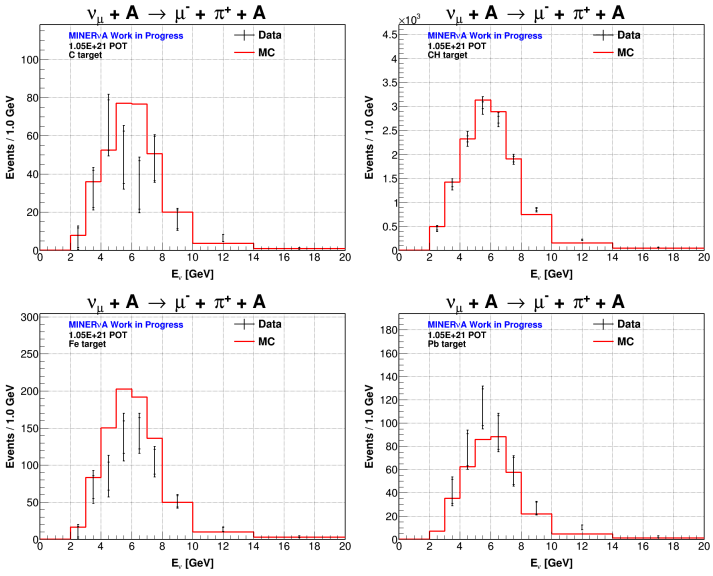

Figure 6.148: E_ν background-subtracted distribution in all four targets. The inner error bands are the statistical errors, and the outer, are the total (statistical + systematic) errors.

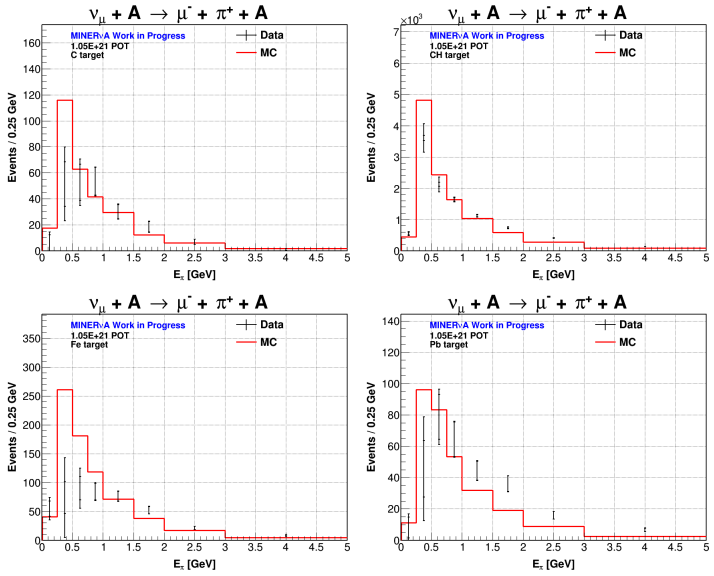

Figure 6.149: E_π background-subtracted distribution in all four targets. The inner error bands are the statistical errors, and the outer, are the total (statistical + systematic) errors.

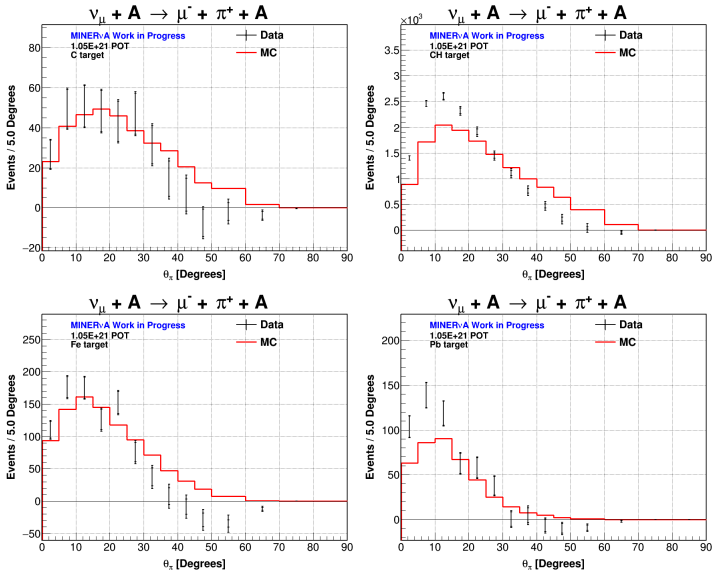

Figure 6.150: θ_π background-subtracted distribution in all four targets. The inner error bands are the statistical errors, and the outer, are the total (statistical + systematic) errors.

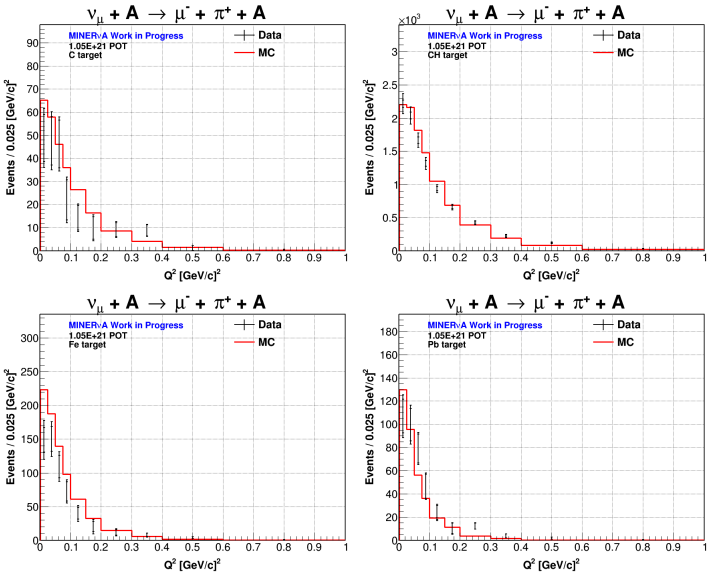

Figure 6.151: Q^2 background-subtracted distribution in all four targets. The inner error bands are the statistical errors, and the outer, are the total (statistical + systematic) errors.

6.9.3 Unfolding

During the reconstruction process, some events get reconstructed into the wrong bin. The reconstructed sample is said to be "smeared" because of this. The sample then needs to be "unsmeared" or "unfolded" (which are equivalent terms) to recover the underlying "true" distribution[3] An unfolding matrix (see odd-number figures in this section) is built with the reconstructed and true quantities in the X and Y axes, respectively. Events off the main diagonal are the ones that where reconstructed into the wrong bin. The matrix is normalized by the number of events in a row

$$U_{ij} = \frac{N_{ij}^{sel}}{\sum_j N_{ij}^{sel}} \tag{6.18}$$

where i and j are the true and reco bins, respectively; N^{sel} are the number of events passing all the cuts in a given ij bin.
The unfolding matrix is then obtained by using Bayes' theorem as implemented by D'Agostini [154]. The unfolded data is then given by

$$\vec{d}_{unfold} = \vec{d}_{subtracted} \times U \tag{6.19}$$

where $\vec{d}_{unfold}$ and $\vec{d}_{subtracted}$ are vectors formed with the bins of the background-subtracted and unfolded data distributions; and U is the unfolding matrix. The unfolding matrix depends on the true distribution of the variable predicted by the model as the initial probability. The unfolded data obtained is used as the initial probability in further iterations, until the shape of a mock data used in an unfolding study, agrees with its true distribution by less than 1σ (appendix B). From that same study, the optimal number of iterations is obtained for each variable in each material. Table 6.9 shows the number of iterations used to unfold all four variables in all four materials.

Figures 6.153 to 6.159 (even numbers) show the unfolded data after taking it through the number of iterations indicated in table 6.9.

[3]The underlying true distribution is obtained from the model, which is the best estimate available.

Material/Variable	E_ν	E_π	θ_π	Q^2
C	2	2	1	2
CH	2	3	3	2
Fe	2	3	2	2
Pb	1	2	2	2

Table 6.9: Number of iterations obtained from the unfolding study in appendix B for each variable, for each material.

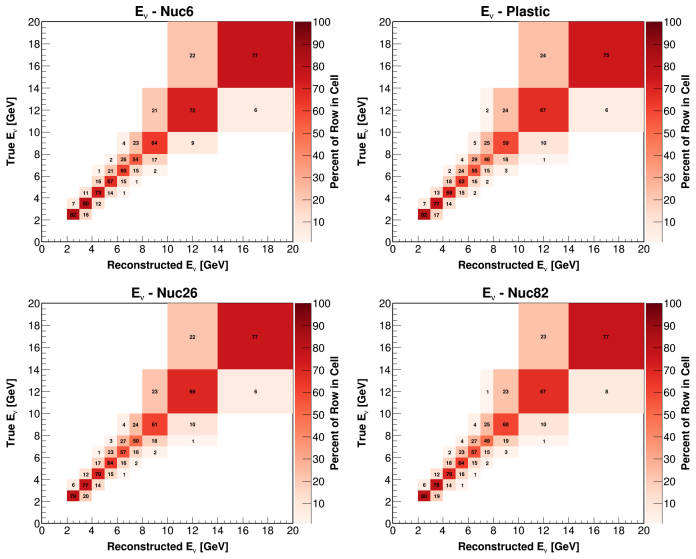

Figure 6.152: E_ν Normalized migration matrix in all four targets.

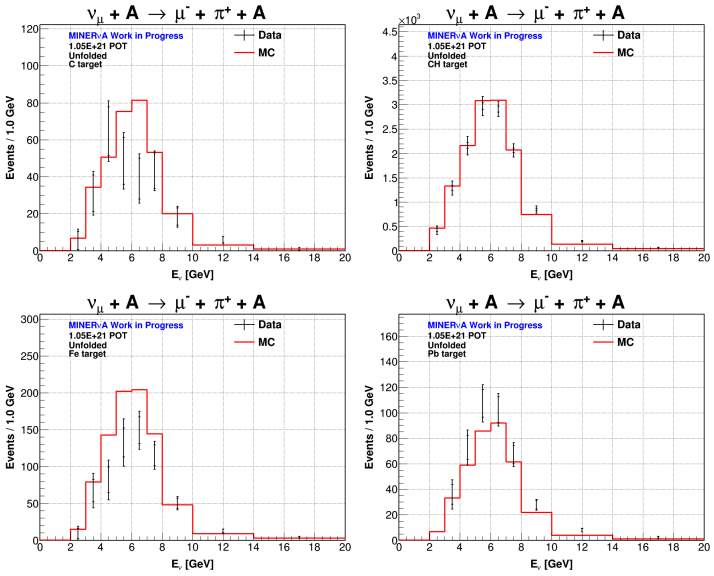

Figure 6.153: E_ν Unfolded distribution in all four targets. The inner error bands are the statistical errors, and the outer, are the total (statistical + systematic) errors.

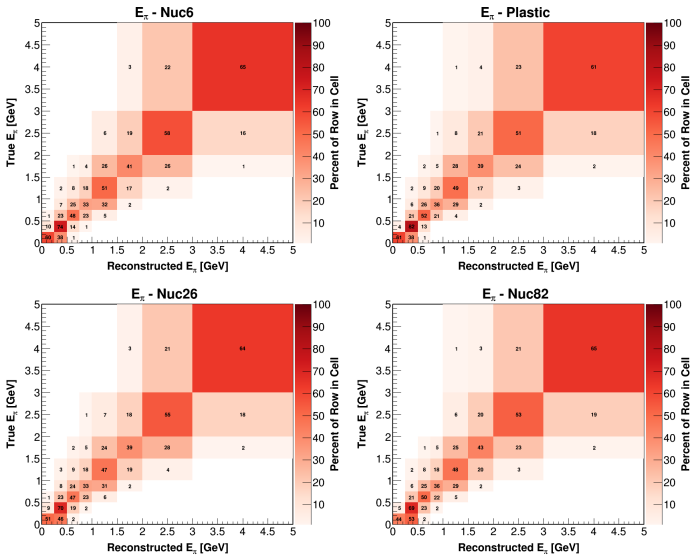

Figure 6.154: E_π Normalized migration matrix in all four targets.

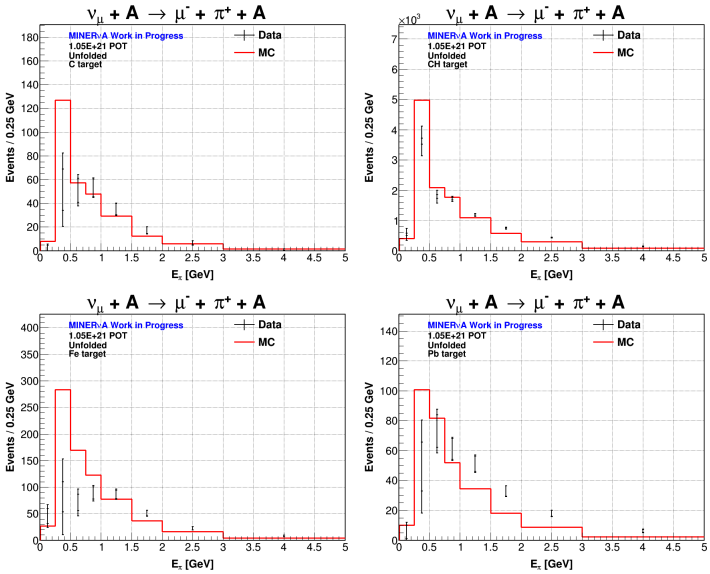

Figure 6.155: E_π Unfolded distribution in all four targets. The inner error bands are the statistical errors, and the outer, are the total (statistical + systematic) errors.

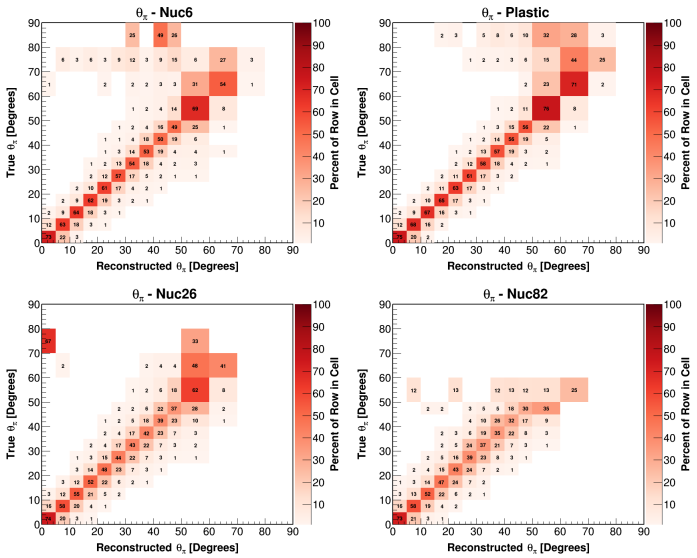

Figure 6.156: θ_π Normalized migration matrix in all four targets.

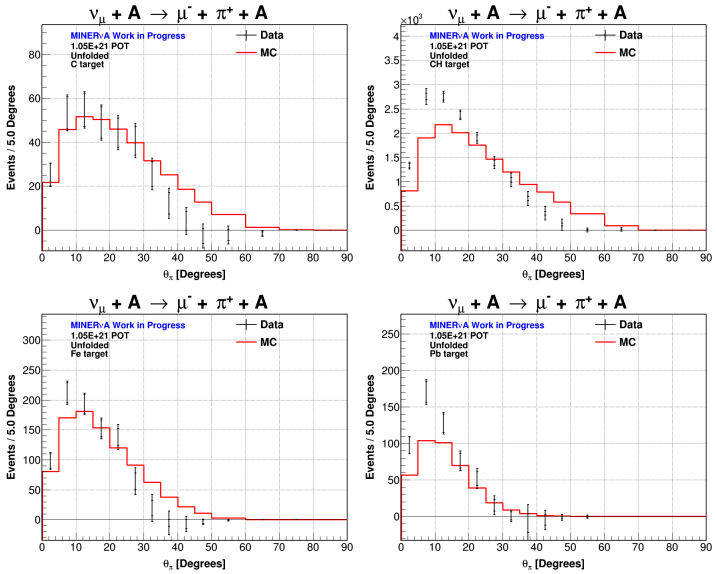

Figure 6.157: θ_π Unfolded distribution in all four targets. The inner error bands are the statistical errors, and the outer, are the total (statistical + systematic) errors.

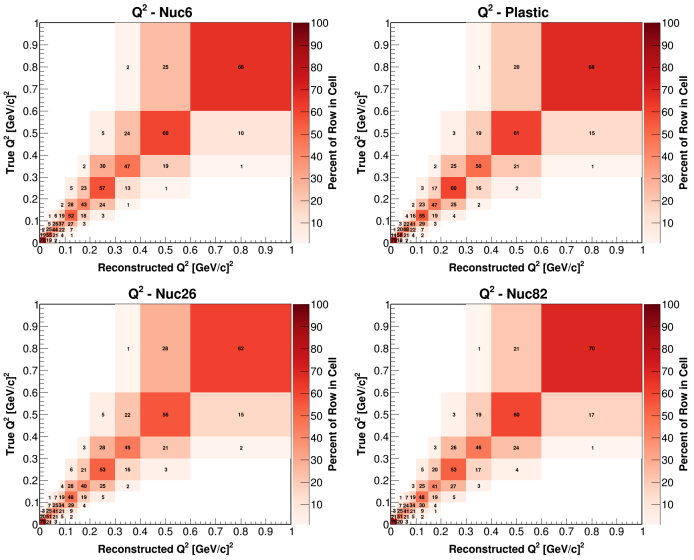

Figure 6.158: Q^2 Normalized migration matrix in all four targets.

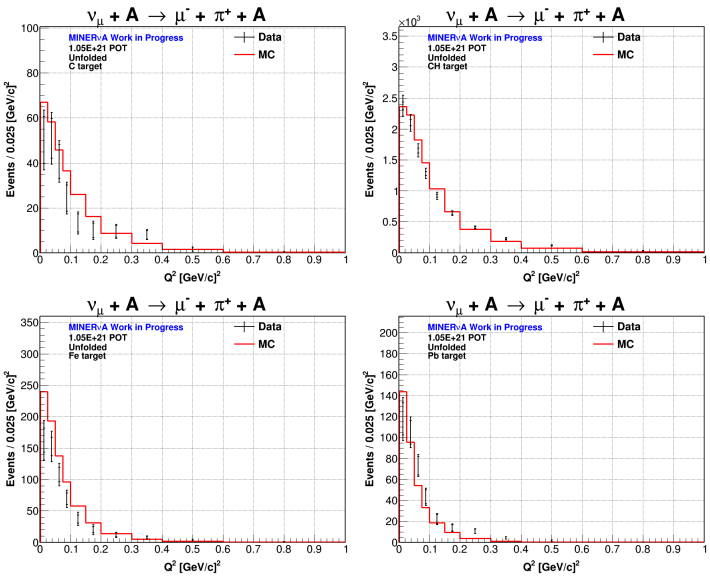

Figure 6.159: Q^2 Unfolded distribution in all four targets. The inner error bands are the statistical errors, and the outer, are the total (statistical + systematic) errors.

6.9.4 Efficiency and Acceptance Correction

The efficiency distributions in figures 6.160 to 6.166 (odd numbers) where obtained after applying all the selection cuts, defined as

$$\epsilon_i = N_i^{sel}/N_i^{gen} \tag{6.20}$$

where N_i^{sel} and N_i^{gen} are the events selected after all the cuts and the true generated signal events within the fiducial volumes, and with $2 < E_\nu < 20$ GeV.
The passive targets are clearly more affected by the MINOS acceptance, due to the fact that they are farther away from it. Signal events where the pion gets absorbed inside the passive material also present a reduction in their efficiency. The tracking algorithm restricts the pion angle to be smaller than 70° in all materials. The muon track is constrained to smaller angles ($\lesssim 20°$).
Figures 6.161 to 6.167 show the unfolded distributions after being corrected by their efficiency distribution, according to equations 6.16 and 6.17.

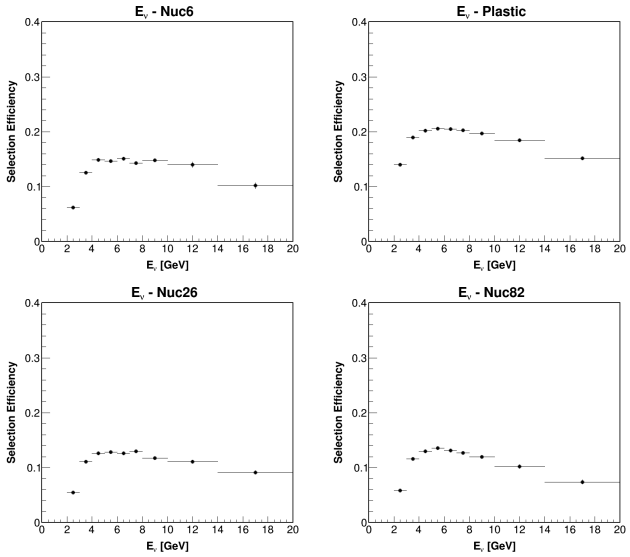

Figure 6.160: E_ν Efficiency distribution after the $|t|$ cut, in all four targets.

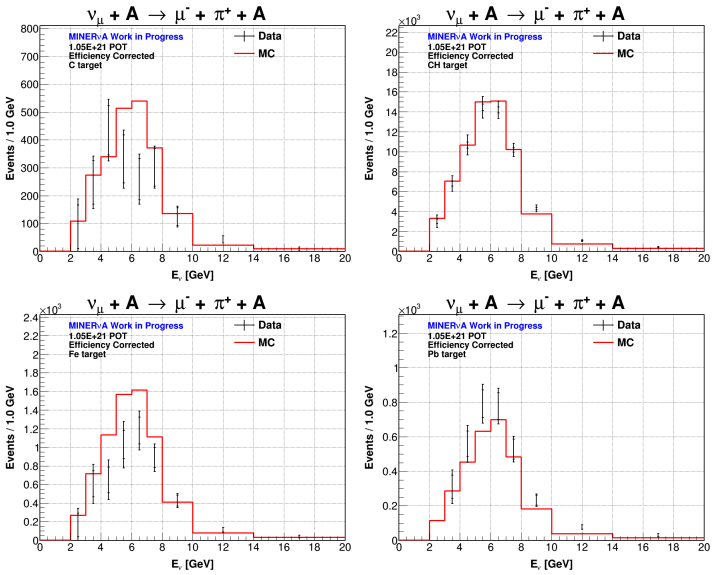

Figure 6.161: E_ν Efficiency-corrected distribution in all four targets. The inner error bands are the statistical errors, and the outer, are the total (statistical + systematic) errors.

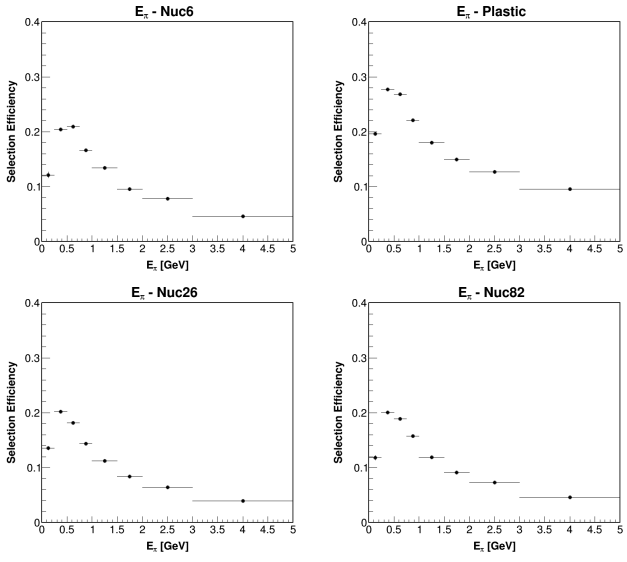

Figure 6.162: E_π Efficiency distribution after the $|t|$ cut, in all four targets.

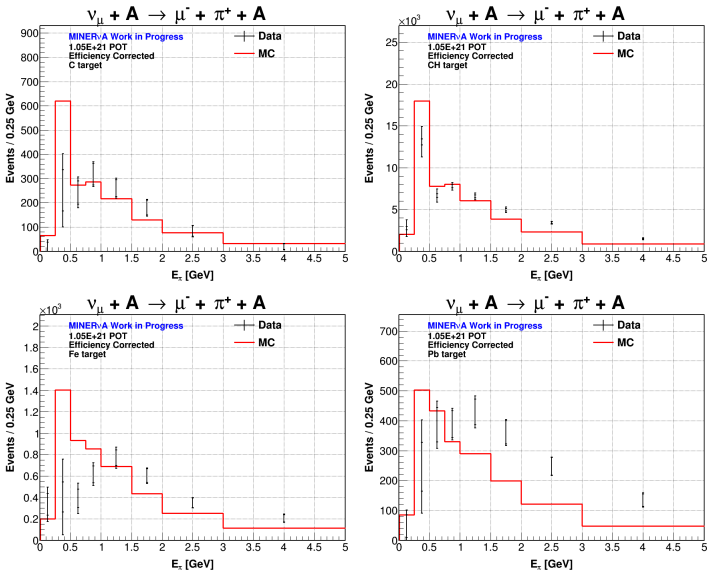

Figure 6.163: E_π Efficiency-corrected distribution in all four targets. The inner error bands are the statistical errors, and the outer, are the total (statistical + systematic) errors.

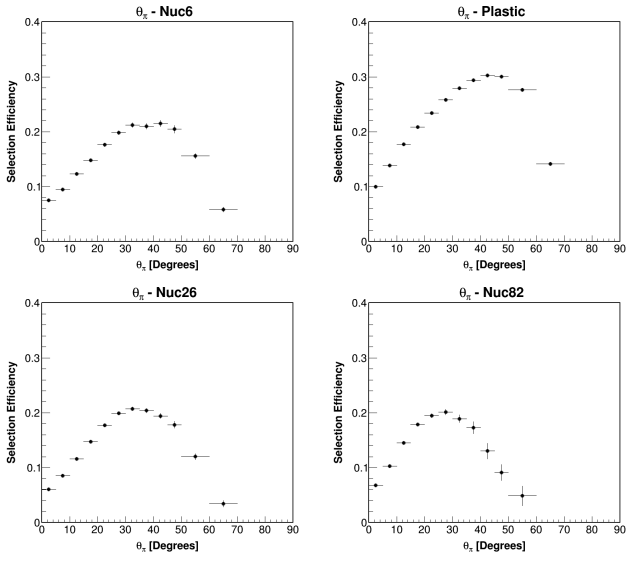

Figure 6.164: θ_π Efficiency distribution after the $|t|$ cut, in all four targets.

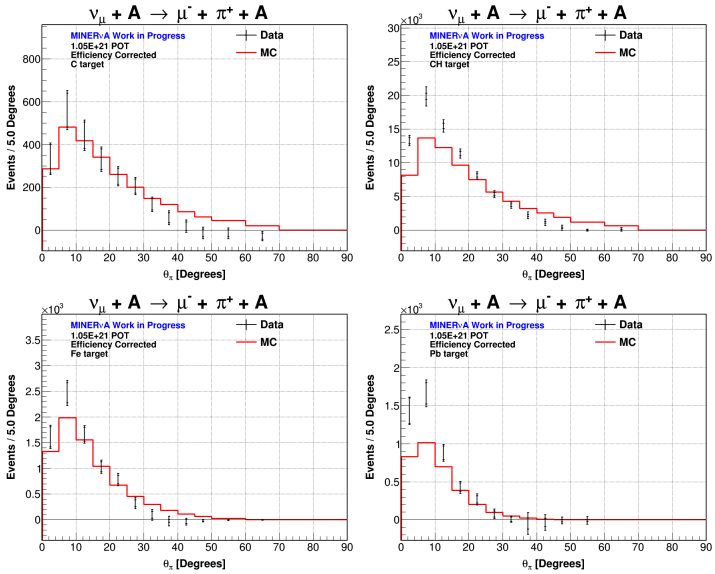

Figure 6.165: θ_π Efficiency-corrected distribution in all four targets. The inner error bands are the statistical errors, and the outer, are the total (statistical + systematic) errors.

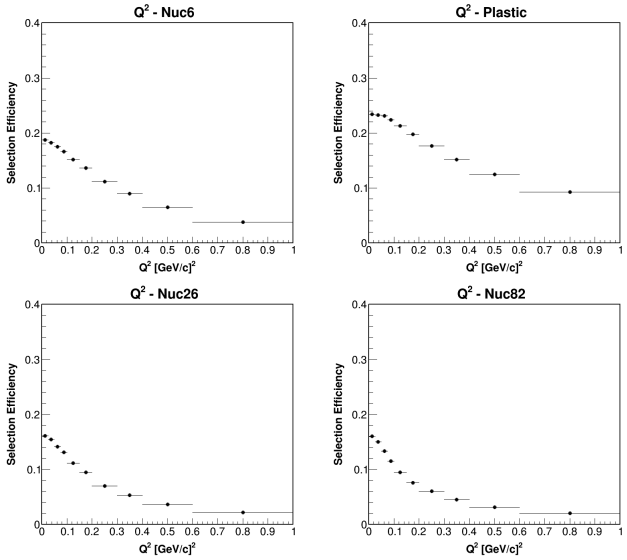

Figure 6.166: Q^2 Efficiency distribution after the $|t|$ cut, in all four targets.

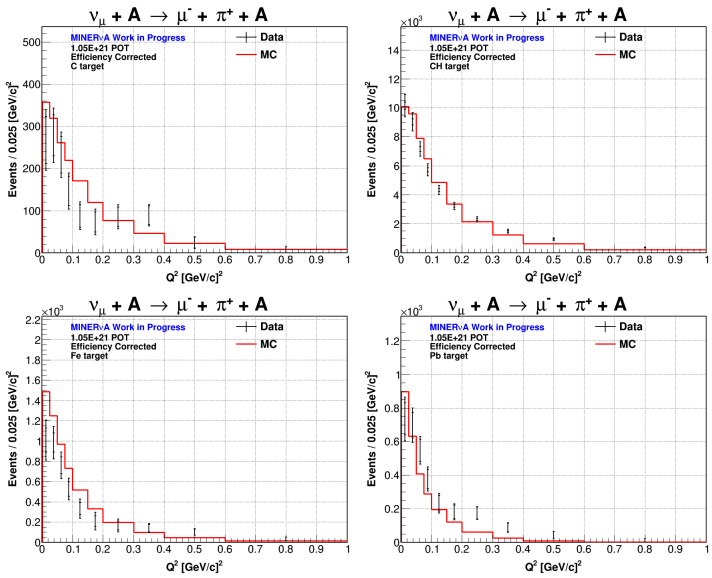

Figure 6.167: Q^2 Efficiency-corrected distribution in all four targets. The inner error bands are the statistical errors, and the outer, are the total (statistical + systematic) errors.

6.9.5 Target and Flux Normalization

Finally, in the cross section expressions 6.16 and 6.17, the efficiency-corrected samples are divided by the flux and the integrated flux, respectively. The flux is expressed in number of neutrinos per unit area, per protons delivered to the beam target $\left(\nu/m^2/POT\right)$. Figure 6.168 shows the ME neutrino flux used by MINERvA.

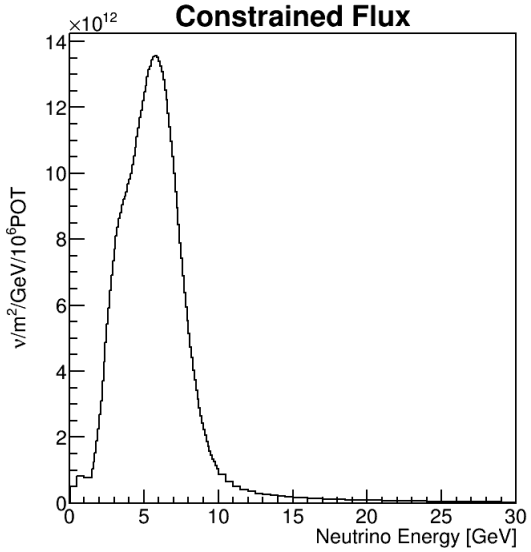

Figure 6.168: ν_μ flux after being constrained using the $\nu + e$ scattering sample (see section 4.2).

This analysis uses a re-binned version of the flux (figure 6.169), to match it with the bin pattern in the neutrino energy distribution.

The $\sigma\left(E_\nu\right)$ is normalized by the flux integrated in every bin. All differential cross sections in E_π, θ_π, and Q^2 are normalized by the flux integrated from 2 to 20 GeV. The flux is then multiplied by the number of protons on target to obtain the total number of neutrinos during the whole data taking period. m^2 are changed to cm^2, and finally the flux is expressed as number of ν/cm^2.

Given that in a CC coherent interaction, the neutrino scatters off the whole nucleus, one also needs to divide by the number of nuclei present in the fiducial volume, to obtain a final cross section per nuclei. The number of targets T in equations 6.16 and 6.17 were already given for each material in table 6.2. The C and Pb target have less than 1% contribution from other materials. The contribution from other materials to the CH and Fe targets is specified in table (6.10).

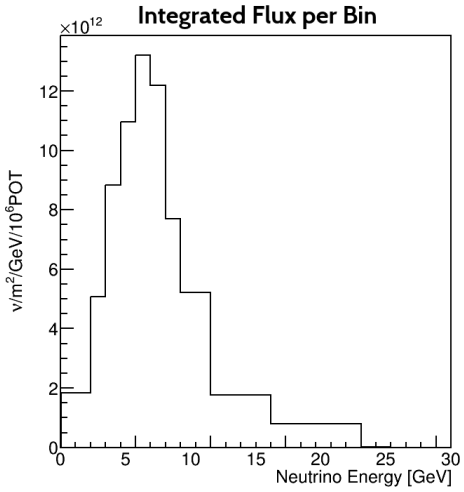

Figure 6.169: Re-binned version of the constrained flux. The bins have been re-arranged to match the neutrino energy distribution bin pattern.

Nucleus in CH target	% of Total Mass	A	T
^{1}H	7.4	1.008	2.425×10^{29}
^{12}C	87.6	12.011	2.404×10^{29}
^{16}O	3.2	15.999	6.548×10^{27}
^{27}Al	0.26	26.982	3.175×10^{26}
^{28}Si	0.27	28.085	3.167×10^{26}
^{35}Cl	0.55	35.453	5.511×10^{26}
^{48}Ti	0.69	47.867	4.749×10^{26}
Nucleus in Fe targets	% of Total Mass	A	T
^{12}C	0.13	12.011	6.137×10^{25}
^{26}Fe	98.7	55.845	1.016×10^{28}
^{28}Si	0.2	28.085	4.038×10^{25}
^{55}Mn	1.0	54.938	1.032×10^{26}

Table 6.10: Mass fraction, mass number A, and number of nuclei from all materials present in the CH and Fe targets. included for every material.

The β factor in the cross section expressions is defined as the number of coherent interactions in the material under study in the fiducial volume of a given target, over the total number of interactions in the same fiducial volume of that target

$$\beta = \left(N_M^{coh}/N^{coh}\right) = \frac{\phi\epsilon_M\sigma_M T_M}{\sum_i \phi\epsilon_i\sigma_i T_i} \approx \frac{A_M^{1/3}T_M}{\sum_i A_i^{1/3}T_i} \tag{6.21}$$

where ϕ_M, ϵ_M, σ_M and T_M are the flux, efficiency, cross section and number of nuclei in each material due to C in the CH target, and due to Fe in the Fe targets; M is either C of Fe. The same quantities with the i sub index, correspond to the remaining materials in the same target. The assumption of equal efficiency in all materials has been made. Also the cross section has been supposed to scale as $A^{1/3}$ for the sake of consistency with the previous MINERvA LE analysis of CC coherent pion production [7]. Using table 6.10, $\beta_{CH} = 0.962$ and $\beta_{Fe} = 0.983$ are obtained. The cross sections in the pure C and Pb targets are not scaled.

6.10 Cross Section Results

Having tuned and subtracted the plastic and non-coherent background; unfolding the non-background sample to correct for events reconstructed in the wrong bin; correcting for efficiency (to account for all signal events removed in each of the selection cuts); normalizing by the flux and number of nuclei in the proper target and material; the measured total cross sections $\sigma(E_\nu)$ and differential cross sections $d\sigma/dE_\pi$, $d\sigma/d\theta_\pi$ and $d\sigma/dQ^2$ from C, CH, Fe and Pb are presented in figures 6.170 to 6.173.

The measurement in the C target represents the first measurement made on a target purely made of this material. Previous cross section measurements off carbon were made on targets having some non-negligible fraction of other elements (see chapter 3). The cross sections in the CH target represent the highest statistical sample of this interaction until now. While the cross sections from Fe and Pb are the first measured cross sections of CC coherent pion production by neutrinos in these materials.

6.10.1 Visual Comparison of the CH Cross Sections to the LE Results

The cross section results in this thesis (ME measurement) out of the CH target and those obtained previously by the MINERvA collaboration in a lower energy beam (LE measurement) from the same target, are compared in this section. Although different fluxes were used, the flux integration regions overlap, and both measurements were flux-normalized, and they are expected to be very similar. This analysis used a slightly different binning to the one used in the LE analysis. During the ME run, the number of protons on target was more than 3 times higher, and the number of signal candidate events increased almost 8 times. Figures 6.174 to 6.177 give a visual comparison of the four cross section variables in the CH target.

The cross sections in the ME analysis are slightly larger, but besides the θ_π distribution, most of the bins total errors overlap.

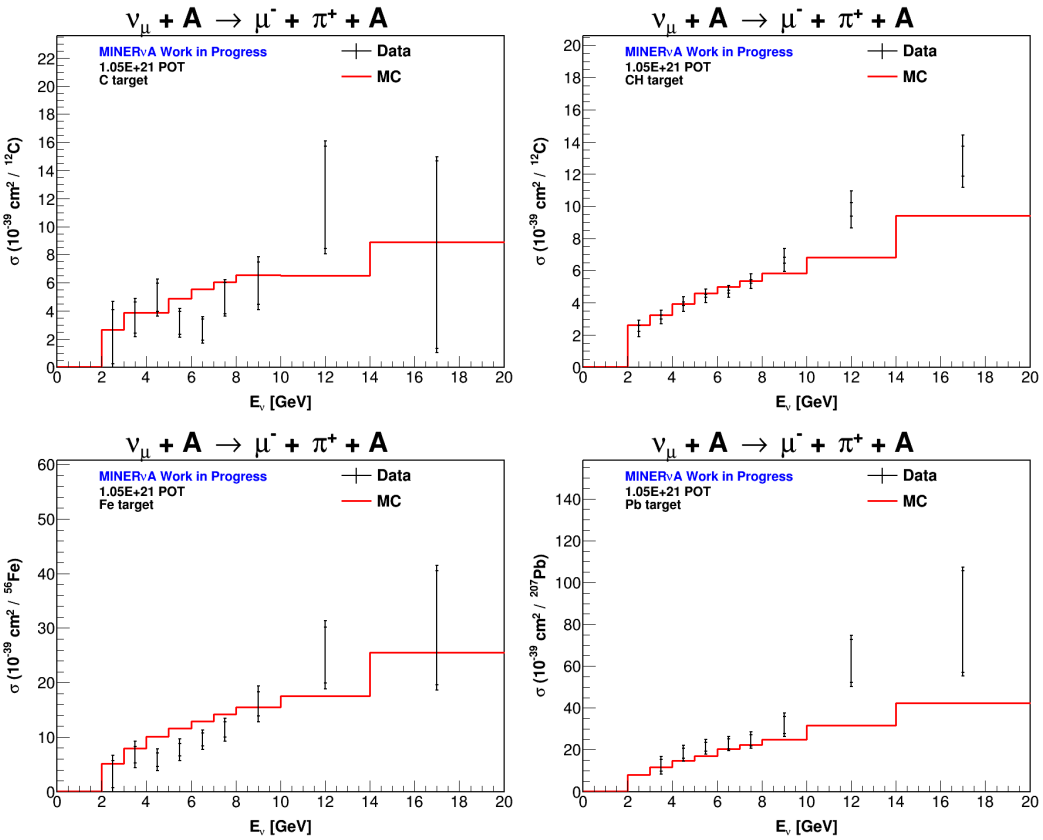

Figure 6.170: E_ν total cross section $\sigma(E_\nu)$ in the C, CH, Fe and Pb targets. The inner and outer error bars are the statistical and total (statistical + systematic) errors.

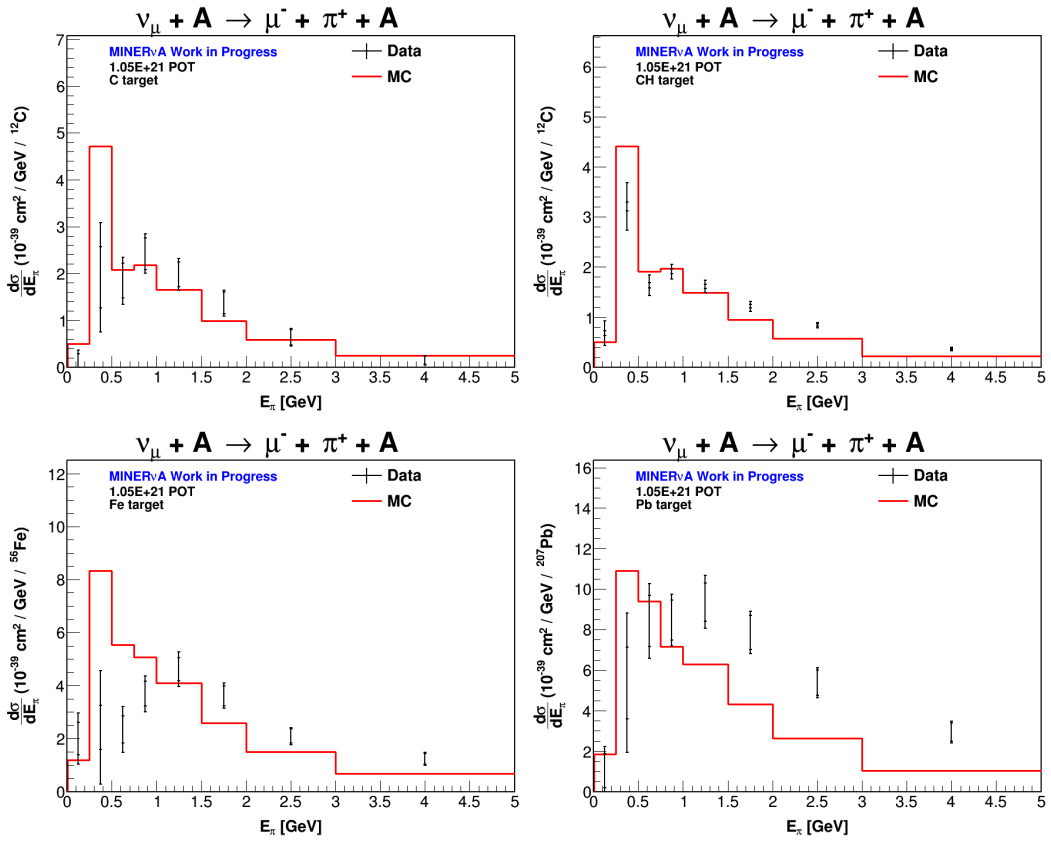

Figure 6.171: E_π differential cross section $d\sigma/dE_\pi$ in the C, CH, Fe and Pb targets. The inner and outer error bars are the statistical and total (statistical + systematic) errors.

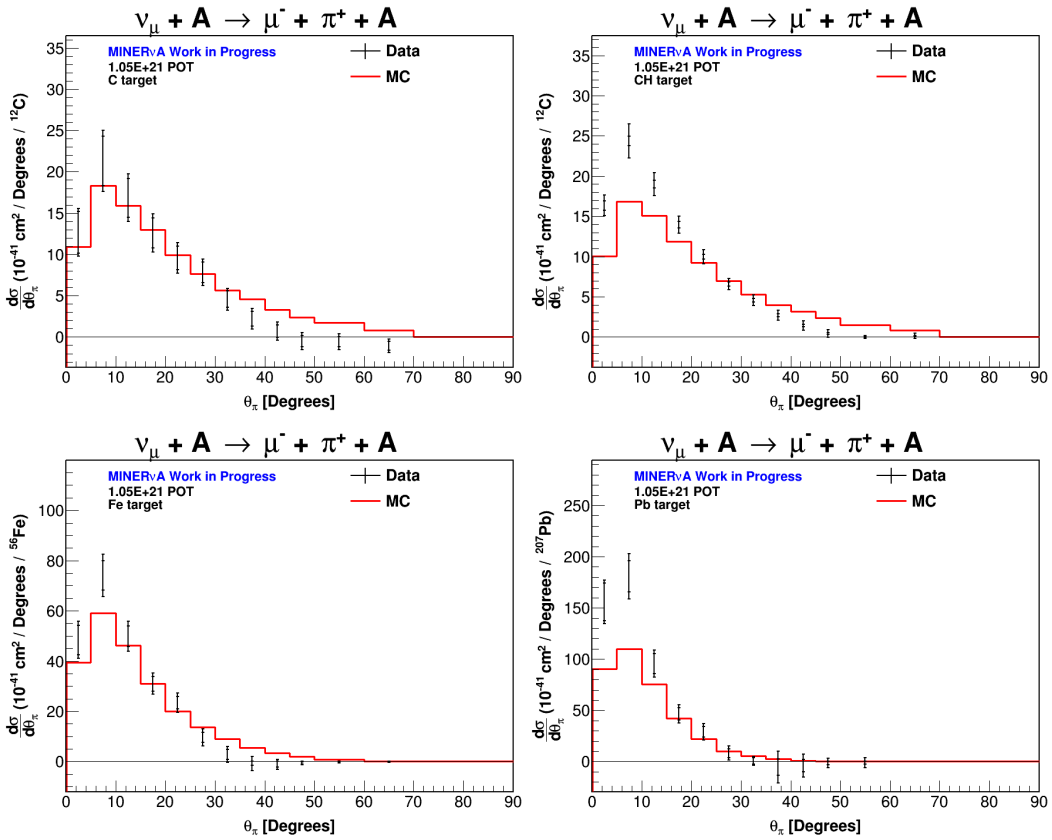

Figure 6.172: θ_π differential cross section $d\sigma/d\theta_\pi$ in the C, CH, Fe and Pb target. The inner and outer error bars are the statistical and total (statistical + systematic) errors.

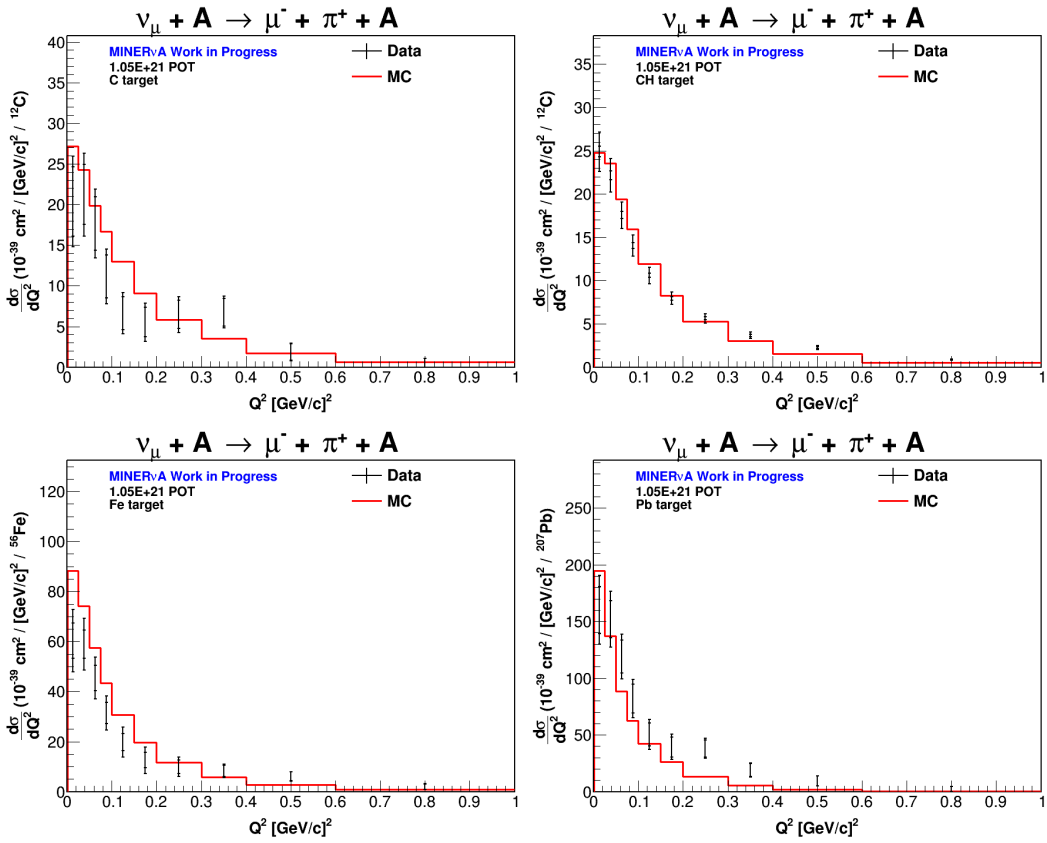

Figure 6.173: Q^2 differential cross section $d\sigma/dQ^2$ in the C, CH, Fe and Pb targets. The inner and outer error bars are the statistical and total (statistical + systematic) errors.

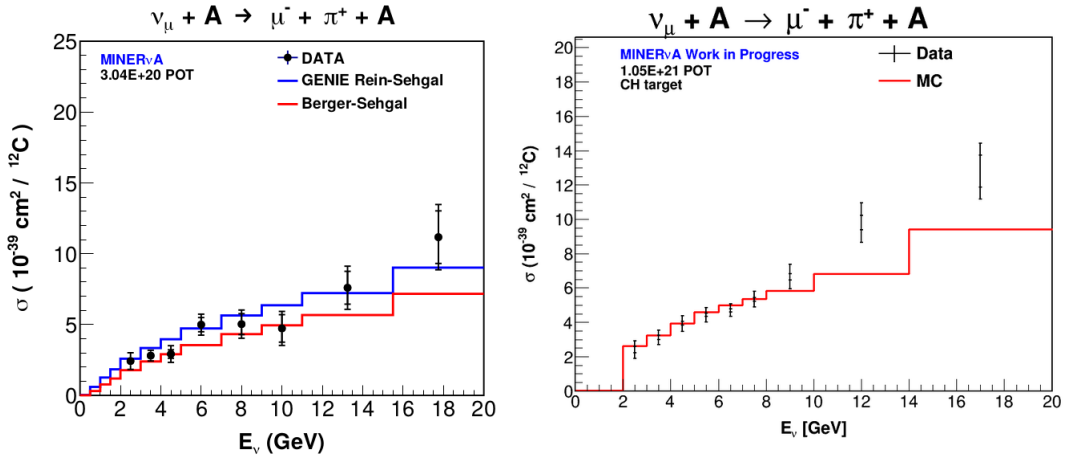

Figure 6.174: $\sigma\left(E_\nu\right)$ in the CH target. The left-hand side plot is the LE cross section. The blue histogram corresponding to the Rein-Sehgal model, is the same model used in this analysis (right plot).

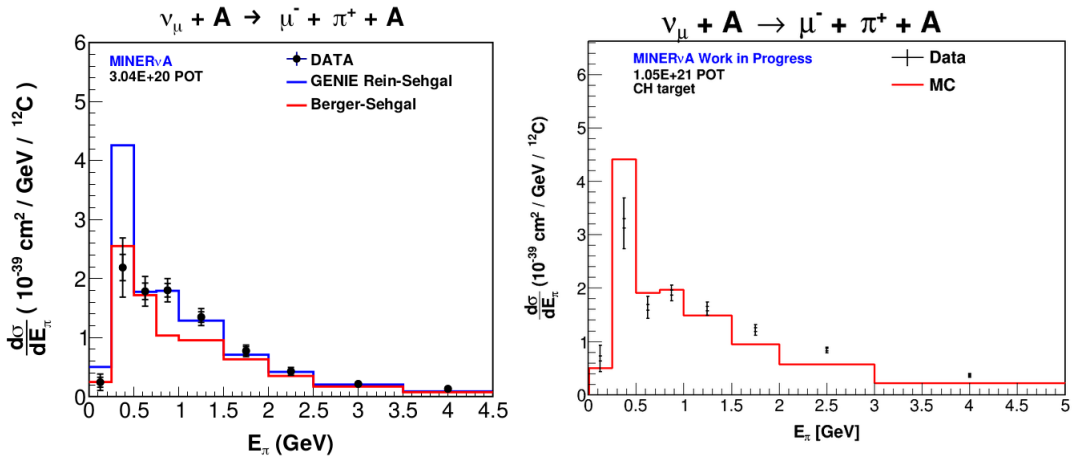

Figure 6.175: $d\sigma/dE_\pi$ in the CH target. The left-hand side plot is the LE cross section. The blue histogram corresponding to the Rein-Sehgal model, is the same model used in this analysis (right plot).

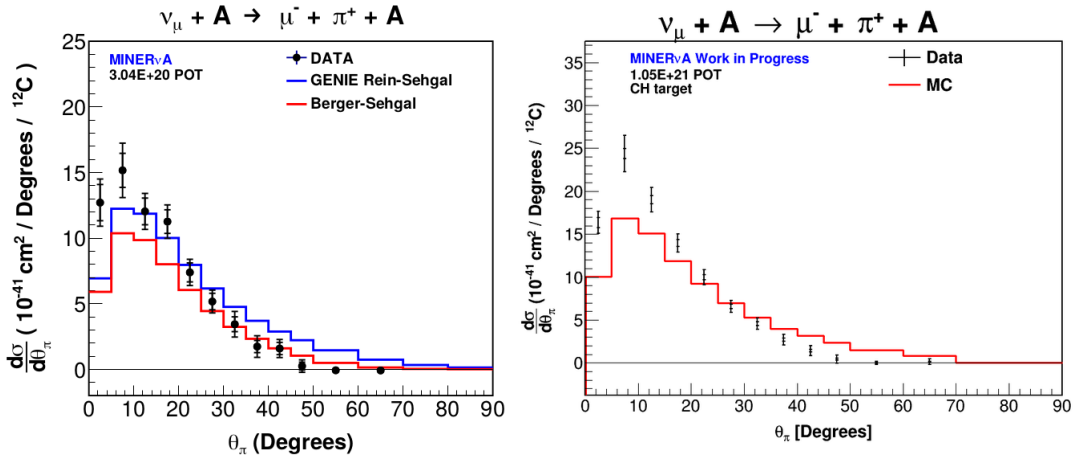

Figure 6.176: $d\sigma/d\theta_\pi$ in the CH target. The left-hand side plot is the LE cross section. The blue histogram corresponding to the Rein-Sehgal model, is the same model used in this analysis (right plot).

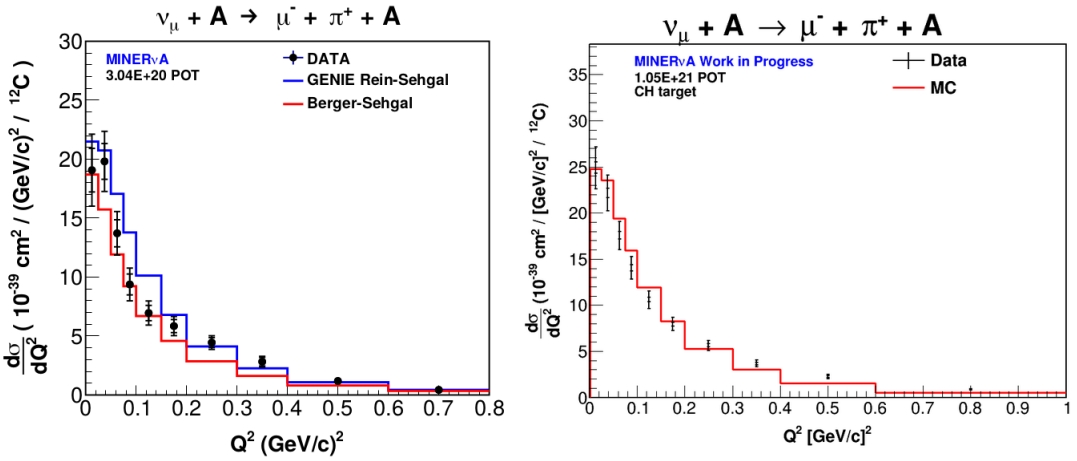

Figure 6.177: $d\sigma/dQ^2$ in the CH target. The left-hand side plot is the LE cross section. The blue histogram corresponding to the Rein-Sehgal model, is the same model used in this analysis (right plot).

6.11 Cross Section Error Summary

This section summarizes the errors in measuring the total $\sigma(E_\nu)$ cross section and E_π, θ_π and Q^2 differential cross sections, in the C, CH, Fe and Pb targets. The error breakdown in the following plots corresponds to the same introduced in section 6.8, but propagated to the cross section. The measurement in the passive material have larger errors because of smaller statistics, and the use of C data to apply weights to the MC model, in iron and lead targets, due to the non-availability of Fe or Pb data.
The dominant error in the E_ν cross sections is the detector model uncertainty, which is dominated by the hadron response uncertainty [4] and the flux, at low and high neutrino energies, respectively.
In the $d\sigma/dE_\pi$ cross section, the dominant error is again the detector model, with important contributions from the interaction model (GENIE systematic errors).
The $d\sigma/d\theta_\pi$ cross section has the flux as its larger error at low angles. It is hard to tell at higher angles, given that as the cross section approaches zero, the fractional uncertainty becomes meaningless.
The $d\sigma/dQ^2$ differential cross section is dominated almost equally by the flux, detector model and interaction model uncertainties.
In all passive targets, the error summary is always statistical dominated. This is understood, given the difference in fiducial mass compared with the hydrocarbon target. Also, as the nuclear radius gets bigger for heavier elements (like those in the passive targets), the number of nuclei targets available for the neutrinos to scatter off, gets reduced. The background events also increase due to the higher number of nucleons at which background interactions can take place.

Figures 6.178 to 6.185 present the fractional and absolute error summary for the cross sections in all four variables, in all four targets.

[4] the breakdown of some of the systematic uncertainties shown in this section, is available in appendix C.

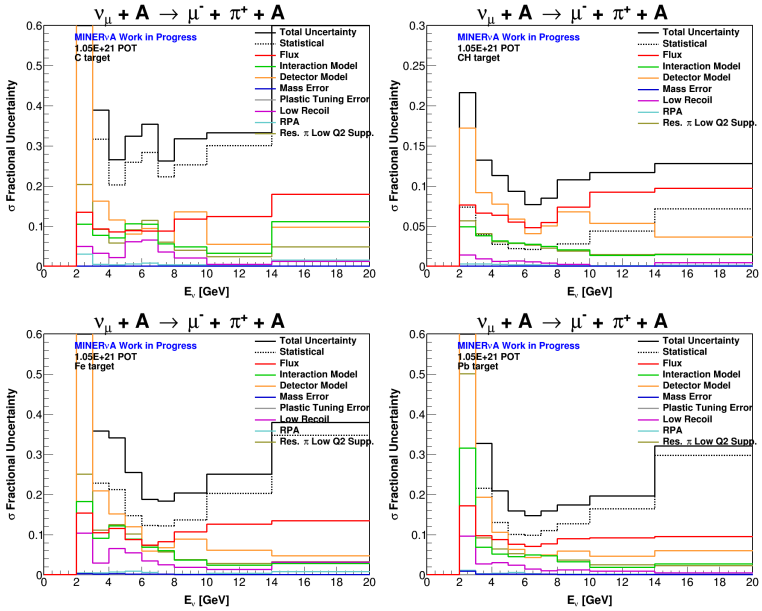

Figure 6.178: Fractional error Summary on the $\sigma\left(E_\nu\right)$ in the C, CH, Fe and Pb targets.

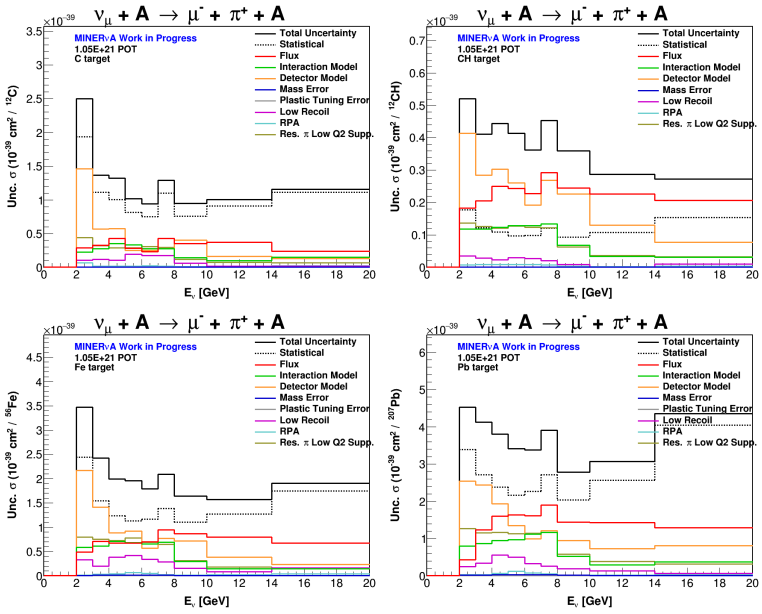

Figure 6.179: Absolute error Summary on the $\sigma\left(E_\nu\right)$ in the C, CH, Fe and Pb targets.

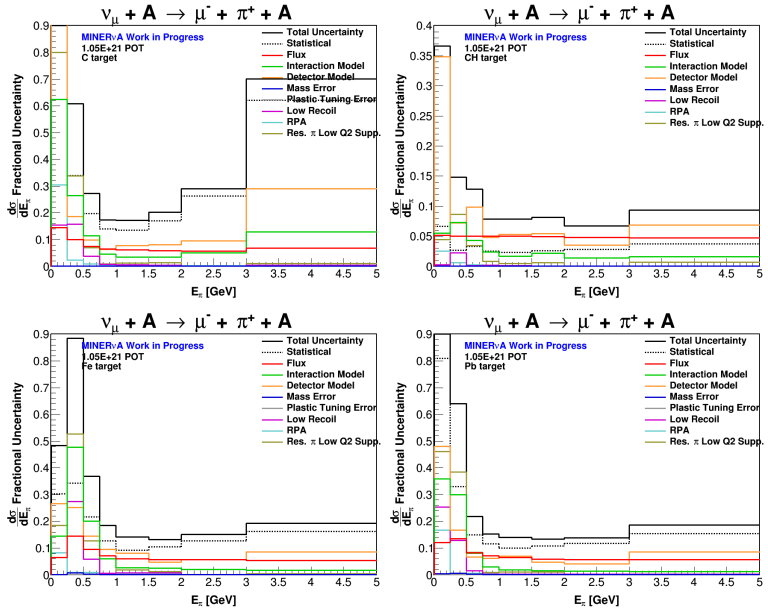

Figure 6.180: Fractional error Summary on the $\frac{d\sigma}{dE_\pi}$ in the C, CH, Fe and Pb targets.

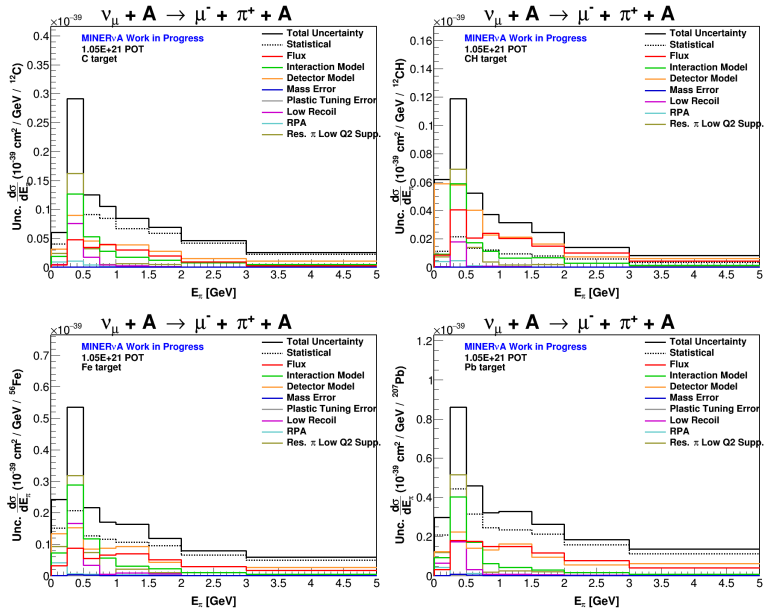

Figure 6.181: Absolute error Summary on the $\frac{d\sigma}{dE_\pi}$ in the C, CH, Fe and Pb targets.

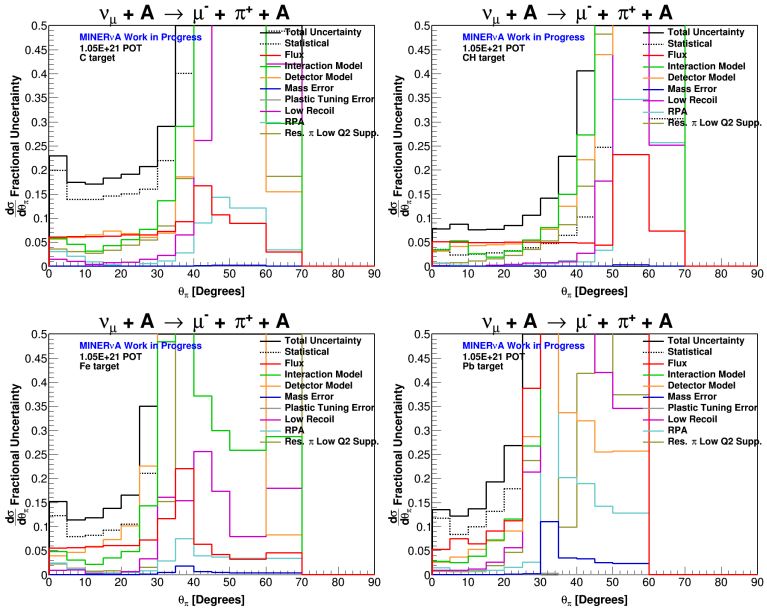

Figure 6.182: Fractional error Summary on the $\frac{d\sigma}{d\theta_\pi}$ in the C, CH, Fe and Pb targets.

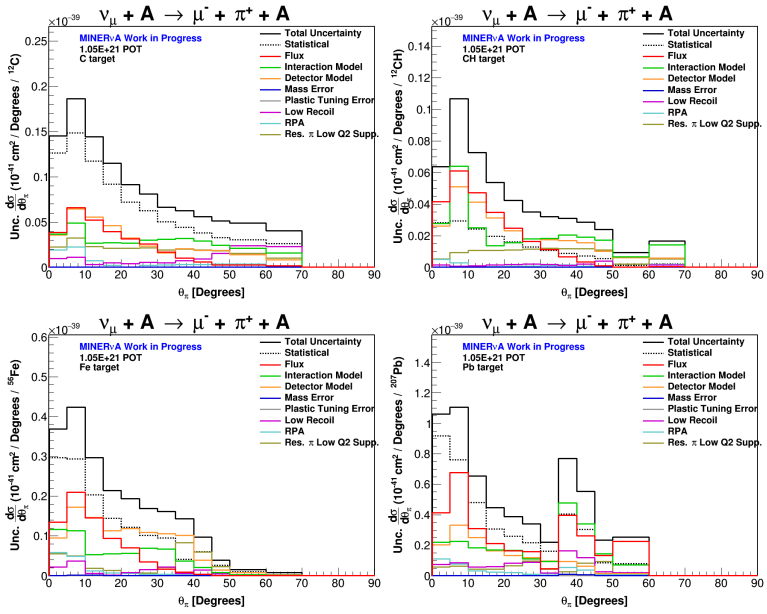

Figure 6.183: Absolute error Summary on the $\frac{d\sigma}{d\theta_\pi}$ in the C, CH, Fe and Pb targets.

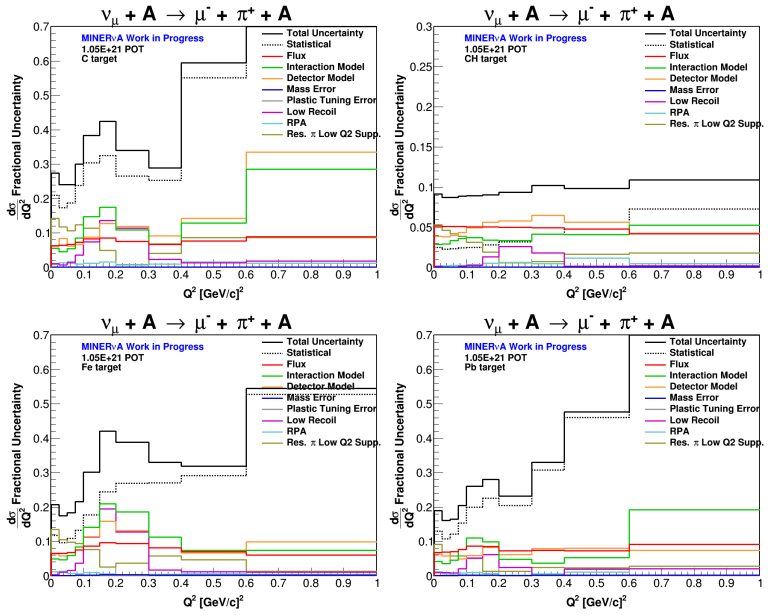

Figure 6.184: Fractional error Summary on the $\frac{d\sigma}{dQ^2}$ in the C, CH, Fe and Pb targets.

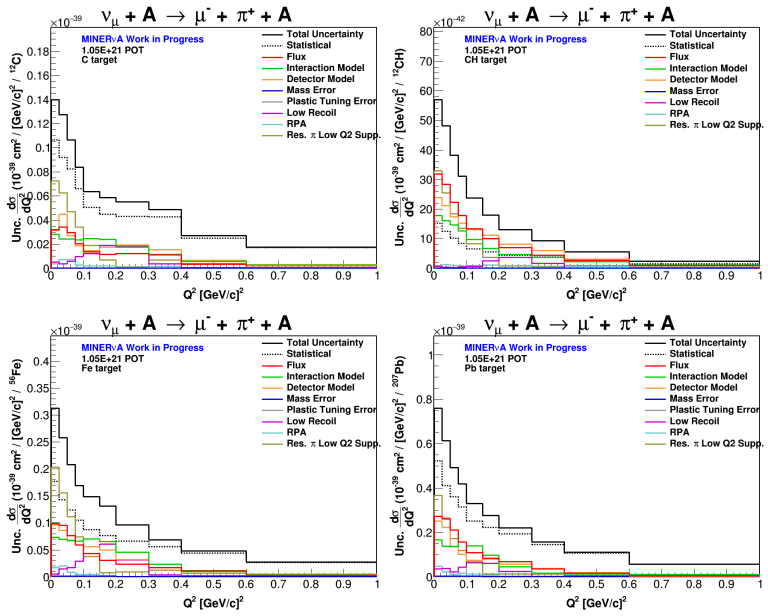

Figure 6.185: Absolute error Summary on the $\frac{d\sigma}{dQ^2}$ in the C, CH, Fe and Pb targets.

Chapter 7

CONCLUSIONS

The signature of the coherent production of pions induced by neutrinos, is the creation of a pion and a lepton in the forward direction, and the absence of nuclear breakup due to a small four-momentum transfer to the target nucleus. The energy transferred to the pion can still be relatively large (up to a few GeV). This makes it a rare interaction, as more energy is needed to create the pion than to break up the nucleus. Despite being a rare neutrino interaction, it has already been observed in both the charged and neutral weak currents, at low (∼2 GeV) and high neutrino energies (∼300 GeV), in materials as light as Carbon ($A \approx 12$), and before this analysis, as heavy as Argon ($A \approx 40$).

This work has measured the CC coherent production of pions, induced by muon neutrinos (ν_μ), isolating a sample with the characteristics of the signal, using model-independent criteria. The measurement was performed simultaneously in four different materials. Using the NuMI beamline at Fermilab, it was possible to obtain the cross section of the interaction, from Carbon (C), Hydrocarbon (CH), Iron (Fe) and Lead (Pb) nuclei. This is the first experiment that achieves a measurement of this process from more than one material at the same time. It is also the first experiment observing the interaction in a pure Carbon target (Graphite, with carbon $> 99.5\%$ of the target composition). All previous measurements of Carbon were done using compounds like CH or CH_2. It is also the first observation of the interaction in Iron ($A \approx 56$) and Lead ($A \approx 207$) at all. And with the sample obtained using the CH target, this work has also achieved the largest statistical sample of the process in any material, at any neutrino energy.

The cross sections measured in the C target may be useful to compare with experiments using C mixed with other elements, to extract the contribution from those other elements.

The results extracted from Iron (Lead) can be used to extrapolate to middle (large) size nuclei, for which until now, assumptions of $A^{1/3}$, $A^{2/3}$, or energy-dependent A-scaling of the cross section, are made to perform such extrapolations to nuclei where the interaction has not been measured. This is specially important for Lead. With $A \approx 207$, it can serve as a standard candle to do extrapolations to rather heavy nuclei.

The hydrocarbon (CH) sample, and the results extracted from it, are highly valuable to perform higher precision studies, and to test models in regions where statistical and systematic dominated experiments, did not allow before.

One of the prospects of this work, is to get an estimate of the scaling of the $\sigma\left(E_\nu\right)$ cross section as a function of the number of nucleons in the nucleus (A). This will be done by looking at the ratios $\sigma\left(E_\nu^{Fe,Pb}\right)/\sigma\left(E_\nu^{CH}\right)$ (see appendix D). In performing these ratios, the total uncertainties associated to the Fe and Pb cross sections will play a crucial role in determining any scaling pattern at all. If the uncertainties end up being too large, any possible scaling would be hard or impossible to obtain. Extracting the cross sections simultaneously, from the different targets involved, means that all targets experienced the changes in energies, intensities, and any other variations in the beamline, in the same manner. This will allow to constraint uncertainties, associated primarily to the neutrino flux.

All cross sections from all materials in this analysis were extracted using, and compared to the Rein-Sehgal model. Which it basically extrapolates Adler's theorem based on the PCAC hypothesis to interactions with $Q^2 > 0$. This model, and any other with predictions about the CC or NC (because of the relation between both, section 3.3) coherent production of pions, can benefit from this new set of data with improved statistics, and from the cross sections in a variety of materials, to make new predictions. Future experiments can also take advantage, even from the hypothetical improved models or from the data itself.

Among such experiments, perhaps the ones where this process will have must impact, are the neutrino oscillation experiments. Coherent pion production plays a crucial role in identifying some of the important backgrounds to those experiments. In electron neutrino appearance experiments, the forward neutral coherent pion can mimic the electron shower of the ν_e signal, if one of the gammas from the decay of the pion is not observed. The CC coherent interaction can mimic the signal of muon neutrino disappearance experiments, if the pion is mistaken as the proton (ν_μ disappearance experiments use the ν_μ-CC quasi-elastic process, where a muon and a proton are created, as their signal), or if the pion is not observed ($\overline{\nu}_\mu$ disappearance experiments use $\overline{\nu}_\mu$-CC quasi-elastic process, where an anti-muon and a neutron are created, as their signal). Ambitious experiments like

DUNE and Hyper Kamiokande, already under construction, will measure these neutrino oscillation channels, in liquid Argon and water, respectively, in a neutrino energy regime that overlaps with the one used in this analysis. If a more appropriate cross section scaling is available, both experiments can make a better extrapolation of the coherent pion cross section to the material of their needs, reducing their uncertainties.

An A-dependence is observed in the suppression of resonant pions at low Q^2 transfer, where collective nuclear effects are believed to play an important role [149]. This was observed in a hight $|t|$, low Q^2 sideband of background events in this analysis, where the suppression extracted from pions produced in the CH targets, perfectly match the suppression of the data, while in the Fe and Pb targets, a much stronger suppression is observed (section 6.7).

The results shown in this thesis confirms the results previously obtained by the MINERvA collaboration [31], [7], ArgoNeuT [32] and T2K [33], at similar neutrino energies, where the SciBooNE [30] and K2K [11] experiments were not able to observe, due to the not-fully contained pions and due to the muon mass correction factor not being available by then in the Rein-Sehgal model.

The MINERvA collaboration has been able to manage all the technical difficulties involved in reconstructing the CC coherent interaction (specially the pion kinematic variables) out of 11 different passive targets, where the 4 materials (C, CH, Fe and Pb) were located, to successfully observe the process in all of them, with a reasonable statistical sample. A sample of anti-neutrinos is being calibrated and reconstructed by the collaboration. It is possible in principle, to make neutrino vs anti-neutrinos comparisons, at least in the CH target, once the sample is ready. It will be complicated to do the same in the passive materials, because of the smaller statistics of the anti-neutrino sample.

Appendices

Appendix A

Fit Resolution Distributions

This chapter shows the fits to all the three distributions from the fractional muon, pion, neutrino energy, and Q^2 resolution, from sections 6.4.4 to 6.4.7.

A.1 E_μ Fits

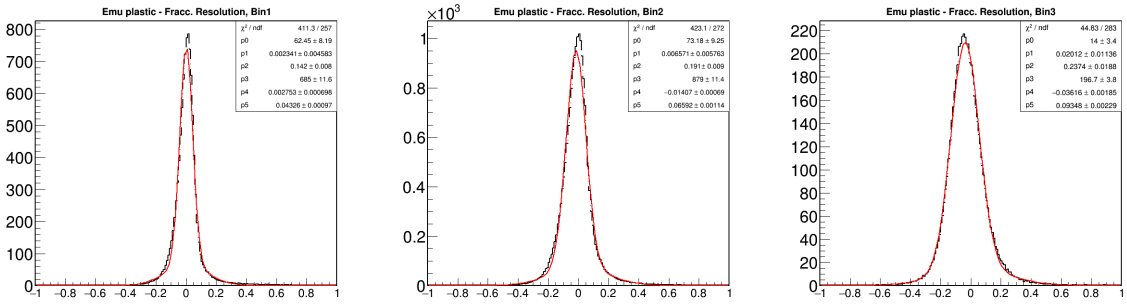

Figure A.1: Fit of each of the three energy regions in the muon fractional energy resolution. CH target.

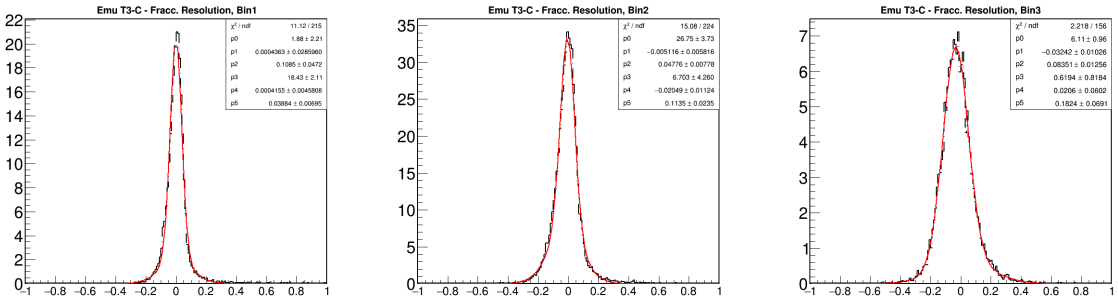

Figure A.2: Fit of each of the three energy regions in the muon fractional energy resolution. C target.

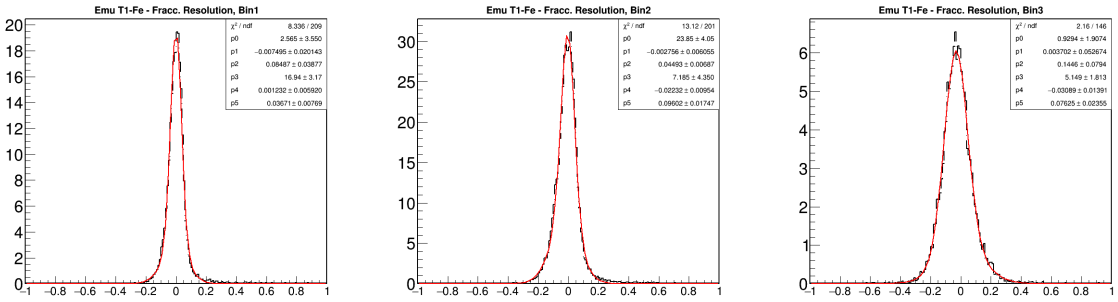

Figure A.3: Fit of each of the three energy regions in the muon fractional energy resolution. Fe in target 1.

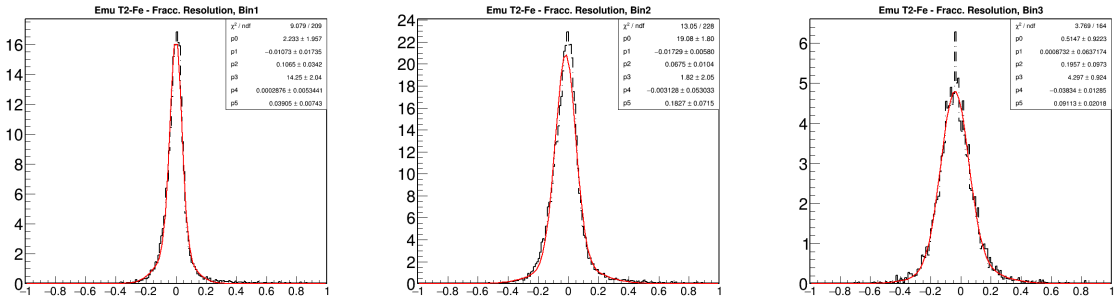

Figure A.4: Fit of each of the three energy regions in the muon fractional energy resolution. Fe in target 2.

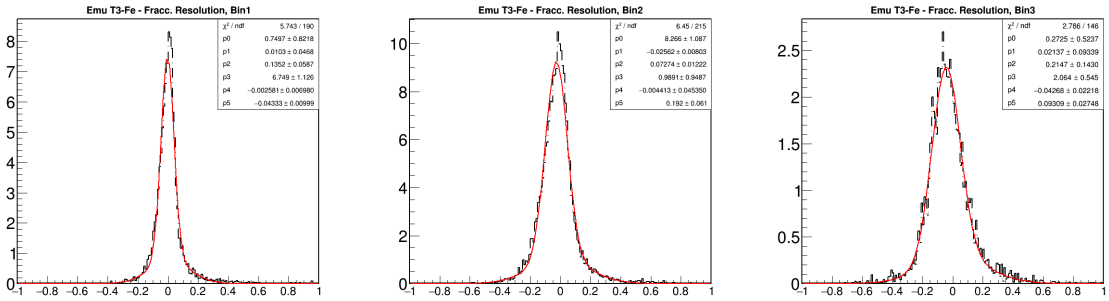

Figure A.5: Fit of each of the three energy regions in the muon fractional energy resolution. Fe in target 3.

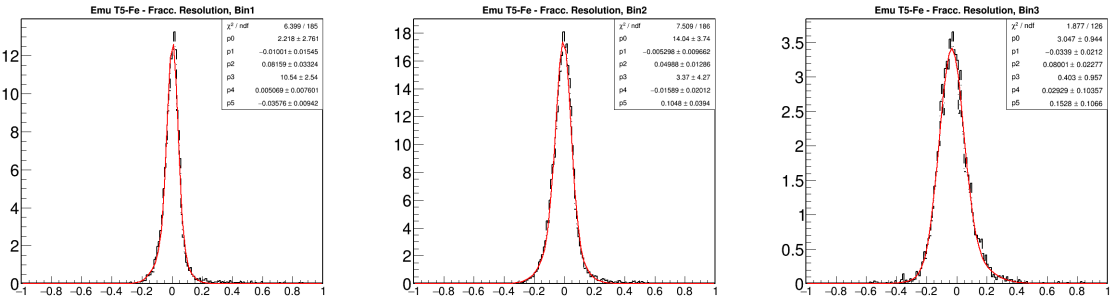

Figure A.6: Fit of each of the three energy regions in the muon fractional energy resolution. Fe in target 5.

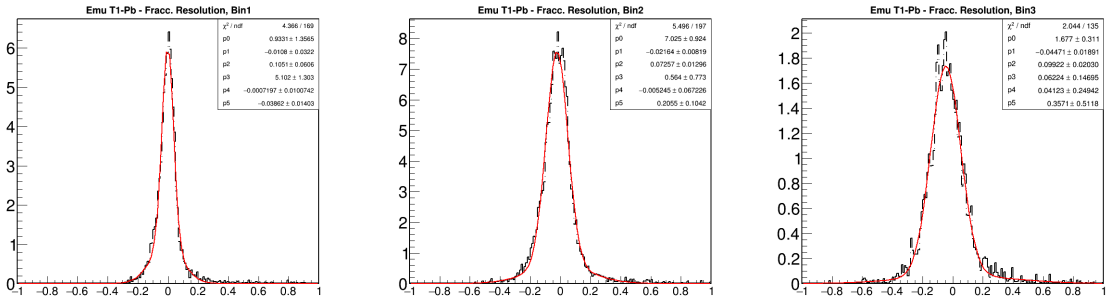

Figure A.7: Fit of each of the three energy regions in the muon fractional energy resolution. Pb in target 1.

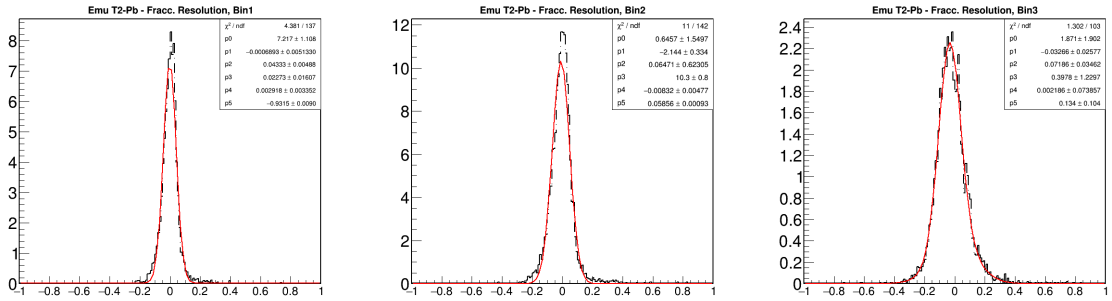

Figure A.8: Fit of each of the three energy regions in the muon fractional energy resolution. Pb in target 2.

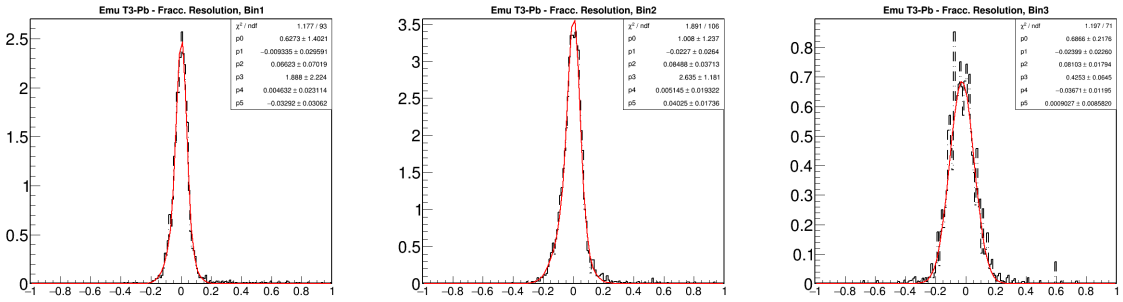

Figure A.9: Fit of each of the three energy regions in the muon fractional energy resolution. Pb in target 3.

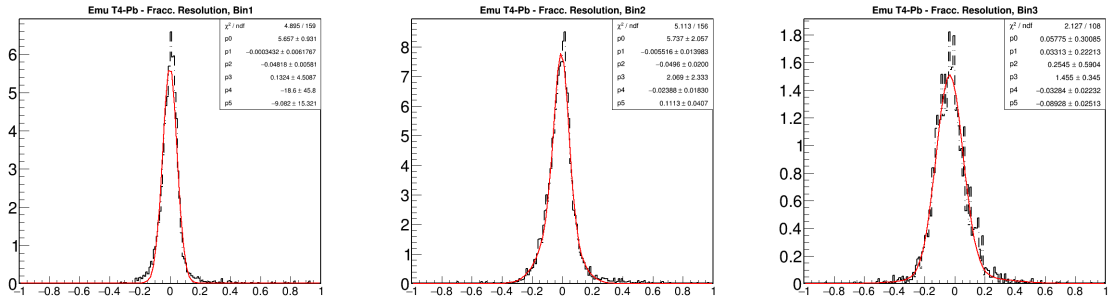

Figure A.10: Fit of each of the three energy regions in the muon fractional energy resolution. Pb in target 4.

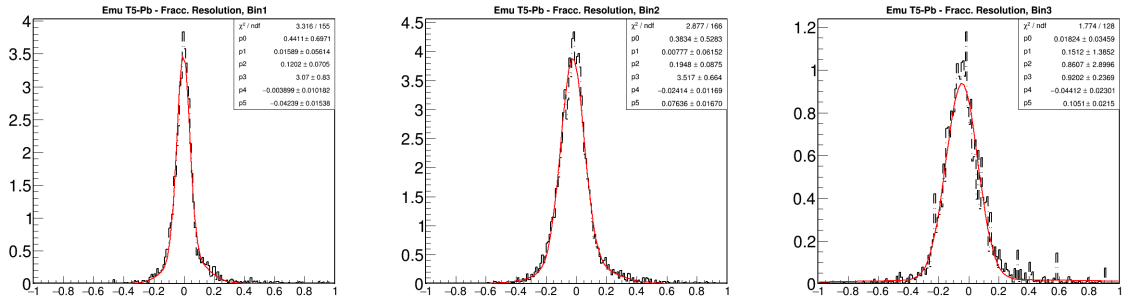

Figure A.11: Fit of each of the three energy regions in the muon fractional energy resolution. Pb in target 5.

A.2 E_π Fits

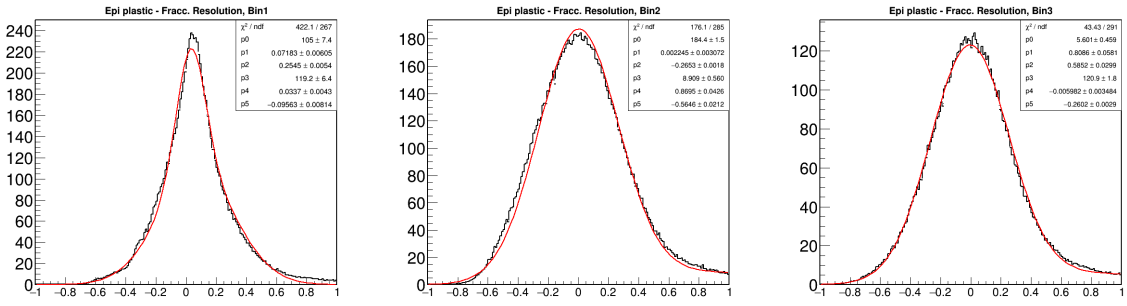

Figure A.12: Fit of each of the three energy regions in the pion fractional energy resolution. CH target.

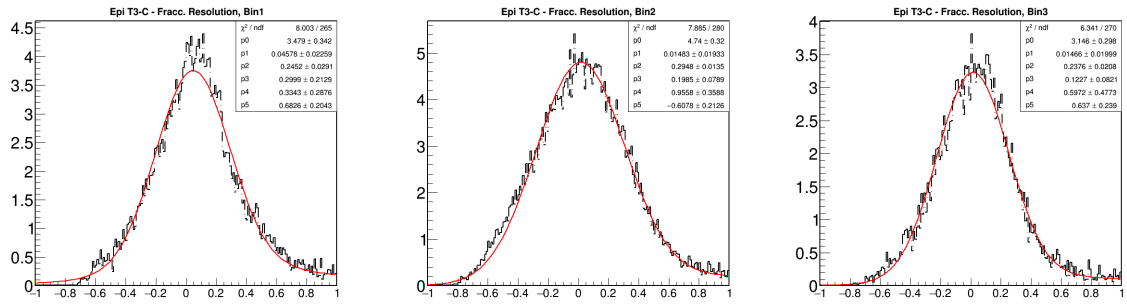

Figure A.13: Fit of each of the three energy regions in the pion fractional energy resolution. C target.

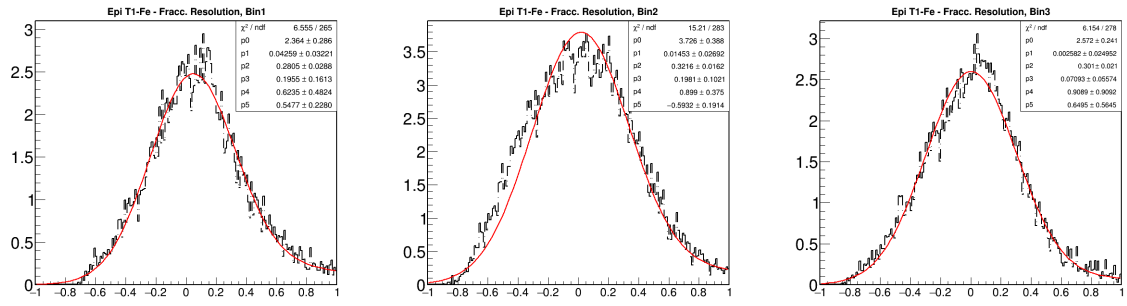

Figure A.14: Fit of each of the three energy regions in the pion fractional energy resolution. Fe in target 1.

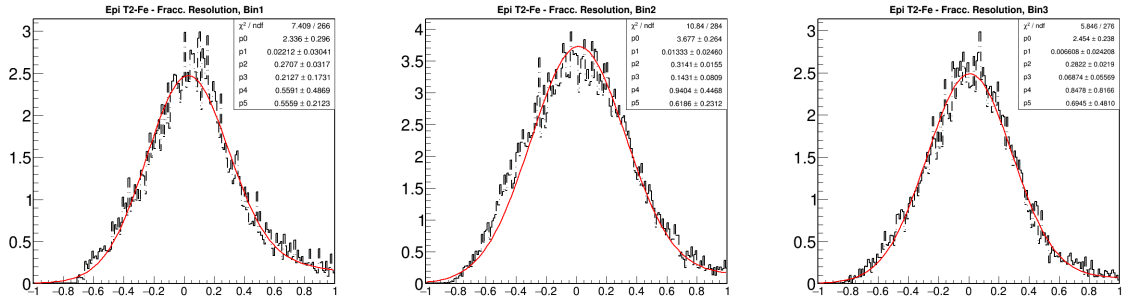

Figure A.15: Fit of each of the three energy regions in the pion fractional energy resolution. Fe in target 2.

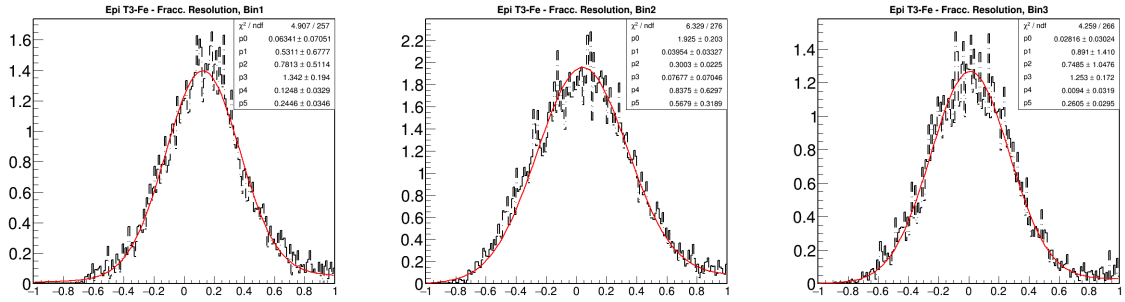

Figure A.16: Fit of each of the three energy regions in the pion fractional energy resolution. Fe in target 3.

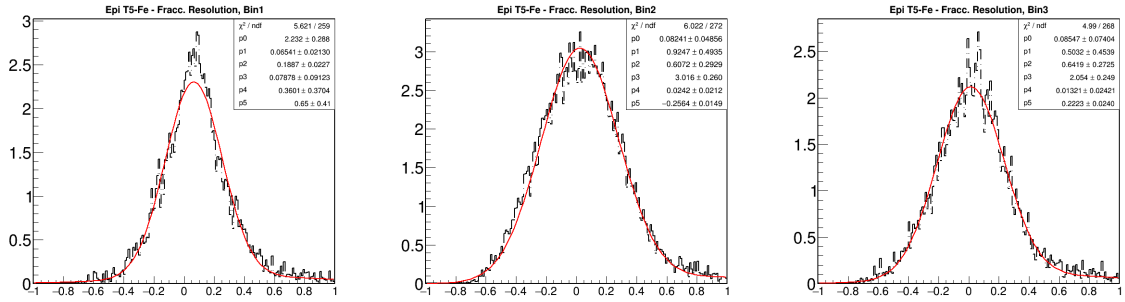

Figure A.17: Fit of each of the three energy regions in the pion fractional energy resolution. Fe in target 5.

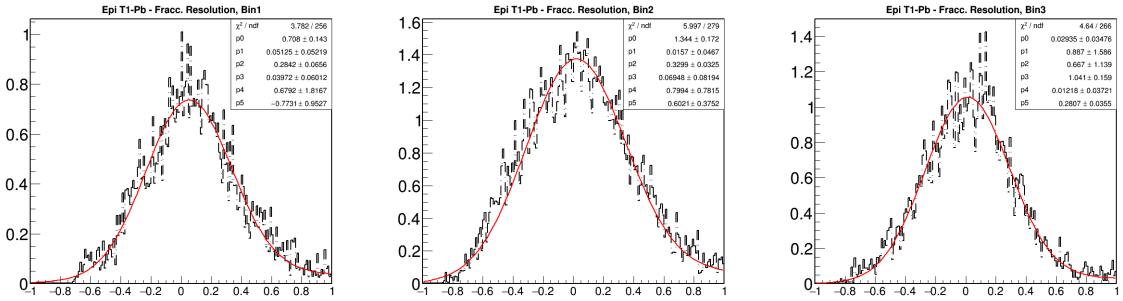

Figure A.18: Fit of each of the three energy regions in the pion fractional energy resolution. Pb in target 1.

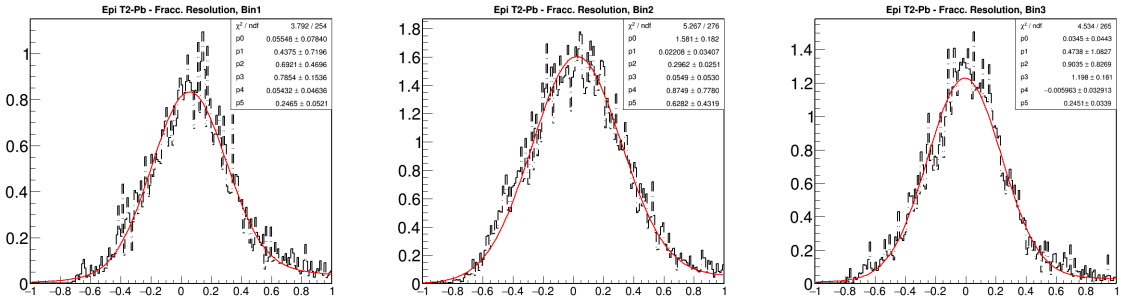

Figure A.19: Fit of each of the three energy regions in the pion fractional energy resolution. Pb in target 2.

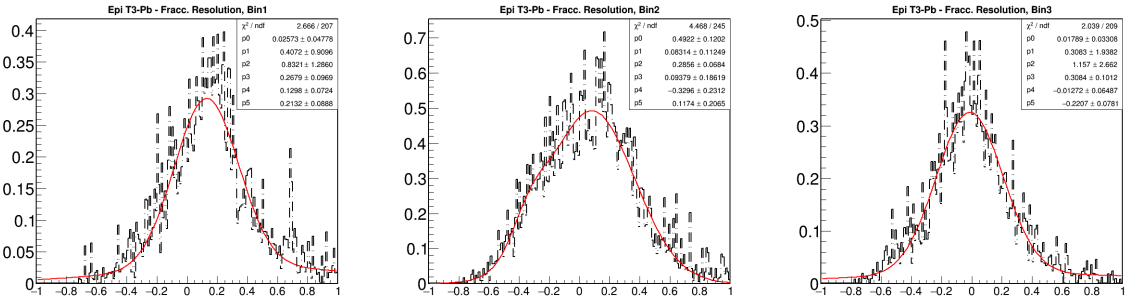

Figure A.20: Fit of each of the three energy regions in the pion fractional energy resolution. Pb in target 3.

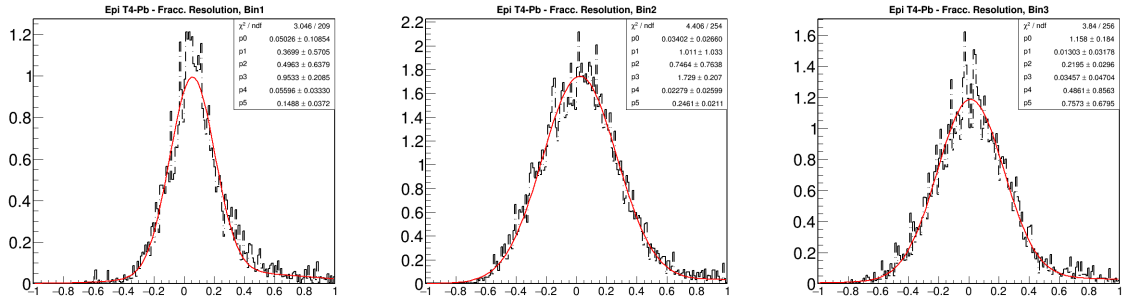

Figure A.21: Fit of each of the three energy regions in the pion fractional energy resolution. Pb in target 4.

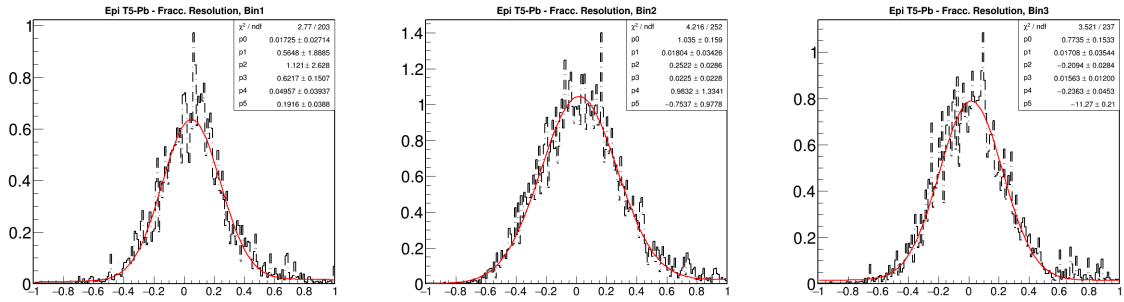

Figure A.22: Fit of each of the three energy regions in the pion fractional energy resolution. Pb in target 5.

A.3 E_ν Fits

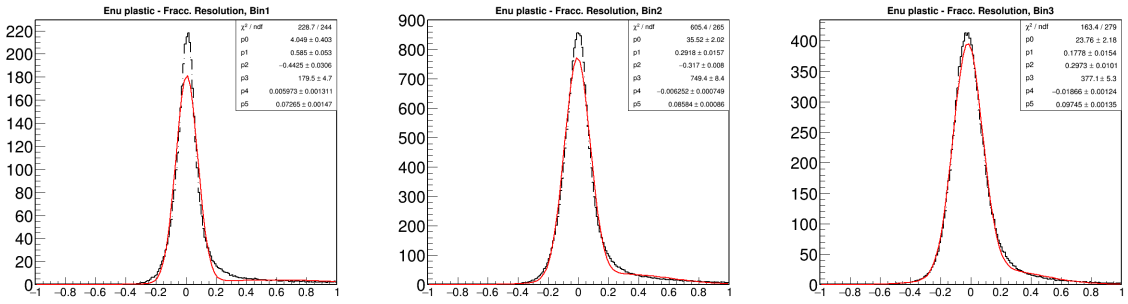

Figure A.23: Fit of each of the three energy regions in the neutrino fractional energy resolution. CH target.

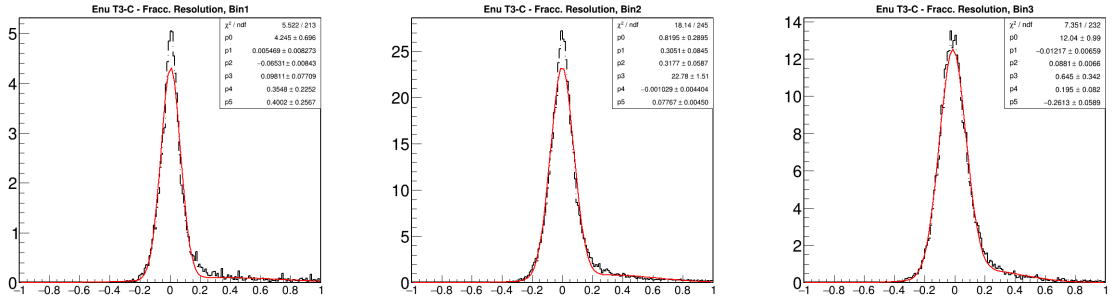

Figure A.24: Fit of each of the three energy regions in the neutrino fractional energy resolution. C target.

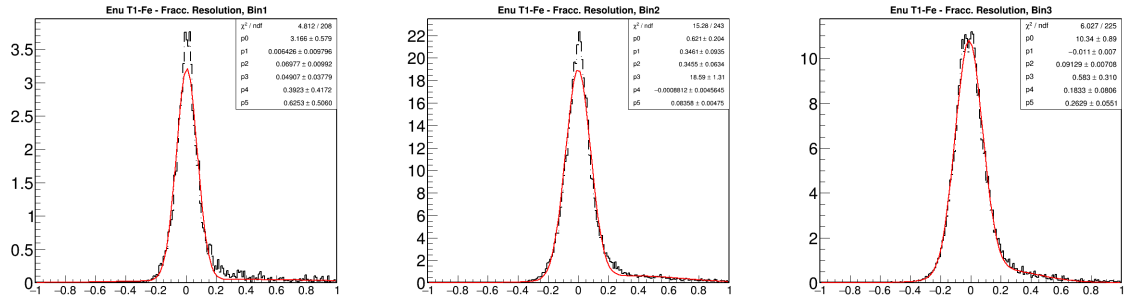

Figure A.25: Fit of each of the three energy regions in the neutrino fractional energy resolution. Fe in target 1.

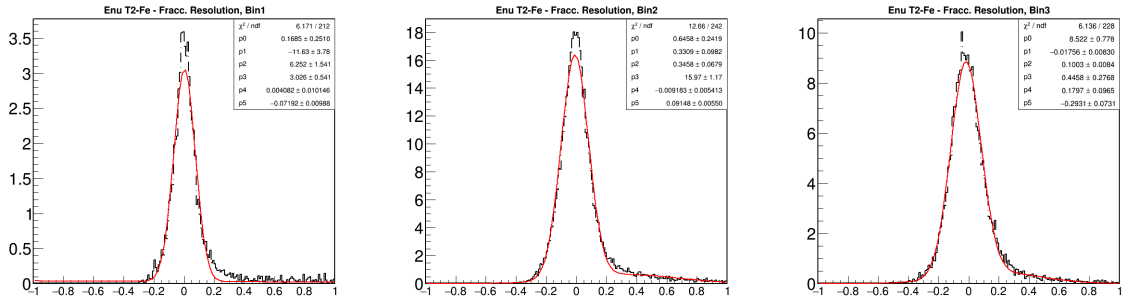

Figure A.26: Fit of each of the three energy regions in the neutrino fractional energy resolution. Fe in target 2.

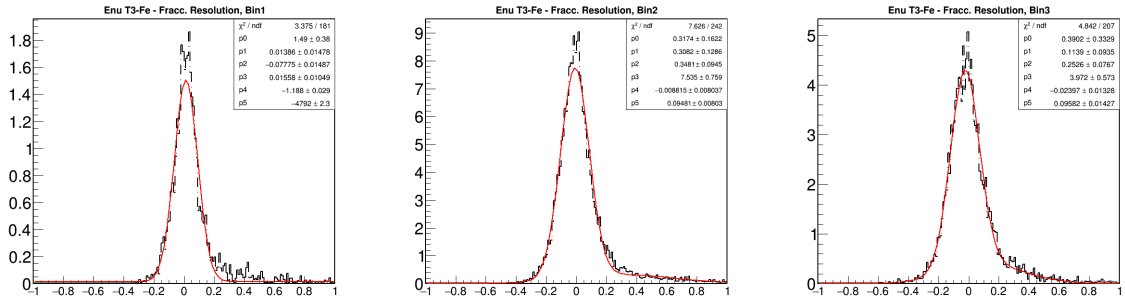

Figure A.27: Fit of each of the three energy regions in the neutrino fractional energy resolution. Fe in target 3.

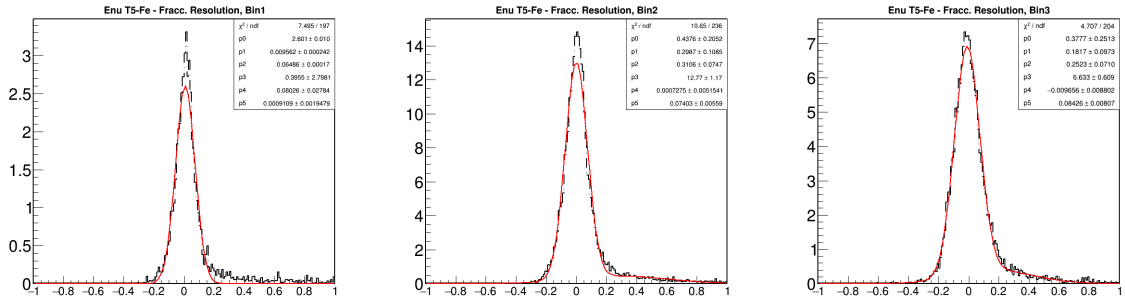

Figure A.28: Fit of each of the three energy regions in the neutrino fractional energy resolution. Fe in target 5.

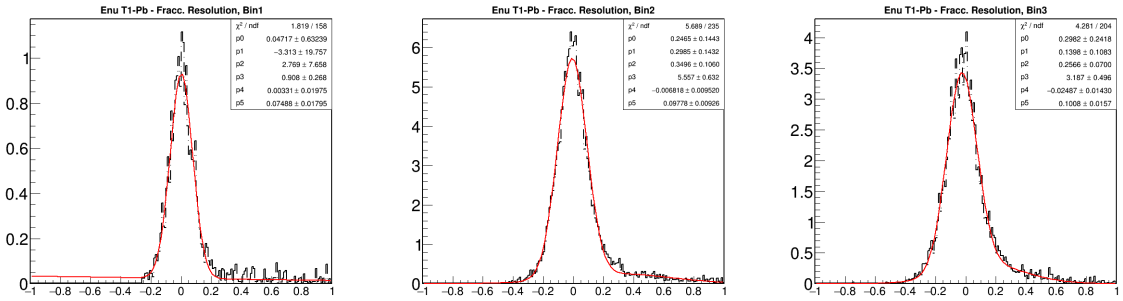

Figure A.29: Fit of each of the three energy regions in the neutrino fractional energy resolution. Pb in target 1.

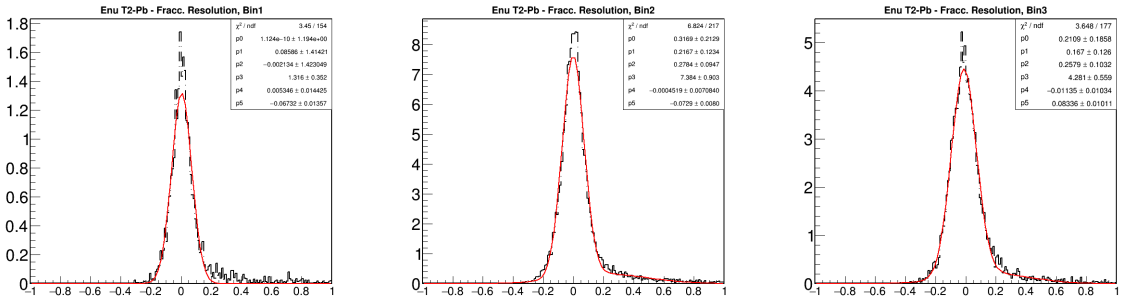

Figure A.30: Fit of each of the three energy regions in the neutrino fractional energy resolution. Pb in target 2.

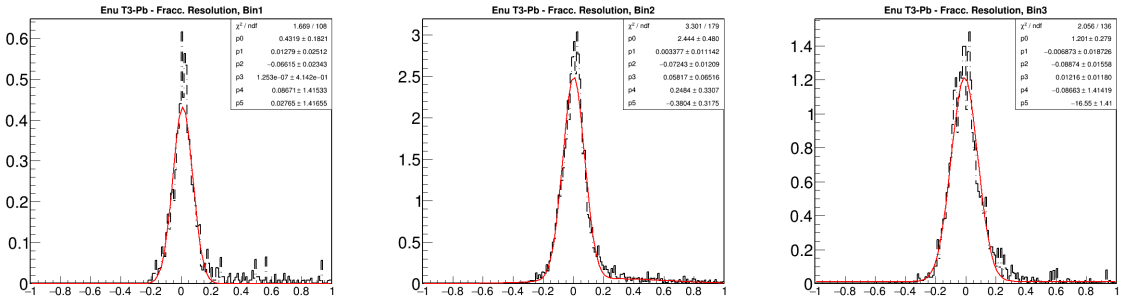

Figure A.31: Fit of each of the three energy regions in the neutrino fractional energy resolution. Pb in target 3.

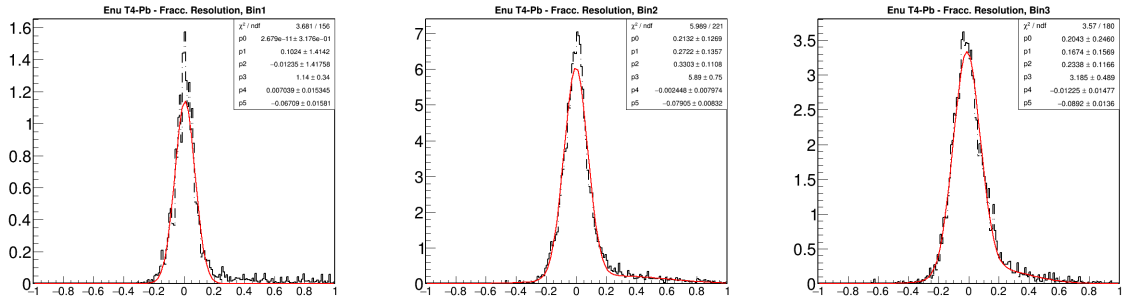

Figure A.32: Fit of each of the three energy regions in the neutrino fractional energy resolution. Pb in target 4.

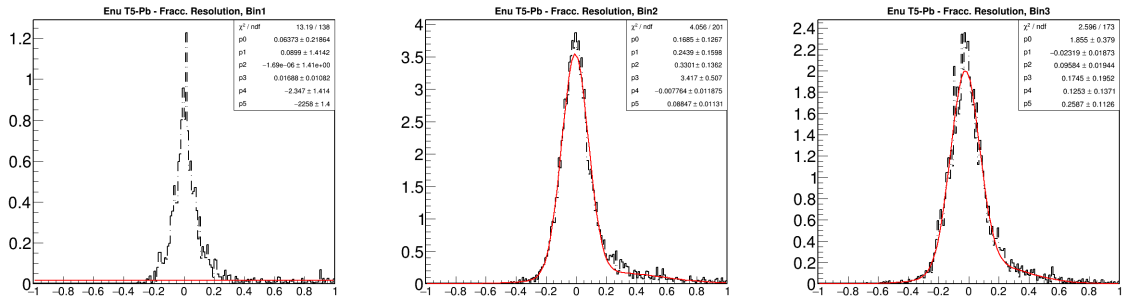

Figure A.33: Fit of each of the three energy regions in the neutrino fractional energy resolution. Pb in target 5.

A.4 Q^2 Fits

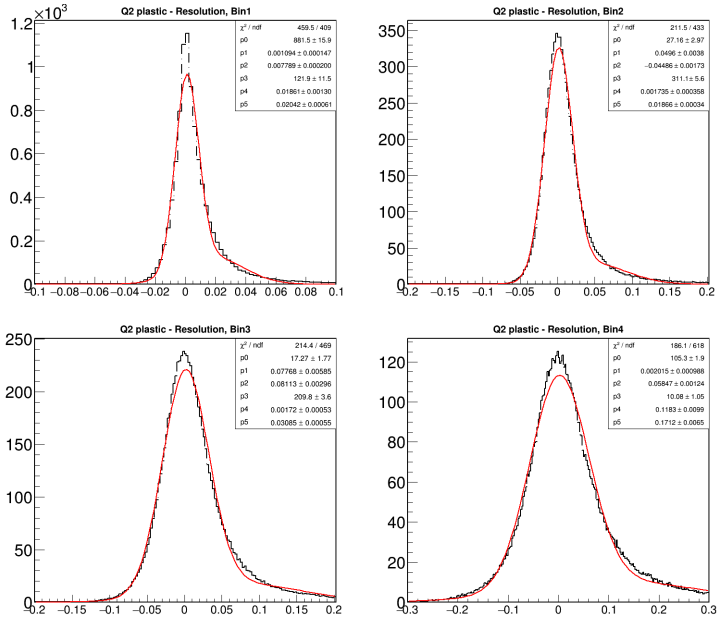

Figure A.34: Fit of each of the four energy regions in the Q^2 fractional energy resolution. CH target.

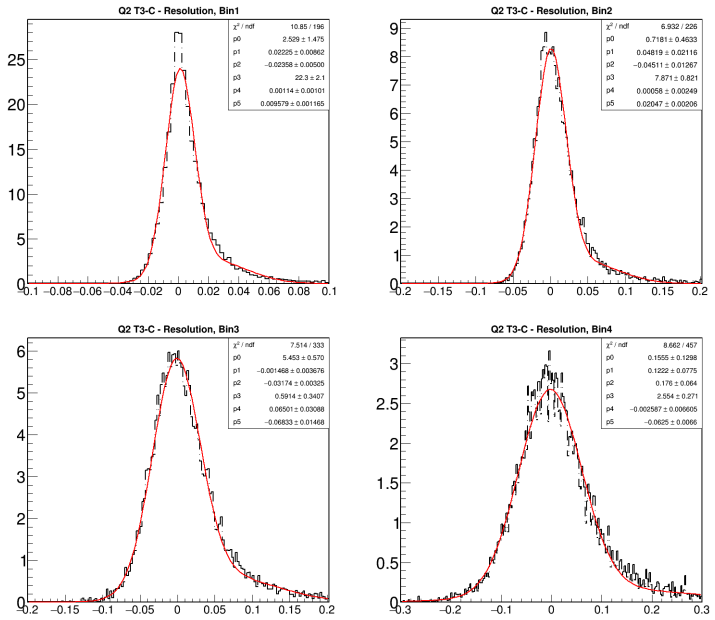

Figure A.35: Fit of each of the four energy regions in the Q^2 fractional energy resolution. C target.

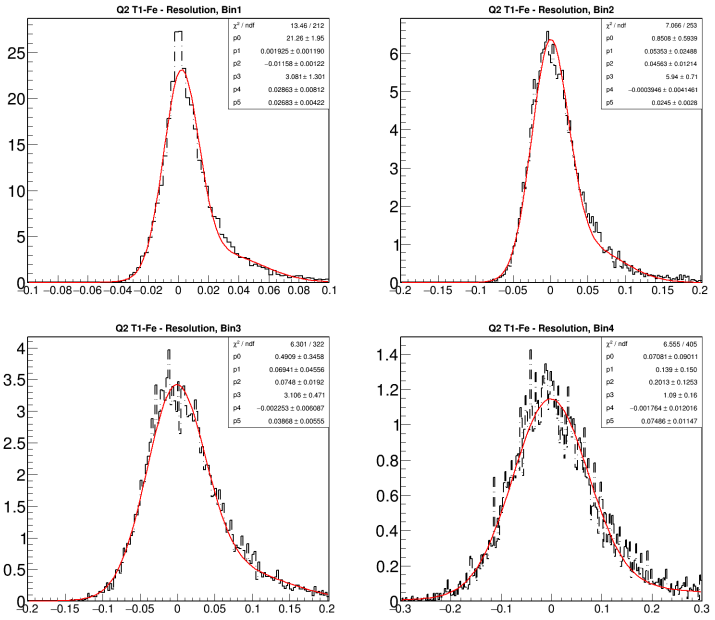

Figure A.36: Fit of each of the four energy regions in the Q^2 fractional energy resolution. Fe in target 1.

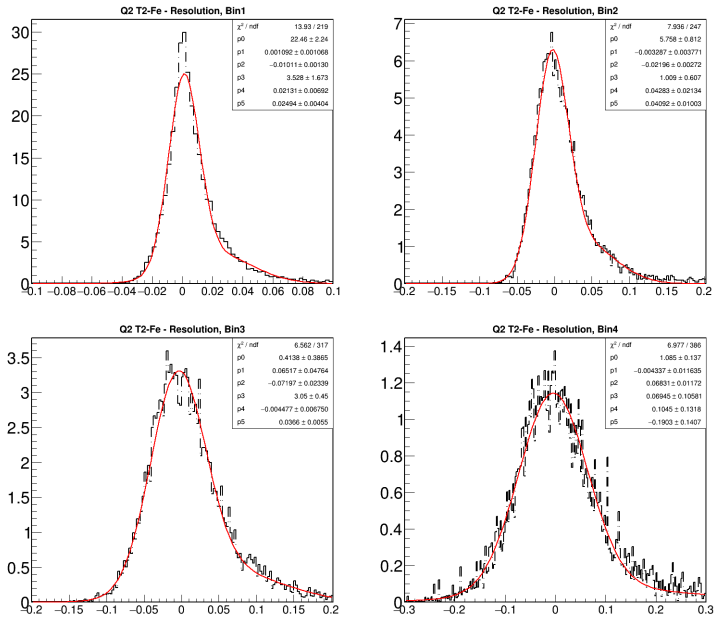

Figure A.37: Fit of each of the four energy regions in the Q^2 fractional energy resolution. Fe in target 2.

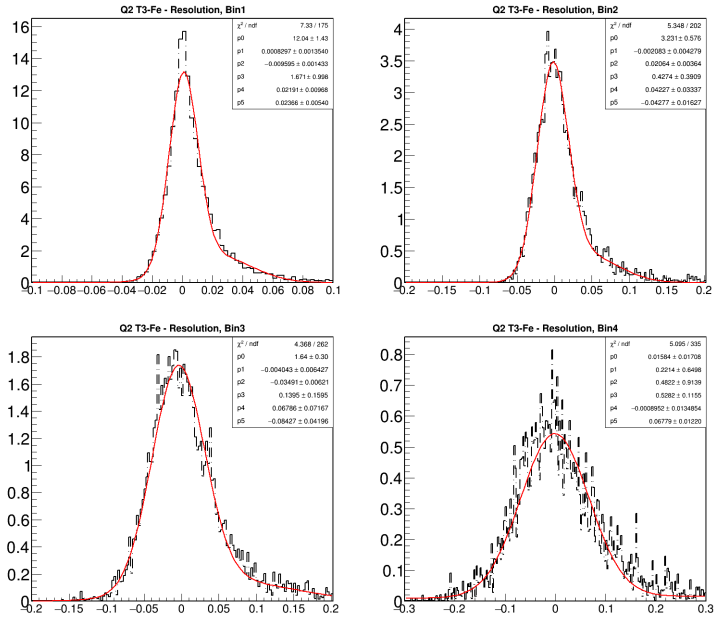

Figure A.38: Fit of each of the four energy regions in the Q^2 fractional energy resolution. Fe in target 3.

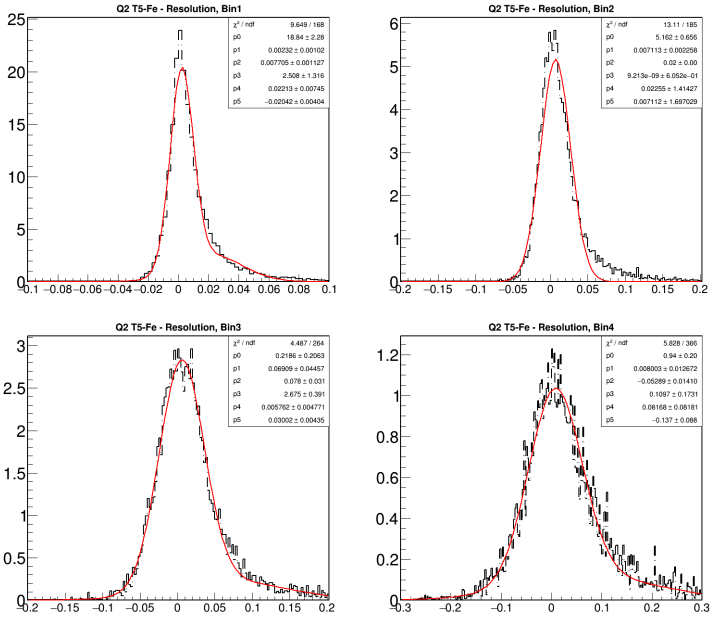

Figure A.39: Fit of each of the four energy regions in the Q^2 fractional energy resolution. Fe in target 5.

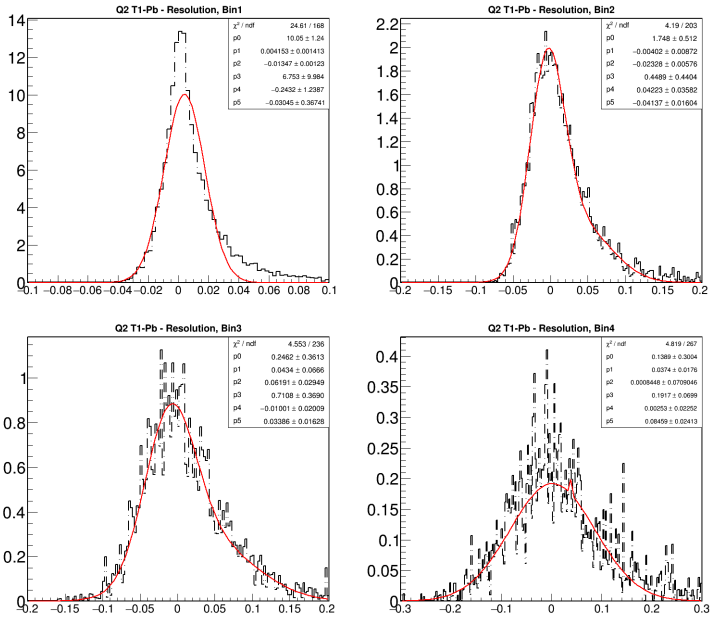

Figure A.40: Fit of each of the four energy regions in the Q^2 fractional energy resolution. Pb in target 1.

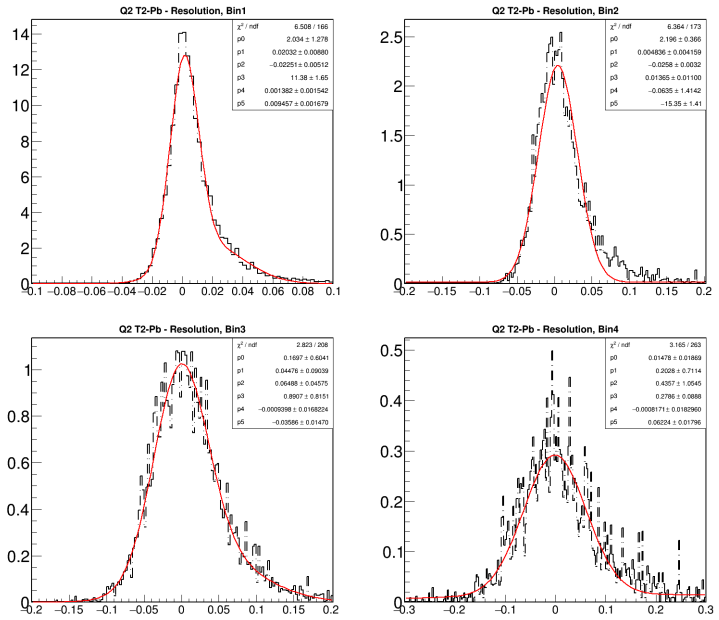

Figure A.41: Fit of each of the four energy regions in the Q^2 fractional energy resolution. Pb in target 2.

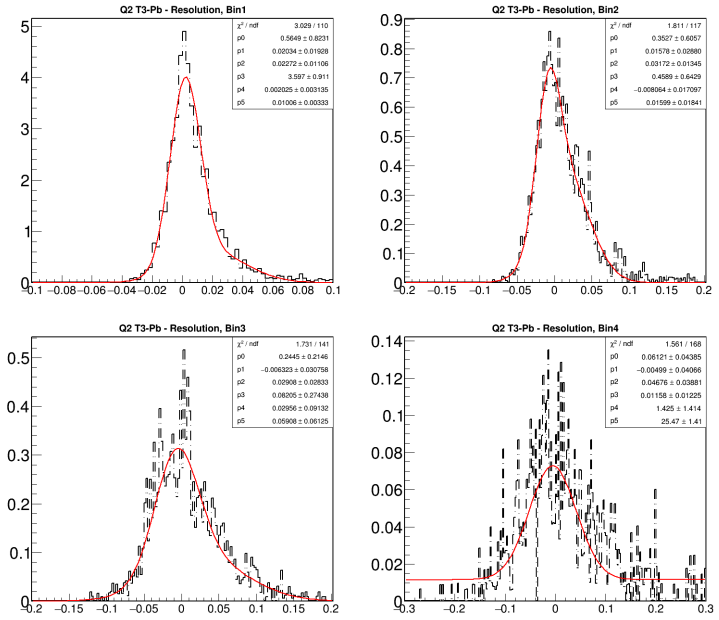

Figure A.42: Fit of each of the four energy regions in the Q^2 fractional energy resolution. Pb in target 3.

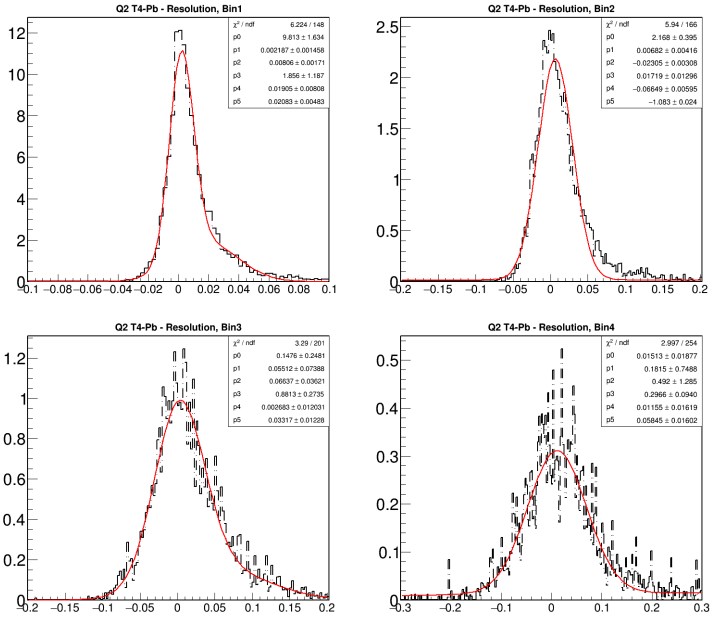

Figure A.43: Fit of each of the four energy regions in the Q^2 fractional energy resolution. Pb in target 4.

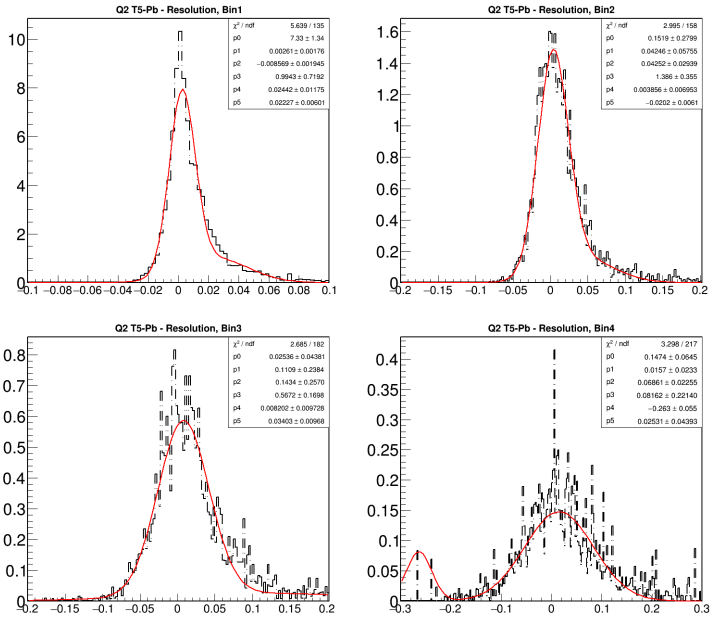

Figure A.44: Fit of each of the four energy regions in the Q^2 fractional energy resolution. Pb in target 5.

Appendix B

Unfolding Study

To determine the appropriate number of iterations for unfolding the data, the background subtracted data was used in a data-driven unfolding technique. The ratio of the data and the MC from the signal-only sample is used as a weight to warp the signal-only MC. The shape of the MC warped then becomes similar to the background-subtracted data. The reconstructed warped MC is unfolded in successive iterations, until the difference with the true warped MC is less or equal to the 1σ statistical error of the reconstructed warped MC.

In the figures below, it can be seen how the original signal-only reconstructed MC in red, becomes closer to the shape of the background-subtracted data (green histogram), after applying the data/MC ratio (top right) weight. After a given number of iterations, the difference in the plots in the middle reduces as the number of iterations increases. Increasing the number of iterations causes that events migrate from some bins to others. Because of this, some bins end up with fewer events and therefore, larger statistical errors.

In bins where the background is higher than the data (specially in the passive materials), the unfolding may struggle with high statistical errors. New MC weights are being developed by the MINERvA collaboration. These should help getting a better agreement between data and MC in the non-coherent background tuning. This might also positively affect the unfolding-related errors in those bins (see chapters 6 and 7). In all cases, the unfolding process is shown up to the second iteration. The number of iterations at which the process converges, is shown in table 6.9, for each variable in each material.

B.1 E_ν Unfolding Study

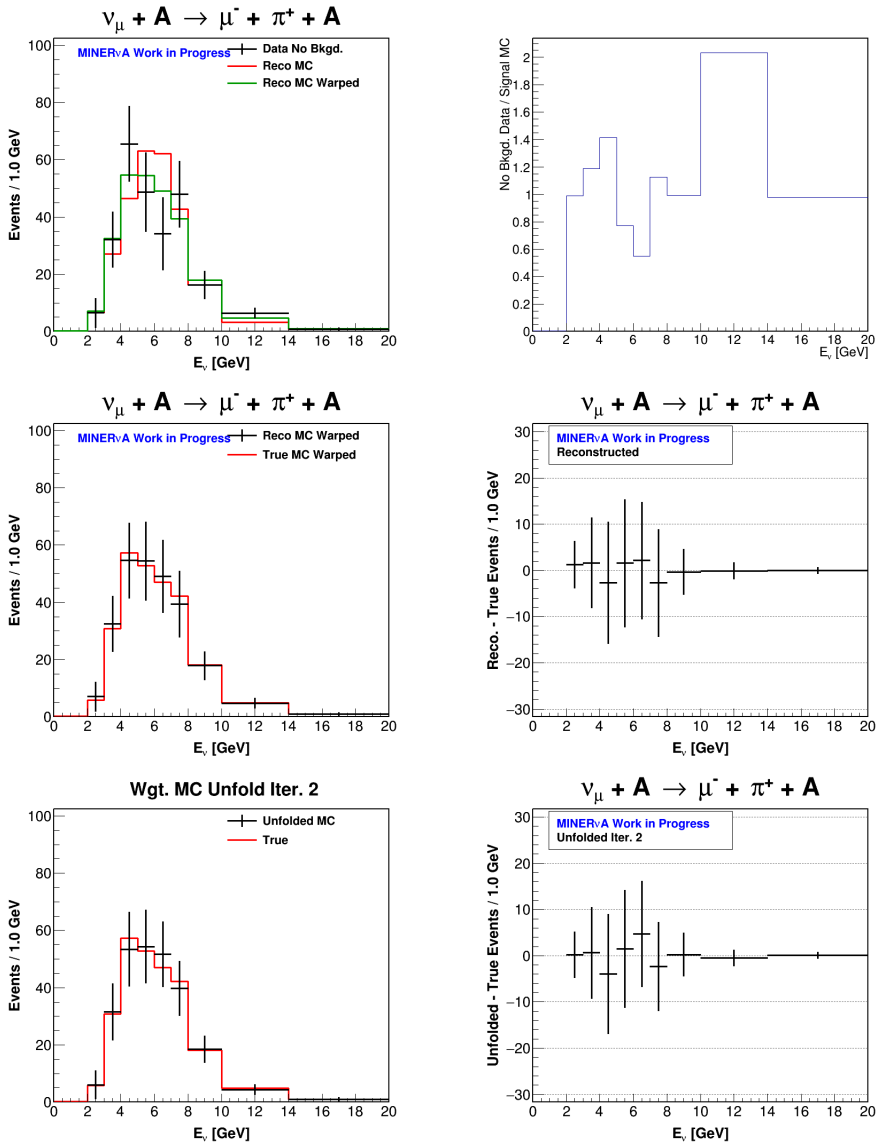

Figure B.1: Unfolding study for the E_ν in the carbon target. Top left: reconstructed MC and reconstructed MC warped compared to the background subtracted data; top right: background-subtracted data/reconstructed MC used as warping function; middle left: warped reconstructed and true MC before unfolding; middle right: reconstructed-true before unfolding; bottom left: unfolded warped MC after the second iteration; bottom right: unfolded-true after the second iteration.

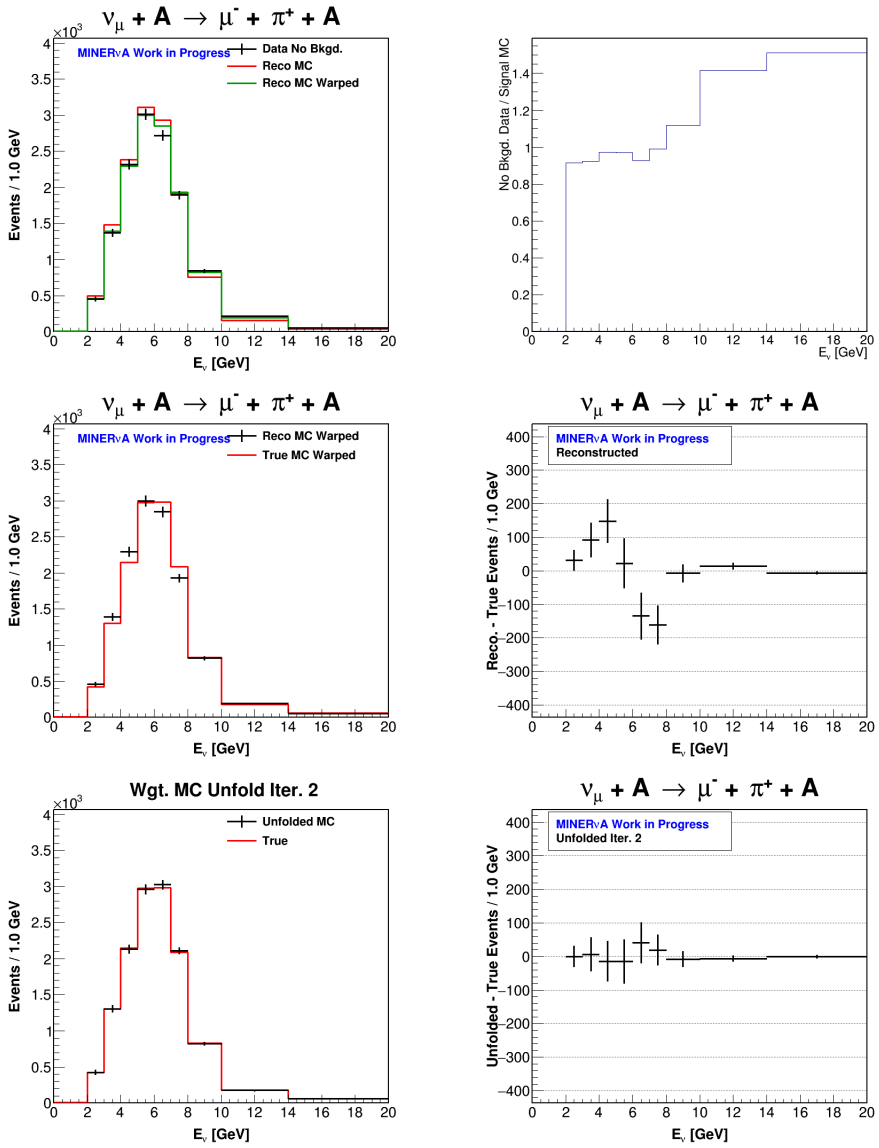

Figure B.2: Unfolding study for the E_ν in the hydrocarbon target. Top left: reconstructed MC and reconstructed MC warped compared to the background subtracted data; top right: background-subtracted data/reconstructed MC used as warping function; middle left: warped reconstructed and true MC before unfolding; middle right: reconstructed-true before unfolding; bottom left: unfolded warped MC after the second iteration; bottom right: unfolded-true after the second iteration.

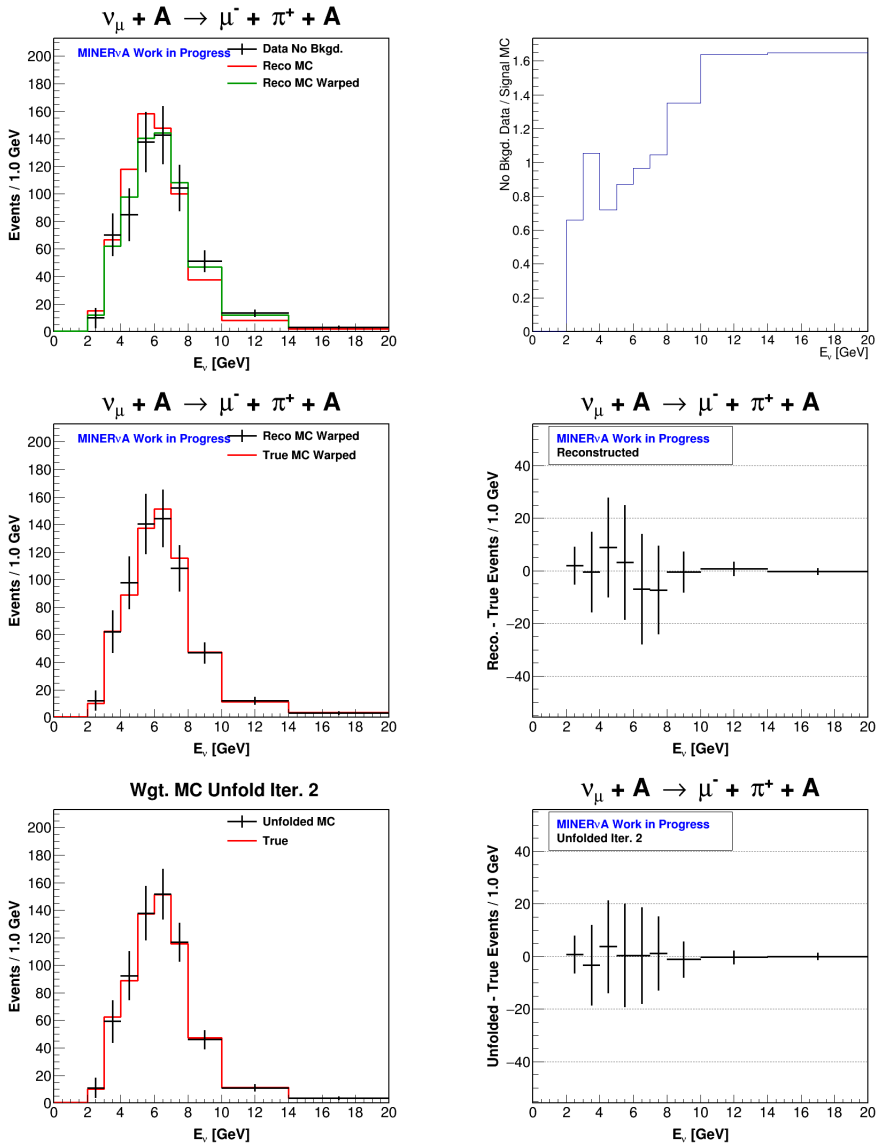

Figure B.3: Unfolding study for the E_ν in the iron target. Top left: reconstructed MC and reconstructed MC warped compared to the background subtracted data; top right: background-subtracted data/reconstructed MC used as warping function; middle left: warped reconstructed and true MC before unfolding; middle right: reconstructed-true before unfolding; bottom left: unfolded warped MC after the second iteration; bottom right: unfolded-true after the second iteration.

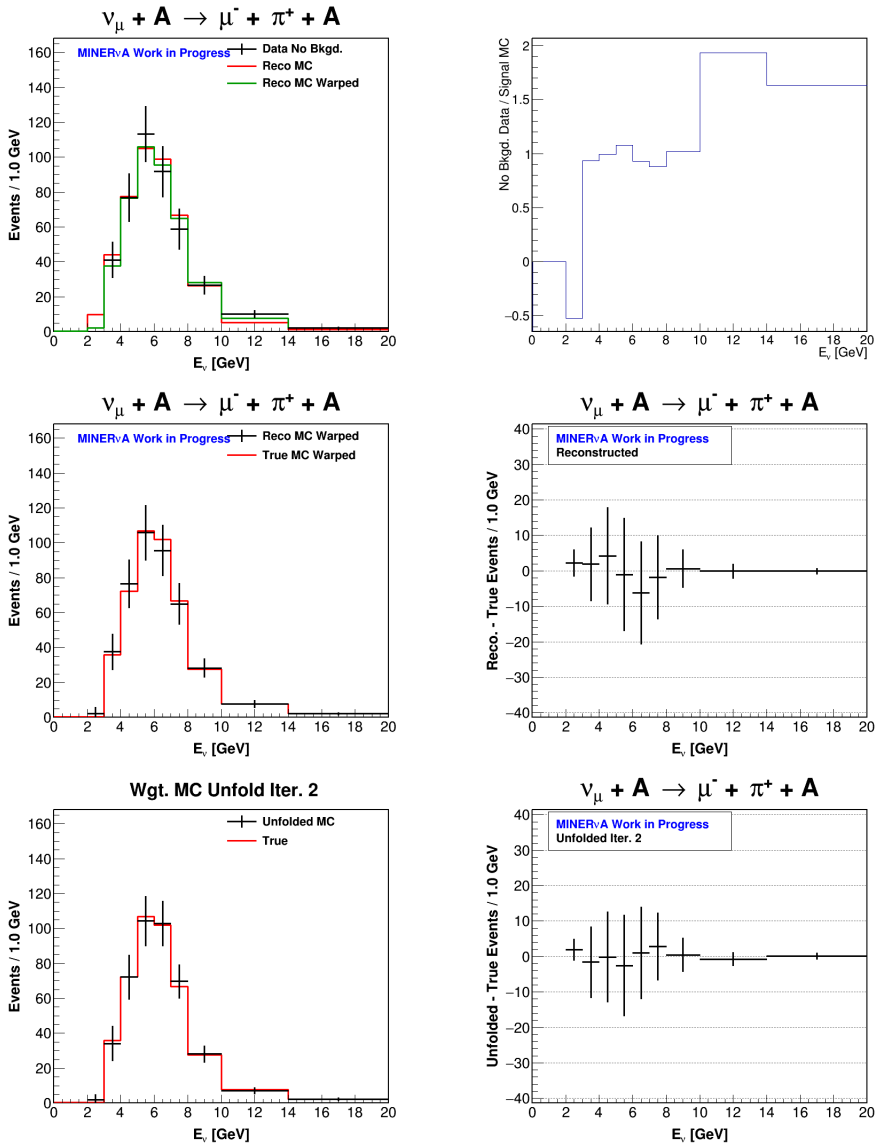

Figure B.4: Unfolding study for the E_ν in the lead target. Top left: reconstructed MC and reconstructed MC warped compared to the background subtracted data; top right: background-subtracted data/reconstructed MC used as warping function; middle left: warped reconstructed and true MC before unfolding; middle right: reconstructed-true before unfolding; bottom left: unfolded warped MC after the second iteration; bottom right: unfolded-true after the second iteration.

B.2 E_π Unfolding Study

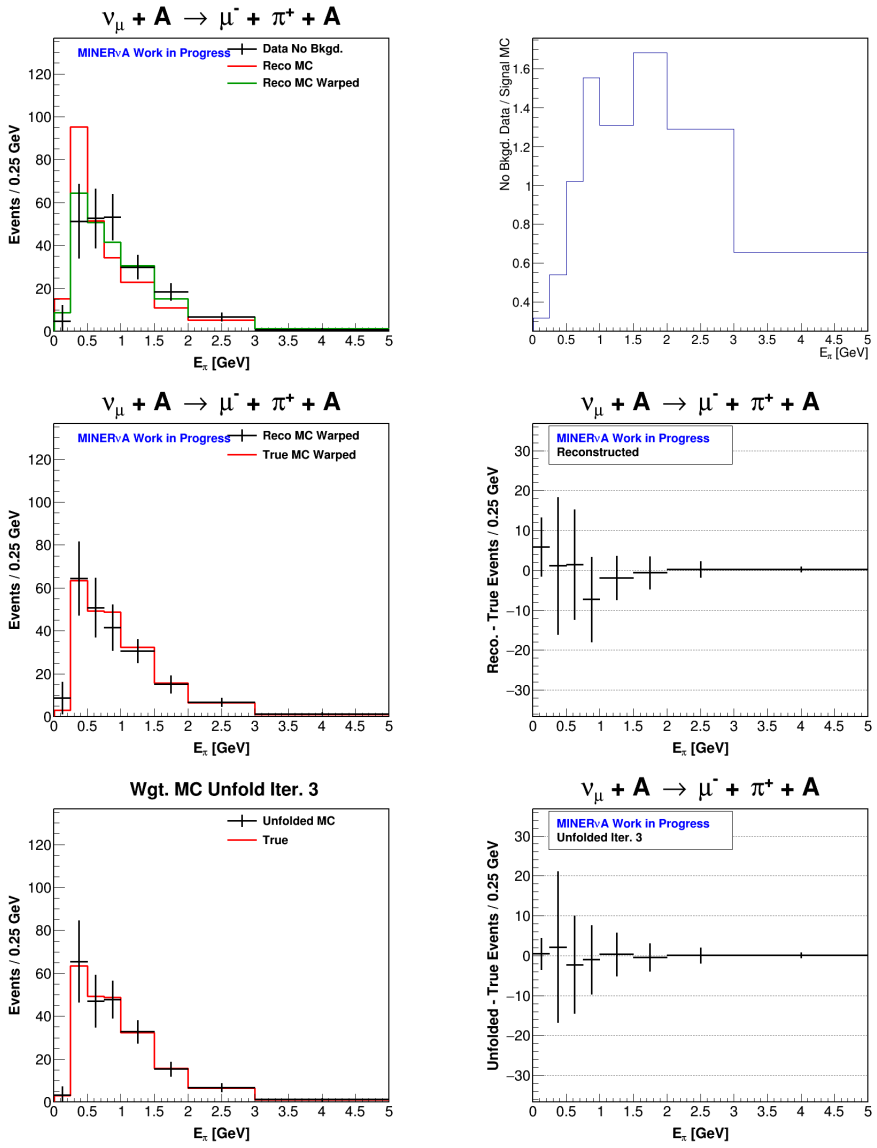

Figure B.5: Unfolding study for the E_π in the carbon target. Top left: reconstructed MC and reconstructed MC warped compared to the background subtracted data; top right: background-subtracted data/reconstructed MC used as warping function; middle left: warped reconstructed and true MC before unfolding; middle right: reconstructed-true before unfolding; bottom left: unfolded warped MC after the second iteration; bottom right: unfolded-true after the second iteration.

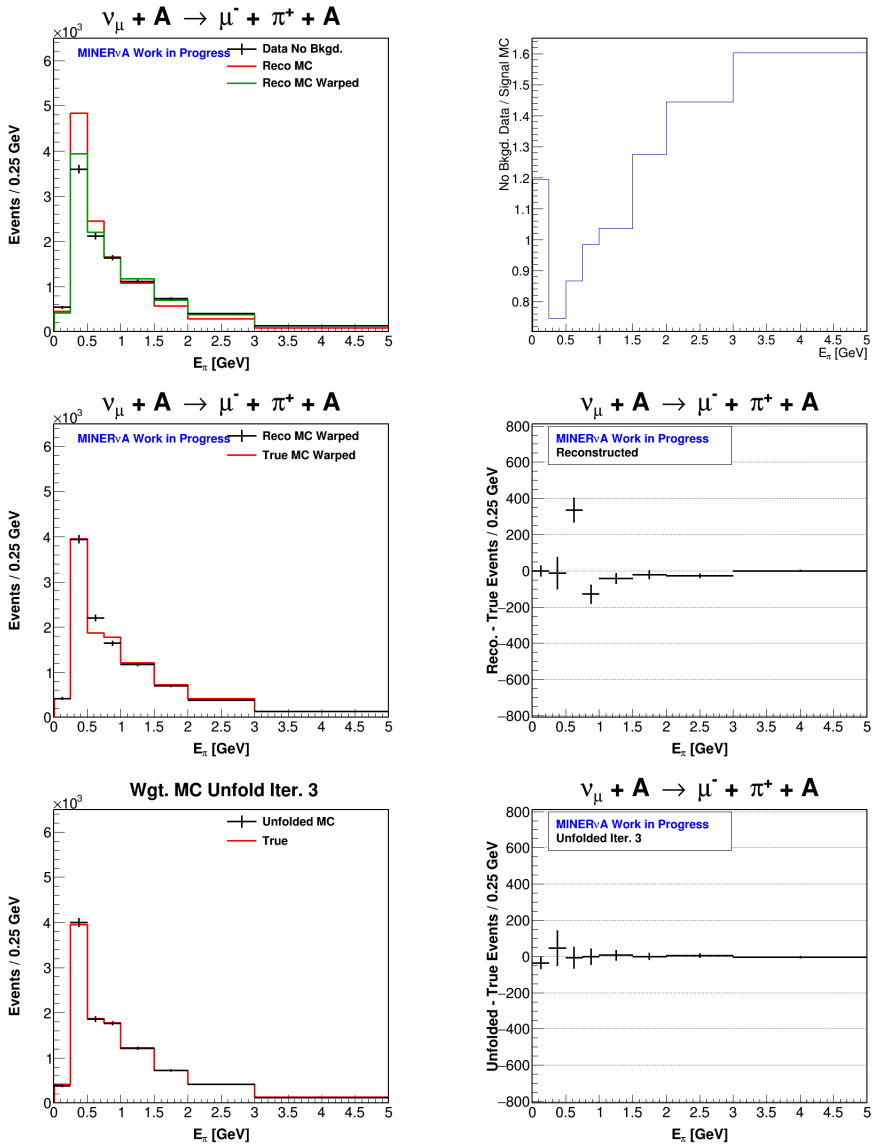

Figure B.6: Unfolding study for the E_π in the hydrocarbon target. Top left: reconstructed MC and reconstructed MC warped compared to the background subtracted data; top right: background-subtracted data/reconstructed MC used as warping function; middle left: warped reconstructed and true MC before unfolding; middle right: reconstructed-true before unfolding; bottom left: unfolded warped MC after the second iteration; bottom right: unfolded-true after the second iteration.

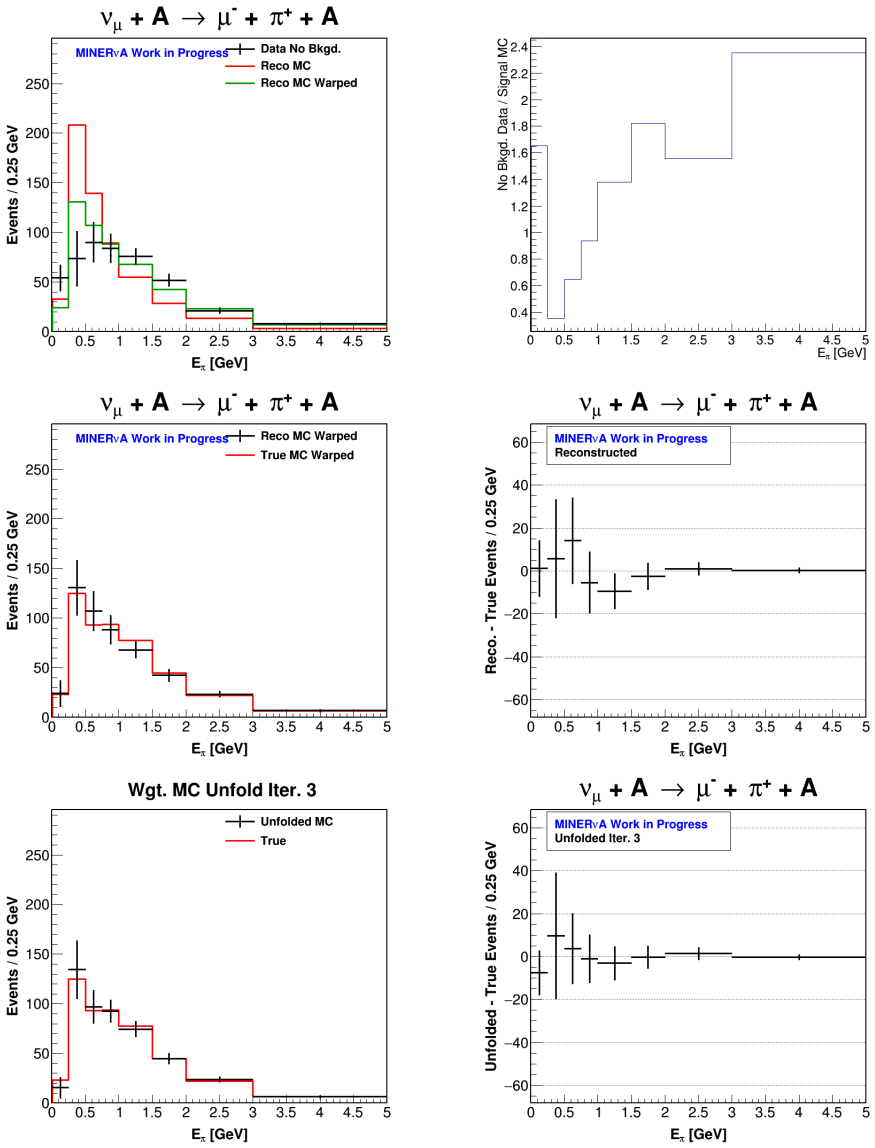

Figure B.7: Unfolding study for the E_π in the iron target. Top left: reconstructed MC and reconstructed MC warped compared to the background subtracted data; top right: background-subtracted data/reconstructed MC used as warping function; middle left: warped reconstructed and true MC before unfolding; middle right: reconstructed-true before unfolding; bottom left: unfolded warped MC after the second iteration; bottom right: unfolded-true after the second iteration.

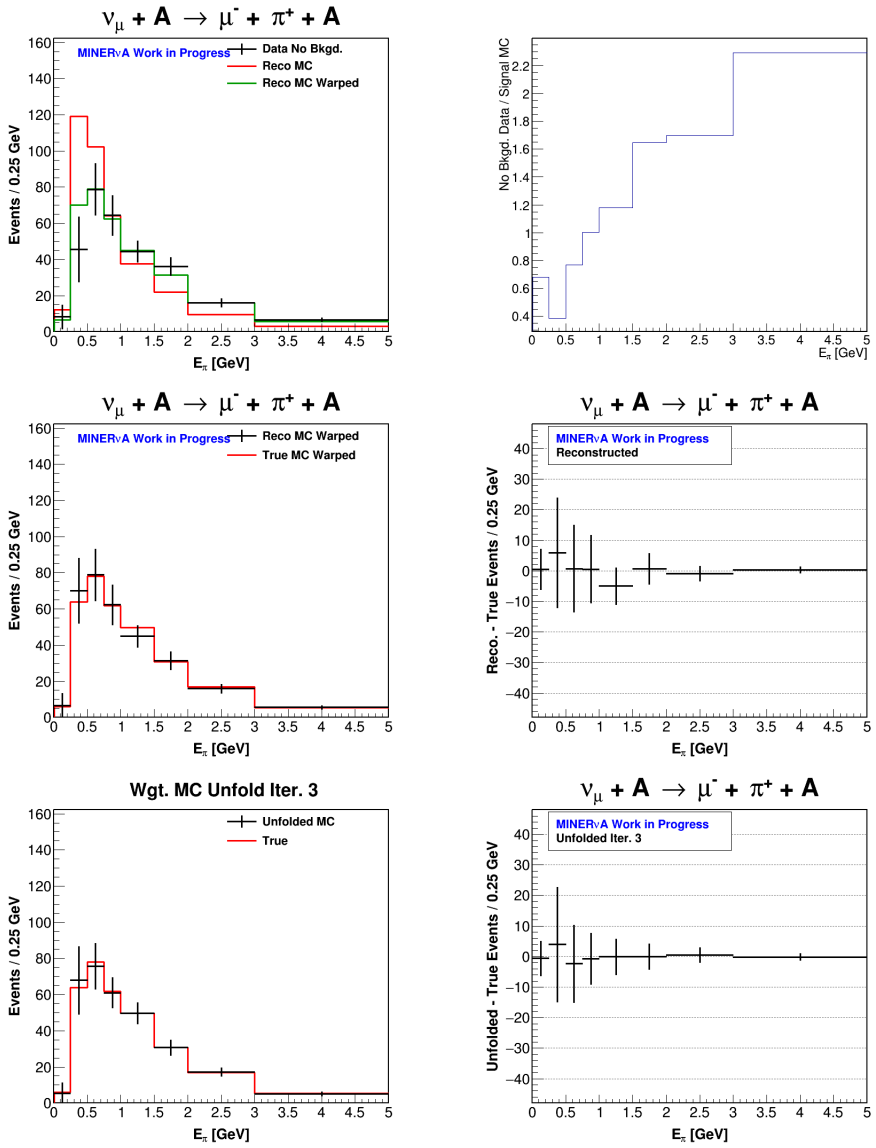

Figure B.8: Unfolding study for the E_π in the lead target. Top left: reconstructed MC and reconstructed MC warped compared to the background subtracted data; top right: background-subtracted data/reconstructed MC used as warping function; middle left: warped reconstructed and true MC before unfolding; middle right: reconstructed-true before unfolding; bottom left: unfolded warped MC after the second iteration; bottom right: unfolded-true after the second iteration.

B.3 θ_π Unfolding Study

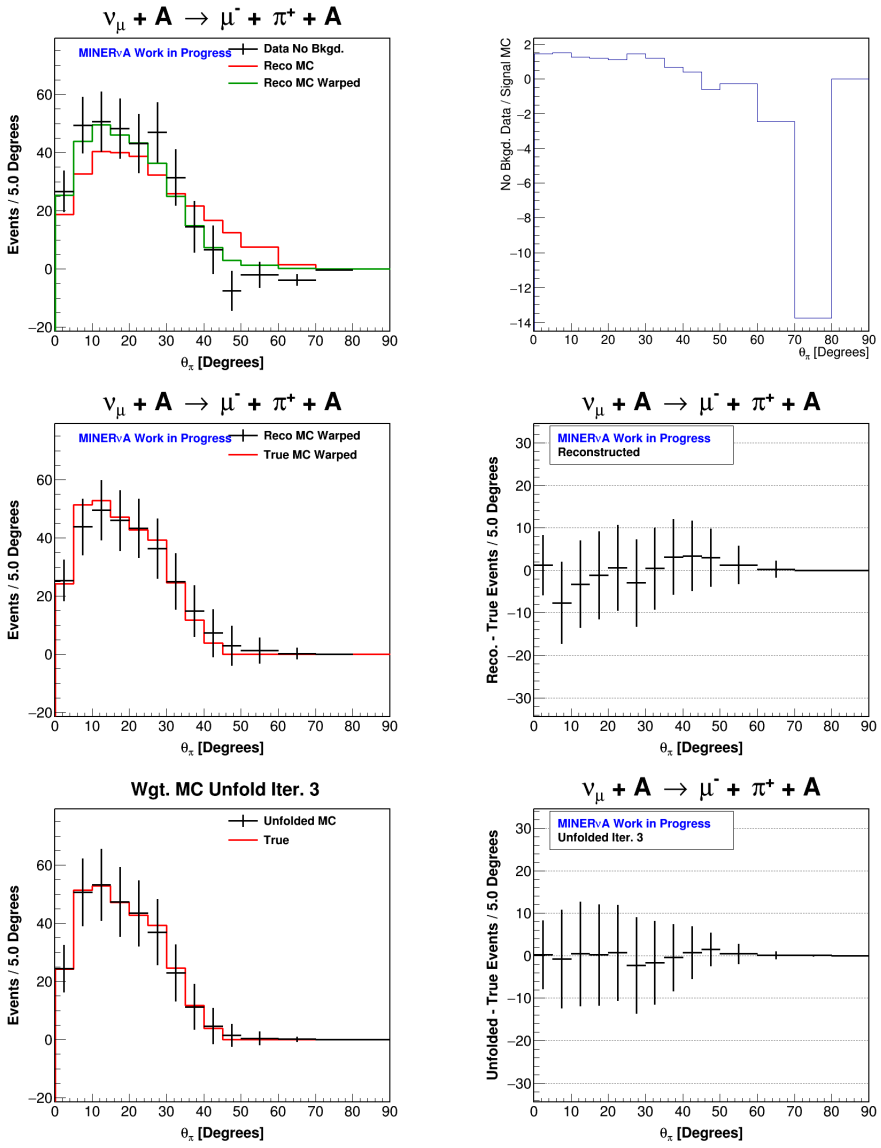

Figure B.9: Unfolding study for the θ_π in the carbon target. Top left: reconstructed MC and reconstructed MC warped compared to the background subtracted data; top right: background-subtracted data/reconstructed MC used as warping function; middle left: warped reconstructed and true MC before unfolding; middle right: reconstructed-true before unfolding; bottom left: unfolded warped MC after the second iteration; bottom right: unfolded-true after the second iteration.

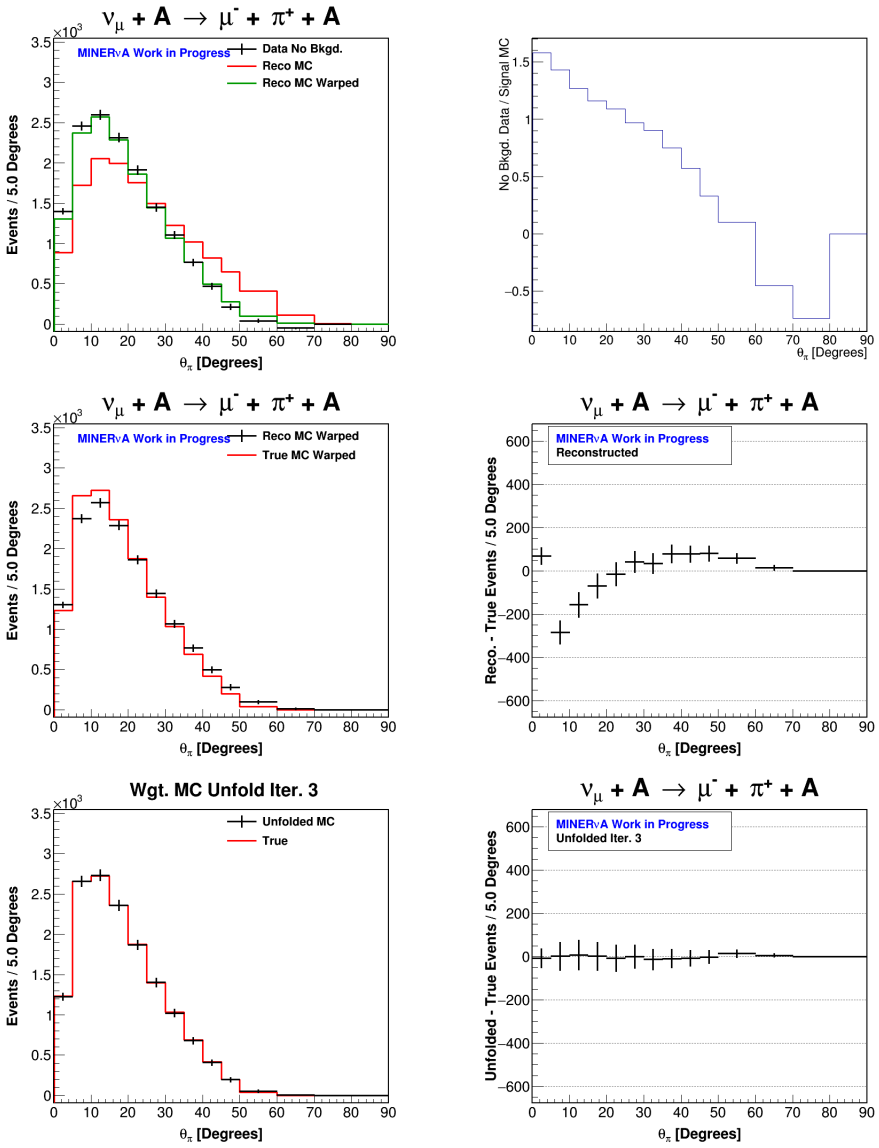

Figure B.10: Unfolding study for the θ_π in the hydrocarbon target. Top left: reconstructed MC and reconstructed MC warped compared to the background subtracted data; top right: background-subtracted data/reconstructed MC used as warping function; middle left: warped reconstructed and true MC before unfolding; middle right: reconstructed-true before unfolding; bottom left: unfolded warped MC after the second iteration; bottom right: unfolded-true after the second iteration.

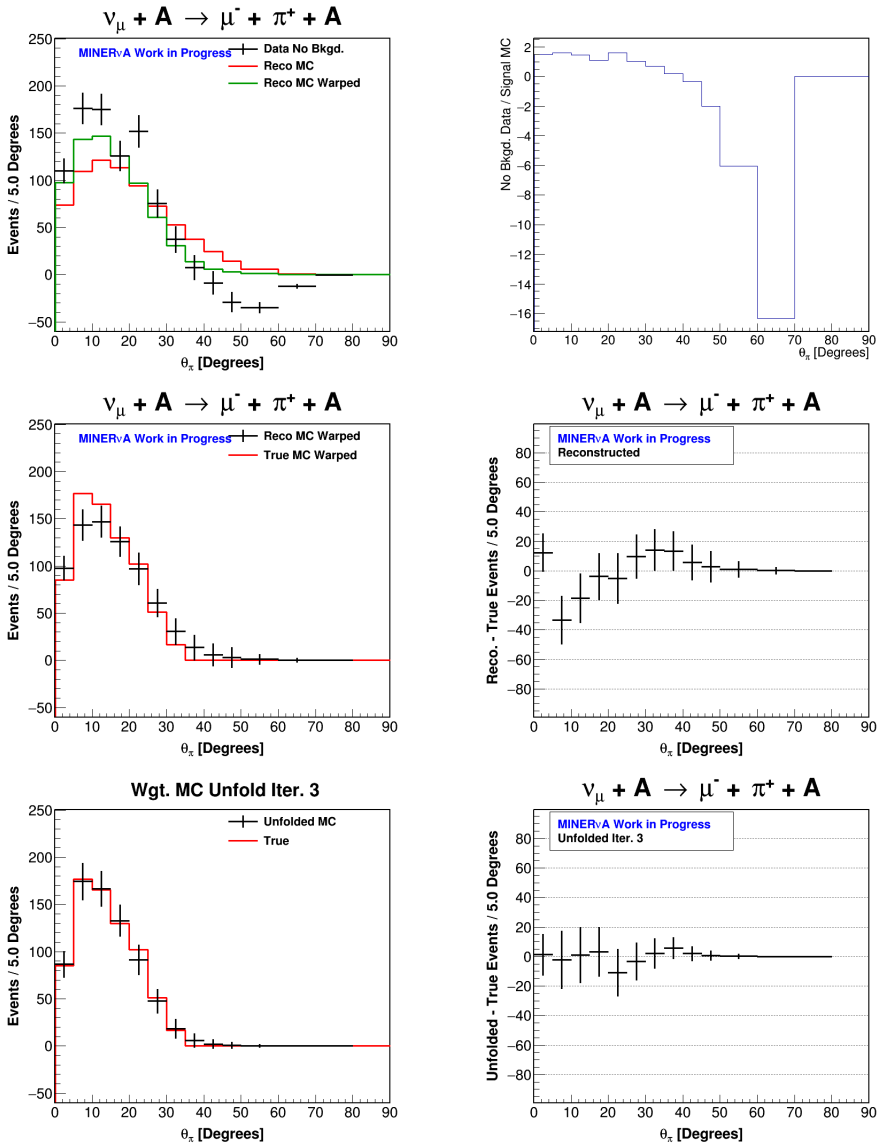

Figure B.11: Unfolding study for the θ_π in the iron target. Top left: reconstructed MC and reconstructed MC warped compared to the background subtracted data; top right: background-subtracted data/reconstructed MC used as warping function; middle left: warped reconstructed and true MC before unfolding; middle right: reconstructed-true before unfolding; bottom left: unfolded warped MC after the second iteration; bottom right: unfolded-true after the second iteration.

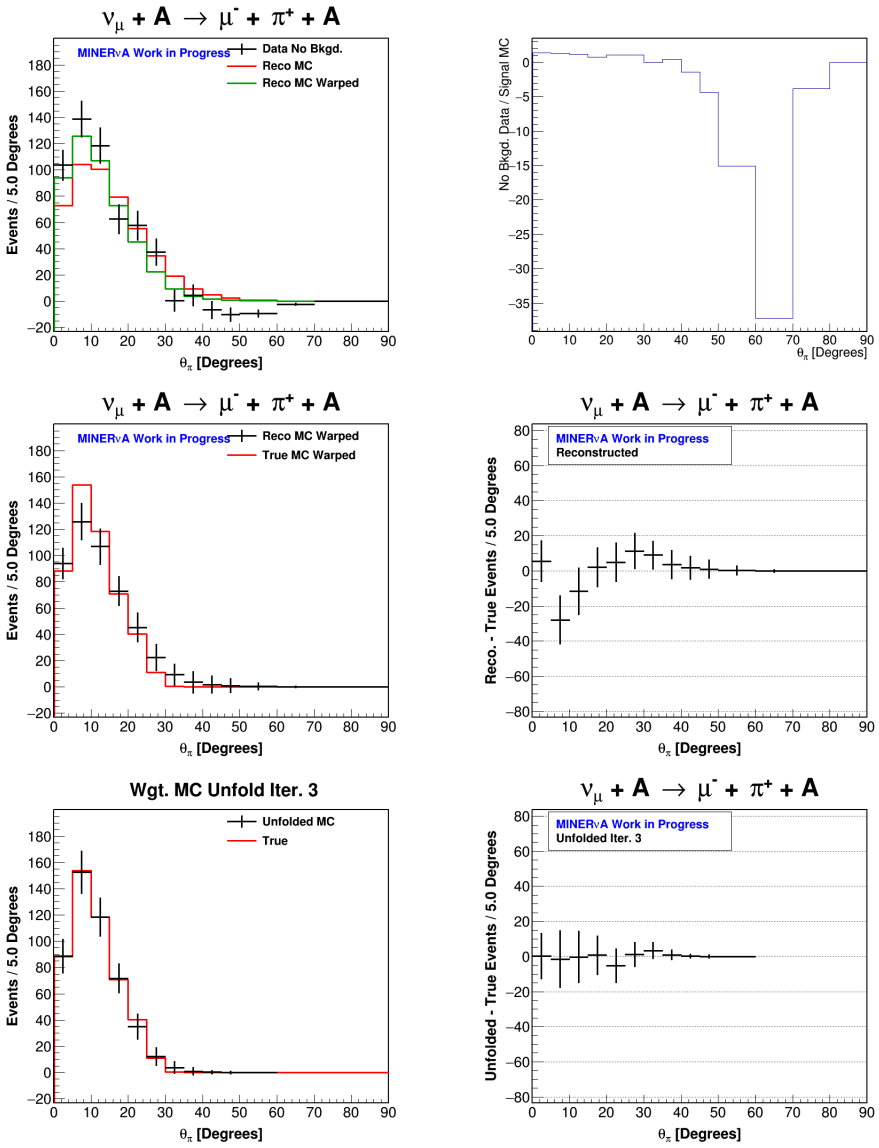

Figure B.12: Unfolding study for the θ_π in the lead target. Top left: reconstructed MC and reconstructed MC warped compared to the background subtracted data; top right: background-subtracted data/reconstructed MC used as warping function; middle left: warped reconstructed and true MC before unfolding; middle right: reconstructed-true before unfolding; bottom left: unfolded warped MC after the second iteration; bottom right: unfolded-true after the second iteration.

B.4 Q^2 Unfolding Study

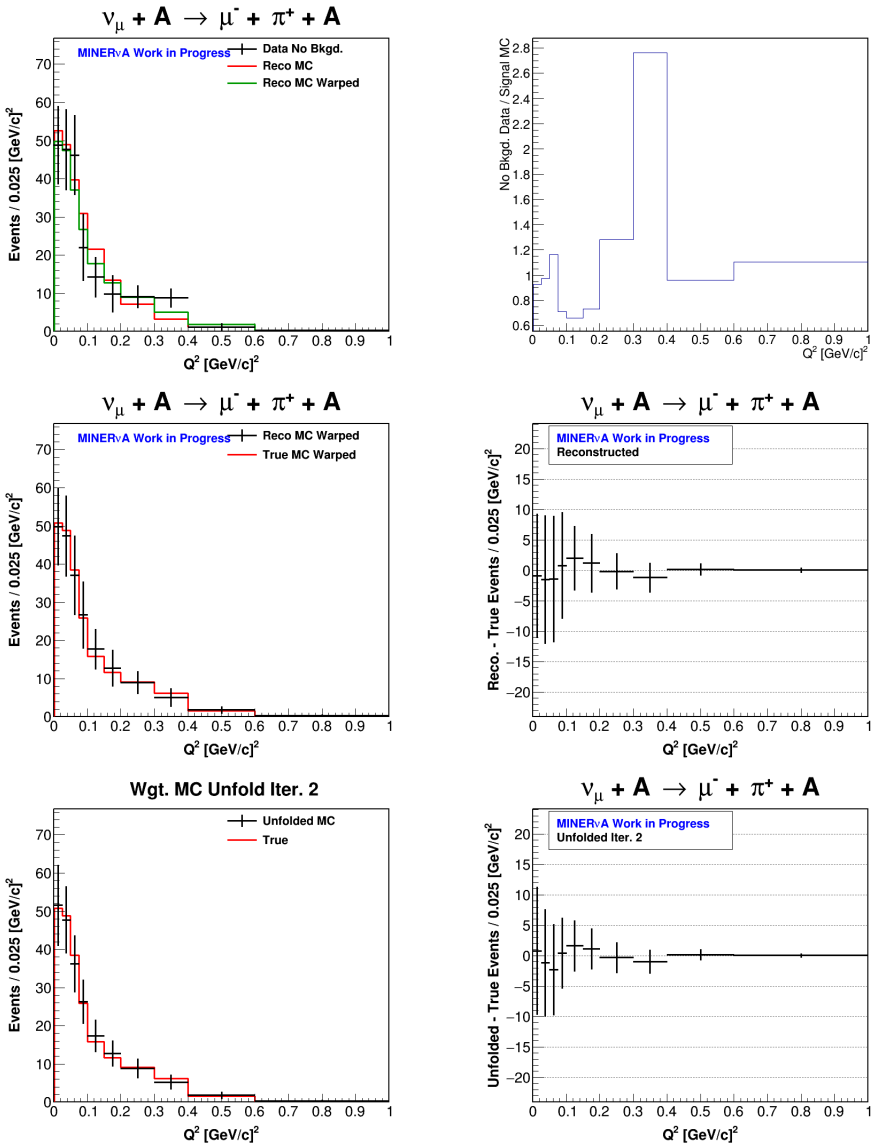

Figure B.13: Unfolding study for the Q^2 in the carbon target. Top left: reconstructed MC and reconstructed MC warped compared to the background subtracted data; top right: background-subtracted data/reconstructed MC used as warping function; middle left: warped reconstructed and true MC before unfolding; middle right: reconstructed-true before unfolding; bottom left: unfolded warped MC after the second iteration; bottom right: unfolded-true after the second iteration.

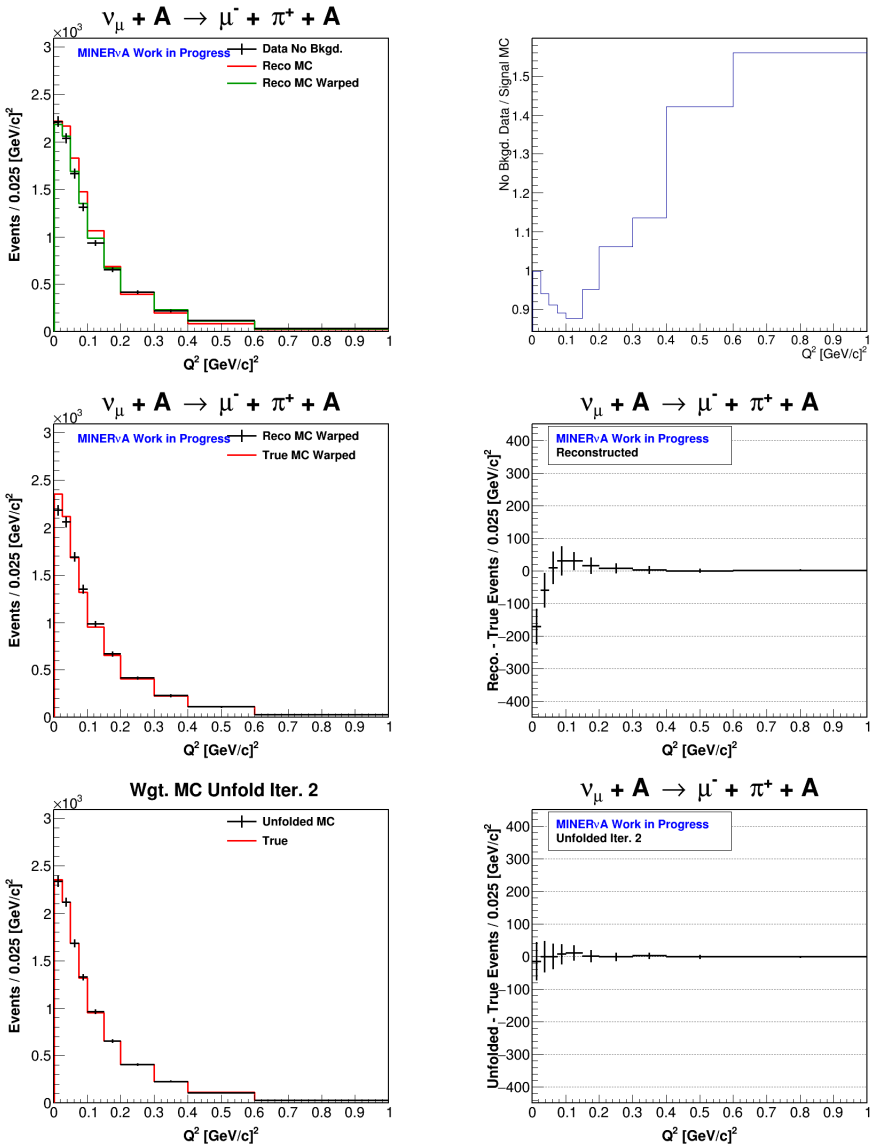

Figure B.14: Unfolding study for the Q^2 in the hydrocarbon target. Top left: reconstructed MC and reconstructed MC warped compared to the background subtracted data; top right: background-subtracted data/reconstructed MC used as warping function; middle left: warped reconstructed and true MC before unfolding; middle right: reconstructed-true before unfolding; bottom left: unfolded warped MC after the second iteration; bottom right: unfolded-true after the second iteration.

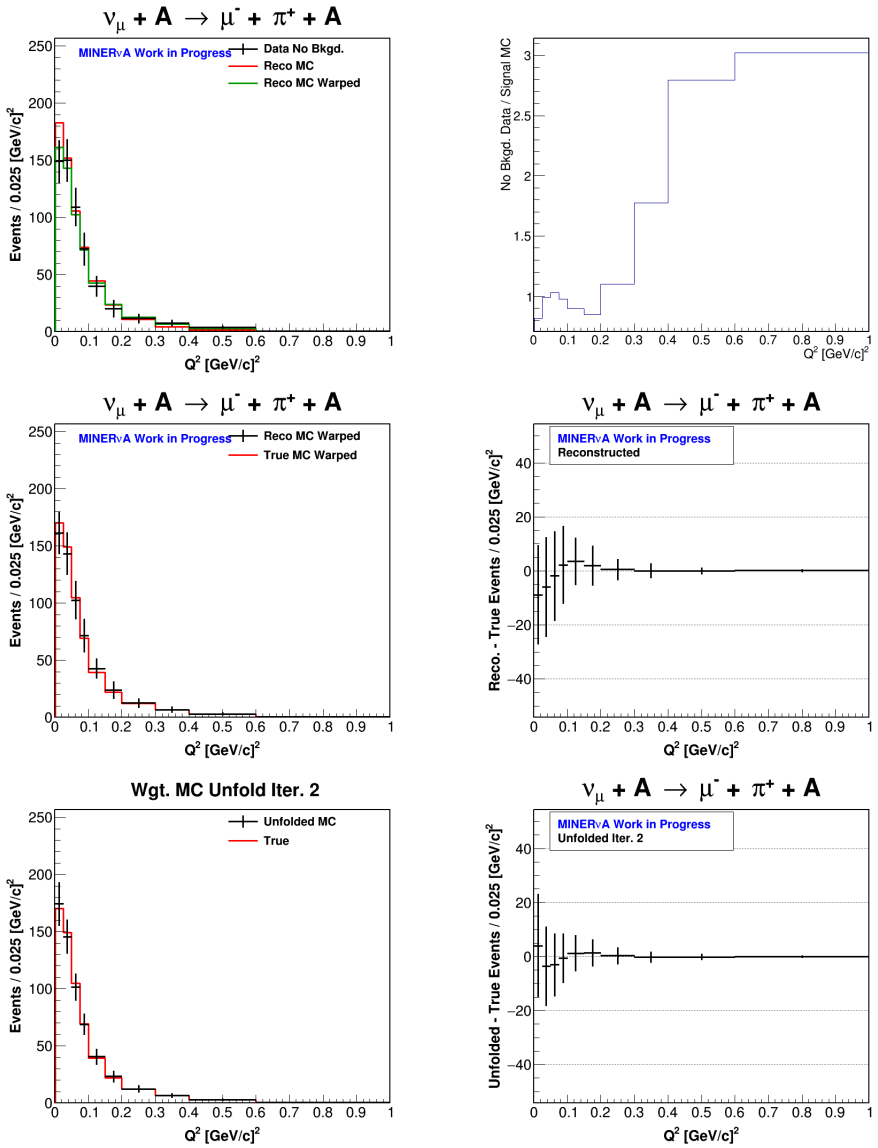

Figure B.15: Unfolding study for the Q^2 in the iron target. Top left: reconstructed MC and reconstructed MC warped compared to the background subtracted data; top right: background-subtracted data/reconstructed MC used as warping function; middle left: warped reconstructed and true MC before unfolding; middle right: reconstructed-true before unfolding; bottom left: unfolded warped MC after the second iteration; bottom right: unfolded-true after the second iteration.

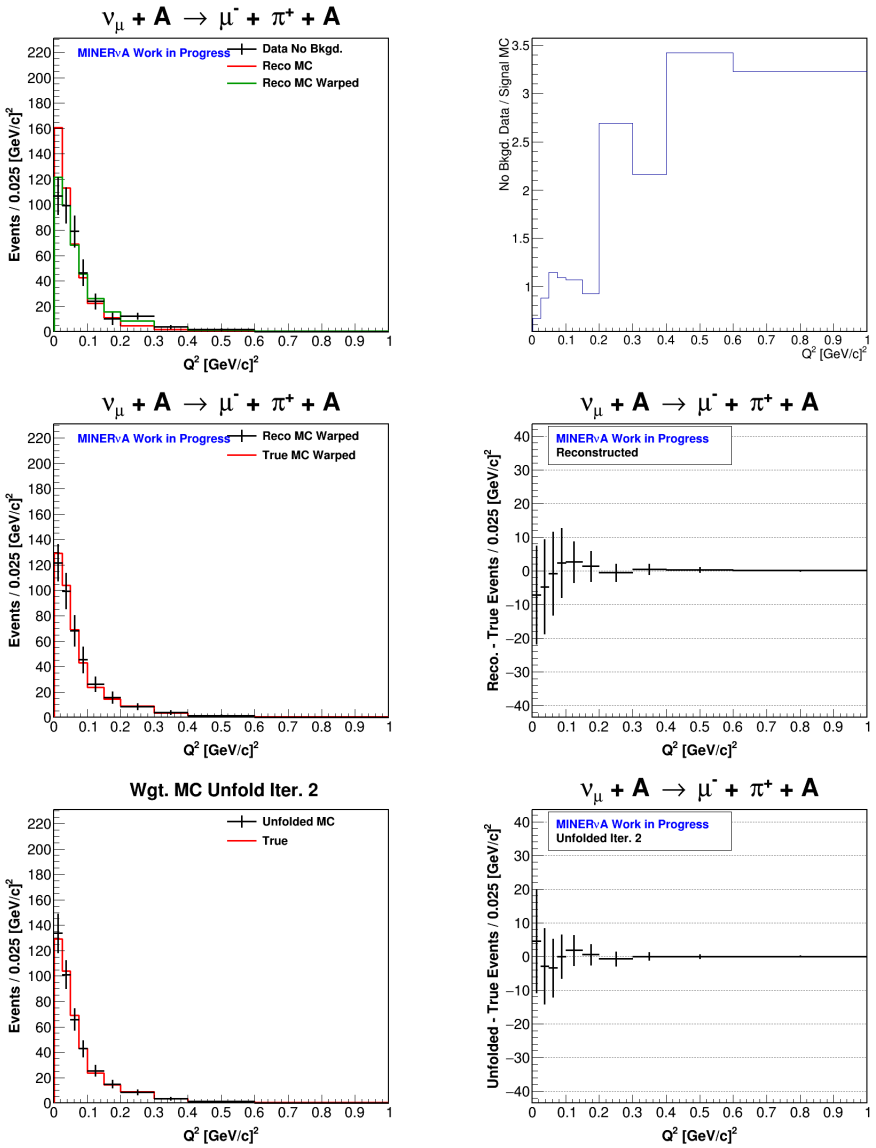

Figure B.16: Unfolding study for the Q^2 in the lead target. Top left: reconstructed MC and reconstructed MC warped compared to the background subtracted data; top right: background-subtracted data/reconstructed MC used as warping function; middle left: warped reconstructed and true MC before unfolding; middle right: reconstructed-true before unfolding; bottom left: unfolded warped MC after the second iteration; bottom right: unfolded-true after the second iteration.

Appendix C

Breakdown of the Cross Section Systematic Errors

The systematic error summary of the measured cross sections in section 6.11 is broken down for the "interaction model" and "detector model" systematic error groups as follows

- Interaction Model
  - CCQE & NCEL (charged current quasi-elastic and neutral current elastic)
  - CC Resonance
  - Non-Resonant π Production
  - Deep Inelastic Scattering
  - Final State Interactions
  - Hadronization & Resonant Decay
- Detector Model
  - Muon Energy
  - Hadron Response
  - Pion Inelastic σ
  - Proton Inelastic σ
  - Neutron Path length
  - Muon Tracking Efficiency
  - Beam Angle

The uncertainties on the "Interaction Model" group, correspond to the uncertainty in each of the neutrino interaction listed, as built in the GENIE generator version 2.8.4 [132]. Figures C.1 to C.4 show the breakdown of the two groups above, in the $\sigma\left(E_\nu\right)$, $d\sigma/dE_\pi$, $d\sigma/d\theta_\pi$ and $d\sigma/dQ^2$ cross sections in all four materials under study.

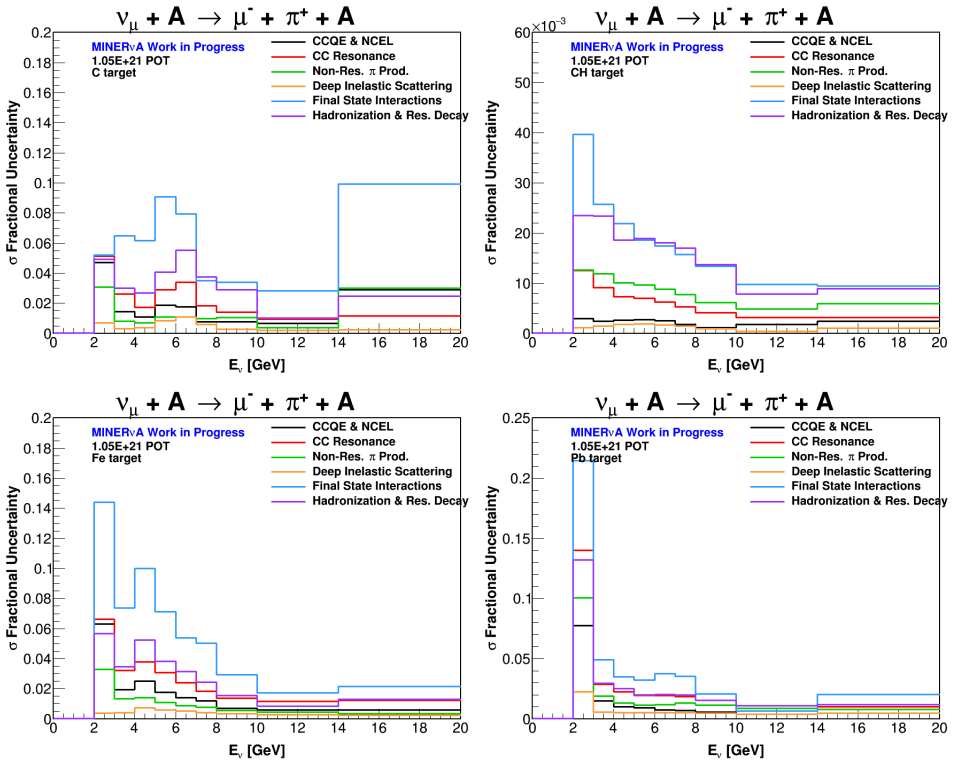

Figure C.1: Fractional uncertainties in the interaction model systematic group, in the $\sigma\left(E_\nu\right)$ cross section, in the C, CH, Fe and Pb targets.

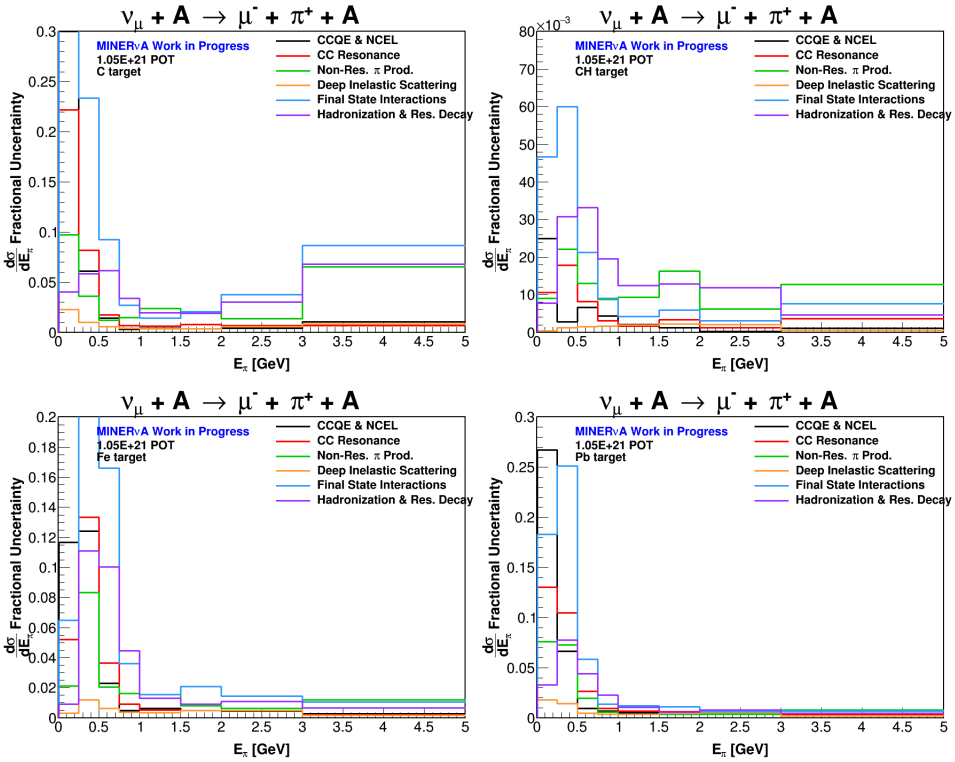

Figure C.2: Fractional uncertainties in the interaction model systematic group, in the $d\sigma/dE_\pi$ cross section, in the C, CH, Fe and Pb targets.

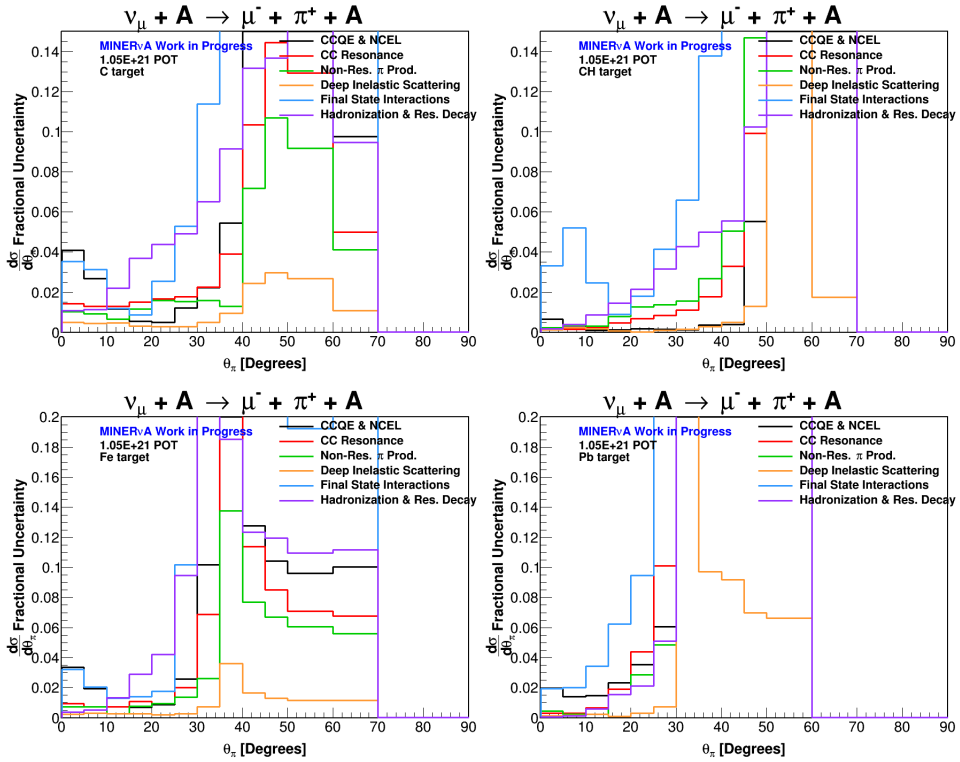

Figure C.3: Fractional uncertainties in the interaction model systematic group, in the $d\sigma/d\theta_\pi$ cross section, in the C, CH, Fe and Pb targets.

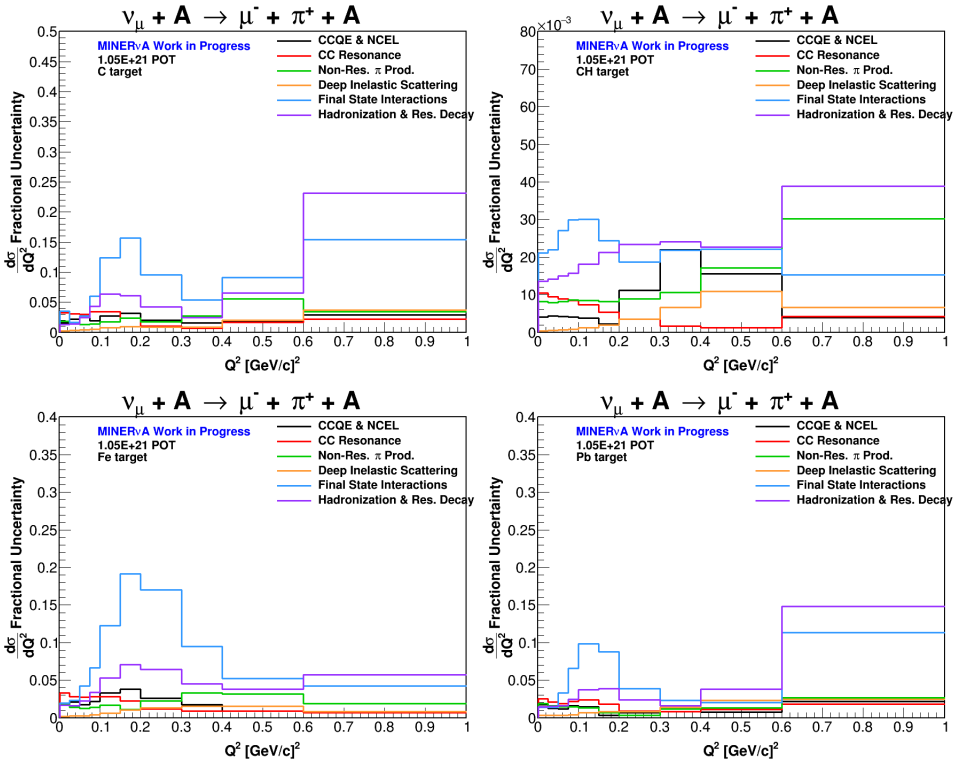

Figure C.4: Fractional uncertainties in the interaction model systematic group, in the $d\sigma/dQ^2$ cross section, in the C, CH, Fe and Pb targets.

Appendix D

Preliminary Cross Section Ratios

This chapter shows a prelimiary look of the ratios of the total cros sections in the Fe and Pb targets with respect to the total cross section in the CH target, which is used as the reference.

The errors in the cross sections need a further treatment of the error propagation. The tuned background in the passive targets is also expected to change due to ongoing improvements of some of the weights applied to the MC predictions (see section 6.1). When not available to the passive materials used, an extra systematic could be applied to cover discrepancies.

The most popular scaling patterns are the $A^{1/3}$ used in the Rein-Sehgal model [4], $A^{2/3}$ used in the Berger-Sehgal model [6]. If the data were close to any of these predictions, one would expect the following ratios

$$\frac{\sigma\left(E_\nu^{Fe}\right)}{\sigma\left(E_\nu^{CH}\right)} \approx \frac{56^{1/3}}{12^{1/3}} = 1.671 \tag{D.1}$$

$$\frac{\sigma\left(E_\nu^{Pb}\right)}{\sigma\left(E_\nu^{CH}\right)} \approx \frac{207^{1/3}}{12^{1/3}} = 2.584 \tag{D.2}$$

$$\frac{\sigma\left(E_\nu^{Fe}\right)}{\sigma\left(E_\nu^{CH}\right)} \approx \frac{56^{2/3}}{12^{2/3}} = 2.793 \tag{D.3}$$

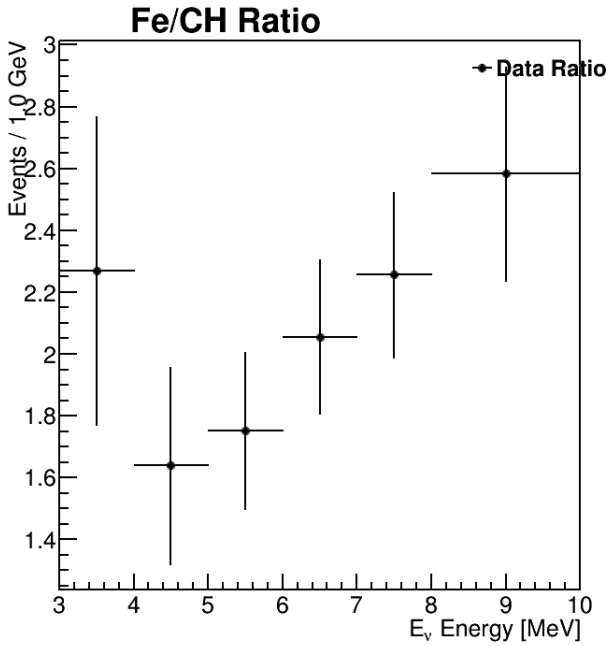

Figure D.1: $\frac{\sigma\left(E_\nu^{Fe}\right)}{\sigma(E_\nu^{CH})}$ preliminary ratio.

$$\frac{\sigma\left(E_\nu^{Pb}\right)}{\sigma\left(E_\nu^{CH}\right)} \approx \frac{207^{2/3}}{12^{2/3}} = 6.676 \tag{D.4}$$

for the $A^{1/3}$ and $A^{2/3}$, respectively. An energy-dependent prediction has also been published [96]. Figures D.1 and D.2 show the preliminary cross section ratios.

It is clear that none of the ratios follow one of the 2 suggested scaling patterns. Of course it might well be that the scaling is a completely different function. In order to obtain a reliable ratio, the adjustments mentioned above need to be applied.

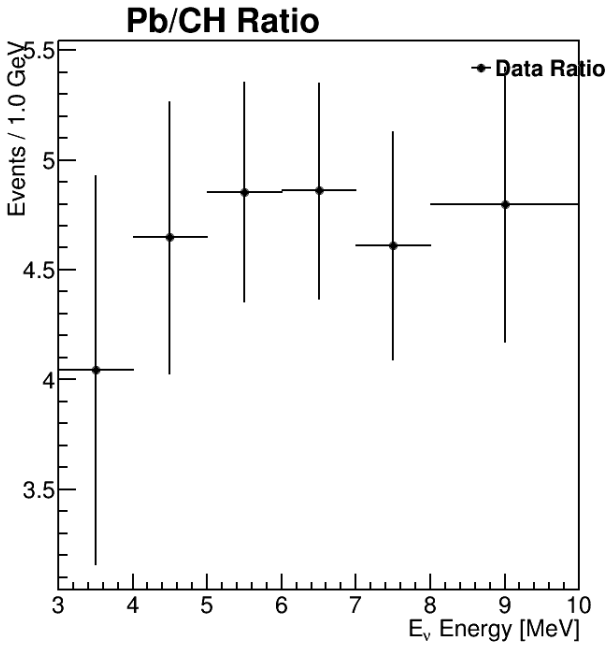

Figure D.2: $\frac{\sigma\left(E_\nu^{Pb}\right)}{\sigma(E_\nu^{CH})}$ preliminary ratio.

Appendix E

Importance of the Analysis

For practical purposes, neutrinos interact only through the weak force, that is, by exchanging a $W^{\pm}$ or Z boson. Whether a neutrino interacts with massive leptons, quarks, nucleons (neutrons and protons) or even entire nuclei, depends on the momentum transferred by the neutrino, the larger the wavelength of the momentum transferred, the larger the target the neutrino can interact with.
The coherent neutrino-production of pions happens when the neutrino scatters off the entire nucleus. The wavelength of the momentum transferred to the nucleus is larger than the nuclear radius, and because of this, the nucleons in the nucleus react in phase (coherently) producing a constructive interference. The phenomenology that leads to the production of a pion during the neutrino-nucleus interaction is not well understood.
Analogous to the electric current, there exists a "weak" current for weak interactions, which has a vector and an axial component. The vector component is conserved in hadronic interactions, while the axial part is not. The non-conservation of the "axial" current is used to build a hypothesis for the creation of the pion, in neutrino-nucleus coherent interactions.

The coherent production of pions by neutrinos can occur through the exchange of a $W^{\pm}$ (Charged Current, or "CC" channel) or through a Z boson (Neutral Current, or "NC" channel). Experiments in the 80s and 90s looked for both channels, to test the models that included the non-conservation of the axial current. These models were not just a test of the hypothesis of the phenomenology of the process, but an extra proof and confirmation of the neutral-current processes, recently discovered by then.
Although these models predicted the process could occur in nuclei of any size, those experiments used nuclei ranging from carbon (number of nucleons "A"= 12) to Bromine (A = 35). They measured the cross section of both the NC and CC channels of the

interaction, at relatively large neutrino energies ($\sim$ 150 GeV) ; and the NC channel at low energies ($\sim$ 2 GeV).

After the discovery of neutrino oscillations (neutrinos changing flavor as they travel), the coherent neutrino-production of pions regained interest because both the CC and NC channels mimic the signal in neutrino oscillation experiments. Considering a beam of muon neutrinos, the interaction's charged current channel (CC, exchange of a $W^{\pm}$ boson) produces a charged pion and a muon; while the neutral current channel (NC, exchange of a Z boson) produces a muon neutrino and a neutral pion, which promptly decays to two gammas. These particles, under some circumstances look the same as those produced in a neutrino interaction used to identify the oscillation of neutrinos.
These experiments work with neutrino energies in between $\sim$ 1 and $\sim$ 10 GeV, and therefore, new experiments were designed to find the CC coherent interaction at those energies. The first two attempts (2005 and 2009) were unsuccessful because of detector limitations and deficiencies in the model.
In 2014 the MINERvA experiment was the first to measure the CC coherent neutrino production of pions, thanks to its detector capabilities to fully contain the produced pions and measure their energy, and due to improvements on the model, which included the effect of the muon mass (neglected in the previous version of the model).

Given that the interaction had not been observed in heavy nuclei like steel or lead, neutrino oscillation experiments using those materials, extrapolated the cross section of the coherent production of pions from nuclei where the interaction was already measured, to those heavy nuclei, assuming a scaling of the cross section dependent on the number of nucleons in the nucleus. The proposed scalings went as $A^{1/3}$, $A^{2/3}$.
This analysis has been able to measure the cross section of the coherent pions produced by neutrinos, in steel and lead for the first time, which will allow a better estimate of their cross sections to be used by neutrino oscillation experiments. It has also achieved the measurement with the highest statistical sample until now, using a hydrocarbon target, which will allow to make more precise measurements of the process (like looking at a sub-sample of low energy neutrino-produced coherent pions for the first time). Finally, the measurement was done simultaneously in all materials, this will enable a measurement of the scaling of the cross section dependent on A, for the first time.

Bibliography

[1] J. N. Bahcall, Solar neutrinos: An overview, Phys. Rept. 333 (2000) 47–62. doi:10.1016/S0370-1573(00)00015-6.

[2] Juno experiment, http://www.staff.uni-mainz.de/wurmm/juno.html, mass hierarchy plots.

[3] David schmitz colloquium, https://minerva-docdb.fnal.gov/cgi-bin/private/RetrieveFile?docid=8273&filename=KU_colloquium.pdf&version=1, fermi National Laboratory.

[4] D. Rein, L. M. Sehgal, Coherent pi0 Production in Neutrino Reactions, Nucl. Phys. B223 (1983) 29–44. doi:10.1016/0550-3213(83)90090-1.

[5] D. Rein, L. M. Sehgal, PCAC and the Deficit of Forward Muons in pi+ Production by Neutrinos, Phys. Lett. B657 (2007) 207–209. arXiv:hep-ph/0606185, doi:10.1016/j.physletb.2007.10.025.

[6] C. Berger, L. M. Sehgal, PCAC and coherent pion production by low energy neutrinos, Phys. Rev. D79 (2009) 053003. arXiv:0812.2653, doi:10.1103/PhysRevD.79.053003.

[7] A. Mislivec, et al., Measurement of total and differential cross sections of neutrino and antineutrino coherent $\pi^{\pm}$ production on carbon, Phys. Rev. D97 (3) (2018) 032014. arXiv:1711.01178, doi:10.1103/PhysRevD.97.032014.

[8] H. Faissner, et al., Observation of Neutrino and Anti-neutrino Induced Coherent Neutral Pion Production Off ^{27}Al, Phys. Lett. 125B (1983) 230–236. doi:10.1016/0370-2693(83)91274-1.

[9] P. Marage, et al., OBSERVATION OF COHERENT DIFFRACTIVE CHARGED CURRENT INTERACTIONS OF ANTI-NEUTRINOS ON NEON NUCLEI, Phys. Lett. 140B (1984) 137–141. doi:10.1016/0370-2693(84)91064-5.

[10] P. Vilain, et al., Coherent single charged pion production by neutrinos, Phys. Lett. B313 (1993) 267–275. doi:10.1016/0370-2693(93)91223-A.

[11] M. Hasegawa, et al., Search for coherent charged pion production in neutrino-carbon interactions, Phys. Rev. Lett. 95 (2005) 252301. arXiv:hep-ex/0506008, doi:10.1103/PhysRevLett.95.252301.

[12] Y. Kurimoto, et al., Improved Measurement of Neutral Current Coherent π^0 Production on Carbon in a Few-GeV Neutrino Beam, Phys. Rev. D81 (2010) 111102. arXiv:1005.0059, doi:10.1103/PhysRevD.81.111102.

[13] Fermilab accelerator complex, https://www.fnal.gov/pub/science/particle-accelerators/accelerator-complex.html, accelerator complex web page.

[14] P. Adamson, et al., The NuMI Neutrino BeamarXiv:1507.06690.

[15] L. Aliaga, et al., Neutrino Flux Predictions for the NuMI Beam, Phys. Rev. D94 (9) (2016) 092005, [Addendum: Phys. Rev.D95,no.3,039903(2017)]. arXiv:1607.00704, doi:10.1103/PhysRevD.94.092005,10.1103/PhysRevD.95.039903.

[16] L. Aliaga, et al., Design, Calibration, and Performance of the MINERvA Detector, Nucl.Instrum.Meth. A743 (2014) 130–159. arXiv:1305.5199, doi:10.1016/j.nima.2013.12.053.

[17] G. N. Perdue, et al., The MINERνA Data Acquisition System and Infrastructure, Nucl. Instrum. Meth. A694 (2012) 179–192. arXiv:1209.1120, doi:10.1016/j.nima.2012.08.024.

[18] A. R. Mislivec, Measurement of Charged Current Coherent Pion Production by Neutrinos on Carbon at MINERνA, Ph.D. thesis, Rochester U. (2016). doi:10.2172/1341803.
URL http://lss.fnal.gov/archive/thesis/2000/fermilab-thesis-2016-30.pdf

[19] B. Messerly, Single Charged Pion Production by Muon Neutrinos in the MINERvA Detector Using the NuMI Beam, Ph.D. thesis, Pittsburgh U. (2019-12-03).
URL https://lss.fnal.gov/archive/thesis/2000/fermilab-thesis-2019-19.pdf

[20] M. Tanabashi, et al., Review of Particle Physics, Phys. Rev. D98 (3) (2018) 030001. doi:10.1103/PhysRevD.98.030001.

[21] E. Isiksal, D. Rein, J. G. Morfin, EVIDENCE FOR NEUTRINO AND ANTI-NEUTRINOS INDUCED COHERENT PI0 PRODUCTION, Phys. Rev. Lett. 52 (1984) 1096–1099. doi:10.1103/PhysRevLett.52.1096.

[22] H. J. Grabosch, et al., COHERENT PION PRODUCTION IN NEUTRINO AND ANTI-NEUTRINO INTERACTIONS ON NUCLEI OF HEAVY FREON MOLECULES, Z. Phys. C31 (1986) 203. doi:10.1007/BF01479528.

[23] F. Bergsma, et al., Measurement of the Cross-section of Coherent π^0 Production by Muon Neutrino and Anti-neutrino Neutral Current Interactions on Nuclei, Phys. Lett. 157B (1985) 469–474. doi:10.1016/0370-2693(85)90402-2.

[24] P. Marage, et al., Coherent Single Pion Production by Anti-neutrino Charged Current Interactions and Test of PCAC, Z. Phys. C31 (1986) 191–197. doi:10.1007/BF01479526.

[25] C. Baltay, et al., Evidence for Coherent Neutral Pion Production by High-energy Neutrinos, Phys. Rev. Lett. 57 (1986) 2629–2632. doi:10.1103/PhysRevLett.57.2629.

[26] A. A. Aguilar-Arevalo, et al., First Observation of Coherent π^0 Production in Neutrino Nucleus Interactions with $E_\nu < 2$ GeV, Phys. Lett. B664 (2008) 41–46. arXiv:0803.3423, doi:10.1016/j.physletb.2008.05.006.

[27] C. T. Kullenberg, et al., A Measurement of Coherent Neutral Pion Production in Neutrino Neutral Current Interactions in NOMAD, Phys. Lett. B682 (2009) 177–184. arXiv:0910.0062, doi:10.1016/j.physletb.2009.10.083.

[28] M. Aderholz, et al., Coherent Production of $\pi^+\pi^-$ Mesons by Charged Current Interactions of Neutrinos and Anti-neutrinos on Neon Nuclei at the Tevatron, Phys. Rev. Lett. 63 (1989) 2349. doi:10.1103/PhysRevLett.63.2349.

[29] S. Willocq, et al., Coherent production of single pions and rho mesons in charged current interactions of neutrinos and anti-neutrinos on neon nuclei at the Fermilab tevatron, Phys. Rev. D47 (1993) 2661–2674. doi:10.1103/PhysRevD.47.2661.

[30] K. Hiraide, et al., Search for Charged Current Coherent Pion Production on Carbon in a Few-GeV Neutrino Beam, Phys. Rev. D78 (2008) 112004. arXiv:0811.0369, doi:10.1103/PhysRevD.78.112004.

[31] A. Higuera, et al., Measurement of Coherent Production of $\pi^{\pm}$ in Neutrino and Antineutrino Beams on Carbon from E_{ν} of 1.5 to 20 GeV, Phys. Rev. Lett. 113 (26) (2014) 261802. arXiv:1409.3835, doi:10.1103/PhysRevLett.113.261802.

[32] R. Acciarri, et al., First Measurement of Neutrino and Antineutrino Coherent Charged Pion Production on Argon, Phys. Rev. Lett. 113 (26) (2014) 261801, [erratum: Phys. Rev. Lett.114,no.3,039901(2015)]. arXiv:1408.0598, doi:10.1103/PhysRevLett.113.261801,10.1103/PhysRevLett.114.039901.

[33] K. Abe, et al., Measurement of Coherent π^{+} Production in Low Energy Neutrino-Carbon Scattering, Phys. Rev. Lett. 117 (19) (2016) 192501. arXiv:1604.04406, doi:10.1103/PhysRevLett.117.192501.

[34] S. Tomonaga, On a relativistically invariant formulation of the quantum theory of wave fields, Prog. Theor. Phys. 1 (1946) 27–42. doi:10.1143/PTP.1.27.

[35] J. S. Schwinger, Quantum electrodynamics. I A covariant formulation, Phys. Rev. 74 (1948) 1439, [,36(1948)]. doi:10.1103/PhysRev.74.1439.

[36] R. P. Feynman, Space - time approach to quantum electrodynamics, Phys. Rev. 76 (1949) 769–789, [,99(1949)]. doi:10.1103/PhysRev.76.769.

[37] D. J. Griffiths, Introduction to elementary particles, TextBook Physics, Wiley, New York, NY, 1987. doi:10.1002/9783527618460.
URL https://cds.cern.ch/record/1260972

[38] E. H. Fradkin, F. A. Schaposnik, Chern-Simons gauge theories, confinement and the chiral spin liquid, Phys. Rev. Lett. 66 (1991) 276–289. doi:10.1103/PhysRevLett.66.276.

[39] K. G. Wilson, Confinement of Quarks, Phys. Rev. D10 (1974) 2445–2459, [,45(1974);,319(1974)]. doi:10.1103/PhysRevD.10.2445.

[40] E. Fermi, Tentativo di una teoria dell'emissione dei raggi beta, Ric. Sci. 4 (1933) 491–495.

[41] N. Cabibbo, Unitary Symmetry and Leptonic Decays, Phys. Rev. Lett. 10 (1963) 531–533, [,648(1963)]. doi:10.1103/PhysRevLett.10.531.

[42] S. L. Glashow, J. Iliopoulos, L. Maiani, Weak Interactions with Lepton-Hadron Symmetry, Phys. Rev. D2 (1970) 1285–1292. doi:10.1103/PhysRevD.2.1285.

[43] C. S. Wu, E. Ambler, R. W. Hayward, D. D. Hoppes, R. P. Hudson, Experimental Test of Parity Conservation in Beta Decay, Phys. Rev. 105 (1957) 1413–1414. doi:10.1103/PhysRev.105.1413.

[44] J. H. Christenson, J. W. Cronin, V. L. Fitch, R. Turlay, Evidence for the 2π Decay of the K_2^0 Meson, Phys. Rev. Lett. 13 (1964) 138–140. doi:10.1103/PhysRevLett.13.138.

[45] D. H. Perkins, Introduction to high energy physics, 1982.

[46] P. W. Higgs, Broken Symmetries and the Masses of Gauge Bosons, Phys. Rev. Lett. 13 (1964) 508–509, [,160(1964)]. doi:10.1103/PhysRevLett.13.508.

[47] F. Englert, R. Brout, Broken Symmetry and the Mass of Gauge Vector Mesons, Phys. Rev. Lett. 13 (1964) 321–323, [,157(1964)]. doi:10.1103/PhysRevLett.13.321.

[48] C. L. Cowan, F. Reines, F. B. Harrison, H. W. Kruse, A. D. McGuire, Detection of the free neutrino: A Confirmation, Science 124 (1956) 103–104. doi:10.1126/science.124.3212.103.

[49] L. M. Lederman, The Two-Neutrino Experiment, Sci. Am. 208N3 (1963) 60–70. doi:10.1038/scientificamerican0363-60.

[50] M. Nakamura, Result from DONUT: Direct observation of nu/tau interaction, Nucl. Phys. Proc. Suppl. 77 (1999) 259–264, [,259(1999)]. doi:10.1016/S0920-5632(99)00425-9.

[51] K. Kodama, et al., Observation of tau neutrino interactions, Phys. Lett. B504 (2001) 218–224. arXiv:hep-ex/0012035, doi:10.1016/S0370-2693(01)00307-0.

[52] M. Goldhaber, L. Grodzins, A. W. Sunyar, Helicity of Neutrinos, Phys. Rev. 109 (1958) 1015–1017. doi:10.1103/PhysRev.109.1015.

[53] T. Katori, Meson Exchange Current (MEC) Models in Neutrino Interaction Generators, AIP Conf. Proc. 1663 (1) (2015) 030001. arXiv:1304.6014, doi:10.1063/1.4919465.

[54] C. H. Llewellyn Smith, Neutrino Reactions at Accelerator Energies, Phys. Rept. 3 (1972) 261–379. doi:10.1016/0370-1573(72)90010-5.

[55] E. J. Beise, The Axial form-factor of the nucleon, Eur. Phys. J. A24S2 (2005) 43–46, [,43(2005)]. arXiv:nucl-ex/0501019, doi:10.1140/epjad/s2005-04-009-y.

[56] D. Rein, L. M. Sehgal, Neutrino Excitation of Baryon Resonances and Single Pion Production, Annals Phys. 133 (1981) 79–153. doi:10.1016/0003-4916(81)90242-6.

[57] A. Bodek, U. K. Yang, Higher twist, xi(omega) scaling, and effective LO PDFs for lepton scattering in the few GeV region, J. Phys. G29 (2003) 1899–1906. arXiv:hep-ex/0210024, doi:10.1088/0954-3899/29/8/369.

[58] R. A. Smith, E. J. Moniz, NEUTRINO REACTIONS ON NUCLEAR TARGETS, Nucl. Phys. B43 (1972) 605, [Erratum: Nucl. Phys.B101,547(1975)]. doi:10.1016/0550-3213(75)90612-4,10.1016/0550-3213(72)90040-5.

[59] H. Hassanabadi, A. Armat, L. Naderi, Relativistic Fermi-Gas Model for Nucleus, Found. Phys. 44 (11) (2014) 1188–1194. doi:10.1007/s10701-014-9836-7.

[60] O. Artiles, Multinucleon Short-Range Correlation Model for Nuclear Spectral Functions, Ph.D. thesis, Florida Intl. U. (2017). arXiv:1805.02778.

[61] J. Schwehr, D. Cherdack, R. Gran, GENIE implementation of IFIC Valencia model for QE-like 2p2h neutrino-nucleus cross sectionarXiv:1601.02038.

[62] J. Nieves, J. E. Amaro, M. Valverde, Inclusive quasi-elastic neutrino reactions, Phys. Rev. C70 (2004) 055503, [Erratum: Phys. Rev.C72,019902(2005)]. arXiv:nucl-th/0408005, doi:10.1103/PhysRevC.70.055503,10.1103/PhysRevC.72.019902.

[63] S. Dytman, GENIE final state interactions, AIP Conf. Proc. 1680 (1) (2015) 020005. doi:10.1063/1.4931864.

[64] O. Buss, T. Gaitanos, K. Gallmeister, H. van Hees, M. Kaskulov, O. Lalakulich, A. B. Larionov, T. Leitner, J. Weil, U. Mosel, Transport-theoretical Description of Nuclear Reactions, Phys. Rept. 512 (2012) 1–124. arXiv:1106.1344, doi:10.1016/j.physrep.2011.12.001.

[65] H. A. Bethe, Energy production in stars, Phys. Rev. 55 (1939) 434–456. doi:10.1103/PhysRev.55.434.

[66] Y. Fukuda, et al., Solar neutrino data covering solar cycle 22, Phys. Rev. Lett. 77 (1996) 1683–1686. doi:10.1103/PhysRevLett.77.1683.

[67] Y. Fukuda, et al., Measurements of the solar neutrino flux from Super-Kamiokande's first 300 days, Phys. Rev. Lett. 81 (1998) 1158–1162, [Erratum: Phys. Rev.

Lett.81,4279(1998)]. arXiv:hep-ex/9805021, doi:10.1103/PhysRevLett.81.1158,10.1103/PhysRevLett.81.4279.

[68] W. Hampel, et al., GALLEX solar neutrino observations: Results for GALLEX IV, Phys. Lett. B447 (1999) 127–133. doi:10.1016/S0370-2693(98)01579-2.

[69] J. N. Abdurashitov, et al., Measurement of the solar neutrino capture rate with gallium metal. III: Results for the 2002–2007 data-taking period, Phys. Rev. C80 (2009) 015807. arXiv:0901.2200, doi:10.1103/PhysRevC.80.015807.

[70] J. N. Bahcall, R. Davis, Jr., On the Problem of Detecting Solar Neutrinos.

[71] V. N. Gribov, B. Pontecorvo, Neutrino astronomy and lepton charge, Phys. Lett. 28B (1969) 493. doi:10.1016/0370-2693(69)90525-5.

[72] Y. Fukuda, et al., Evidence for oscillation of atmospheric neutrinos, Phys. Rev. Lett. 81 (1998) 1562–1567. arXiv:hep-ex/9807003, doi:10.1103/PhysRevLett.81.1562.

[73] Q. R. Ahmad, et al., Measurement of the rate of $\nu_e + d \to p + p + e^-$ interactions produced by ^8B solar neutrinos at the Sudbury Neutrino Observatory, Phys. Rev. Lett. 87 (2001) 071301. arXiv:nucl-ex/0106015, doi:10.1103/PhysRevLett.87.071301.

[74] M. Kobayashi, T. Maskawa, CP Violation in the Renormalizable Theory of Weak Interaction, Prog. Theor. Phys. 49 (1973) 652–657. doi:10.1143/PTP.49.652.

[75] Z. Maki, M. Nakagawa, S. Sakata, Remarks on the unified model of elementary particles, Prog. Theor. Phys. 28 (1962) 870–880, [,34(1962)]. doi:10.1143/PTP.28.870.

[76] J. A. Thomas, P. L. Vahle, Neutrino oscillations: Present status and future plans, World Scientific, Hackensack, USA, 2008. doi:10.1142/6615.

[77] A. Aguilar-Arevalo, et al., Evidence for neutrino oscillations from the observation of $\bar{\nu}_e$ appearance in a $\bar{\nu}_\mu$ beam, Phys. Rev. D64 (2001) 112007. arXiv:hep-ex/0104049, doi:10.1103/PhysRevD.64.112007.

[78] A. A. Aguilar-Arevalo, et al., Significant Excess of ElectronLike Events in the MiniBooNE Short-Baseline Neutrino Experiment, Phys. Rev. Lett. 121 (22) (2018) 221801. arXiv:1805.12028, doi:10.1103/PhysRevLett.121.221801.

[79] E. Aliu, et al., Evidence for muon neutrino oscillation in an accelerator-based experiment, Phys. Rev. Lett. 94 (2005) 081802. arXiv:hep-ex/0411038, doi:10.1103/PhysRevLett.94.081802.

[80] D. G. Michael, et al., Observation of muon neutrino disappearance with the MINOS detectors and the NuMI neutrino beam, Phys. Rev. Lett. 97 (2006) 191801. arXiv:hep-ex/0607088, doi:10.1103/PhysRevLett.97.191801.

[81] T. Araki, et al., Measurement of neutrino oscillation with KamLAND: Evidence of spectral distortion, Phys. Rev. Lett. 94 (2005) 081801. arXiv:hep-ex/0406035, doi:10.1103/PhysRevLett.94.081801.

[82] F. P. An, et al., Observation of electron-antineutrino disappearance at Daya Bay, Phys. Rev. Lett. 108 (2012) 171803. arXiv:1203.1669, doi:10.1103/PhysRevLett.108.171803.

[83] R. Acciarri, et al., Long-Baseline Neutrino Facility (LBNF) and Deep Underground Neutrino Experiment (DUNE)arXiv:1512.06148.

[84] K. Abe, et al., Hyper-Kamiokande Design ReportarXiv:1805.04163.

[85] N. Agafonova, et al., Observation of a first ν_τ candidate in the OPERA experiment in the CNGS beam, Phys. Lett. B691 (2010) 138–145. arXiv:1006.1623, doi:10.1016/j.physletb.2010.06.022.

[86] L. Wolfenstein, Neutrino Oscillations in Matter, Phys. Rev. D17 (1978) 2369–2374, [,294(1977)]. doi:10.1103/PhysRevD.17.2369.

[87] J. Schechter, J. W. F. Valle, Neutrino Masses in SU(2) x U(1) Theories, Phys. Rev. D22 (1980) 2227. doi:10.1103/PhysRevD.22.2227.

[88] A. Giuliani, A. Poves, Neutrinoless Double-Beta Decay, Adv. High Energy Phys. 2012 (2012) 857016. doi:10.1155/2012/857016.

[89] D. Akimov, et al., First Constraint on Coherent Elastic Neutrino-Nucleus Scattering in Argon, Phys. Rev. D100 (11) (2019) 115020. arXiv:1909.05913, doi:10.1103/PhysRevD.100.115020.

[90] M. Gell-Mann, M. Levy, The axial vector current in beta decay, Nuovo Cim. 16 (1960) 705. doi:10.1007/BF02859738.

[91] B. Z. Kopeliovich, PCAC and shadowing of low energy neutrinos, Nucl. Phys. Proc. Suppl. 139 (2005) 219–225, [,219(2004)]. arXiv:hep-ph/0409079, doi:10.1016/j.nuclphysbps.2004.11.222.

[92] F. Paccanoni, Pomeron exchange and t dependence of the scattering amplitude, Eur. Phys. J.direct 4 (1) (2002) 17. arXiv:hep-ph/0201062, doi:10.1007/s1010502c0017.

[93] E. A. Paschos, A. Kartavtsev, G. J. Gounaris, Coherent pion production by neutrino scattering off nuclei, Phys. Rev. D74 (2006) 054007. arXiv:hep-ph/0512139, doi:10.1103/PhysRevD.74.054007.

[94] K. S. Lackner, Coherent Meson Production as a Test for Neutral Weak Currents of Exotic Space-time Structure, Nucl. Phys. B153 (1979) 526–545. doi:10.1016/0550-3213(79)90615-1.

[95] H. Alvensleben, et al., Determination of strong-interaction nuclear radii, Phys. Rev. Lett. 24 (1970) 792–796. doi:10.1103/PhysRevLett.24.792.

[96] A. A. Belkov, B. Z. Kopeliovich, Adler Relation and Neutrino Production of Single Hadrons, Sov. J. Nucl. Phys. 46 (1987) 499, [Yad. Fiz.46,874(1987)].

[97] S. S. Gershtein, Yu. Ya. Komachenko, M. Yu. Khlopov, Fast Pion Production in Exclusive Neutrino Processes, Sov. J. Nucl. Phys. 32 (1980) 861, [Yad. Fiz.32(1980)].

[98] Yu. Ya. Komachenko, M. Yu. Khlopov, Exclusive Neutrino Production of Pseudoscalar Mesons in Neutral Currents, Yad. Fiz. 45 (1987) 467–477, [Sov. J. Nucl. Phys.45,295(1987)].

[99] E. A. Paschos, D. Schalla, Coherent Pion Production by Neutrinos, Phys. Rev. D80 (2009) 033005. arXiv:0903.0451, doi:10.1103/PhysRevD.80.033005.

[100] A. Higuera, E. A. Paschos, Angular Dependence of Coherent Pion Production by Neutrinos, Eur. Phys. J. Plus 129 (2014) 43. arXiv:1311.5149, doi:10.1140/epjp/i2014-14043-1.

[101] S. K. Singh, M. Sajjad Athar, S. Ahmad, Nuclear effects in neutrino induced coherent pion production at K2K and MiniBooNE, Phys. Rev. Lett. 96 (2006) 241801. arXiv:nucl-th/0601045, doi:10.1103/PhysRevLett.96.241801.

[102] L. Alvarez-Ruso, L. S. Geng, S. Hirenzaki, M. J. Vicente Vacas, Charged current neutrino induced coherent pion production, Phys. Rev. C75 (2007) 055501, [Erratum:

Phys. Rev.C80,019906(2009)]. arXiv:nucl-th/0701098, doi:10.1103/PhysRevC.75.055501,10.1103/PhysRevC.80.019906.

[103] J. E. Amaro, E. Hernandez, J. Nieves, M. Valverde, Theoretical study of neutrino-induced coherent pion production off nuclei at T2K and MiniBooNE energies, Phys. Rev. D79 (2009) 013002. arXiv:0811.1421, doi:10.1103/PhysRevD.79.013002.

[104] T. Leitner, U. Mosel, S. Winkelmann, Neutrino-induced coherent pion production off nuclei reexamined, Phys. Rev. C79 (2009) 057601. arXiv:0901.2837, doi:10.1103/PhysRevC.79.057601.

[105] E. Hernandez, J. Nieves, M. J. Vicente-Vacas, Neutrino Induced Coherent Pion Production off Nuclei and PCAC, Phys. Rev. D80 (2009) 013003. arXiv:0903.5285, doi:10.1103/PhysRevD.80.013003.

[106] S. L. Adler, Tests of the Conserved Vector Current and Partially Conserved Axial-Vector Current Hypotheses in High-Energy Neutrino Reactions, Phys. Rev. 135 (1964) B963–B966, [,136(1964)]. doi:10.1103/PhysRev.135.B963.

[107] R. P. Feynman, M. Gell-Mann, Theory of Fermi interaction, Phys. Rev. 109 (1958) 193–198, [,417(1958)]. doi:10.1103/PhysRev.109.193.

[108] R. M. Frank, J. L. Gammel, K. M. Watson, Optical Model Potential for Pion-Nucleus Scattering, Phys. Rev. 101 (1956) 891–901. doi:10.1103/PhysRev.101.891.

[109] S. L. Adler, Adventures in theoretical physics: Selected papers of Stephen L. Adler: Drafts of commentariesarXiv:hep-ph/0505177, doi:10.1142/5856.

[110] H. Faissner, H. Reithler, P. M. Zerwas (Eds.), Proceedings, International Neutrino Conference 1976, Vieweg, Vieweg, Braunschweig, 1977.
URL http://link.springer.com/book/10.1007%2F978-3-322-90614-4

[111] cern web page, https://home.cern/, conseil Européen pour la Recherche Nucléaire.

[112] R. Florent, Status report of bebc, Conf. Proc. C700610V2 (1970) 703–713.

[113] K. Abe, et al., The T2K Experiment, Nucl. Instrum. Meth. A659 (2011) 106–135. arXiv:1106.1238, doi:10.1016/j.nima.2011.06.067.

[114] I. Ambats, et al., The MINOS Detectors Technical Design Report.

[115] D. S. Ayres, et al., NOvA: Proposal to Build a 30 Kiloton Off-Axis Detector to Study $\nu_\mu \to \nu_e$ Oscillations in the NuMI BeamlinearXiv:hep-ex/0503053.

[116] C. Anderson, et al., The ArgoNeuT Detector in the NuMI Low-Energy beam line at Fermilab, JINST 7 (2012) P10019. arXiv:1205.6747, doi:10.1088/1748-0221/7/10/P10019.

[117] Fermilab web page, http://www.fnal.gov/, online; accesed 16-July-2015.

[118] F. G. Garcia, W. Pellico, FNAL Proton Source High Intensity Operations and Beam Loss Control, 2012. arXiv:1409.0039.
URL http://lss.fnal.gov/cgi-bin/find_paper.pl?conf-12-552

[119] Fermilab switchyard rookie book. a complete explanation of fermilab's beamlines and their components., http://www-bdnew.fnal.gov/operations/rookie_books/Switchyard_v3.3.pdf, online; accesed 16-July-2015.

[120] P. M. Lapostolle, PROTON LINEAR ACCELERATORS: A THEORETICAL AND HISTORICAL INTRODUCTION.

[121] R. Prakash, J. D. Kellenberger, A. Saini, Initial Assessment of Availability and Reliability for the PIP-II Superconducting Radio Frequency Linear Accelerator Facility, Submitted to: Reliable Eng. Sys. Safety.

[122] R. Ainsworth, P. Adamson, B. Brown, D. Capista, K. Hazelwood, I. Kourbanis, D. Morris, M. Xiao, M.-J. Yang, High Intensity Proton Stacking at Fermilab: 700 kW Running, in: Proceedings, 61st ICFA Advanced Beam Dynamics Workshop on High-Intensity and High-Brightness Hadron Beams (HB2018): Daejeon, Korea, June 17-22, 2018, 2018, p. TUA1WD04. doi:10.18429/JACoW-HB2018-TUA1WD04.
URL http://lss.fnal.gov/archive/2018/conf/fermilab-conf-18-262-ad.pdf

[123] R. P. Feynman, Very high-energy collisions of hadrons, Phys. Rev. Lett. 23 (1969) 1415–1417, [,494(1969)]. doi:10.1103/PhysRevLett.23.1415.

[124] C. Alt, et al., Inclusive production of charged pions in p+C collisions at 158-GeV/c beam momentum, Eur. Phys. J. C49 (2007) 897–917. arXiv:hep-ex/0606028, doi:10.1140/epjc/s10052-006-0165-7.

[125] S. Agostinelli, et al., GEANT4: A Simulation toolkit, Nucl. Instrum. Meth. A506 (2003) 250–303. doi:10.1016/S0168-9002(03)01368-8.

[126] E. Valencia, et al., Constraint of the MINERνA medium energy neutrino flux using neutrino-electron elastic scattering, Phys. Rev. D100 (9) (2019) 092001. arXiv:1906.00111, doi:10.1103/PhysRevD.100.092001.

[127] Minerva wiki, https://cdcvs.fnal.gov/redmine/projects/minerva/wiki/MINOS_and_MINERvA_Coordinate_Systems, mINERvA's Wiki Page.

[128] G. Barrand, et al., GAUDI - A software architecture and framework for building HEP data processing applications, Comput. Phys. Commun. 140 (2001) 45–55. doi:10.1016/S0010-4655(01)00254-5.

[129] L. Aliaga, et al., MINERvA neutrino detector response measured with test beam data, Nucl. Instrum. Meth. A789 (2015) 28–42. arXiv:1501.06431, doi:10.1016/j.nima.2015.04.003.

[130] B. Eberly, et al., Charged Pion Production in ν_μ Interactions on Hydrocarbon at $\langle E_\nu \rangle$= 4.0 GeV, Phys. Rev. D92 (9) (2015) 092008. arXiv:1406.6415, doi:10.1103/PhysRevD.92.092008.

[131] C. Andreopoulos, et al., The GENIE Neutrino Monte Carlo Generator, Nucl. Instrum. Meth. A614 (2010) 87–104. arXiv:0905.2517, doi:10.1016/j.nima.2009.12.009.

[132] C. Andreopoulos, C. Barry, S. Dytman, H. Gallagher, T. Golan, R. Hatcher, G. Perdue, J. Yarba, The GENIE Neutrino Monte Carlo Generator: Physics and User ManualarXiv:1510.05494.

[133] T. Golan, C. Juszczak, J. T. Sobczyk, Final State Interactions Effects in Neutrino-Nucleus Interactions, Phys. Rev. C86 (2012) 015505. arXiv:1202.4197, doi:10.1103/PhysRevC.86.015505.

[134] Y. Hayato, A neutrino interaction simulation program library NEUT, Acta Phys. Polon. B40 (2009) 2477–2489.

[135] T. T. Böhlen, F. Cerutti, M. P. W. Chin, A. Fassò, A. Ferrari, P. G. Ortega, A. Mairani, P. R. Sala, G. Smirnov, V. Vlachoudis, The FLUKA Code: Developments and Challenges for High Energy and Medical Applications, Nucl. Data Sheets 120 (2014) 211–214. doi:10.1016/j.nds.2014.07.049.

[136] W. J. Marciano, Z. Parsa, Neutrino electron scattering theory, J. Phys. G29 (2003) 2629–2645. arXiv:hep-ph/0403168, doi:10.1088/0954-3899/29/11/013.

[137] K. S. Kuzmin, V. V. Lyubushkin, V. A. Naumov, How to sum contributions into the total charged-current neutrino-nucleon cross sectionarXiv:hep-ph/0511308.

[138] Qsgp bert geant4 physics list, https://geant4.web.cern.ch/node/155, gEANT4 Physics List.

[139] H. W. Bertini, M. P. Guthrie, News item results from medium-energy intranuclear-cascade calculation, Nucl. Phys. A169 (1971) 670–672. doi:10.1016/0375-9474(71)90710-X.

[140] A. B. Kaidalov, The Quark-Gluon Structure of the Pomeron and the Rise of Inclusive Spectra at High-Energies, Phys. Lett. 116B (1982) 459–463. doi:10.1016/0370-2693(82)90168-X.

[141] Minerva event display., https://minerva05.fnal.gov/Arachne/arachne.html, mINERvA Event display webpage.

[142] R. Fruhwirth, Application of Kalman filtering to track and vertex fitting, Nucl. Instrum. Meth. A262 (1987) 444–450. doi:10.1016/0168-9002(87)90887-4.

[143] M. O. Wospakrik, Measurement of Neutrino Absolute Deep Inelastic Scattering Cross Section in Iron, Lead, Carbon, and Plastic Using MINERvA Detector at $E_\nu = 6GeV$, Ph.D. thesis, Florida U. (2018). doi:10.2172/1484178.
URL http://lss.fnal.gov/archive/thesis/2000/fermilab-thesis-2018-22.pdf

[144] C. Marshall, Measurement of charged kaon production by neutrinos at MINERvA, Ph.D. thesis, U. Rochester (2016). doi:10.2172/1325973.
URL http://lss.fnal.gov/archive/thesis/2000/fermilab-thesis-2016-12.pdf

[145] Z. Wang, et al., First evidence of coherent K^+ meson production in neutrino-nucleus scattering, Phys. Rev. Lett. 117 (6) (2016) 061802. arXiv:1606.08890, doi:10.1103/PhysRevLett.117.061802.

[146] C. E. Patrick, et al., Measurement of the Muon Antineutrino Double-Differential Cross Section for Quasielastic-like Scattering on Hydrocarbon at $E_\nu \sim 3.5$GeV, Phys. Rev. D97 (5) (2018) 052002. arXiv:1801.01197, doi:10.1103/PhysRevD.97.052002.

[147] C. Wilkinson, P. Rodrigues, S. Cartwright, L. Thompson, K. McFarland, Reanalysis of bubble chamber measurements of muon-neutrino induced single pion production, Phys. Rev. D90 (11) (2014) 112017. arXiv:1411.4482, doi:10.1103/PhysRevD.90.112017.

[148] P. Rodrigues, C. Wilkinson, K. McFarland, Constraining the GENIE model of neutrino-induced single pion production using reanalyzed bubble chamber data, Eur. Phys. J. C76 (8) (2016) 474. arXiv:1601.01888, doi:10.1140/epjc/s10052-016-4314-3.

[149] P. Stowell, et al., Tuning the GENIE Pion Production Model with MINERνA Data, Phys. Rev. D100 (7) (2019) 072005. arXiv:1903.01558, doi:10.1103/PhysRevD.100.072005.

[150] C. L. McGivern, et al., Cross sections for ν_μ and $\bar{\nu}_\mu$ induced pion production on hydrocarbon in the few-GeV region using MINERvA, Phys. Rev. D94 (5) (2016) 052005. arXiv:1606.07127, doi:10.1103/PhysRevD.94.052005.

[151] O. Altinok, et al., Measurement of ν_μ charged-current single π^0 production on hydrocarbon in the few-GeV region using MINERvA, Phys. Rev. D96 (7) (2017) 072003. arXiv:1708.03723, doi:10.1103/PhysRevD.96.072003.

[152] L. Aliaga Soplin, Neutrino Flux Prediction for the NuMI Beamline, Ph.D. thesis, William-Mary Coll. (2016). doi:10.2172/1250884.
URL http://lss.fnal.gov/archive/thesis/2000/fermilab-thesis-2016-03.pdf

[153] J. Neyman, E. S. Pearson, On the Problem of the Most Efficient Tests of Statistical Hypotheses, Phil. Trans. Roy. Soc. Lond. A231 (694-706) (1933) 289–337. doi:10.1098/rsta.1933.0009.

[154] G. D'Agostini, A Multidimensional unfolding method based on Bayes' theorem, Nucl. Instrum. Meth. A362 (1995) 487–498. doi:10.1016/0168-9002(95)00274-X.